THE CONSTITUTIVE RESPONSE OF BRAZING ALLOYS AND THE RESIDUAL STRESSES IN CERAMIC-METAL JOINTS

THÈSE N^{O} 3869 (2007)

PRÉSENTÉE LE 23 AOÛT 2007
À LA FACULTÉ DES SCIENCES ET TECHNIQUES DE L'INGÉNIEUR
LABORATOIRE DE MÉCANIQUE APPLIQUÉE ET D'ANALYSE DE FIABILITÉ
PROGRAMME DOCTORAL EN MÉCANIQUE

ÉCOLE POLYTECHNIQUE FÉDÉRALE DE LAUSANNE

POUR L'OBTENTION DU GRADE DE DOCTEUR ÈS SCIENCES

PAR

Matteo GALLI

laurea in ingegneria civile, Politecnico di Milano, Italie
et de nationalité italienne

acceptée sur proposition du jury:

Prof. L. Laloui, président du jury
Prof. I. Botsis, directeur de thèse
Dr J. Janczak-Rusch, rapporteur
Dr A. Rossoll, rapporteur
Prof. W. Tillmann, rapporteur

ÉCOLE POLYTECHNIQUE
FÉDÉRALE DE LAUSANNE

Suisse
2007

Ad Alberto, Anna e Francesca

Abstract

Nowadays the joining of dissimilar materials is often the only solution to fulfill the complex requirements of high technology applications. One of the fields in which the research activity is more intense and promising is that of the brazing of ceramics with metals. The performance of brazed ceramic-metal joints is limited by residual stresses which develop in the bonded assembly as it cools down after brazing. The magnitude and influence of these stresses can be particularly high because of the large difference between the thermomechanical properties of the two joining partners. Given the base materials and the joint geometry the relief of residual stresses mainly depends on the thermomechanical properties of the filler metal.

To study how variations of the properties of the braze alloy influence the residual stresses, an active brazing filler metal, Incusil™ABA®, was reinforced with SiC particles and was used to join the ceramic composite Si_3N_4/TiN to steel.

The characterization of the properties of the filler was carried out with a combined experimental and numerical approach: an experimental procedure for the production and mechanical testing of bulk specimens of reinforced and unreinforced braze filler metal was established and in parallel a three dimensional elastoplastic homogenization model was developed. The model was used both in an inverse homogenization approach, to identify the elastoplastic behaviour of the matrix alloys in the composite fillers at room temperature, and in the framework of straightforward homogenization, to obtain their temperature dependent properties.

Once the production procedures for the fabrication of joints were established, the experimental investigation on the joints followed two main directions: on one hand the residual strains were measured by X-ray diffraction while on the other hand the joint performance was evaluated by 4-point bend tests. Furthermore, optical microscopy and SEM/EDX investigations were carried out to compare the composite filler microstructures in the joints and in the tensile specimens. In parallel, finite element models were developed both for the prediction of residual stresses and for the evaluation of the evolution of the stress state in the joints during the bend tests. Finally a parametric study was carried out to study different joint layouts.

Keywords: ceramic-metal joints, active brazing, homogenization, residual stresses.

Resumé

De nos jours, la combinaison des matériaux différents est souvent la seule solution qui permet de remplir toutes les conditions requises pour des applications de haute technologie. Un des champs dans lesquels l'activité de recherche est la plus intense et prometteuse est celui du brasage des matériaux céramiques avec des métaux. La performance des joints brasés céramique-métal est limitée par les contraintes résiduelles qui se développent dans les assemblages pendant le refroidissement après le brasage. La magnitude et l'importance de ces contraintes peuvent être particulièrement grandes à cause de la grande différence entre les propriétés thermomécaniques des deux composants. Si les deux matériaux à joindre et la géométrie sont donnés, la relaxation des contraintes résiduelles dépend principalement des propriétés thermomécaniques de l'alliage de brasage. Pour étudier comment les variations de ces propriétés peuvent influencer les contraintes résiduelles, un alliage de brasage actif, Incusil™ABA®, a été renforcé avec des particules de SiC. Ce matériau de brasage composite actif a été ensuite utilisé pour joindre le composite céramique Si_3N_4/TiN à l'acier.

La caractérisation des propriétés de l'alliage a été réalisée avec une méthode combinée numérique-expérimentale: une procédure expérimentale a été établie pour la fabrication et le test des éprouvettes massives en alliage pur et renforcé. Parallèlement, un modèle tridimensionnel pour l'homogénéisation des propriétés elastoplastiques a été développé. Le modèle a été utilisé à la fois dans le cadre d'une homogénéisation inverse, pour identifier les propriétés elastoplastiques des matrices métalliques dans les composites, ainsi que pour l'homogénéisation directe des propriétés des composites en fonction de la température.

Après avoir établi les procédures pour la fabrication des joints, l'activité expérimentale sur les joints a suivi deux directions principales: d'un coté les contraintes résiduelles ont étés mesurées à l'aide de la technique basée sur la diffraction des rayons X, de l'autre la performance des joints a été testée au travers de tests de flexion quatre points. En outre, les microstructures ont étés étudiées par microscopie optique et électronique pour comparer la microstructure des éprouvettes en alliage massif avec celle dans les joints produits. En parallèle, des modèles d'éléments finis ont été développés pour la prédiction des contraintes résiduelles et de l'état de sollicitation dans les joints pendant les tests de flexion. Finalement, différentes configurations des joints ont été comparées à l'aide d'un modèle paramétrique.

Mots clés: joints céramique-métal, brasage actif, homogénéisation, contraintes résiduelles.

Acknowledgements

First of all, I would like to thank Prof. John Botsis and Dr. Jolanta Janczak-Rusch who gave me this unique opportunity and who trusted me throughout the whole project. I am very grateful to Prof. John Botsis for having supervised my thesis and for having supported and encouraged my work even in hard times, when results were lacking.

Merci to Dr. Joël Cugnoni for all the fruitful discussions during which he gave me ideas, suggestions and insights and above all for his friendship.

Special thanks to those who helped me in the experimental work: Dr. Daniele Piazza and Dr. HansRuedi Elsener for their help in developing the specimen production procedures, Venkatesh Sivasubramanian for his help with electron microscopy and Vinzenz Bissig, with whom I broke quite a lot of things in the labs at EMPA. Of course I have to mention the staff of the atelier: Marc Jeanneret, Gino Crivellari, Nicolas Favre and Stéphane Haldner.

I am grateful to Prof. Nava Setter, head of the Ceramics Laboratory at EPFL, and to her co-workers Jacques Castano and Dr. Dragan Damijanovic who welcomed me in their laboratory and let me be the only user of a brand new vacuum furnace.

A fundamental experiment, the measurement of residual strains, was carried out at Max Planck Institut in Stuttgart, where I enjoyed working with Dr. Udo Welzel and Gerd Maier, vielen Dank!

This work has also benefited from the collaboration with Marta Szankowska who carried out her master thesis under my supervision.

Many thanks to my colleagues for the coffee breaks (although you should drink coffee a bit faster) and the beer breaks (nothing to say in this case), I have enjoyed staying at LMAF for four years.

Since a PhD is not only a professional experience but also, if not mainly, an attempt to put off your boring adult life, I would like to thank those with whom I shared this prolongation of student life:

Fabiano, because sharing a flat and a lab for four years with someone who is not your wife is not trivial!

Anna, a close neighbour not only because her flat is one hundred metres from mine… Have a little faith!

Angelo and Ric for being worse than me both at bowling and at xboxing, aren't you?
Arianna for being worse than me at bowling, xboxing and SuperMarioKarting… No doubt!
DD with whom I spent some unforgettable hours at Malley ice rink waiting for girls who never turned up.
Thomas and the two other emigrants Alessandro and Davide, who gave me a place to stay when I was homeless in Dübendorf.
This work is dedicated to my family, I am sorry I cannot dedicate a nicer piece of writing but I suspect I will not have many other chances to write something like a book. Grazie.

TO DR. JUAN PUFI
FOR WHAT HE DID

TO FELIPE
FOR WHAT HE DID

WHAT
DID I DO?

Contents

List of Tables

List of Figures

List of Symbols

B	breadth
B	hardening parameter in Voce's hardening law
b	width
b	intercept of linear regression
C_{ijkl}	stiffness tensor
$\overline{C}_{ijkl}$	effective stiffness tensor
D_{ijkl}	compliance tensor
$\overline{D}_{ijkl}$	effective compliance tensor
D_1, $\frac{1}{2}D_2$	elastic constants in X-ray diffraction
d	lattice spacing
d_0	stress-free lattice spacing
E	Young's modulus
δE	energy variation
$F(\boldsymbol{x})$	objective function
$\boldsymbol{F}'(\boldsymbol{x})$	gradient of the objective function
$\boldsymbol{F}''(\boldsymbol{x})$, $\boldsymbol{H}$	Hessian matrix of the objective function
F_C	cubic interpolation of the objective function
F_L	linear extrapolation of the objective function
$\boldsymbol{f}$	vector of the residuals
f_i	i^{th} tetrahedron
G	shear modulus
g	acceleration of gravity
h	height
h	hardening parameter in the exponential hardening law
$\boldsymbol{h}$	descent direction
$\boldsymbol{J}_f$	Jacobian matrix
J_2'	second invariant of the stress deviator
K	hardening parameter in Voce's hardening law
k	hardening

L_{ijkl}	localization tensor
l_1	lower load span
l_2	upper load span
m	Weibull's parameter
M	fitting model
M	moment
m	Weibull's parameter
m	slope of linear regression
P	set of valid particles
P	dissipated energy
P	applied load
P_f	failure probability
p_i	i^{th} particle
$\overline{p}$	applied pressure
q	hardening parameter in the exponential hardening law
r	radius
δr	radius variation
r_{max}	maximum radius to edge ratio
S	set of nucleation points
$\widetilde{S}$	set of imposed nucleation points
s_i	i^{th} point
$\widetilde{s}_i$	i^{th} imposed nucleation point
T	temperature
t	time
t_i	i^{th} tetrahedron
U	Elastic energy
U^r	micro-stored elastic energy
$\overline{u}$	applied displacement
(u_i, y_i)	i^{th} data point
V_{uc}	unit cell volume
$\overline{V}_p$	particle volume
V_r	reinforcement volume fraction
v^t_{max}	maximum tetrahedron volume
W	width
$\boldsymbol{x}$	vector of unknown parameters
$\boldsymbol{x}^{id}$	identified parameters
$\Delta\boldsymbol{x}^{id}$	variation of the identified parameters
α	metric of the non-linearity of the objective function

α	coefficient of thermal expansion
$\overline{\alpha}$	effective coefficient of thermal expansion
α_{ij}	thermal expansion tensor
$\overline{\alpha}_{ij}$	effective thermal expansion tensor
β	optimization step length
γ	surface energy
δ_{ij}	Kronecker delta
ε_{ij}	strain tensor
ε^p	equivalent plastic strain
$\dot{\varepsilon}_{ij}$	strain rate tensor
η	ratio between actual and apparerent surface area
θ	contact angle
λ	wavelength
μ	damping parameter in Levenberg-Marqardt algorithm
ν	Poisson's ratio
ξ	unit cell size
ρ	density
σ_y	yield stress
$\sigma_I, \sigma_{II}, \sigma_{III}$	principal stresses
σ_∞	hardening parameter in Voce's hardening law
σ_0	Weibull's parameter
σ_{ij}	stress tensor
σ^r_{ij}	residual stress tensor
σ_{max}	nominal bend stress
φ	observed contact angle
φ	yield surface
φ	specimen rotation around the surface normal
ψ	tilt angle
Ω	three dimensional domain
$\partial\Omega$	boundary of Ω
$\ldots^0$	initial parameter value
$\ldots^{id}$	identified parameter value
$\langle\ldots\rangle$	volumetric average
$\ldots^{hkl}$	quantity referred to the *hkl* lattice planes
$\{\ldots\}$	average over diffracting crystallites

List of Abbreviations

ABA	Active Brazing Alloy
BSE	Back-Scattered Electron (image)
CDT	Constrained Delaunay Tetrahedralization
CTE	Coefficient of Thermal Expansion
EDM	Electro-Discharge Machining
EDX	Energy Dispersive X-ray (spectroscopy)
FE	Finite Element
MMC	Metal Matrix Composite
PRMMC	Particle Reinforced Metal Matrix Composite
RT	Room Temperature
RVE	Representative Volume Element
SEM	Scanning Electron Microscopy
XRD	X-Ray Diffraction

Chapter 1

Introduction

1.1 Why Join?

In the vast world related to materials and to their applications, there is an increasing request of highly reliable products to be used in extremely demanding conditions, in environments which require performances that no single material can offer by itself. Thus the approach is to select different materials providing, when assembled in the same structure, the required mechanical, thermal and chemical properties.

Nowadays the joining of dissimilar materials is very common and one of the fields where the research activity is more intense is that of the joining of ceramics with metals. Ceramics usually have low densities, are stiff and hard but brittle, are poor electrical and thermal conductors, are refractory and expand little when heated; they also can have very unique and very wide ranging properties: for example aluminum oxide is both electrically and thermally insulating while aluminum nitride, despite being strongly electrically insulating exhibits an high thermal conductivity. Metals tend to have different properties such as easier fabricability, electrical conductivity, low cost, but they generally lack the corrosion resistance and high durability of ceramics. There are many applications in which both ceramics and metals can be employed to maximize the performance and minimize the respective shortcomings; these include parts of engines, heat exchangers, cutting tools, articular prostheses, etc.

The possibility to exploit commercially the "peculiar" characteristics of metallic and ceramic materials often depends to a great extent on the ability to produce reliable joints, that is to say joints which have high mechanical strength, high durability and low production costs.

To this end five major processes for bonding can be identified:

- fusion welding, in which mating surface regions of components are melted and mixed before solidifying to form a permanent bond;

- brazing, in which liquid metal flows into a narrow gap between the mating surfaces and solidifies to form a permanent bond;
- diffusion bonding, in which mating surface regions of components are pressed together and heated to cause bonding and interdiffusion of the components;
- glass sealing or glazing, which uses a fluid glass to bond mating surfaces in a process analogous to brazing or fusion welding;
- adhesive bonding, in which component gaps are filled by fluid organic compounds which polymerize to form rigid bonding interlayers.

The number of various processes which can be used in principle to make a joint is very large but those which can be applied in practice, to satisfy a particular joining need, are often very limited in number. This restriction arises because there can be incompatibility between the fabrication or joint working conditions and the characteristics of the product or joining material. Usually conventional fusion welding is not performed due to the risk of brittle fracture initiation as a result of the high thermal stresses developed on cooling, in addition the high melting temperature of ceramics presupposes the use of high power sources (for example laser welding). Moreover, silicon-based ceramics such as silicon carbide and nitride sublime without melting and therefore cannot be subjected to fusion welding at normal pressures. Adhesive bonding is not suitable for high service temperature applications and tends to lose strength with long service. Hence, diffusion bonding and various types of brazing are currently applied to join ceramic to metals with the objective of maintaining the excellent base-material properties of ceramics.

In the case of brazing, ceramic-metal joints can be obtained in two different ways:

- indirect brazing, where the ceramic surfaces are metallized prior to brazing with conventional filler[1] metals;
- direct brazing, where the filler alloys contain active[2] elements such as titanium.

Brazing possesses a major advantage compared with conventional welding as the base materials do not melt. This allows brazing to be applied in the joining of dissimilar materials which cannot be joined by fusion processes due to metallurgical incompatibility. In general brazing produces less thermally induced distortion since the entire component is subject to the same heat treatment, thus preventing the localized thermal gradients which may cause distortion in welding. Moreover brazing can be easily adopted for mass production.

---

[1] In the brazing vocabulary the term “filler” indicates the material which is introduced between the two joining partners.

[2] In the brazing vocabulary the term “active” indicates the ability to wet ceramic materials.

1.2 The State of the Art

In the last twenty years much effort has been devoted to fabricating and understanding metal-ceramic joints [51, 94]. The problem should be studied with a multidisciplinary approach since the success in joining a ceramic material to a metal by brazing depends at least on two main aspects: the thermodynamics and chemistry of the materials to be joined, that is to say the possibility and the way in which the materials are bonded, and the mismatch in the thermomechanical properties of the components, on which the level of residual stress and, along with it, the mechanical behaviour, depends [6].

1.2.1 Basic Thermodynamics of Joint Formation

Successful brazing depends on the ability of a liquid metal or alloy to wet the ceramic being joined so that it flows readily over its surfaces and fills gaps to form joints. It is important that the flow of liquid fill the joint gaps completely and do not result in voids attached to the component surfaces. Every part of the component should be in close contact with the liquid and the wetting should be good enough for small degradations of surface characteristics be accommodated.

The Wetting Process

The most widely accepted and best established scientific measure of wetting behaviour is the contact angle, defined as the angle at a liquid front subtended by the liquid surface and the solid liquid interface (Figure 1.1). The contact angle depends solely on the surface tensions of the materials and its value is governed by Young's equation:

$$\gamma_S = \gamma_L \cos\theta + \gamma_{SL} \tag{1.1}$$

where γ is the surface tension and the suffixes S and L refer to the solid and liquid surfaces while SL refers to the solid-liquid interface.

Young's equation can be derived by considering the energy changes that will occur when the edge of a sessile drop advances over a smooth horizontal solid substrate to approach an equilibrium configuration [86]. In a short time during this process, the contact area radius will increase slightly from r to $r + \delta r$ and the contact angle will decrease from $\theta + \delta\theta$ to θ (Figure 1.2). Thus the area of the solid surface will decrease by $\pi\left[(r+\delta r)^2 - r^2\right]$ and that of the interface will increase by the same amount. The radial change from r to $r + \delta r$ will also increase the area of the liquid surface by $2\pi r\delta r\cos\theta$ so that the energy change δE can be written as

$$\delta E = \pi\left[(r+\delta r)^2 - r^2\right]\gamma_{SL} + 2\pi r\delta r\cos\theta\gamma_L - \pi\left[(r+\delta r)^2 - r^2\right]\gamma_S$$

which can be rearranged as

$$\delta E = \pi \left[2r\delta r + \delta r^2\right] \gamma_{SL} + 2\pi r\delta r \cos\theta \gamma_L - \pi \left[2r\delta r + \delta r^2\right] \gamma_S$$

$$\frac{\delta E}{\delta r} = \pi 2r\gamma_{SL} + 2\pi r \cos\theta \gamma_L - \pi 2r\gamma_S$$

No further advance will occur or be energetically favourable when the drop attains an equilibrium configuration so that both δr and $\delta E/\delta r$ will be zero

$$0 = \pi 2r\gamma_{SL} + 2\pi r \cos\theta \gamma_L - \pi 2r\gamma_S$$

which may be rewritten as Young's equation (1.1) by rearranging the terms and dividing throughout by $2\pi r$

$$\gamma_S = \gamma_L \cos\theta + \gamma_{SL}$$

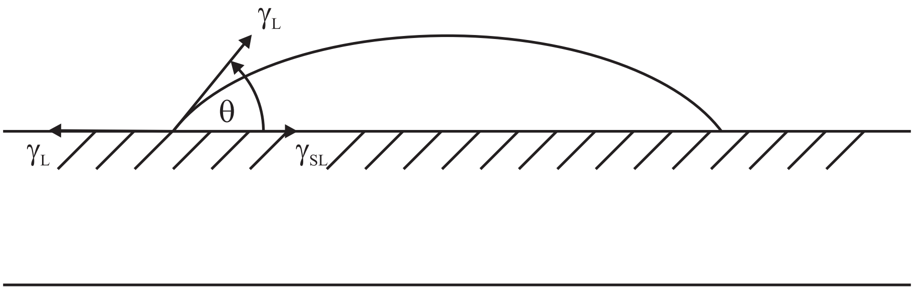

Figure 1.1: Surface and interfacial tensions acting at the periphery of a sessile drop resting on a solid substrate.

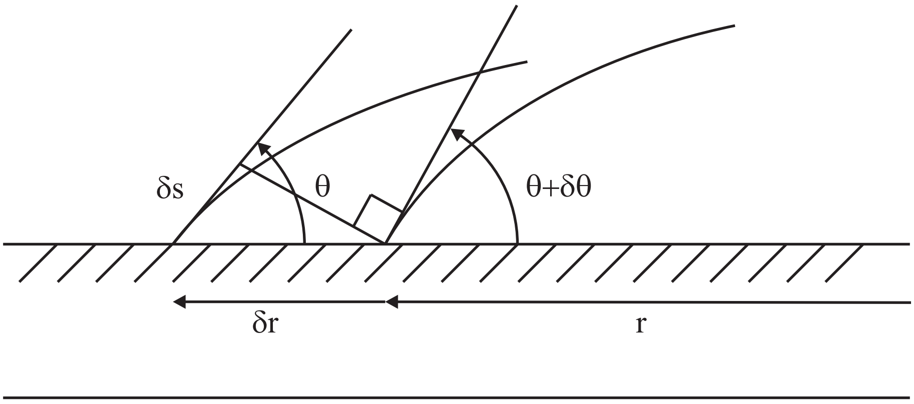

Figure 1.2: The advance of a liquid front over a smooth solid surface.

The Filling of Capillary Gaps

While the analysis of the configuration of sessile drops gives insight into wetting processes, the configurations of higher importance in brazing involve flow of the liquid metal into capillary gaps. An expression for the rise of a wetting liquid in a capillary gap can be derived by using the surface and the interfacial energies (Figure 1.3). A height increase of δh, while the liquid rises to its equilibrium configuration between two plates of breadth B, will increase the total interfacial energy of the system by $2\left(W+B\right)\delta h \gamma_{SL}$ and the potential energy of the liquid by $BWh\delta h \rho_L g$ and will decrease the total solid surface energy by $2\left(W+B\right)\delta h \gamma_S$. The rise does not involve any extension or decrease in the area of the curved liquid meniscus and hence will have no effect on the energy of the liquid surface. Thus the total energy change δE caused by the rise of δh, can be written as

$$\delta E = \delta h \gamma_{SL} 2\left(W+B\right) + h\delta h \rho_L g W B - \delta h \gamma_S 2\left(W+B\right)$$

$$\frac{\delta E}{\delta h} = \gamma_{SL} 2\left(W+B\right) + h\rho_L g W B - \gamma_S 2\left(W+B\right)$$

No further rise will be energetically favourable when the liquid column attains its equilibrium height so that $\delta E/\delta h$ is zero and the expression can be rewritten as

$$\left(\gamma_S - \gamma_{SL}\right) 2\left(W+B\right) = h\rho_L g W B$$

Combining it with Young's equation, it is written

$$2\gamma_L \cos\theta \left(W+B\right) = h\rho_L g W B$$

If the capillary gap is so narrow that $(W+B)$ can be approximated by B the expression can be simplified by dividing by B

$$2\gamma_L \cos\theta = h\rho_L g W \tag{1.2}$$

Influence of the Surface Roughness

So far the analysis applies to flat surfaces only, which in practice do not exist. Surface energy measurements are all based on surfaces possessing a certain degree of roughness. The wetting and filling of brazed joints is expected to be dependent on the roughness in two ways:

- surface and interfacial energy changes depend on the real area over which the liquid flows;
- roughness of the surface in the capillary gap may cause a transition from laminar to complex flow, resulting in an increased resistance to flow.

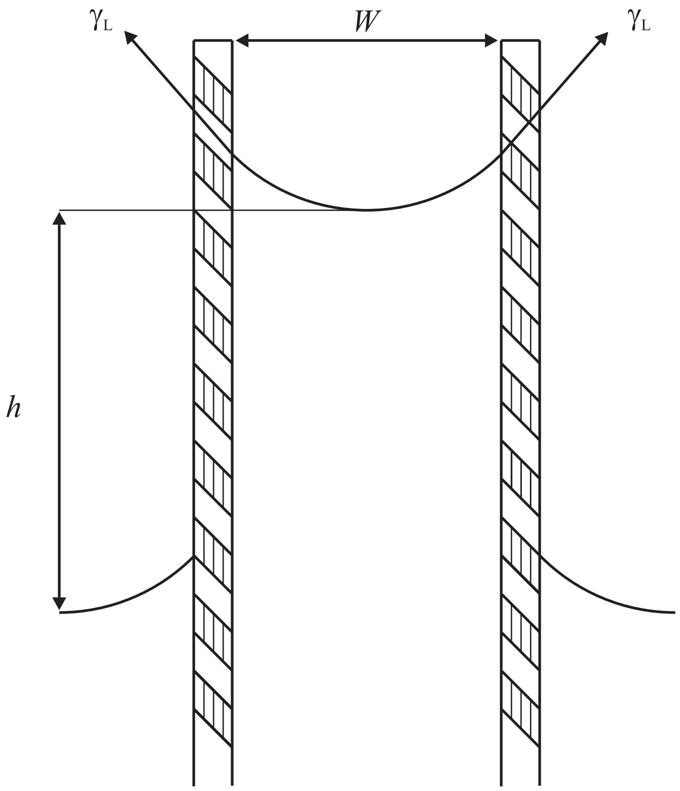

Figure 1.3: The rise of a liquid up a capillary gap.

The evaluation of energy changes requires the knowledge of the ratio between the real and apparent area, while the flow pattern is determined by the shape and probably by the height of the surface asperities. In the case of ceramics, their brittleness may facilitate the formation of small cracks, either from processing stages or during manufacturing or surface preparation (grinding and/or polishing). The effect of the surface roughness can be taken into account by replacing the theoretical contact angle θ with the observed one φ in (1.1) and (1.2):

$$\gamma_S = \gamma_L \cos\varphi + \gamma_{SL}$$

$$2\gamma_L \cos\varphi = h\rho_L g W$$

where θ is related to φ through η, the ratio between the real and the apparent surface area.

$$\cos\varphi = \eta \cos\theta$$

In practice equations (1.1) and (1.2) will still be the most frequently used since it is difficult to measure the real surface area.

The Wettability of Ceramics

Equations (1.1) and (1.2) demonstrate that the wettability depends on the contact angle. Thus neither spreading nor capillary penetration will occur unless the angle is less than 90° so that $\cos\theta$ is positive. Many important ceramic materials, such as silicon nitride, silicon carbide and alumina, are poorly wet by metals such as copper, silver or tin and exhibit contact angle values well above 90°. The most direct and convenient way to achieve an important reduction in the contact angle of a liquid metal on a ceramic substrate is by adding other metallic elements to the brazing alloy, typically group IVB elements, especially titanium, but also other elements as chromium, which can be used with silicon nitride [95]. The addition of an active element induces a considerable improvement in the wettability, thanks to its chemical reactivity with the ceramic surface, which gives rise to a modification of metal-ceramic interface chemistry [73]. The chemical reactions and the microstructures at interfaces are very complex and, since they can relate to the bond strength and the reliability of the joint, they have been the subject of thorough investigations [90]. Much of the literature on ceramic-metal active brazing has been focused on the nature of the interactions between the ceramic substrate and active brazing alloys with the aim of understanding how the wetting behaviour can be improved but also the metal substrate can play an important role because it can affect the thermochemical behaviour of the brazing alloy [7, 47].

1.2.2 Residual Stresses

Making a joint by brazing involves the formation of interfaces between dissimilar materials and this inevitably results in the generation of residual stresses as the bonded assembly cools: at the interface the material with the lower coefficient of thermal expansion will be in compression while the other in tension. The intensity and influence of these contraction stresses can be particularly marked for assemblies of ceramic and metallic components because of their often very different thermal expansions and of the negligible ductility of ceramics. High integrity interfaces produced by selecting suitable materials and process parameters usually do not fail because of these residual stresses but their ability to resist external loads will be degraded. Thus it is of vital importance to mitigate the effects of cooling stresses as much as possible and this is mainly a matter of a careful design aimed at minimizing the influence of the mismatched thermal expansions.

In the last twenty years great efforts have been devoted to study this problem: the matter has been tackled from different points of view, some aspects of it have been highlighted and some possible “stress-reduction” strategies have been proposed. The research has followed three interrelated main directions:

- evaluation of the residual stress field by analytical and numerical models and by experimental techniques;

- characterization of the effect of residual stresses on the strength and on the fracture behaviour of the joint;
- study of the influence of residual stresses on the fatigue behaviour and durability of the joint.

Some solutions have been proposed in order to reduce the amount of residual stresses in joints:

- choice of suitable materials;
- interposition of interlayers between the two joining partners;
- optimization of the shape of the joint;
- reinforcement of the braze;
- thermal treatments after cooling.

Evaluation of Residual Stresses

Some analytical models for the estimation of residual stresses have been formulated. They are usually developed from precise and strong hypotheses both on the geometry of the joint and on the constitutive laws of the components (e.g. linear elastic behaviour): there are models specially designed for coatings [45, 26], for joints with interlayers [124] and for layered plates [48, 50]. Such strong hypotheses limit the applicability of these models (residual stresses often exceed the elastic limit both of the metal partner and of the brazing or interlayer alloy). In some cases they can constitute an efficient and easy-to-use guide for preliminary design, but they can often be misleading.

A much more powerful way of investigating residual stresses is provided by finite element modelling, which has been massively used with increasing calculating power of computers [78]. One first aspect to cope with is the joint geometry, as the more commonly used configurations, such as joints between two flat surfaces, lead to singularities in the stress field (as predicted by analytical models), which can sensibly affect the model response. This problem can be tackled by adopting two different strategies: either by minimizing the parts of the mesh influenced by singularities (a very refined mesh around the singularity points is required [62], or by choosing an alternative strength metric other than stress values, such as strain energy [91]. The second important issue is represented by the constitutive laws assigned to the different materials which form the interfacial layers: despite knowing the rheology of both the joining partners and the interlayer, it is difficult to determine the joint behaviour because of the presence of different phases at the interface, due to its complex chemistry [57, 72]. In most models reported in literature, the ceramic partner is assumed to be elastic while the metal and the interlayer are assumed to be elastoplastic (the introduction of non linear behaviours being a major improvement with respect to analytical models); in some of them (for example [121, 126]) temperature dependence is introduced, this factor being especially determinant for metals [96]. Since the brazing of ceramic-metal joints is carried out at relatively high temperatures (700-1100 ℃), the inclusion of creep in the constitutive law in finite element analyses would make it possible to calculate the effect of a particular cooling rate from the braze temperature on residual stresses [105], unluckily time-dependence can rarely be implemented because of the lack of experimental data, as valid calculations require a constitutive law for the braze metal which accurately predicts the strain rate over a wide range of temperatures.

Numerical models can provide meaningful results only if pertinent experimental strategies are followed in parallel and experiments need the guideline provided by numerics. Along with finite element analyses some experimental methods for measuring residual stresses have been tested with different levels of success, depending on the joined materials and on the geometry of the joint:

- X-ray diffraction (XRD): it can provide reliable measurements of residual stresses on the external surface of the specimen (up to a depth of some microns) and, as a consequence, it is particularly suited for coatings [75]. However it can be a significant stress indicator also with bulk specimens, because the highest stress values are always located in the surface regions of specimens (where theoretical models foresee singularities) [66, 85].

- Neutron diffraction: it is particularly suited for probing the residual stresses within the bulk of a specimen because neutrons penetrate deep into most engineering materials, while XRD measurements are limited to the superficial part [89, 116]. The main drawback is that the gauge volume is quite large, e.g. in the order of 1 mm^3. Thus in order to be representative the measurements should be carried out only in large regions under almost uniform stress.

- Micro-indentation methods: they have been used to investigate residual stresses in the ceramic portion (e.g. the indentation fracture method [66], whose main limitation is the finite size of the produced cracks) or to have a rough estimate of the gradient of the elastic properties in the interlayer. Of course they can be applied only with relatively thick brazing gaps [4].

- Crack compliance methods: residual stresses are estimated by residual strain relaxation. The general procedure is to progressively cut through the specimen, measure released strain and use it to compute residual stresses via an analytical or numerical model. The most difficult problem in this method is the cutting of the ceramic which has to be performed without introducing additional stresses in the material. In case the ceramic is electrically conductive electro discharge machining (EDM) can be used [41].

- Layer peeling methods: this technique can be applied to beam- or plate-shaped specimens. A strain gauge is attached on one face of the sample to measure the strain induced by incremental grinding of the opposite face [53, 113]. The limitations of this method are again related to the nature of ceramics: grinding can be troublesome due to their hardness especially when removal of thin layers is required for the determination of high gradient stress profiles (a suitable alternative, when feasible, is chemical etching) [99].

- Hole drilling methods: in several drilling processes a hole is machined. This material removal relieves residual stresses which can be estimated by measuring surface strains around the hole [21]. The drilling procedure is particularly delicate: a low drilling depth per drilling step should be adopted and heat development has to be negligible.

Joint Strength and Fracture Behaviour

The most direct way of qualifying a joint is the evaluation of its strength. Because of the absence of any standardized method, the mechanical strength of ceramic-metal joints has been conventionally evaluated by either shear, tension, three- or four-point bend tests. The relationship between the various kinds of tests has not been clarified yet (even if some effort has been devoted in this direction [68]) and both the geometry of the specimen and the test configuration influence the measured strength values; these factors make results hardly comparable, unless the adopted test method is the same (in Figure 1.4 some of the specimen geometries reported in literature are depicted).

In order to understand how residual stresses affect the overall strength of the joint, two main aspects have been investigated:

- cracking due to cooling: residual stresses can cause cracking in the ceramic (and plastic deformation in the metal), especially for higher temperature joining processes. Joints in which the CTE of the ceramic partner is lower than that of the metal tend to crack in the ceramic while those with a higher CTE for the ceramic tend to fail along the interface [9] and various types of cracks can be identified (e.g. radial, branch and perimeter cracks in axisymmetric specimens [63]). Indeed there are no unique trends in the variables that govern residual stresses and cracking patterns; consequently it is

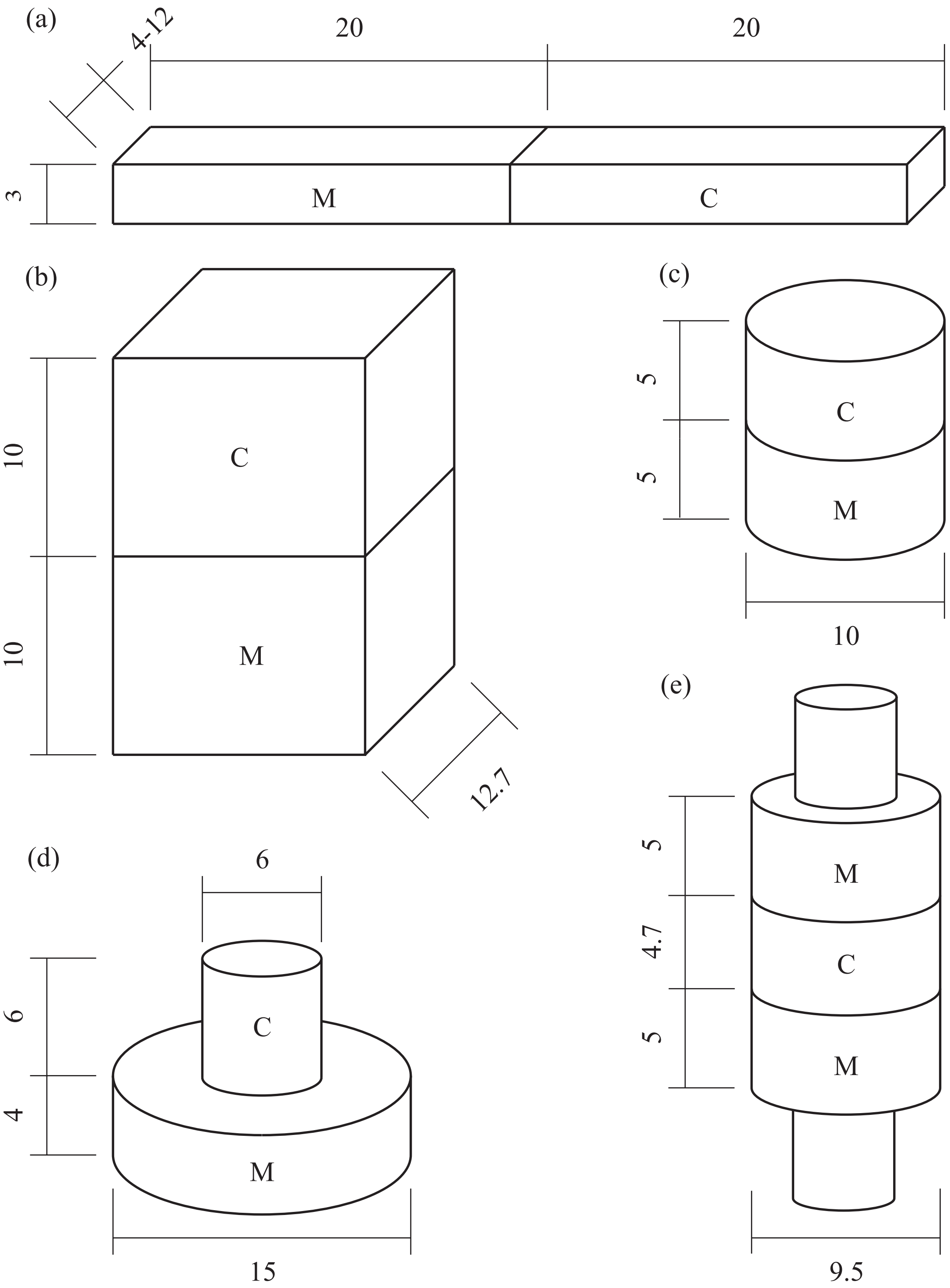

Figure 1.4: Specimen geometries reported in literature (units: mm): (a) four point bending, [108, 111, 112, 126, 127]; (b), (c), (d) shear, [92], [110] and [96, 125], respectively; (e) tensile, [68].

critically important for bond strength optimization to identify the dominant fracture characteristics of the material combination being considered [22];

- crack propagation in bend tests: when the bond has a sufficiently high fracture energy that failure does not occur at the interface, the major limitation on the joint strength concerns stress concentrations in the ceramic near the interface. Several characteristics of the joint govern its fracture behaviour: the magnitude of the stress and of the energy release at edge flaws depend on the thermal expansion misfit and on plastic strain relaxation [40] while the mode mixity of interface cracks seems to be governed by the interlayer thickness [103, 122] and by the their distance from the interface [56]. Despite the complexity of the problem some criteria have been formulated in order to study and predict such a phenomenology (e.g. one proposed approach consists in the separation of elastic and plastic contributions to the energy release rates [60]) but they lack generality.

Fatigue Behaviour

Durability is perhaps the most important keyword in ceramic-metal joint design: if the joints cannot enjoy a long service life the choice of ceramic-metal tools instead of bulk metal ones will be almost senseless, because the peculiarities of ceramics will not be exploited. Joints are usually evaluated either in terms of mechanical fatigue strength [67] or in terms of resistance to thermal cycles [93, 123]; in both cases a sensible decrease in strength can be observed (as expected) but the novelty with respect to static tests is that the failure of the joint is shifted from the ceramic near the interface to the ductile interlayer at the interface, that is to say that its plasticity dominates the fatigue strength of the joint.

Residual Stress Reduction

A ceramic-metal joint is a system consisting of materials that are both physically and mechanically different. The strength of the joint is governed mainly by residual stresses, which depend on a number of variables that include the mismatch between the elastic properties of the two materials, the plastic flow at the interface and the defects introduced into the joint and interface. It is possible to reduce the amount of residual stress by working on each of the mentioned aspects:

- choice of the materials: the materials to be joined have to be “economically alluring” and chemically compatible; these two criteria usually do not leave much room to the designer’s choice. However, in the few cases in which one can choose among different alternatives, the criterion should be the similarity in the coefficients of thermal expansion of the components, that is to say ceramics with relatively high CTEs (such as zirconia) and metals or alloys with relatively low ones (for example Kovar®);

- interposition of layers between the two joining partners: ductile metal interlayers at the joint interface can significantly relieve the residual stresses. However, single interlayers have drawbacks. For example, copper interlayers provide maximum reduction of residual stresses, but their applicability in real systems is limited due to their low resistance to corrosion and oxidation at high temperatures. To overcome these limitations and for a more effective release of residual stresses, multiple [91] and functionally graded interlayers [118, 119] have been developed with some success, but there is still only a quite qualitative understanding. In addition, experimental results reported in literature sometimes are not in agreement;

- optimization of the shape of the joint: high stress gradients and concentrations depend on the geometry of the joints; they can be eliminated by adopting non-planar interfaces that would offer also another advantage: the increase in the bond area [49, 109]. In joint design this approach is seldom practicable, but in the few cases it is, it can lead to significant improvements;

- introduction of controlled porosity in the interlayer: the idea is to increase strength by reducing the bonded area. A certain degree of porosity can improve residual stress relief in the joint but weakens the interface. Thus to apply this strategy this trade-off has to be studied carefully. Moreover this approach introduces additional complexities in the manufacturing procedure [92];

- reinforcement of the braze: the addition of low CTE materials (particles or fibers) to the brazing paste can alleviate the problem of residual stresses; the main difficulty to overcome in this approach is related to the chemical compatibility of the reinforcement: in literature some successful couplings are reported, such as carbon fibers in a brazed alumina-steel joint [128, 129] and zirconia particles in a hot-pressed zirconia-steel joint [74];

- thermal treatments after cooling: they are a well-known way of releasing stresses in metal production and have already been successfully adopted in the case of joints between ceramic and metals with slight differences in CTE [96].

1.3 Goals and Approach

As synthetically summarized in Section 1.2, much work has been done in the field of ceramic-metal brazing. However, while the aspects belonging to the field of materials science, e.g. the problems related to wetting, have been thoroughly investigated, a comparable understanding from the point of view of solid mechanics, e.g. the prediction and reduction of residual stress, has not yet been achieved.

The objective of this thesis is to make progress in this direction by exploring the potential of active filler metals reinforced with ceramic particles. In this framework, a methodology is developed to assess the mechanical properties of filler alloys and to study how they influence the residual stress field in joints. Moreover, the particles allow producing thicker brazes since they prevent the melted filler from flowing out of the joint region. Thus by using reinforced fillers it is possible to study not only the influence of the filler metal mechanical properties but also that of the brazing gap.

Since this work aims at improving the understanding of the mechanics of ceramic-metal joints rather than maximizing their performance, the study concentrates on one material system, that is to say one ceramic and one metal joining partner, the ceramic composite Si_3N_4/TiN and a case-hardening steel, joined by means of a AgCuTiIn active filler reinforced with SiC particles. By varying the amount of reinforcement it is possible to tailor the mechanical properties of the filler and to study their effect on the joint.

Thus the first task of this work was the study of this composite brazing filler, which, due its active nature, revealed to be challenging both experimentally, especially in terms of specimen production, and from the modelling point of view, since it required an inverse homogenization approach.

Once the mechanical properties of the braze filler were assessed, it was possible to focus on the characterization of the joints in terms of residual stresses and strength, with X-ray diffraction measurements and bend tests being accompanied by pertinent finite element models.

The understanding of the studied system eventually provided some guidelines for the choice of the brazing filler for the best design of ceramic-metal assemblies in terms of residual stresses.

1.4 Thesis Outline

The present work is structured in six chapters (including the present introduction):

Chapter 2 contains the description of the specimen fabrication procedures and discusses the aspects related to this part of the experimental work carried out during this project.

Chapter 3 is dedicated to the developed three-dimensional model for the homogenization of the elastic and plastic properties of particle reinforced composites. The microstructure is described by means of a novel technique, consisting of generating particles in a pre-existent constrained Delaunay tetrahedralization of a cubic volume by means of a modified random adsorption algorithm. Moreover, a criterion to assess the model representativeness in the case of elastoplasticity is proposed based on the amount of elastic energy stored in the composite.

Chapter 4 addresses the characterization of composite braze fillers. The microstructure is investigated by electron and optical microscopy accompanied by energy dispersive analysis using X-rays and image analysis for phase identification and quantification. The mechanical properties are obtained by means of a combined experimental and numerical approach, in which the results of traction tests at room temperature are studied by means of inverse homogenization and extended to a larger temperature range by classic homogenization.

Chapter 5 deals with the characterization of ceramic-metal joints. Residual stress are measured by means of the X-ray diffraction technique and the results are compared with the predictions obtained by finite element modelling. Joints are tested in four-point bending and also in this case the experiments are accompanied by pertinent finite element models. Finally the influence of different parameters (related to the joint geometry and to the mechanical properties of the materials) on the joint performance is analysed with the help of a parametric finite element model and general guidelines for the design of ceramic-metal joints are provided.

Chapter 6 consists of a summary of the obtained results and provides an outlook on the possible future work both on the techniques specifically developed during this project, such as the mechanical testing of bulk fillers or the homogenization model, and more in general in the field of ceramic-metal joints.

Chapter 2

Specimen Fabrication

A major part of the experimental work carried out in this thesis has been dedicated to the fabrication of specimens. Two specimens have been designed: a beam shaped ceramic-metal joint and a bulk braze alloy dogbone specimen for tensile tests. The manufacturing of these specimens is not a straightforward process and requires several intermediate steps and the use of some special equipment such as a vacuum furnace and brazing accessories. In this Chapter the fabrication procedures developed and adopted in the project are presented as well as the related equipment. This description is preceded by an introduction on the used materials.

2.1 Materials

Making a ceramic-metal joint is a process which involves at least three materials: the ceramic, the metal and the brazing filler. Actually in this work many additional materials were used, besides those three: some, such as the binder, were used for the fabrication of the specimens themselves, others in the vacuum brazing equipment, such as molybdenum. In the following the used materials will be listed, grouped in three categories, according to their function: joining partners, braze fillers and other materials.

Joining Partners

- Si_3N_4/TiN: sintered silicon nitride ceramic features an excellent combination of mechanical, thermal, and chemical properties. The incorporation of titanium nitride in silicon nitride leads to two major improvements: an increase of the fracture toughness and a decrease of the electrical resistivity down to a level at which it is possible to machine the material by electro discharge machining [35, 46, 65]. A commercial-grade Si_3N_4-30 wt.% TiN composite, which was subject of previous research at EMPA [13], was used in this work (its mechanical properties are summarized in Chapter 5, Table 5.5).

- Steel: a case-hardening steel, Böhler E200 (DIN 1.5752, ECN35, AISI3310), was chosen as metal joining partner, since it had already been successfully used in previous work on ceramic-metal joints at EMPA [14]. The mechanical properties are summarized in Table 5.6.

Braze Fillers

- Incusil™ABA®: it is an active filler produced by WESGO®, Erlangen, Germany. Its composition, $Ag_{59}Cu_{27.25}In_{12.5}Ti_{1.25}$, is based on an AgCu eutectic alloy with addition of In to lower the melting point and Ti to activate the braze. It has solidus and liquidus temperatures of 605 ℃ and 715 ℃ respectively. It was used in foil form (50 µm thick) and in powder form (mesh 325, grain size less than 45 µm) for brazing and for the fabrication of dogbone specimens, while a small amount in wire form (diameter 1 mm) was used for additional tensile tests (as reported in Section 4.1). The use of AgCuTi and AgCuTiIn for the production of ceramic-ceramic and ceramic-metal joints is widely reported in literature, typically for joining Si_3N_4, but also other ceramics. For instance in [70, 71] Incusil™ABA® is used for various ceramic-metal combinations while in [130] AlN is brazed to different metals by a AgCuTiIn alloy.

- $Cu_{73.9}Sn_{14.4}Ti_{10.2}Zr_{1.5}$: it is an experimental active braze filler [11] which has a brazing temperature of 950 ℃, about 200 ℃ higher than that of Incusil™ABA®. It was used to manufacture additional parts such as molybdenum moulds.

- SiC: although it is a ceramic, SiC is listed among the braze fillers since, to make composite fillers, Incusil™ABA® was reinforced with SiC particles (Alfa Aesar® SiC 99% mesh 325, particle size less than 45 µm).

- Binder: in the process of production of the composite filler a binder (octyl acetate - 0.4 wt.% cellulose nitrate) was used.

Additional Materials

- Molybdenum: it is a refractory metal typically used for vacuum technology applications due to its high melting temperature (about 2600 ℃). Actually, it can work at temperatures above 1100 ℃ (in non-oxidizing conditions), which are higher than the service temperatures of steels and nickel-based superalloys. When exposed to temperatures in excess of 760 ℃ in air rapid oxidation can result. Thus, molybdenum performs best in vacuum environments. In this project it was used for the fabrication of crucibles and of the metallic parts of the jig for brazing ceramic-metal joints.

- MACOR: it is a glass ceramic which is machinable with ordinary metal working tools. Nevertheless it exhibits a rather high service temperature, 1000 ℃, and almost no porosity and degassing. Thus it is widely used in high vacuum applications (in the present case the jig for brazing ceramic-metal joints is mainly made of it).
- Alumina (Al_2O_3): it is a ceramic material which has a wide range of applications due to its versatility and low cost. Here it was used for the fabrication of accessories for the vacuum furnace, e.g. supporting plates, and for some parts of the jig for brazing ceramic-metal joints.
- PTFE: it was used in foil form as anti-stick for the casting of the composite filler.

2.2 The Vacuum Furnace

In active brazing the most important requirement for a successful result is the quality of furnace in terms of vacuum level and temperature control. During this thesis all the specimens were produced in a GERO F-VS 100-200/13 system which is a standard electrically heated ceramic tube furnace combined with a high vacuum system (Figure 2.1). The furnace allows a maximum heating rate of 300 ℃/min and a maximum continuous operating temperature of 1350 ℃. No cooling system is provided, thus all the specimens underwent the characteristic cooling of the furnace itself (Figure 2.2). The vacuum system consists of turbomolecular pump (Leybold PT151) combined with a preliminary vacuum pump (Leybold TRIVAC B) and is linked to the furnace tube by water-cooled flanges. This furnace allowed to carry out all the sintering and brazing processes in optimal conditions (at pressures lower than $1 \cdot 10^{-5}$ mbar).

2.3 Production of the Reinforced Filler

To make a composite active braze filler, Incusil™ABA® was reinforced with 9, 18, 27 vol.% SiC particles. The composite fillers were produced in two forms: dogbone specimens for tensile tests and pills to be inserted between the joining partners in ceramic-metal joints.

2.3.1 Brazing Pills for Ceramic-Metal Joints

Incusil™ABA® and SiC powders were weighed and mixed with the addition of an equivalent volume of binder (for Incusil™ABA® and SiC densities the values 9.7 g/cm^3 and 3.2

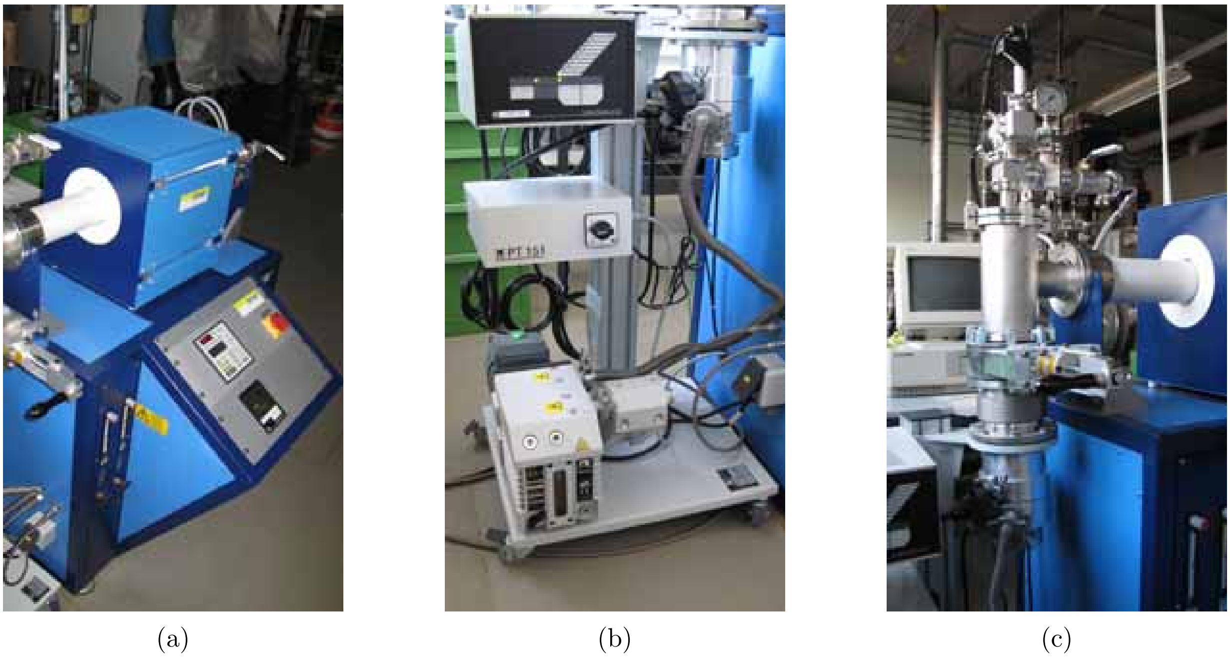

(a) (b) (c)

Figure 2.1: The vacuum furnace system: (a) overall view of the furnace; (b) the preliminary vacuum pump, the turbomolecular pump and the vacuum control system; (c) the vacuum flange and the pressure measuring tubes.

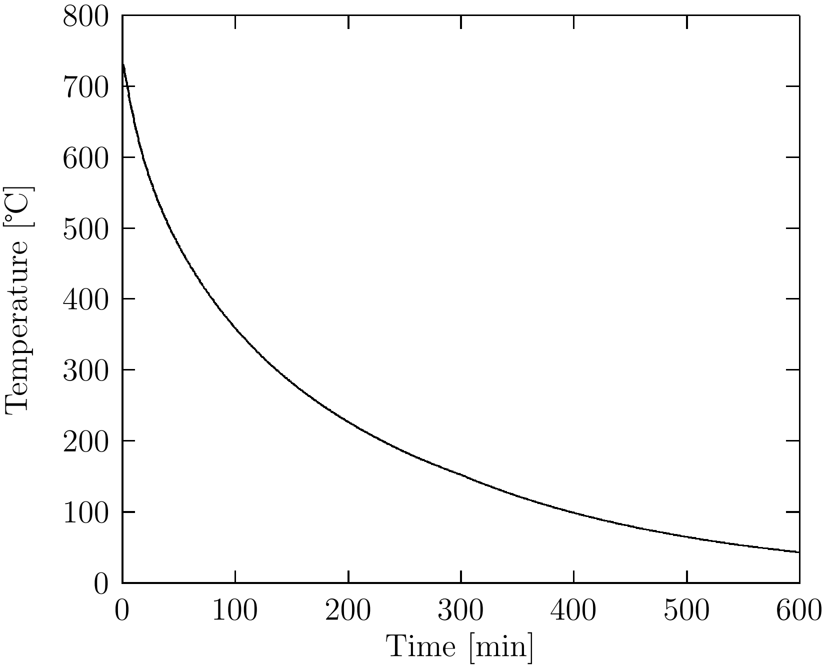

Figure 2.2: Typical cooling process after brazing.

Figure 2.3: Incusil™ABA®-18 vol.% SiC pills after sintering.

g/cm^3 were assumed) The slurry was cast on a glass plate coated with PTFE and spread manually. To control the thickness of the pills the slurry was confined in a crucible formed by superposing layers of tape. The slurry was dried for four hours at 100 °C to obtain a green preform from which small pills of 4×5 mm^2 were cut. Since the pills were too fragile to be handled in the assembly of ceramic-metal joints they were sintered in vacuum for 240 minutes at 640 °C (in Figure 2.3 some Incusil™ABA®-18 vol.% SiC pills are shown).

2.3.2 Dogbone Specimens for Filler Characterization

The fabrication of active braze filler bulk specimens is a challenging task because the dogbone specimens have to be representative of the braze fillers actually obtained in the ceramic-metal joints; thus the histories of the two materials have to be as similar as possible. Moreover the whole processing is made more difficult by the active nature of these materials (this explains why in literature only few attempts of producing bulk active filler specimens are reported, despite the widespread interest in active brazing, e.g. in [104] a procedure for the production of bulk Nioro®ABA, $Au_{82}Ni_{15.5}V_{1.75}Mo_{0.75}$, and CusilABA®, $Ag_{63}Cu_{35.25}Ti_{1.75}$, is developed).

In the present work the bulk filler specimen were produced by melting Incusil™ABA® powder in molybdenum crucibles. High purity molybdenum in sheet and bar form was used for the crucible fabrication: a 1 mm thick sheet was cut and plied to obtain vessels whose ends were capped by means of fitting molybdenum pieces machined out of a bar. The caps were brazed onto the vessels by using the CuSnTiZr braze filler (a crucible can

Figure 2.4: A molybdenum crucible used for the fabrication of braze filler bulk specimens.

be seen in Figure 2.4). Incusil™ABA® and SiC were weighed and mixed without the aid of the binder, as in this case there was no need of shaping the filler alloy, and the composite powders were poured into the crucibles (each crucible was filled with about 40 g of powder). The crucibles were introduced into the vacuum furnace (due to the dimensions of the furnace hot zone a maximum of two crucibles could be processed at the same time) to undergo the thermal cycle reported in Figure 2.6. This thermal cycle is characterized by three dwell temperatures:

1. 510 ℃ (dwell time 150 min): between 400 ℃ and 500 ℃ the dehydrogenation of TiH_2 takes place [10]. Since the two crucibles contain a total of about 80 g of Incusil™ABA® a considerable amount of H_2 is released with a consequent increase of pressure in the furnace chamber. The dwell step allows the vacuum system to evacuate the H_2 and to re-establish a sufficiently good vacuum;

2. 640 ℃ (dwell time 240 min): the powders undergo the same sintering as the composite filler pills for joints;

3. 750 ℃ (dwell time 20 min): at the same brazing temperature adopted for ceramic-metal joints the powders are melted. The dwell time in this case is slightly longer (5 minutes) due to the much larger amount of material to be molten.

Two rectangular plates ($6 \times 2 \times 55$ mm^3) of bulk braze filler were mechanically machined out of each mould (Figure 2.5). The last step of the fabrication procedure consisted in

Figure 2.5: A molybdenum crucible before the machining of the dogbone specimens.

cutting the dogbone specimens out of the plates by electrical discharge machining (Figure 2.7, the dimensions were derived from ASTM standards [2]). An image of a specimen can be found in Chapter 4 (Figure 4.2).

2.4 Fabrication of Ceramic-Metal Joints

As highlighted in Chapter 1, one of the problems when directly comparing the joint strengths with data reported in literature is the absence of standard testing methods and the wide range of the used specimen types and geometries (some are displayed in Figure 1.4). In the present study the joint geometry was chosen with the aim of carrying out 4-point bend tests based on the standard EN 843-1 for advanced ceramic flexural testing, with a specimen size of $3 \times 4 \times 50$ mm^3. Thus the ceramic and steel joining partners were machined to form $3 \times 4 \times 25$ mm^3 bars and Incusil™ABA® in sheet form was cut into 4×5 mm^2 foils (the same size as the composite filler pills).

All the materials were degreased and cleaned prior to brazing by using wet chemical methods: the steel and the braze filler with acetone in an ultrasonic bath while the ceramic with aqua regia (nitric acid and hydrochloric acid in a volumetric ratio of one to three). The materials were then separately degassed in the vacuum furnace at temperatures of 550 ℃, 950 ℃ and 1100 ℃ for the braze foils, steel and ceramic, respectively.

The brazing experiments were performed by placing the joining partners in a specially

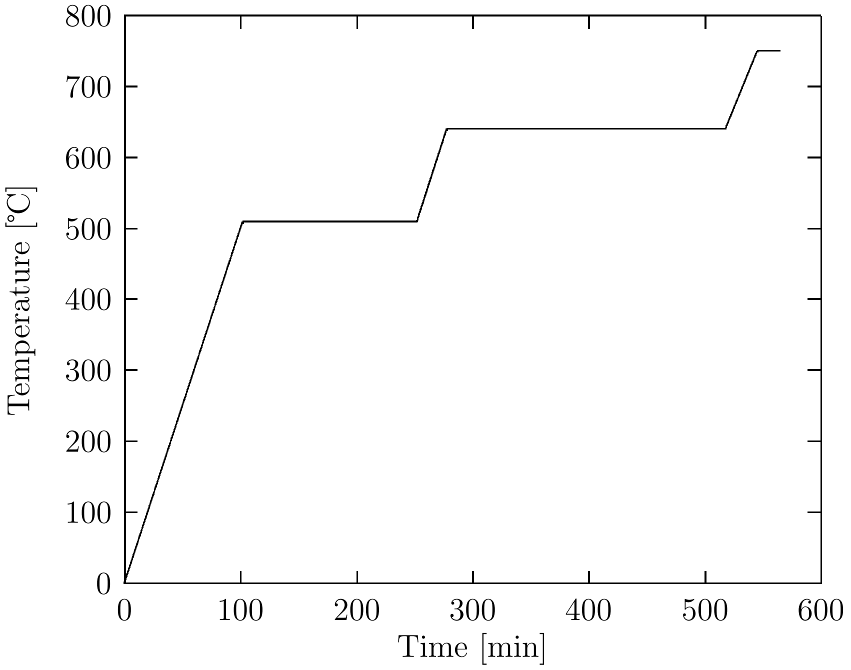

Figure 2.6: Thermal cycle for the fabrication of braze filler bulk specimens.

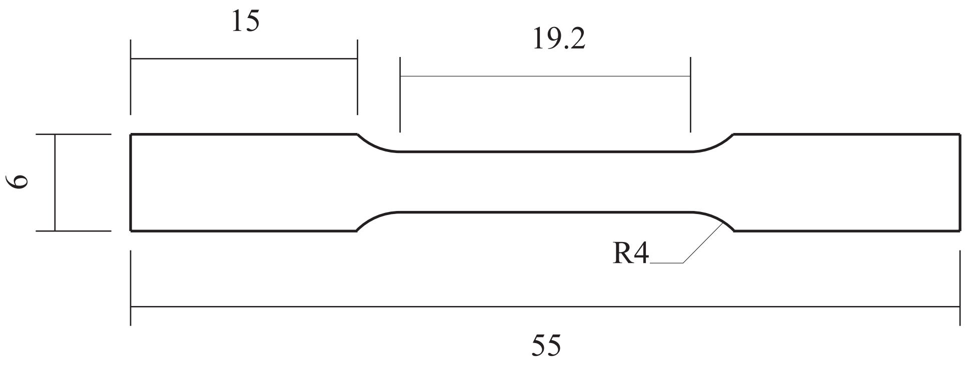

Figure 2.7: Braze filler dogbone specimen dimensions (units: mm).

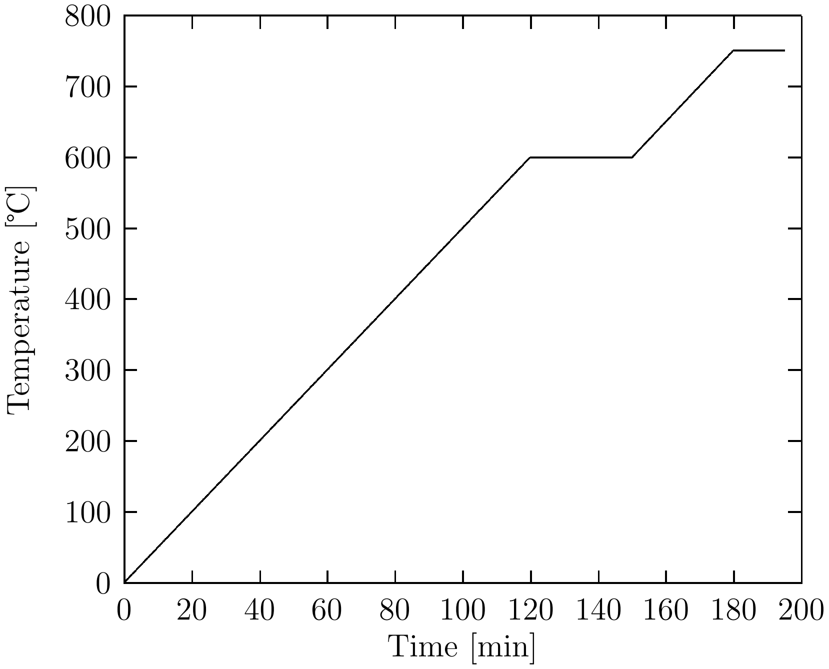

Figure 2.8: Brazing cycle for ceramic-metal joint.

constructed brazing jig (Figures 2.9 and 2.10) which was designed to host four joints and to guarantee the correct alignment. In the final stage of the assembly, the brazing filler was placed between the steel and the ceramic. To keep the braze in the correct position and to assure contact throughout the process, a small compressive load was applied on the ceramic joining partner, which was allowed to slide on the jig. Then the brazing jig was placed on an alumina plate and introduced into the vacuum furnace. Brazing was performed according to the thermal cycle reported in Figure 2.8: the specimens were heated up to a brazing temperature of 750 °C and held there for 15 minutes before cooling down in vacuum. After brazing, the quality of the brazed joint was checked by visual inspection to confirm that wetting of the ceramic had occurred and that neither misalignments of the joining partners nor significant defects in the braze region were present.

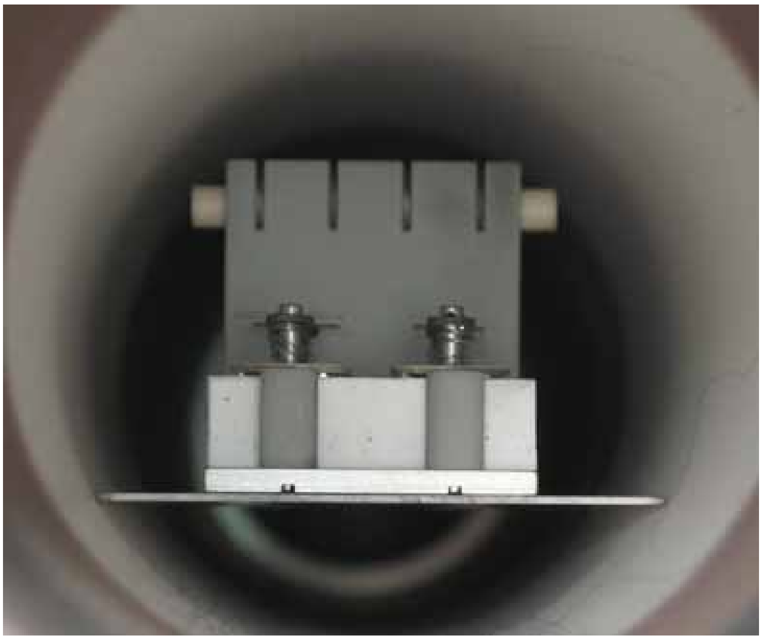

Figure 2.9: The brazing jig inside the vacuum furnace

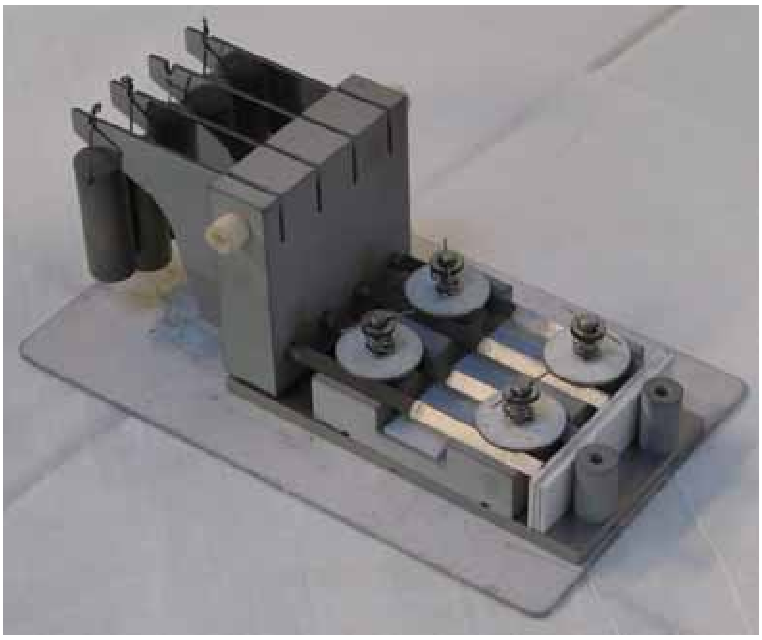

Figure 2.10: The brazing jig with four brazed joints.

Chapter 3

Homogenization Model

The composite fillers Incusil™ABA®-SiC can be classified as particle reinforced metal matrix composites (PRMMC). The family of particle reinforced or particulate composites has emerged as a possible alternative to conventional fiber reinforced composites. For example, PRMMCs have shown great potential and have been the object of intense research for the last twenty years in the aerospace field: typically, these materials consist of an aluminium alloy matrix reinforced with ceramic particles. Another important group of particulate composites is that of reinforced polymers with many applications for instance in the automotive industry. The particulate morphology can also be found in a number of other material systems: reinforced concrete can also be thought of as a particle reinforced composite or ceramics can also be modelled as particulate composites and are candidate materials for many high temperature applications. Consequently, the characterization and modelling of the mechanical behaviour of such materials are fundamental to their reliable use.

3.1 Review of Existing Models

The existing modelling approaches can be divided into two main groups [15]: the first includes methods which statistically describe the microstructures (mean field approaches and variational bounding methods) and the second those which are based on (numerical) modelling of discrete microstructures (periodic microfield, embedded cell and windowing approaches). Thanks to the progressive increase of available computing power, several models of the latter type have been proposed in recent years to study both linear and non-linear mechanical behaviours of heterogeneous systems. However, most reported models are two dimensional. The morphology of the microstructure can be either directly derived from an experimental image, on which a finite element mesh is superposed, e.g. [33, 24], or reconstructed by assigning the particles a shape, usually circular or rectangular, e.g. [17]. Although they capture some of the physical aspects of the actual material properties, planar models are not able to predict the effective behaviour of composites with randomly distributed particles, especially in the elastoplastic range as suggested in [52] and extensively demonstrated in [16]. Plane stress models tend to underestimate the strengthening effect of the particles whereas plane strain models tend to overestimate it. As a consequence, three dimensional models are required.

The geometrical description of a three dimensional microstructure is much more challenging than in the planar case. Experimental techniques to obtain three dimensional images of actual microstructures are complex and expensive and can be used only in rare cases (e.g. in [55, 18] a real three dimensional image of microstructure obtained by holotomography is directly used as input for the model, while in [25, 102] the three dimensional microstructure is reconstructed from two dimensional images by means of a serial Sectioning process). As for the two dimensional approaches the alternative is constituted by methods in which particles are assumed to have arbitrary shapes (in most cases spherical). These approaches give more accurate results [37], but present two main drawbacks: particles with an imposed shape are not always representative of the real microstructure (as in the two dimensional case); moreover the generation and meshing of the geometry can be quite demanding especially if composites with different compositions and particle distributions are to be studied.

In the present work a novel technique to generate the microstructure geometry is proposed. This method allows reproducing the actual shape of ceramic particles normally used in particle reinforced composites. Unlike other methods, particles do not need to be drawn and then meshed but are generated in an existing finite element mesh; this makes it possible to easily model particle reinforced composites with different reinforcement volume fractions since the geometry does not need to be redefined for each composition.

The size of the representative volume element (RVE) is assessed for the thermoelastic behaviour and a procedure is developed to check the representativeness when plasticity is taken into account. No attempt is made to compare the present results with existing numerical and analytical models; however the developed model is tested on a real PRMMC for which the elastoplastic behaviour both of the matrix metal and of the actual composite are known.

3.2 Generation of the Multi-Particle Cell

A cubic multi-inclusion unit cell microstructural model is proposed. The domain is discretized by the Constrained Delaunay Tetrahedralization (CDT), a variation of the Delaunay tetrahedralization.

The Delaunay tetrahedralization can be defined as follows: Let S be a finite set of points in $\mathbb{R}^3$. Four non-coplanar points s_i, s_j, s_k and s_l are the vertices of a Delaunay tetrahedron t if and only if there exists a location x which is equally close to s_i, s_j, s_k and s_l and closer to s_i, s_j, s_k and s_l than to any other $s_m \in S$. The location x is the center of circumsphere of t.

The decomposition of a three dimensional geometric object Ω into a tetrahedral mesh implies that the boundary (including internal boundaries and holes) of the object $\partial\Omega$ has to be respected by mesh faces. The Delaunay tetrahedralization of the object vertices generally does not satisfy this requirement. The CDT is a variation of the Delaunay tetrahedralization which can respect an imposed boundary, thus allows meshing domains of a given shape. To define a constrained Delaunay tetrahedron it is necessary to introduce the concept of visibility between two points. The visibility between two points s_i and s_j is occluded if there is a constraining polygon $f \in \partial\Omega$ such that s_i and s_j lie on opposite sides of the plane which includes f and the line segment $\overline{s_i s_j}$ intersects f. Four non-coplanar points are the vertices of a constrained Delaunay tetrahedron t_c if its circumsphere encloses no $s_m \in S$ visible from any location in the relative interior of t_c. Note that the two definitions are the same except for the fact that in the CDT the portion of volume of the circumsphere which lies outside $\partial\Omega$ is ignored.

In our application the CDT is carried out by the software TetGen [101] which ensures quality mesh generation by controlling element distortion (the adopted metric is the maximum radius-edge ratio r_{max}, which is the ratio between the radius of a tetrahedron circumsphere and its shortest edge). Moreover, it provides additional features such as the possibility to limit the maximum tetrahedron volume v^t_{max} and to impose the coordinates of an additional set of vertices $\widetilde{S}$. The latter feature is exploited to create vertices in random positions both on the surface and inside the domain, in order to allow a certain degree of perturbation in the CDT, which otherwise would lead to too regular meshes, not suitable for the purposes of this work.

In the present work the process of generating the multi-inclusion unit cell is divided into two main stages: the discretization of the cell volume and the creation of the microstructure. The first stage is made of four main steps:

1. Definition of the cell domain Ω and of its boundary $\partial\Omega$.
2. Creation of a set $\widetilde{S}$ of imposed vertices: $\widetilde{S} = \{\widetilde{s}_1, \ldots, \widetilde{s}_n : \widetilde{s}_i \in (\Omega \cup \partial\Omega)\}$.
3. Definition of r_{max} and v^t_{max}.
4. CDT of Ω with respect to r_{max} and v^t_{max}.

The composite microstructure is produced in the second stage: the reinforcement volume fraction V_r, the minimum and maximum particle volume (v^p_{min} and v^p_{max}, respectively) are

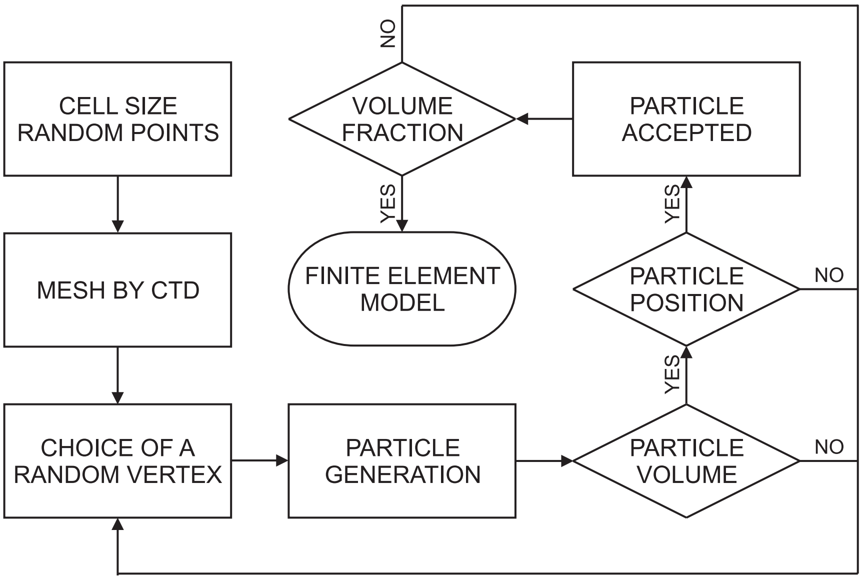

Figure 3.1: Flowchart of the algorithm developed to generate the model.

imposed and particles are generated in the tetrahedralized cubic domain according to the following iterative procedure:

1. Choice of a random vertex s as nucleation point for a particle p: the particle is the set of tetrahedra which share s: $p = \{t_1, \ldots, t_n : s \in t_i\}$.
2. Test on the particle volume: if the particle volume does not satisfy the prescribed constraints the particle is discarded and another random vertex is chosen.
3. Tests on the particle position: the particle is discarded if it overlaps (shares a tetrahedron t_k) or touches (shares a facet f_k) another particle, nevertheless particles are allowed to share edges.
4. The particle p is included in the set P of valid particles:
   $P = \{p_1, \ldots, p_n : v^p_{min} \leq v^p_i \leq v^p_{max}; \forall f_k, t_k \in p_i, \forall p_j \in P \Rightarrow f_k, t_k \notin p_j\}$.

The procedure is repeated until the design reinforcement volume fraction V_r is obtained (the algorithm flowchart is reported in Figure 3.1). The proposed approach is suitable to obtain statistically homogeneous particle distributions and is a variant of the Random Sequential Adsorption (RSA), in which particles placed sequentially at random positions are accepted if they do not overlap any of the formerly created particles and rejected otherwise [43]. The RSA has attracted a lot of attention in the last thirty years and has been applied in several fields, e.g. to reconstruct dispersions [97]. The most immediate way to characterize the RSA is by means of the jamming limit, which is the maximum obtainable inclusion volume fraction and has been determined for different particle shapes, e.g. for two dimensional discs it is 0.547 ± 0.002 while for aligned squares it is 0.562 ± 0.002 [34].

The present algorithm has been applied to study almost monodisperse reinforcement powders (a 13% tolerance on the particle volume is allowed) randomly distributed in the volume under consideration (figure 3.2). Typically one particle consists of about 24-26 elements (12-13 in case of particles generated from nodes lying on the cube faces) and exhibits an almost convex shape which resembles that of ceramic powders actually used in composites, which are made of irregular polyhedral particles (figure 3.3).

To obtain a rough estimate of the jamming limit, tests were carried out with up to 10^7 iterations and a value of about 0.26 was observed (in the case of identical spheres it is 0.382 ± 0.003 [100]). Note that particles were allowed to share edges in order to raise the jamming limit in the case of monodisperse reinforcement. However, in the case of a composite with 0.25 reinforcement volume fraction (the largest considered in the present work), the number of shared edges is less than 4% of the total number of edges on the surface of particles (the average particle surface consists of 36-39 edges). Moreover, due to the way particles are generated, one edge can be shared by no more than two particles and shared edges are randomly oriented. Thus it is very unlikely to find in the model chains of shared edges sufficiently long to significantly influence the strain field in the matrix material. Following these considerations it is assumed that the effect of particle shared edges on the model global response is negligible.

To achieve higher volume fractions without relaxing the constraints on the particle size distribution, more sophisticated algorithms are required: one possible strategy could be to identify all the particles having a compatible size and then to choose those leading to a higher V_r.

The obtained finite element model is solved and post processed with ABAQUS® software package [1]. Quadratic elements are employed to model the thermoelastic behaviour while in elastoplasticity modified 10-node elements are employed to avoid possible volumetric locking in yielded matrix regions. Perfect adhesion between particles and matrix is assumed throughout the whole study.

3.3 Elastic Behaviour

For heterogeneous elastic materials admitting a RVE, the effective stiffness tensor $\overline{C}_{ijkl}$ and the effective compliance tensor $\overline{D}_{ijkl}$ are linked to the average stress tensor $\langle\sigma\rangle_{ij}$ and the average strain tensor $\langle\varepsilon\rangle_{ij}$

$$\langle\sigma\rangle_{ij} = \overline{C}_{ijkl} \langle\varepsilon\rangle_{kl} \tag{3.1}$$

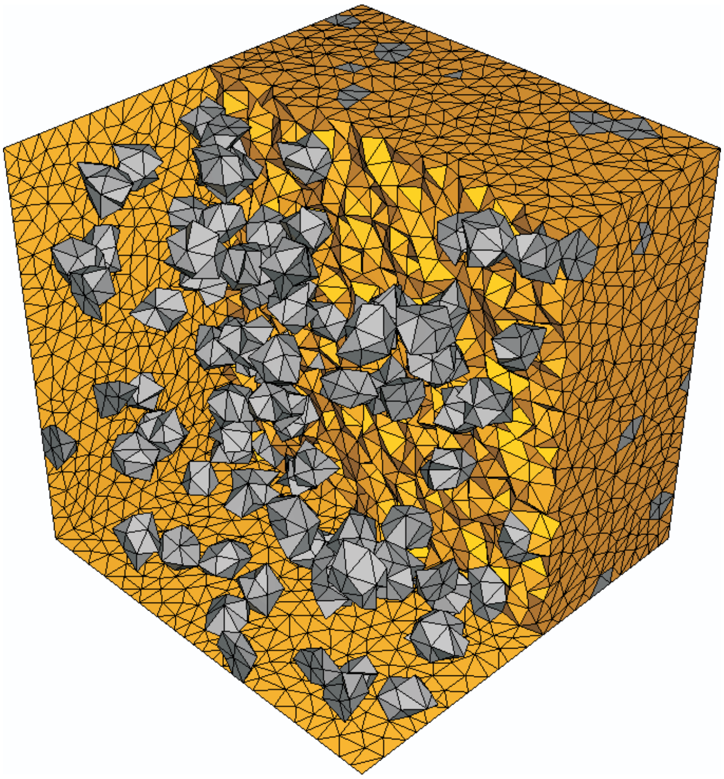

Figure 3.2: An example of a unit cell with $V_r = 0.05$ (part of the matrix elements are not displayed to show the particles).

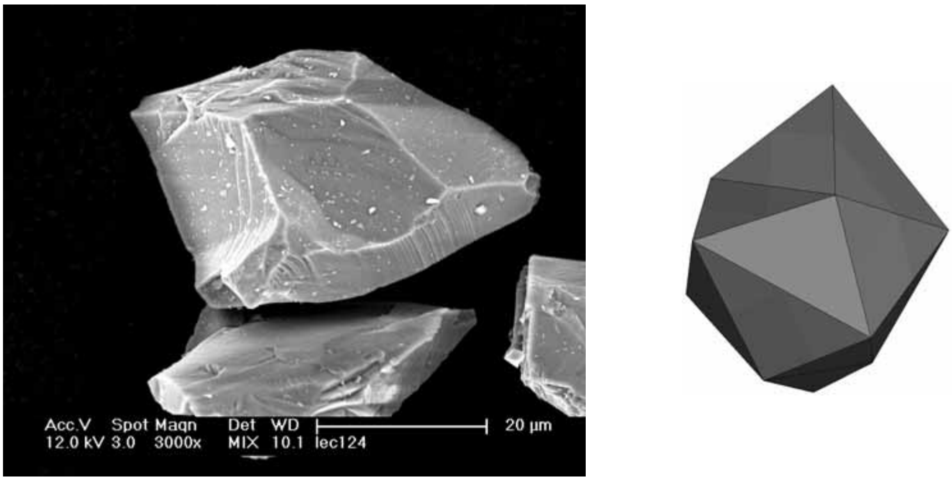

Figure 3.3: A typical SiC powder used as reinforcement in composites (image obtained by scanning electron microscopy) and a typical model particle.

$$\langle\varepsilon\rangle_{ij} = \overline{D}_{ijkl}\,\langle\sigma\rangle_{kl} \tag{3.2}$$

The macroscopic responses $\langle\sigma\rangle_{ij}$ and $\langle\varepsilon\rangle_{ij}$ are defined as

$$\langle\sigma\rangle_{ij} = \frac{1}{\Omega}\int_{\Omega}\sigma_{ij}\left(\boldsymbol{x}\right)d\Omega \tag{3.3}$$

$$\langle\varepsilon\rangle_{ij} = \frac{1}{\Omega}\int_{\Omega}\varepsilon_{ij}\left(\boldsymbol{x}\right)d\Omega \tag{3.4}$$

where Ω stands for the volume of the region under consideration while $\sigma_{ij}\left(\boldsymbol{x}\right)$ and $\varepsilon_{ij}\left(\boldsymbol{x}\right)$ are the local stress and strain fields.

Comparison of (3.1) with (3.2) yields

$$\overline{C}_{ijkl} = \left(\overline{D}_{ijkl}\right)^{-1} \tag{3.5}$$

By definition the effective stiffness tensor $\overline{C}_{ijkl}$ and the effective compliance tensor $\overline{D}_{ijkl}$ are assumed to be boundary condition independent. Actually Ω can be considered a RVE when the responses under static and kinematic uniform boundary conditions coincide [42]. This approach in principle is valid only for bodies of infinite dimensions, nevertheless, if applied on sufficiently large volumes, leads to very precise estimates of the effective mechanical properties.

To evaluate the stiffness tensor under kinematic uniform boundary conditions $\overline{C}^{\langle\varepsilon\rangle}_{ijkl}$ six simulations are required, one for each column (the matrix notation is employed):

$$\left\{\begin{array}{c}\langle\sigma\rangle_{11}\\ \langle\sigma\rangle_{22}\\ \langle\sigma\rangle_{33}\\ \langle\sigma\rangle_{12}\\ \langle\sigma\rangle_{23}\\ \langle\sigma\rangle_{31}\end{array}\right\} = \left[\begin{array}{cccccc}\overline{C}^{\langle\varepsilon\rangle}_{1111} & \overline{C}^{\langle\varepsilon\rangle}_{1122} & \overline{C}^{\langle\varepsilon\rangle}_{1133} & \overline{C}^{\langle\varepsilon\rangle}_{1112} & \overline{C}^{\langle\varepsilon\rangle}_{1123} & \overline{C}^{\langle\varepsilon\rangle}_{1131}\\ \overline{C}^{\langle\varepsilon\rangle}_{2211} & \overline{C}^{\langle\varepsilon\rangle}_{2222} & \overline{C}^{\langle\varepsilon\rangle}_{2233} & \overline{C}^{\langle\varepsilon\rangle}_{2212} & \overline{C}^{\langle\varepsilon\rangle}_{2223} & \overline{C}^{\langle\varepsilon\rangle}_{2231}\\ \overline{C}^{\langle\varepsilon\rangle}_{3311} & \overline{C}^{\langle\varepsilon\rangle}_{3322} & \overline{C}^{\langle\varepsilon\rangle}_{3333} & \overline{C}^{\langle\varepsilon\rangle}_{3312} & \overline{C}^{\langle\varepsilon\rangle}_{3323} & \overline{C}^{\langle\varepsilon\rangle}_{3331}\\ \overline{C}^{\langle\varepsilon\rangle}_{1211} & \overline{C}^{\langle\varepsilon\rangle}_{1222} & \overline{C}^{\langle\varepsilon\rangle}_{1233} & \overline{C}^{\langle\varepsilon\rangle}_{1212} & \overline{C}^{\langle\varepsilon\rangle}_{1223} & \overline{C}^{\langle\varepsilon\rangle}_{1231}\\ \overline{C}^{\langle\varepsilon\rangle}_{2311} & \overline{C}^{\langle\varepsilon\rangle}_{2322} & \overline{C}^{\langle\varepsilon\rangle}_{2333} & \overline{C}^{\langle\varepsilon\rangle}_{2312} & \overline{C}^{\langle\varepsilon\rangle}_{2323} & \overline{C}^{\langle\varepsilon\rangle}_{2331}\\ \overline{C}^{\langle\varepsilon\rangle}_{3111} & \overline{C}^{\langle\varepsilon\rangle}_{3122} & \overline{C}^{\langle\varepsilon\rangle}_{3133} & \overline{C}^{\langle\varepsilon\rangle}_{3112} & \overline{C}^{\langle\varepsilon\rangle}_{3123} & \overline{C}^{\langle\varepsilon\rangle}_{3131}\end{array}\right]\left\{\begin{array}{c}\langle\varepsilon\rangle_{11}\\ \langle\varepsilon\rangle_{22}\\ \langle\varepsilon\rangle_{33}\\ \langle 2\varepsilon\rangle_{12}\\ \langle 2\varepsilon\rangle_{23}\\ \langle 2\varepsilon\rangle_{31}\end{array}\right\} \tag{3.6}$$

With the same procedure the compliance tensor under static uniform boundary conditions $\overline{D}^{\langle\sigma\rangle}_{ijkl}$ can be calculated along with its inverse $\overline{C}^{\langle\sigma\rangle}_{ijkl}$, the stiffness tensor under static uniform boundary conditions

$$\overline{C}^{\langle\sigma\rangle}_{ijkl} = \left(\overline{D}^{\langle\sigma\rangle}_{ijkl}\right)^{-1} \tag{3.7}$$

The RVE size is achieved when the difference $\left(\overline{C}^{\langle\varepsilon\rangle}_{ijkl} - \overline{C}^{\langle\sigma\rangle}_{ijkl}\right)$ is negligible, typically less than 5%.

Homogenization was carried out for the elastic behaviour of a typical particle reinforced metal matrix composite with the mechanical properties of the components shown in Table

Material	E [GPa]	ν	CTE [°C-1]
Matrix	73	0.33	$2.15 \cdot 10^{-5}$
Particles	480	0.17	$3.8 \cdot 10^{-6}$

Table 3.1: Young's moduli, Poisson's ratios and coefficients of thermal expansion of the components.

N. Particles	Vol. Frac.	ξ
6	0.257	2.85
46	0.252	5.69
150	0.251	8.43
360	0.250	11.29
705	0.250	14.12

Table 3.2: Unit cell models for the assessment of the RVE size.

3.1 [77]. In this study composites with amounts of reinforcement up to $V_r = 0.25$ were considered. The RVE size was assessed for the composite with the largest amount of reinforcement and five unit cells of increasing dimensions were modelled: the smallest contained 6 particles while the largest 705. The main features of the models are summarized in Table 3.2. To measure the cell size with respect to the particle dimension the metric ξ is defined:

$$\xi = \sqrt[3]{\frac{V_{uc}}{\overline{V}_p}} \tag{3.8}$$

where V_{uc} is the unit cell volume and $\overline{V}_p$ is the average particle volume.

It can be seen that the developed algorithm allows to obtain the prescribed composition very precisely: even in the case of the smallest volume the difference between the prescribed and the actual reinforcement volume fraction is less than 1% of the total volume. Effective stiffness tensors under static and kinematic uniform boundary conditions were determined for all the models and average stress and strain components (3.3) and (3.4) were computed by weighting the values in each integration point by the associated volume.

In Figure 3.4 the calculated Young's moduli are reported. The difference between the Young's moduli calculated under kinematic and static uniform boundary conditions $\overline{E}^{\langle\varepsilon\rangle}$ and $\overline{E}^{\langle\sigma\rangle}$ is already about 3% for the 360 particle model, however for the sake of consistency with the rest of the work the composite effective elastic properties were computed for the cell with the largest size ($\xi = 14.12$).

The calculated stiffness tensor was that of a linear elastic isotropic material. No appreciable difference could be observed between the shear modulus as a function of Young's

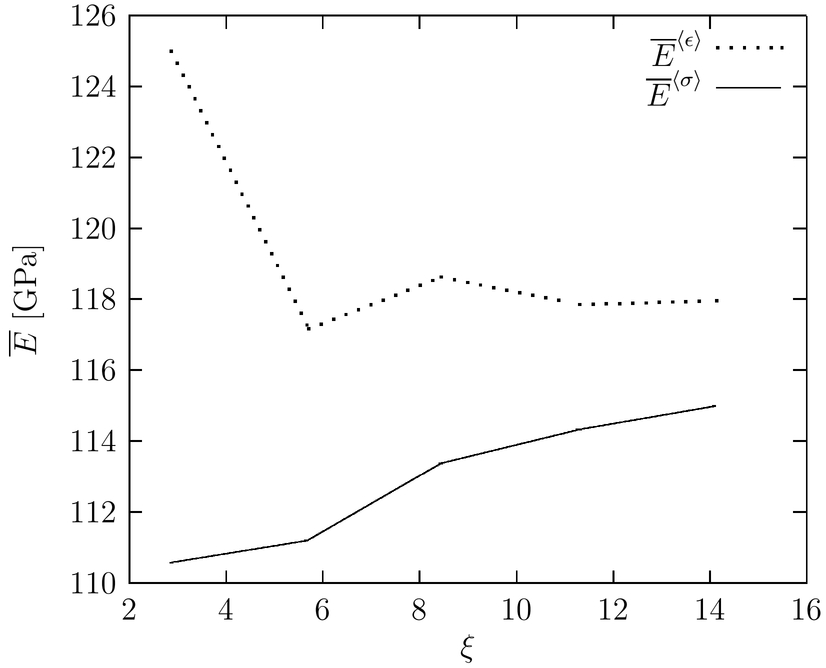

Figure 3.4: Young's modulus $\overline{E}$ under kinematic and static uniform boundary conditions as a function of the unit cell size.

Modulus and Poisson's ratio and that obtained in case of pure shear boundary conditions. The results for all the considered compositions are reported in Table 3.3.

Note that all the models provide results which respect the Hashin-Shtrikman bounds [38] as shown by the data obtained for the shear modulus in Figure 3.5.

V_r	E [MPa]	ν	$G\,(E,\nu)$ [MPa]	G [MPa]
0.05	79973	0.323	30226	30433
0.10	87897	0.315	33414	33714
0.15	96538	0.308	36912	37427
0.20	106784	0.299	41107	41661
0.25	117984	0.290	45725	46397

Table 3.3: Elastic properties of the different composites.

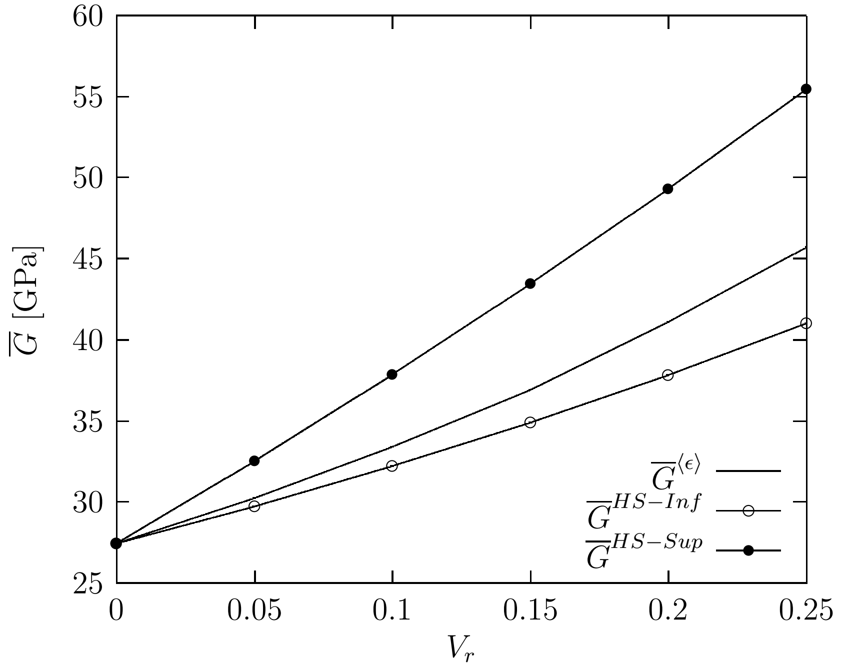

Figure 3.5: Comparison between the calculated shear moduli and Hashin-Shtrikman bounds.

3.4 Thermoelastic Behaviour

If thermal expansion is taken into account and a linear thermoelastic behaviour is assumed for both the matrix and the reinforcement, the overall stress-strain relations can be written in the form

$$\langle\varepsilon\rangle_{ij} = \overline{D}_{ijkl}\,\langle\sigma\rangle_{kl} + \overline{\alpha}_{ij}^{\langle\sigma\rangle}\Delta T \tag{3.9}$$

$$\langle\sigma\rangle_{ij} = \overline{C}_{ijkl}\left(\langle\varepsilon\rangle_{kl} - \overline{\alpha}_{ij}^{\langle\varepsilon\rangle}\Delta T\right) \tag{3.10}$$

where $\overline{\alpha}_{ij}^{\langle\sigma\rangle}$ and $\overline{\alpha}_{ij}^{\langle\varepsilon\rangle}$ are the effective thermal expansion tensors under kinematic and static uniform boundary conditions, respectively; ΔT is a spatially uniform temperature difference with respect to the stress-free reference temperature. Comparison of (3.9) and (3.10) with (3.5) yields

$$\overline{\alpha}_{ij}^{\langle\sigma\rangle} = \overline{\alpha}_{ij}^{\langle\varepsilon\rangle} \tag{3.11}$$

There is no need to check the size of the RVE for the CTE since $\overline{\alpha}_{ij}$ for two-phase materials is directly related to the elastic moduli of the composite [69]. Simulations were carried out under both types of boundary conditions on the same unit cells adopted to characterize the elastic behaviour and the material proved to be isotropic

$$\overline{\alpha}_{ij} \approx \delta_{ij}\overline{\alpha} \tag{3.12}$$

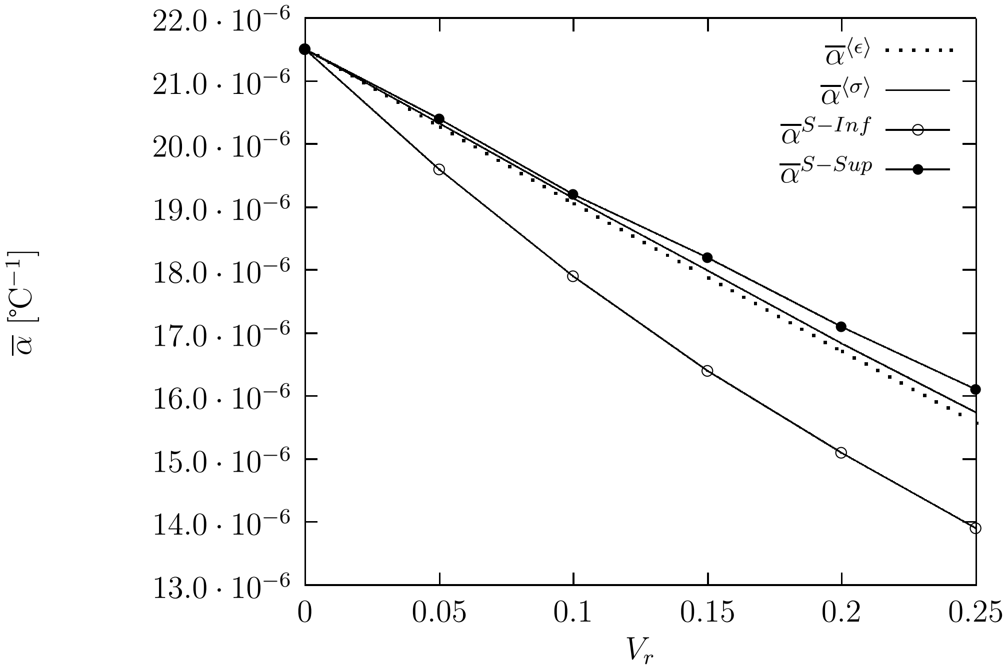

Figure 3.6: Comparison between Schapery's bounds and the calculated coefficients of thermal expansions $\overline{\alpha}$ under static and kinematic uniform boundary conditions.

where δ_{ij} is Kronecker delta. The calculated CTEs for the different compositions and the comparison with the Schapery's bounds [98] are depicted in Figure 3.6.

3.5 Elastoplastic Behaviour

In the case of linear elastic statistically isotropic particle reinforced composites, cubic cells with edges five times the inclusion characteristic size lead to very precise effective moduli as indicated in [32] and confirmed in the present work: the difference between the computed effective Young's moduli under static and kinematic uniform boundary conditions is about 5% for the cell with $\xi = 5.69$. For elastoplastic matrix behaviours, considerably larger cells are required to achieve the RVE size, especially when large plastic strain develops, because the strain field is significantly more inhomogeneous than in the elastic case. In such cases a criterion to define the RVE is needed.

The same typical particle reinforced metal matrix composite considered for the elastic behaviour was modelled. The matrix was assumed to be elastoplastic and to follow the von Mises yield criterion

$$\varphi\left(\sigma_{ij}, \varepsilon^p\right) = \sqrt{3J_2'} - k\left(\varepsilon^p\right) \tag{3.13}$$

where ε^p is the equivalent plastic strain, J_2' is the second invariant of the stress deviator and $k(\varepsilon^p)$ is the isotropic hardening law with the form

$$k(\varepsilon^p) = \sigma_y + h(\varepsilon^p)^q \tag{3.14}$$

where σ_y, h and q are the yield stress and the strain hardening parameters, respectively. The matrix material is assumed to have the elastic properties reported in Table 3.1, the uniaxial yield stress $\sigma_y = 170$ MPa, the strain hardening parameters $h = 577$ MPa and $q = 0.37$ [77]. Preliminary studies showed that, for up to 0.05 imposed strain, the model response did not vary significantly whether small or large displacements were considered. Thus the simulations were carried out within the framework of the small displacements assumption.

Due to the presence of particles the stress-strain curve of the composite is expected to present a larger hardening than that of the matrix material. This effect can be described by following the approach proposed in [19, 106], in which the microstress $\sigma_{ij}(\boldsymbol{x})$ is split into two parts: the one which would occur if the constituents were elastic and a self equilibrated residual stress field

$$\sigma_{ij}(\boldsymbol{x}) = L_{ijkl}(\boldsymbol{x})\langle\sigma\rangle_{kl} + \sigma^r_{ij}(\boldsymbol{x}) \tag{3.15}$$

where $L_{ijkl}(\boldsymbol{x})$ stands for the elastic stress localization tensor. The average elastic energy in the material can be written as

$$\langle U\rangle = \frac{1}{2\Omega}\int_\Omega D_{ijkl}(\boldsymbol{x})\,\sigma_{ij}(\boldsymbol{x})\,\sigma_{kl}(\boldsymbol{x})\,d\Omega \tag{3.16}$$

where $D_{ijkl}(\boldsymbol{x})$ is the local compliance tensor. By introducing (3.15) in (3.16) the following expression is obtained

$$\langle U\rangle = \frac{1}{2}\overline{D}_{ijkl}\langle\sigma\rangle_{ij}\langle\sigma\rangle_{kl} + \frac{1}{2\Omega}\int_\Omega D_{ijkl}(\boldsymbol{x})\,\sigma^r_{ij}(\boldsymbol{x})\,\sigma^r_{kl}(\boldsymbol{x})\,d\Omega \tag{3.17}$$

The first term is the average macroscopic elastic energy $\overline{U}$ while the second is the average micro-stored elastic energy due to the residual stresses $\langle U^r\rangle$. For the sake of simplicity (3.17) is rewritten as

$$\langle U\rangle = \overline{U} + \langle U^r\rangle \tag{3.18}$$

In an analogous manner the average dissipated energy $\langle P\rangle$ can be computed

$$\langle P\rangle = \int_0^t \frac{1}{\Omega}\int_\Omega \sigma_{ij}(\boldsymbol{x})\,\dot{\varepsilon}^p_{ij}(\boldsymbol{x})\,d\Omega dt \tag{3.19}$$

where $\dot{\varepsilon}^p_{ij}(\boldsymbol{x})$ is the local plastic strain rate. At the macroscopic level the plastic strain is the difference between the average total strain and the macroscopic elastic strain

$$\overline{\varepsilon}^p_{ij} = \langle\varepsilon\rangle_{ij} - \overline{D}_{ijkl}\langle\sigma\rangle_{ij} \tag{3.20}$$

note that

$$\overline{\varepsilon}^{p}_{ij} \neq \frac{1}{\Omega}\int_{\Omega}\varepsilon^{p}_{ij}\left(\boldsymbol{x}\right)d\Omega \tag{3.21}$$

By introducing (3.15) in (3.19) the following expression for the average macroscopic plastic work is obtained

$$\int_{0}^{t}\left\langle\sigma\right\rangle_{ij}\dot{\overline{\varepsilon}}^{p}_{ij}dt = \left\langle P\right\rangle + \left\langle U^{r}\right\rangle \tag{3.22}$$

Therefore two contributions to the average plastic work at the macroscopic level are identified: the average dissipated energy $\langle P\rangle$ and the average elastic energy due to residual stresses $\langle U^r\rangle$, which is stored in the material and contributes to the macroscopic hardening (for further details refer to [106]).

In the present work the uniaxial tensile behaviour of the same increasingly larger cells (except for that with $\xi = 2.85$) modelled in the framework of linear elasticity was considered (table 3.2). Their response was studied under four different sets of boundary conditions, all of them representative of a pure tensile test (additional boundary conditions to constrain rigid body displacements are not indicated):

$$\begin{cases} u_1\left(0,x_2,x_3\right)=0\\ u_1\left(L,x_2,x_3\right)=\overline{u}\\ u_2\left(x_1,0,x_3\right)=0\\ u_2\left(x_1,L,x_3\right)|_{x_2,x_3\neq L}=u_2(0,L,L)\\ u_3\left(x_1,x_2,0\right)=0\\ u_3\left(x_1,x_2,L\right)|_{x_2,x_3\neq L}=u_3\left(0,L,L\right)\end{cases} \tag{3.23}$$

$$\begin{cases} f_1\left(0,x_2,x_3\right)=-\overline{p}\\ f_1\left(L,x_2,x_3\right)=\overline{p}\\ u_2\left(x_1,0,x_3\right)=0\\ u_2\left(x_1,L,x_3\right)|_{x_2,x_3\neq L}=u_2(0,L,L)\\ u_3\left(x_1,x_2,0\right)=0\\ u_3\left(x_1,x_2,L\right)|_{x_2,x_3\neq L}=u_3\left(0,L,L\right)\end{cases} \tag{3.24}$$

$$\begin{cases} u_1\left(0,x_2,x_3\right)=0\\ u_1\left(L,x_2,x_3\right)=\overline{u}\\ f_2\left(x_1,0,x_3\right)=0\\ f_2\left(x_1,L,x_3\right)=0\\ f_3\left(x_1,x_2,0\right)=0\\ f_3\left(x_1,x_2,L\right)=0\end{cases} \tag{3.25}$$

$$\begin{cases} f_1\left(0, x_2, x_3\right) = -\overline{p} \\ f_1\left(L, x_2, x_3\right) = \overline{p} \\ f_2\left(x_1, 0, x_3\right) = 0 \\ f_2\left(x_1, L, x_3\right) = 0 \\ f_3\left(x_1, x_2, 0\right) = 0 \\ f_3\left(x_1, x_2, L\right) = 0 \end{cases} \tag{3.26}$$

Here u_i and f_i are the nodal displacement and the surface load in the x_i direction and L is the length of the edge of the cell. In (3.23) all faces are forced to stay planar during the deformation process while in (3.24) only those parallel to the tensile axis. Boundary conditions (3.25) are mixed static-kinematic with imposed uniform displacements on the tensile faces while (3.26) are purely static.

In this work periodic boundary conditions [16, 37, 54] were not adopted since they require mesh periodicity [107]. However, the effective composite behaviour obtained under mixed static-kinematic boundary conditions (3.23, 3.24, 3.25) is always bounded by those obtained under static and kinematic uniform boundary conditions [39].

The obtained effective uniaxial stress-strain curves for the unit cell with $\xi = 14.12$ and $V_r = 0.25$ are shown in Figure 3.7. The response of the model depends on the applied boundary conditions while, if the material were homogeneous, the four different sets of boundary conditions would lead to the same stress-strain curve. Results show that the effective curves obtained by imposing that two or four faces keep planar, (3.25) and (3.24), are bounded by those resulting from (3.23) and (3.26), where all faces keep planar or are free to deform, respectively. It can also be observed that the curve due to (3.26) flattens for $\langle\varepsilon\rangle_{11} = 0.015$. This is caused by the concentration of plastic strain in the corner regions of the cell because of the lack of confinement. This phenomenon increasingly affects the results as the prescribed tension $\overline{p}$ nears the load carrying capacity of the material and eventually causes the model to loose representativeness.

The effective mechanical behaviour of the composite resulting from the model and especially the macroscopic hardening strongly depends on the size of the unit cell (figure 3.8). To assess the size of the RVE the evolution of $\langle U^r\rangle$ as a function of the cell size ξ was studied for unit cells with $V_r = 0.25$: pure traction simulations were carried out under boundary conditions (3.24) and (3.25), with applied macrostress $\langle\sigma\rangle_{11} = 800$ MPa and applied macrostrain $\langle\varepsilon\rangle_{11} = 0.05$, respectively. The value of $\langle U^r\rangle$ was obtained by means of (3.18), where $\langle U\rangle$ was computed during the elastoplastic simulation and $\overline{U}$ was evaluated by simulating the material elastic behaviour under (3.24) and (3.25). To obtain a better accuracy, the energy $\overline{U}$ was calculated directly and not by using the results of the homogenization of the elastic properties reported in Table 3.3.

Results are reported in Figures 3.9 and 3.10. The values of $\overline{U}$ and $\langle U^r\rangle$ are normalized

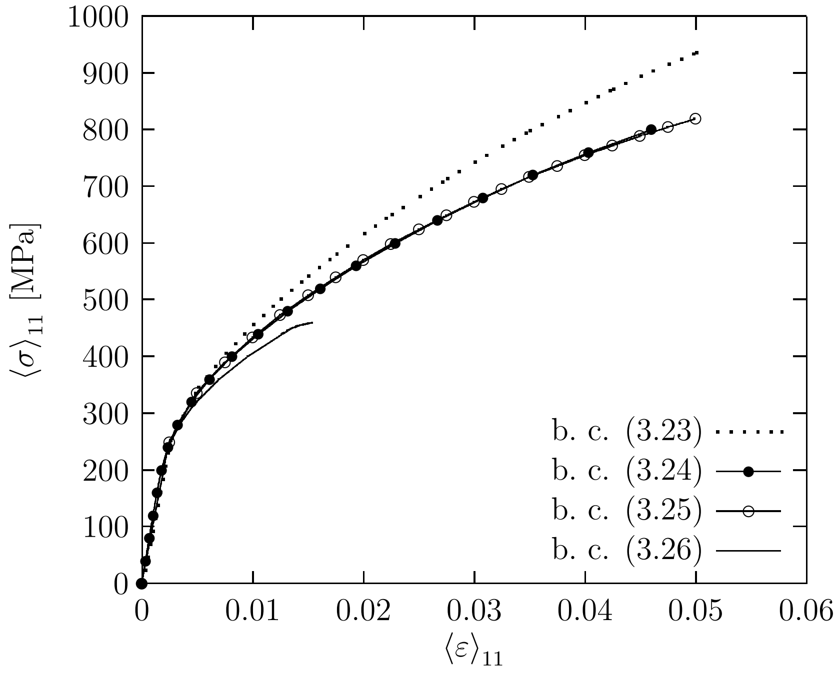

Figure 3.7: Effective uniaxial stress-strain curves under different boundary conditions.

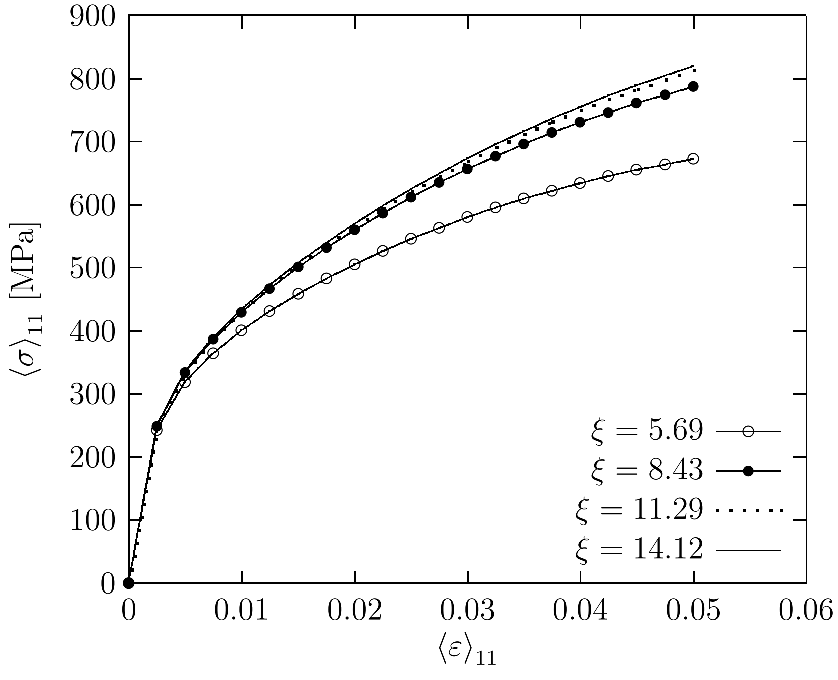

Figure 3.8: Effective uniaxial stress-strain curves under boundary conditions (3.25) for the considered unit cell sizes.

by U_0, the average strain energy of the inclusion material under an applied tension of 800 MPa. With both sets of boundary conditions the average macroscopic elastic energy $\overline{U}$ at convergence is already achieved for a cell size $\xi = 8.43$, this can be explained by the fact that with mixed boundary conditions (3.24) the convergence of the effective elastic properties is faster in the case of uniform static or kinematic boundary conditions [39]. In the case of boundary conditions (3.24) the average elastic energy due to residual stresses $\langle U^r \rangle$ decreases significantly (about 25%) with the cell size for $5.69 \leq \xi \leq 11.29$, while its value varies slightly (about 6%) between $\xi = 11.29$ and $\xi = 14.12$ (figure 3.9). With boundary conditions (3.25), $\langle U^r \rangle$ exhibits an opposite trend: it increases with the cell size with variations of about 75% for $5.69 \leq \xi \leq 11.29$ and of only 1% between $\xi = 11.29$ and $\xi = 14.12$. The convergence of $\langle U^r \rangle / U_0$ implies that the unit cell with $\xi = 14.12$ can be considered a RVE for the elastoplastic uniaxial behaviour up to the considered applied average stress or strain.

The steadiness of the elastic energy due to residual stresses with respect to the cell size proves to be a valid criterion to evaluate the RVE for the uniaxial elastoplastic behaviour. This assessment is confirmed by the fact that the stress-strain curves obtained under different boundary conditions, (3.24) and (3.25), almost coincide up to $\langle \varepsilon \rangle_{11} = 0.05$, as shown in Figure 3.7 as well.

The cubic symmetry of the composite was verified for the elastoplastic behaviour as well. Pure traction simulations were carried out for the 1, 2, 3 directions and no significant difference could be observed in the effective stress-strain curves (boundary conditions of the type (3.25) were applied as they are less demanding in terms of computing time since they do not include the face planarity condition). The uniaxial tensile behaviour was determined for all the considered compositions (table 3.2) on unit cells with $\xi \approx 14$. The strengthening effect of the particles on the effective stress-strain curves (up to $\langle \varepsilon \rangle_{11} = 0.05$) can be observed in Figure 3.11.

3.6 Application to Experimental Data

The model was applied to the real case of the 2124 aluminum alloy reinforced with SiC particles studied in [80]. The composite contains 17 vol.% SiC particles of an average size of 1.4 µm. The authors carried out tensile tests at different temperatures both on the matrix metal and on the composite. The negligible amount of reaction products between 2124 aluminum alloy and SiC particles [8] allows to assume for the matrix material in the composite the uniaxial stress-strain curve obtained by testing the bulk material.

For the purposes of this work the mechanical behaviour at room temperature is considered and tensile tests are simulated under boundary conditions (3.25) up to 5% strain, a value which is compatible both with the small displacement assumption and with the

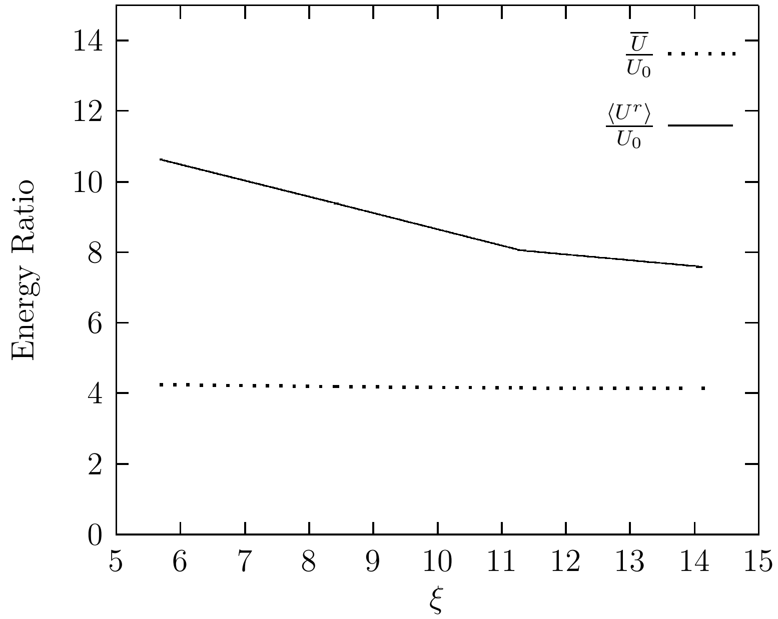

Figure 3.9: Normalized average macroscopic elastic energy $\overline{U}/U_0$ and normalized average elastic energy due to residual stresses $\langle U^r \rangle / U_0$ as functions of the unit cell size under boundary conditions (3.24) with an applied tensile stress of 800 MPa.

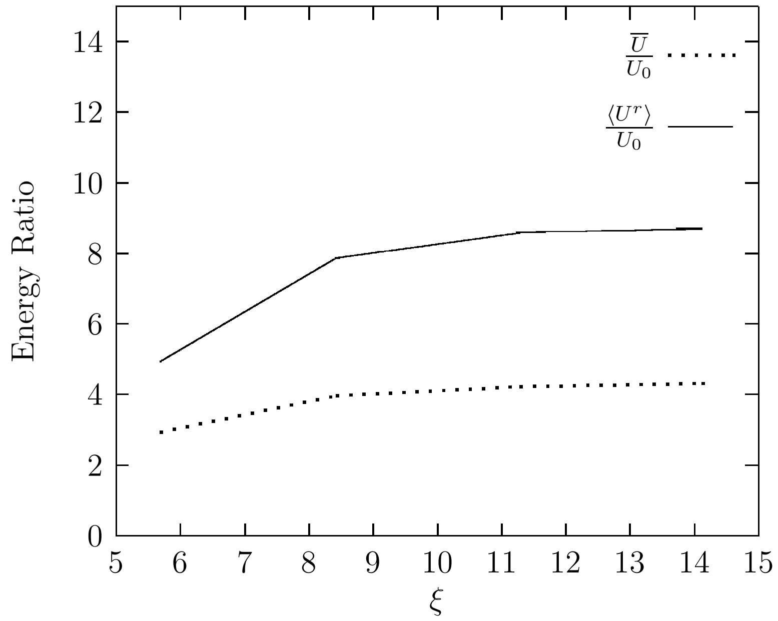

Figure 3.10: Normalized average macroscopic elastic energy $\overline{U}/U_0$ and normalized average elastic energy due to residual stresses $\langle U^r \rangle / U_0$ as functions of the unit cell size under boundary conditions (3.25) with an applied tensile strain of 0.05.

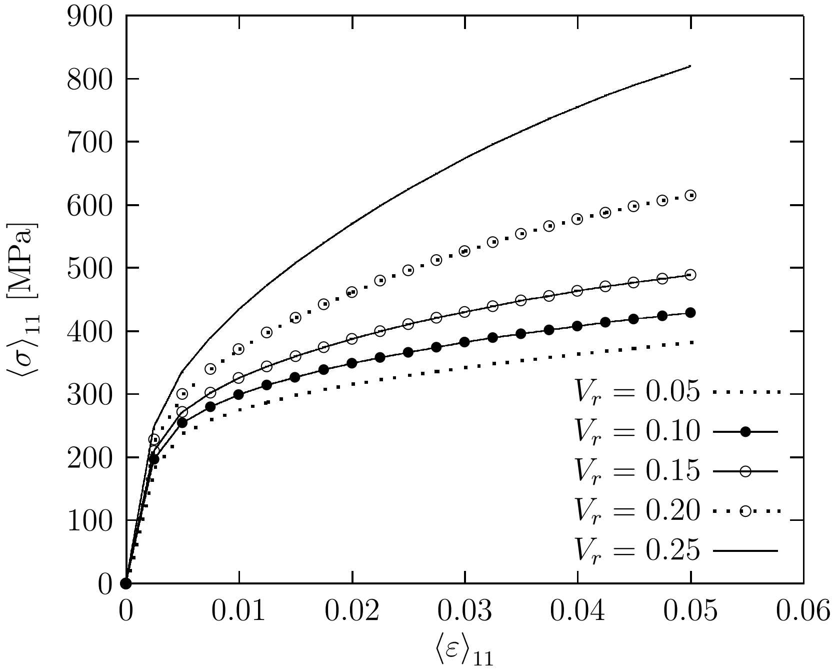

Figure 3.11: Effective uniaxial stress-strain curves of the different composites.

chosen mechanical behavior. Moreover in this strain interval it is reasonable to assume that damage can be neglected thus the model hypotheses of particle and matrix integrity and of perfect interfaces between the two are acceptable.

The homogenization model consisted of a unit cell of 3375 µm^3 (corresponding to an edge length of 15 µ) containing about 380 particles. The particle average volume was 1.5 µm^3 with 0.1 µm^3 standard deviation, corresponding to an average equivalent diameter of 1.42 µm. The SiC particles were assigned linear elastic behaviour; the values $E = 415$ GPa and $\nu = 0.16$ were chosen [82]. The matrix material was assigned an elastoplastic behaviour following the Von Mises criterion with isotropic hardening (3.13). The strain hardening profile was extracted from the experimental uniaxial stress-strain curves at room temperature reported by the authors.

The stress-strain curve obtained by homogenization is compared with the experimental one in Figure 3.12, it can be noted that there is full agreement between the two up to $\langle\varepsilon\rangle_{11} = 0.05$.

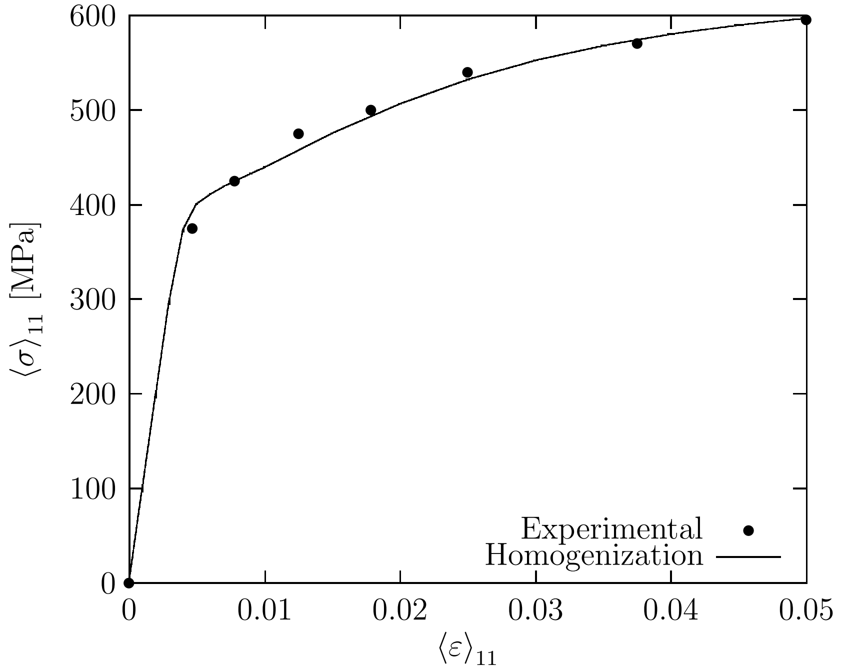

Figure 3.12: Comparison between the Al2124-17 vol.% SiC experimental stress-strain curve and that obtained by homogenization.

Chapter 4

Characterization of the Braze Filler

The optimization of the braze layout with respect to residual stress relief can be carried out by finite element analyses. However, the accuracy of these analyses is critically dependent on the knowledge of the mechanical behaviour of the braze metal and of the effect of the reinforcement on it. In this chapter the combined numerical-experimental strategy developed for the assessment of the elastoplastic properties of Incusil™ABA® and of the composite braze fillers is described. The experimental investigation proceeded in two main directions: on one hand the mechanical behaviour was studied by means of tensile tests, on the other the microstructure was characterized by scanning electron microscopy and energy dispersive analysis using X-rays (SEM-EDX) and by optical microscopy. The experimental results highlighted that the matrix materials in the composite fillers are quite different from the original Incusil™ABA®. In [20] the plastic properties of the aluminium matrix in a composite reinforced with continuous alumina fibers are assessed by nano-indentation and other studies in which indentation is used to characterize the plastic properties of a metal are reported in literature [23, 64]. However, in the present case indentation-based methods could not be adopted, because, due to the presence of particles, the scatter in the experimental results would be too large (this was also confirmed by some preliminary tests whose results are not reported). Thus an inverse homogenization procedure was developed to identify the mechanical properties of the matrix alloys in the composites. The results of the identification were eventually used to carry out a classical homogenization which led to obtain temperature dependent mechanical properties of the composite fillers, suitable to be used as input data for the simulation of the cooling process which the joints undergo after brazing.

4.1 tensile Tests

The dogbone specimens described in Section 2.3.2 were tested in tension on a MTS 809 Axial/Torsional Test System. Custom self-centering grips were used (Figure 4.1). The tests were carried out under displacement control with an imposed strain rate of 0.0001 s^{-1} up to 0.02 strain and 0.001 s^{-1} until rupture. The specimens were instrumented with electric resistance strain gauges with a gauge length of 1.5 mm (Figure 4.2). Since the experiments showed a high repeatability, four specimens (coming from two or three different batches) were tested for each braze filler composition: pure Incusil™ABA® and Incusil™ABA® reinforced with 9, 18, 27 vol% SiC. The experimental tensile stress-strain curves for the different materials are summarized in Figures 4.3, 4.4, 4.5 and 4.6.

For each material the average stress-strain curve $\bar{\sigma}(\varepsilon)$ and the standard deviation $\hat{\sigma}(\varepsilon)$ are plotted. The scatter of the experimental data, which was computed up to the minimum experimental values of the ultimate strain, is quite limited for all the four materials, thus it can be assumed that $\bar{\sigma}(\varepsilon)$ is representative of the material behaviour. The mechanical behaviour of the filler varies as a function of the amount of reinforcement. Two main effects can be identified:

1. the ultimate strain decreases with the amount of reinforcement: while Incusil™ABA® breaks at a nominal strain of about 0.1, the composites exhibit much lower ultimate strains (about 0.03, 0.01 and 0.005 for 9, 18, 27 vol.% SiC respectively);

2. the ultimate stress decreases with the amount of reinforcement: Incusil™ABA® breaks at about 370 MPa while for the composites with 9, 18, 27 vol% SiC the average ultimate stress is 330, 310 and 290 MPa respectively.

The addition of reinforcement leads also to an increase of Young's modulus. This effect was not assessed experimentally because the geometry of the specimens and the experimental setup were not suitable for this purpose but it can be predicted by performing the homogenization of the elastic properties of the composite (e.g. by computing Hashin-Shtrikman's bounds [38]). The mechanical properties of Incusil™ABA®, like other metal alloys, strongly depend on the manufacturing process. For the sake of comparison, tensile tests were carried out also on a set of eight wire specimens (length 120 mm and diameter 1 mm, one of the possible forms in which the material is supplied by the producer). The results summarized in Figure 4.7 show that Incusil™ABA® in wire form exhibits a yield stress, a hardening and an ultimate strain which are much higher than those obtained with the dogbone specimens and closer to those declared by the producer. These significant differences, which may be due to several reasons (cooling profile, extrusion process, . . .) highlight once more that characterizing this material is all but a trivial task and support the choice of the adopted manufacturing procedure which is as near as possible to the actual process undergone by the filler during the production of joints.

Figure 4.1: Self-centering grips for tensile tests.

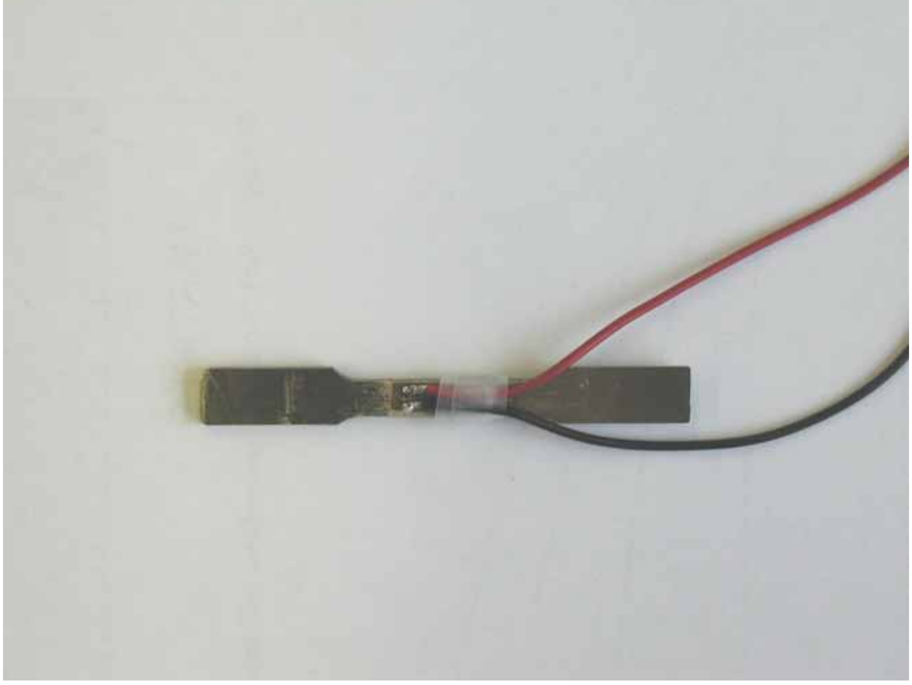

Figure 4.2: Tensile specimen instrumented with a strain gauge.

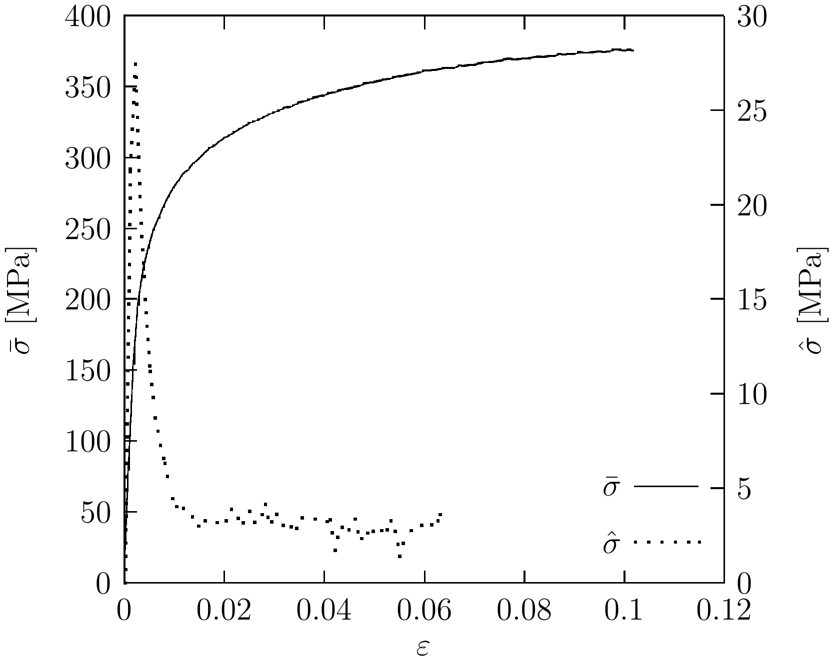

Figure 4.3: Experimental uniaxial tensile stress-strain curve for Incusil™ABA®.

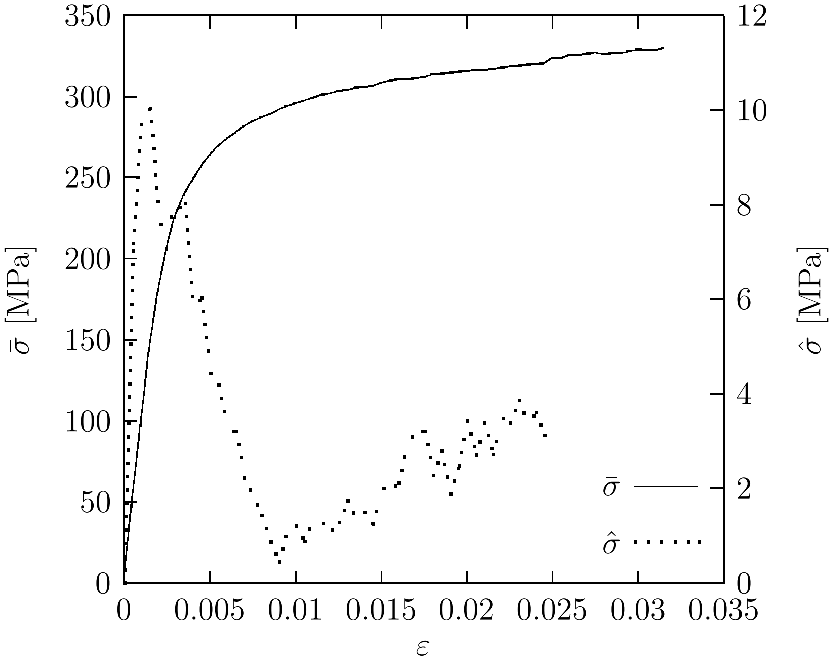

Figure 4.4: Experimental uniaxial tensile stress-strain curve for Incusil™ABA®-9 vol.% SiC.

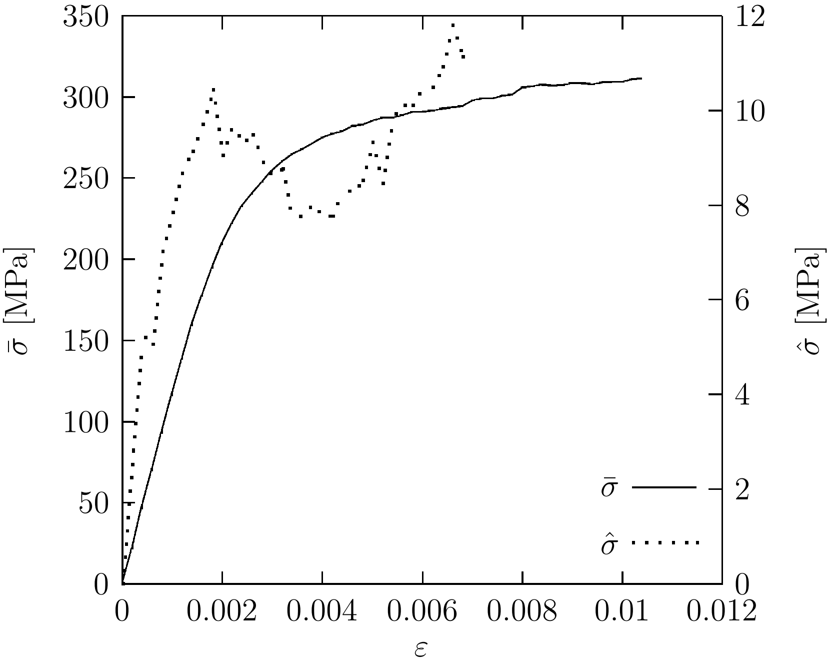

Figure 4.5: Experimental uniaxial tensile stress-strain curve for Incusil™ABA®-18 vol.% SiC.

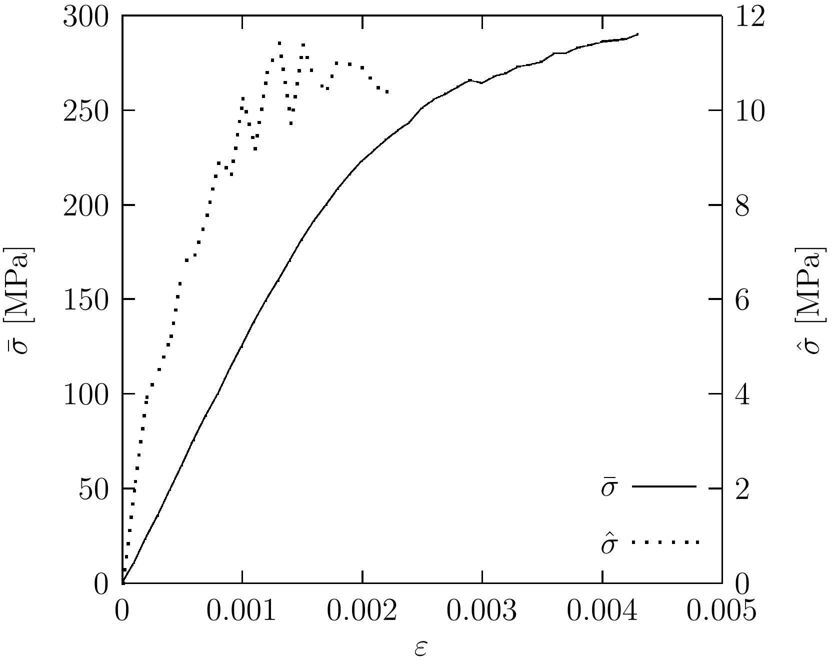

Figure 4.6: Experimental uniaxial tensile stress-strain curve for Incusil™ABA®-27 vol.% SiC.

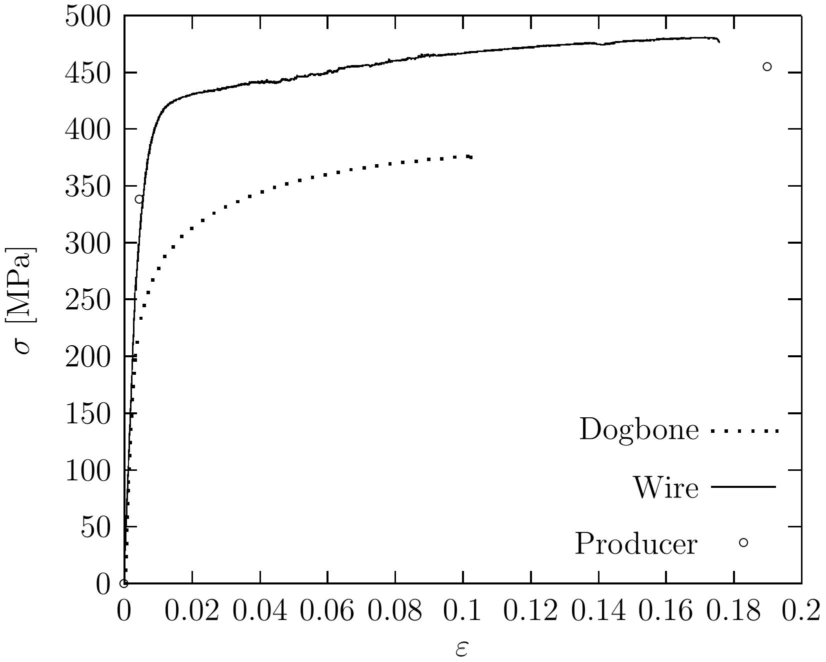

Figure 4.7: Comparison between the data declared by the producer and Incusil™ABA® stress-strain curves obtained from dogbone and wire specimens.

4.2 Microstructural Analysis

Specimens for optical and electron microscopy analyses were extracted from the dogbone specimens both in the longitudinal and in the transverse direction and hot mounted in a conductive phenolic resin (Struers PolyFast). Then coarse grinding and fine grinding were performed by using SiC paper, down to a grit size of 1200. The last phase of the specimen preparation, polishing, was carried out by using diamond suspensions with a minimum grain size of 1 µm for the final stage of the process. A total of twelve specimens were prepared, three for each material.

4.2.1 SEM-EDX

The microstructure of pure Incusil™ABA® and of the Incusil™ABA®-based composite fillers was investigated by EDX technique in a Philips XL 30 scanning electron microscope. All the micrographs were taken by using Back Scattered Electron (BSE) signal to improve phase contrast. The phase weight compositions were assessed by EDX point measurements (three measurements were taken for each phase). In the series of Figures 4.8-4.11 one optical microscopy image and three BSE images at different magnifications are shown for each composition. The results of EDX point measurements are summarized in Table 4.1

Material	Phase	Ag[wt.%]	In[wt. %]	Ti[wt.%]	Cu[wt.%]
Incusil™ABA®	AgIn	80.5	13.3	0.1	6.1
	Cu	4.0	2.6	1.3	92.1
	Cu_4Ti	1.8	0.6	14.9	85.7
	Cu_2InTi	2.4	26.8	16.1	54.7
Incusil™ABA®-9 vol.% SiC	AgIn	81.0	13.1	0.2	5.7
	Cu	5.1	3.2	1.7	90.0
	Cu_4Ti	4.0	1.3	15.2	79.4
	Cu_2InTi	2.6	25.5	15.9	56.1
Incusil™ABA®-18 vol.% SiC	AgIn	80.3	13.3	0.3	6.1
	Cu	6.0	3.5	1.9	88.6
	Cu_4Ti	2.6	1.4	15.2	80.9
	Cu_2InTi	3.1	25.9	15.2	55.8
Incusil™ABA®-27 vol.% SiC	AgIn	80.9	12.1	0.2	6.8
	Cu	4.8	1.9	1.7	91.7
	Cu_4Ti	2.1	0.5	15.0	82.4
	Cu_2InTi	3.8	23.1	14.0	59.1

Table 4.1: Weight composition of the phases in the four materials.

while the BSE images of the locations where the measurements were taken are shown in Figure 4.12.

Since the obtained results are analogous to those provided in [58], where Incusil™ABA® is investigated in the framework of the active brazing of diamond grits, their interpretation is based on the cited study itself. The microstructure of the brazing alloy consists of two main phases: primary precipitates of a Cu-rich solid solution phase, from now on indicated as Cu, and a AgIn-rich (labelled AgIn) solid solution phase, in which fine precipitates of the Cu phase can be found. Titanium is concentrated in two other phases: a phase having a composition close to Cu_4Ti and an intermetallic phase which Ti forms with Cu and In with a composition close to Cu_2InTi.

Experimental data highlight that, while the compositions of the single phases do not depend on SiC volume fraction, the matrix materials differ in terms of volume fraction of each phase. This is particularly evident if the microstructures of Incusil™ABA® and the matrix material in the 27 vol.% SiC composite are compared (Figures 4.8 and 4.11): in the composite the two titanium containing phases (grey in optical microscope images) have almost disappeard while they are well present in the original alloy.

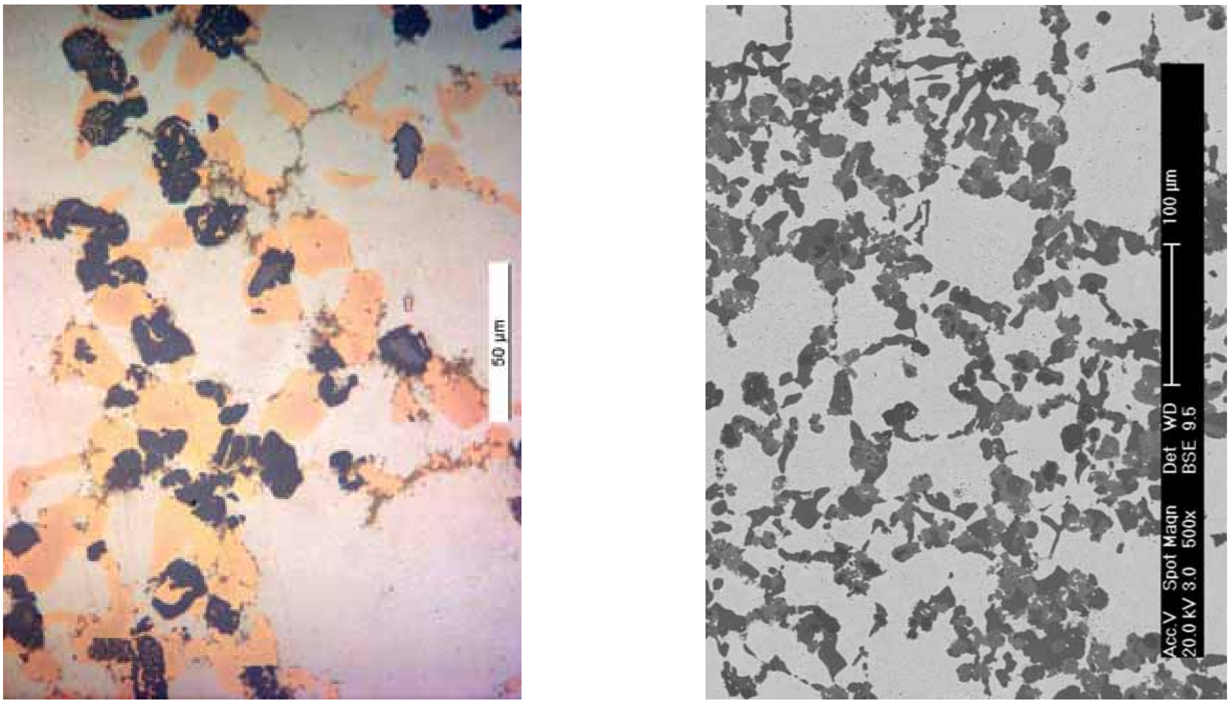

(a) Optical microscope

(b) SEM 500x

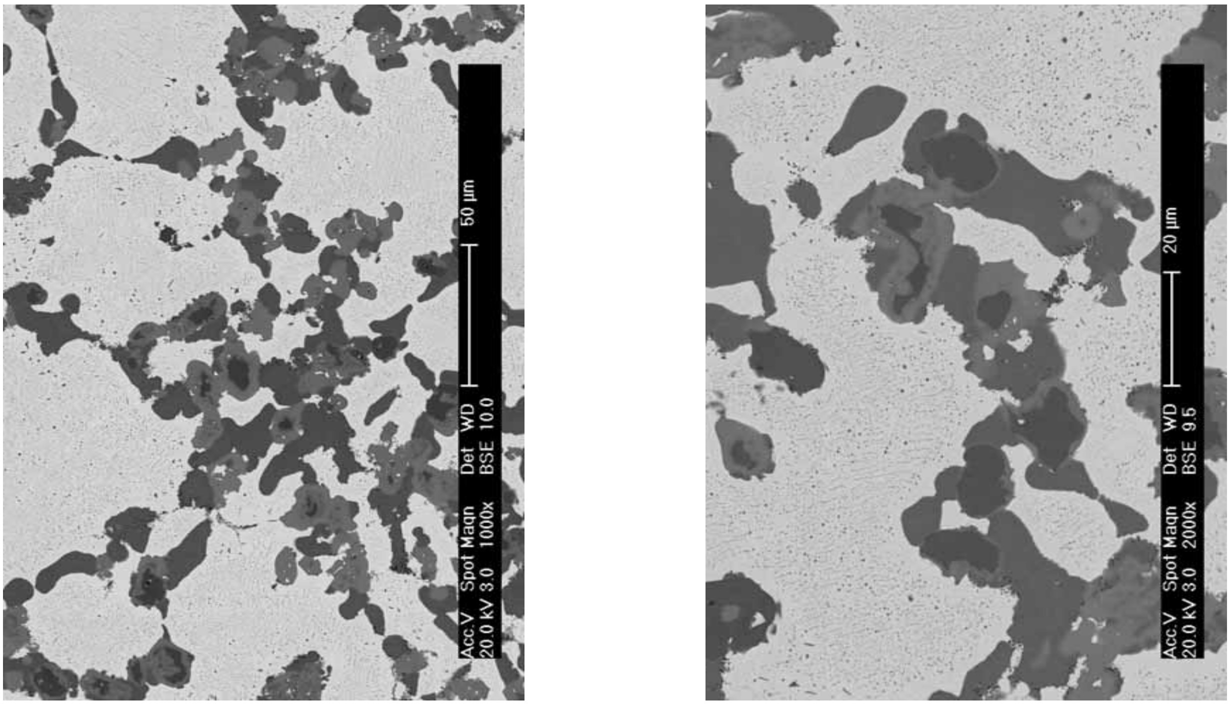

(c) SEM 1000x

(d) SEM 2000x

Figure 4.8: Microstructure of Incusil™ABA®.

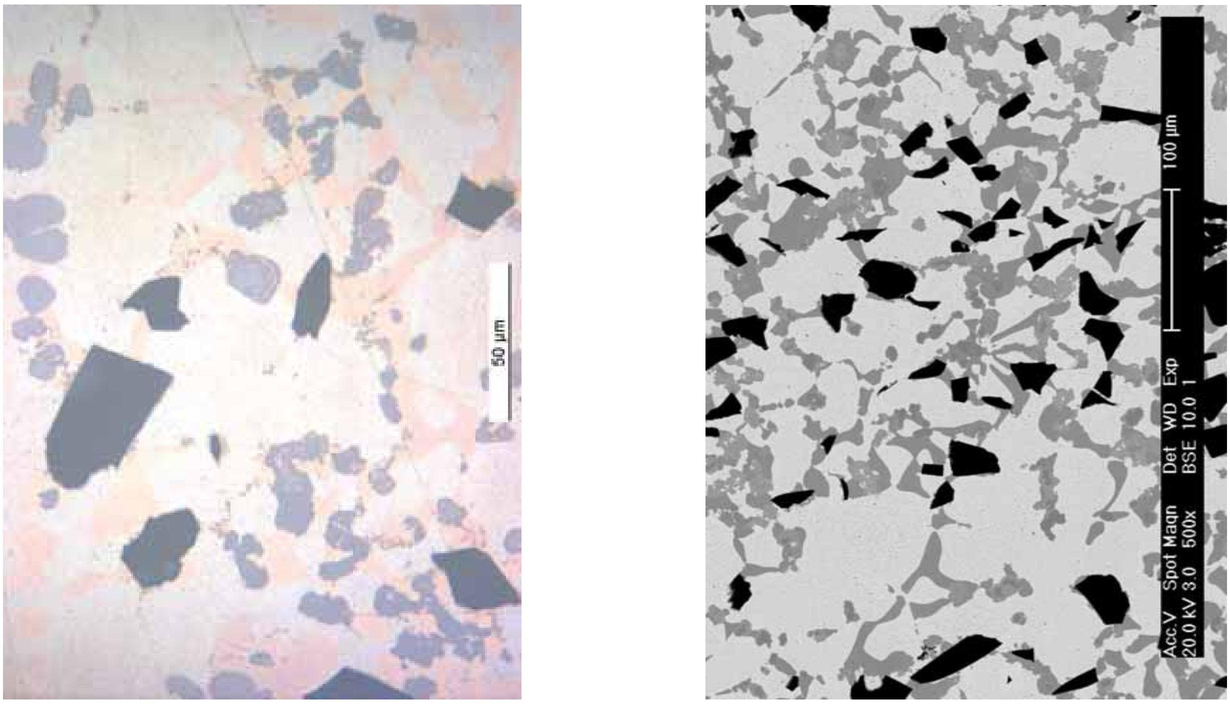

(a) Optical microscope

(b) SEM 500x

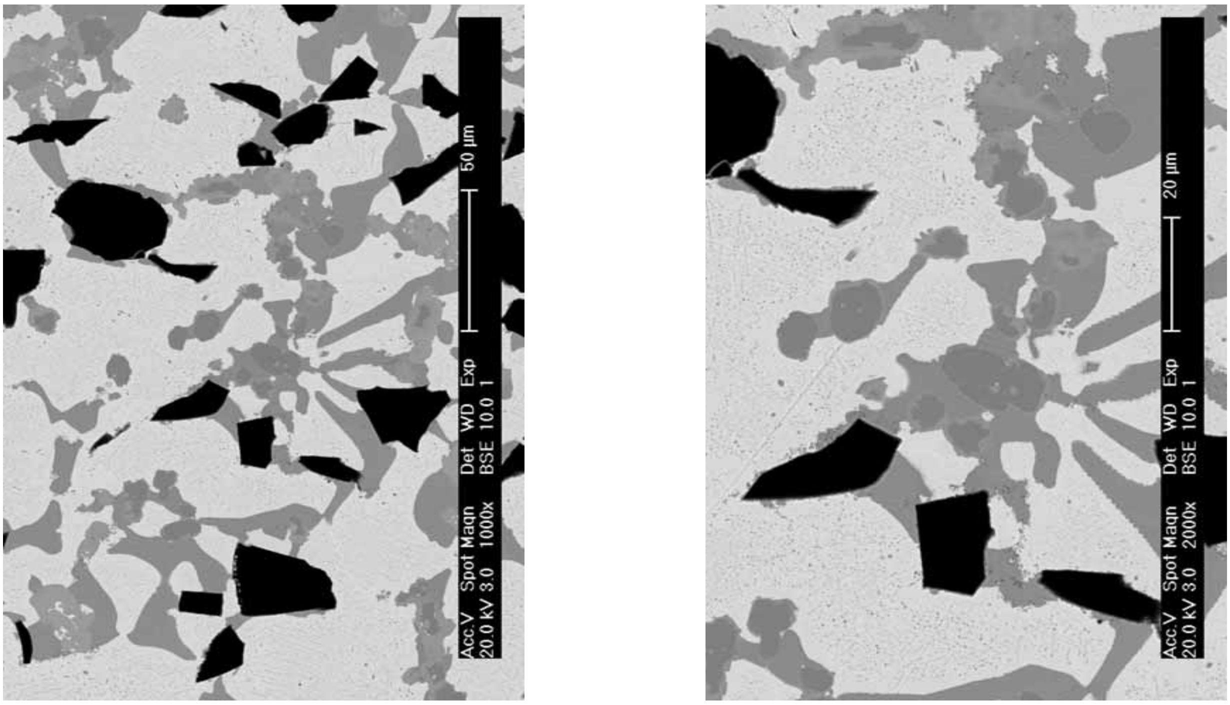

(c) SEM 1000x

(d) SEM 2000x

Figure 4.9: Microstructure of Incusil™ABA®-9 vol.% SiC.

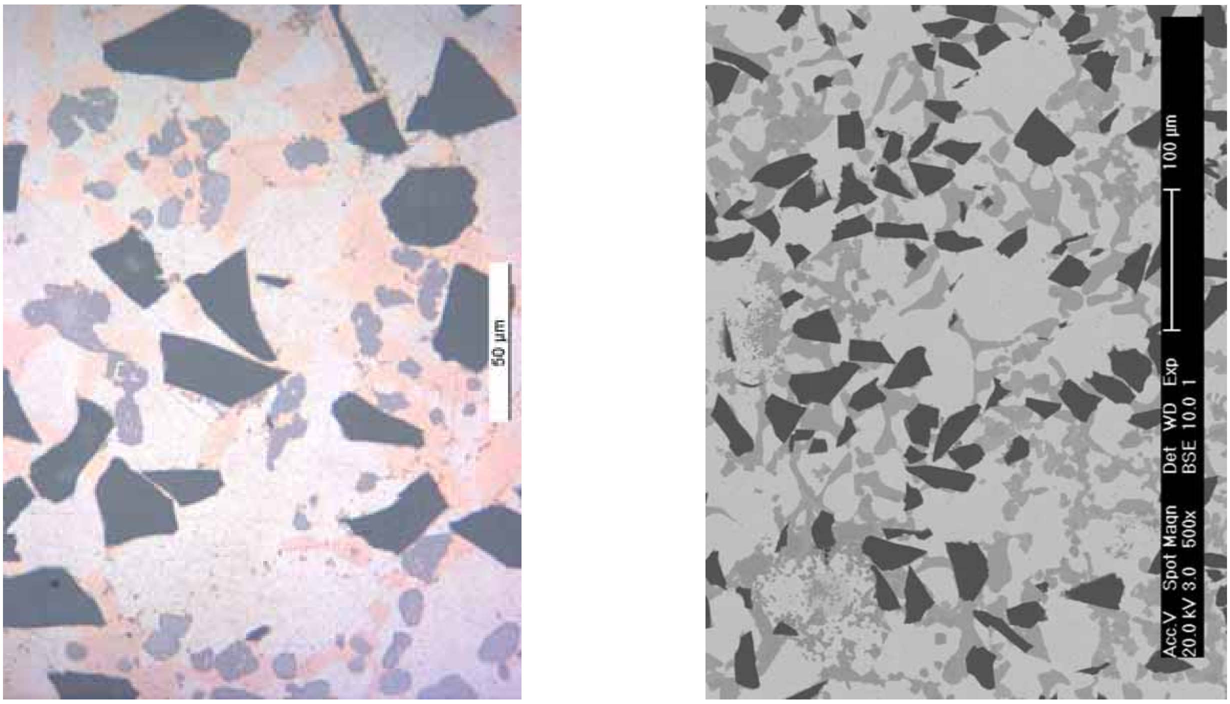

(a) Optical microscope (b) SEM 500x

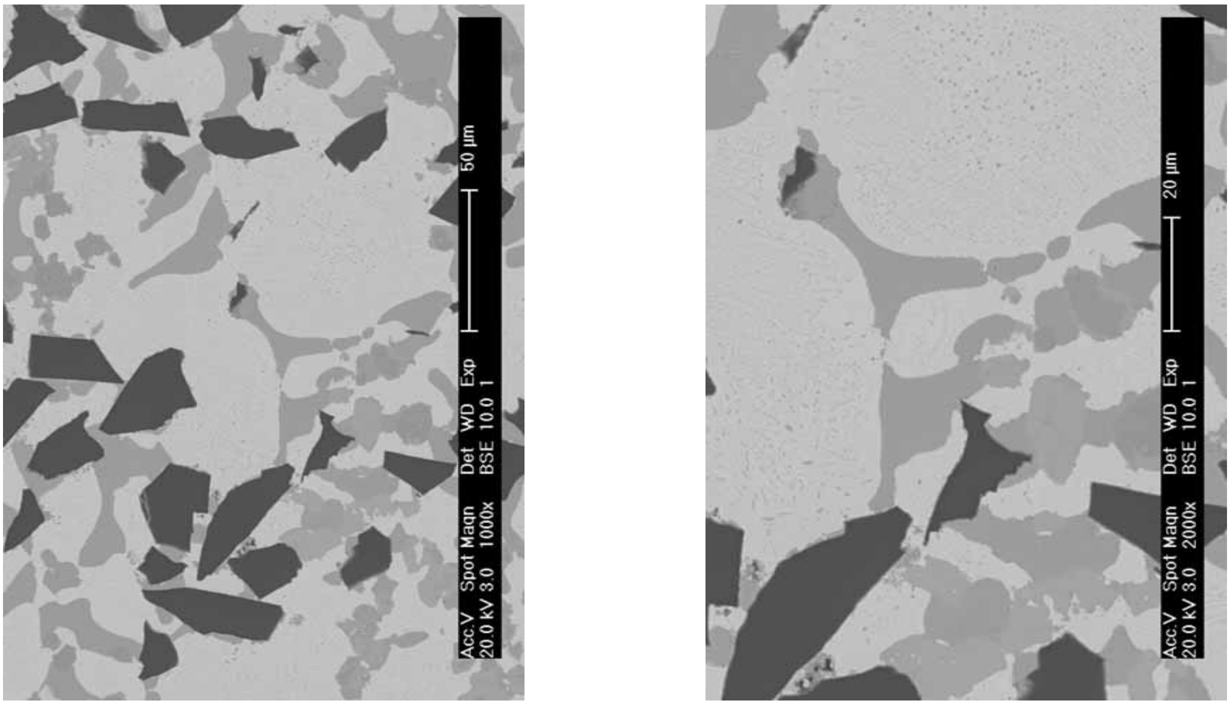

(c) SEM 1000x (d) SEM 2000x

Figure 4.10: Microstructure of Incusil™ABA®-18 vol.% SiC.

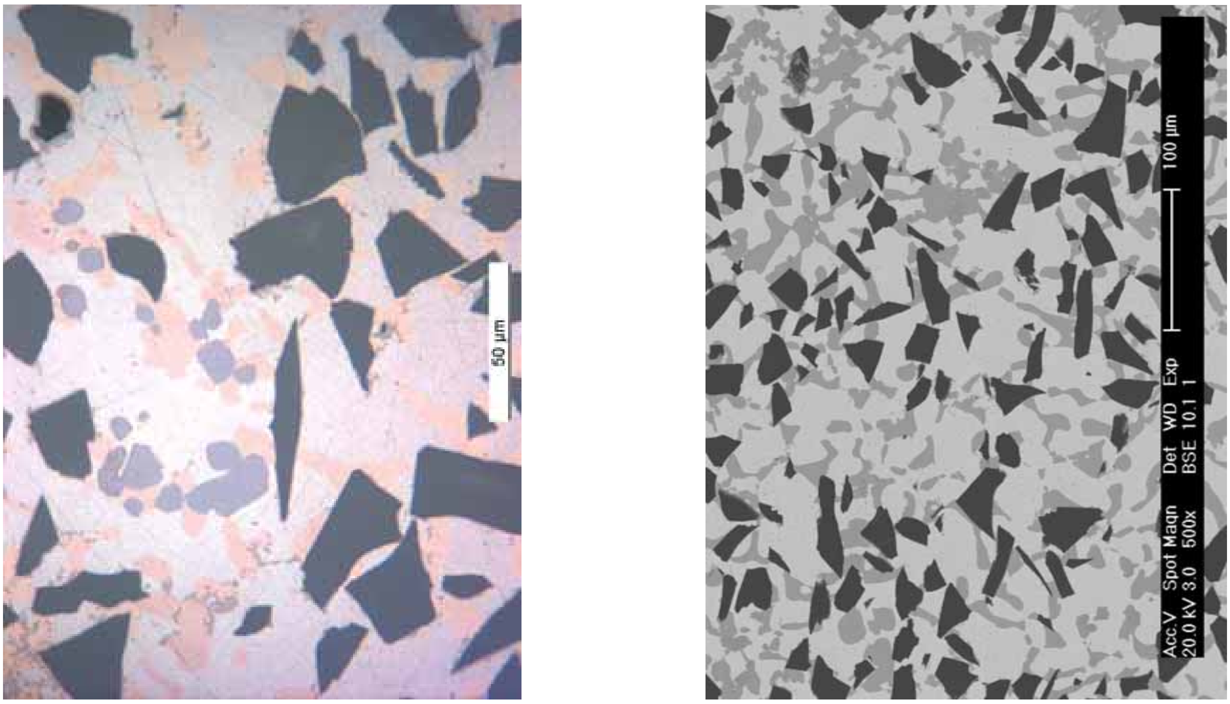

(a) Optical microscope

(b) SEM 500x

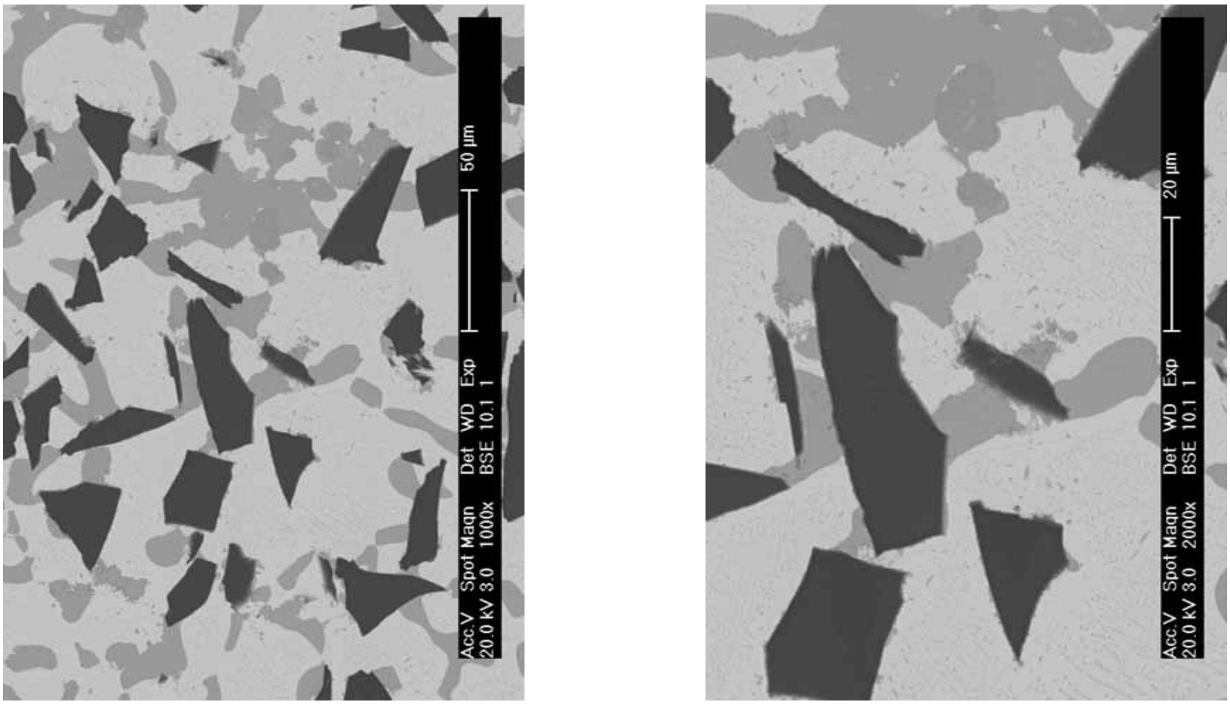

(c) SEM 1000x

(d) SEM 2000x

Figure 4.11: Microstructure of Incusil™ABA®-27 vol.% SiC.

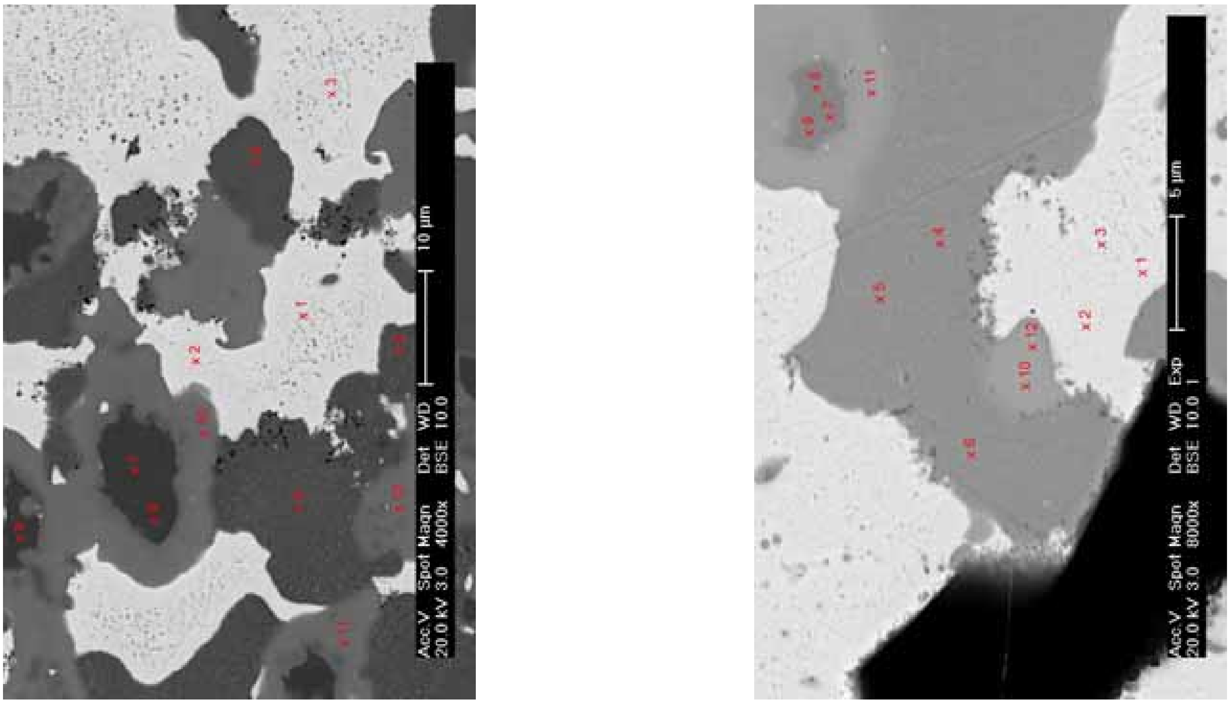

(a) Incusil™ABA®

(b) Incusil™ABA®-9 vol.% SiC

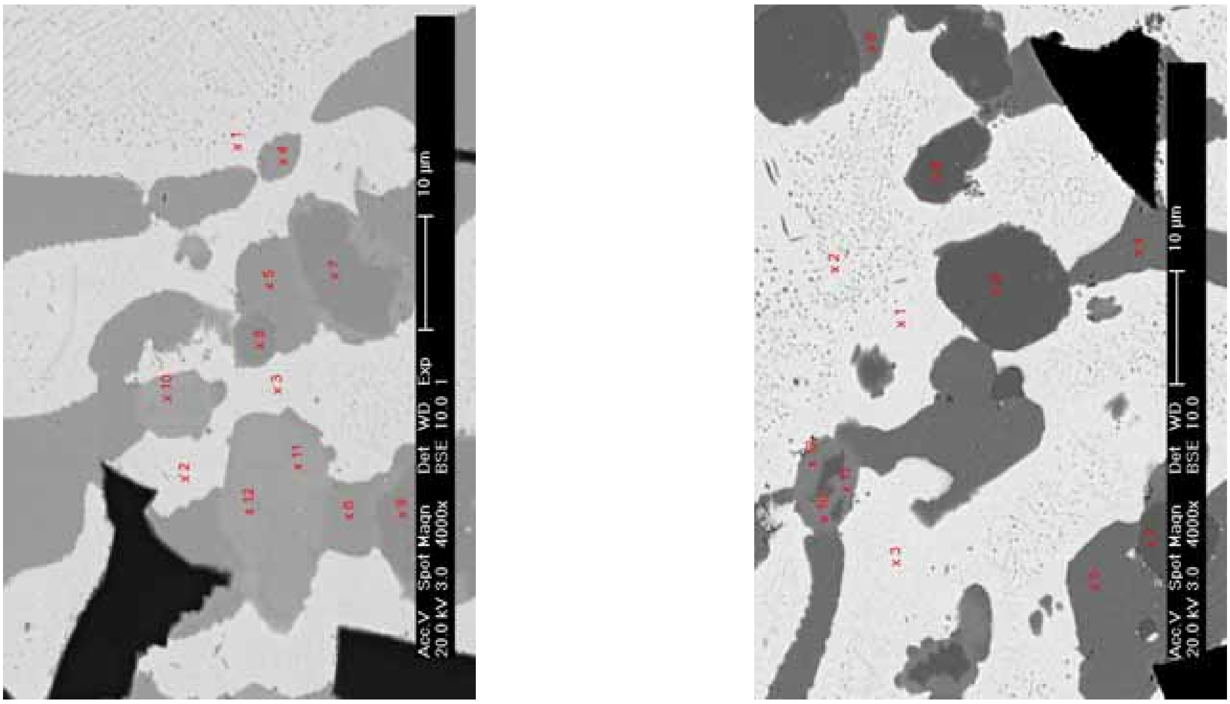

(c) Incusil™ABA®-18 vol.% SiC

(d) Incusil™ABA®-27 vol.% SiC

Figure 4.12: EDX measurement points for the four materials.

4.2.2 Stereological Analyses

Stereological analyses were carried out with the two main objectives of evaluating the actual amount of reinforcement in the composites and of quantifying the amount of the titanium containing phases in Incusil™ABA® and in the composite matrix materials. In this case optical microscopy was preferred to SEM because images need to be taken at a lower magnification to be quantitatively representative of the microstructure. Moreover, while BSE images are greyscale, in optical microscope images the phases have different colours (white, orange, dark grey and light grey for AgIn, Cu, Cu_4Ti and Cu_2InTi, respectively), which is a major advantage if image analysis has to be performed.

The detection and quantification of particles was carried out by means of the software library IMAQ Vision Builder. For each composition ten images were analysed. The measured reinforcement volume fractions are close to the expected values but in all the three composites they are slightly larger (of about 0.01); this may be due a difference between the assumed and the actual value of SiC density which had not been measured.

The automatic detection and quantification of titanium containing phases is more difficult than that of the particles since the difference in colour is less marked; thus phase identification was performed manually (Corel DRAW© software was used) and followed by the quantification by IMAQ Vision Builder. For each image the volume fraction of titanium containing phases was calculated with respect to the volume of matrix alloy which is the difference between the total volume and that of the particles, computed previously. The results are summarized in Figure 4.13: as observed in Section 4.2.1 the volume fraction of titanium containing phases decreases as the amount of reinforcement increases with an almost linear trend which is to be expected since titanium participates in the wetting reactions between the particles and Incusil™ABA®, and the surface to be wetted increases linearly with the reinforcement volume fraction.

4.3 Inverse Homogenization

The results of the metallographic analyses show that the matrix materials in the composite fillers exhibit microstructures and compositions which differ significantly from those of Incusil™ABA®; as a consequence, it would be senseless to assume that their mechanical behaviour is that obtained by tensile testing of pure Incusil™ABA®. This was confirmed by applying under this assumption the homogenization model presented in Chapter 3 to Incusil™ABA®-9 vol.% SiC (Figure 4.14): experimental and numerical results are in agreement in the first part of the curve while, as soon as the non linearity of the matrix behaviour becomes dominant, the stress-strain curve predicted by the model differs significantly from that obtained experimentally, which has a much lower hardening.

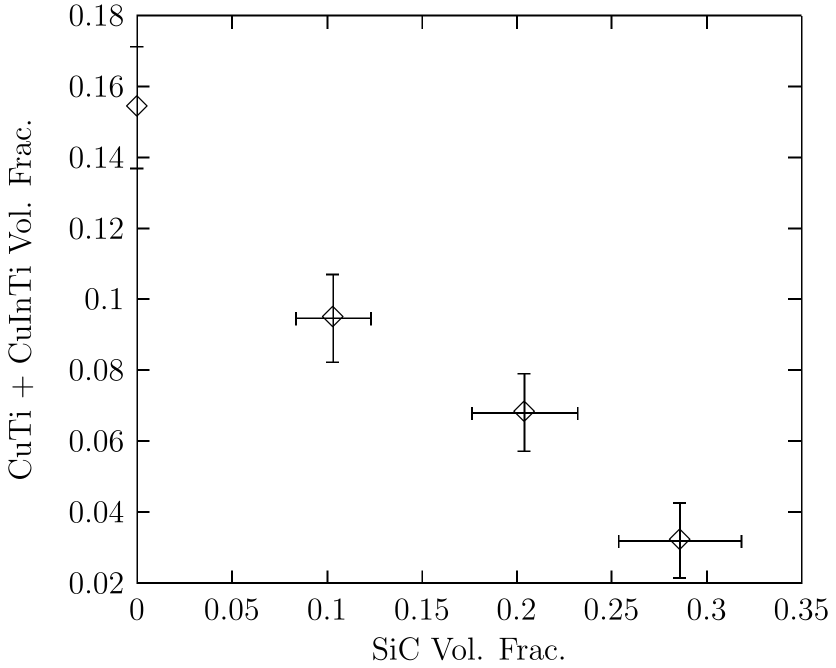

Figure 4.13: Evolution of the volume fraction of Titanium containing phases as a function of SiC volume fraction.

The challenge of assessing the mechanical properties of the matrix material in the composite can be tackled by means of an inverse homogenization approach. In straightforward homogenization problems, the properties of the constituents are given and the unknowns are the composite properties whereas in the case of inverse homogenization the properties of the composite are known while those of the constituents need to be determined. In order to achieve this goal the homogenization model was introduced into an identification loop in which it was combined with an optimization algorithm. The implementation of this identification procedure was based on the framework developed in previous optimization studies in the field of modal analysis carried out at LMAF [28].

4.3.1 Mixed Numerical-Experimental Identification

Chosen a fitting model $M(\boldsymbol{x}, u)$ (governed by a set $\boldsymbol{x}$ of n parameters), the goal of the identification procedure is to find the set of parameters $\tilde{\boldsymbol{x}}$ which gives the best approximation of the experimental results. Given the experimental data points $(u_1, y_1), \ldots, (u_m, y_m)$, for any choice of $\boldsymbol{x}$ it is possible to compute the residuals

$$f_i = y_i - M(\boldsymbol{x}, u_i) \tag{4.1}$$

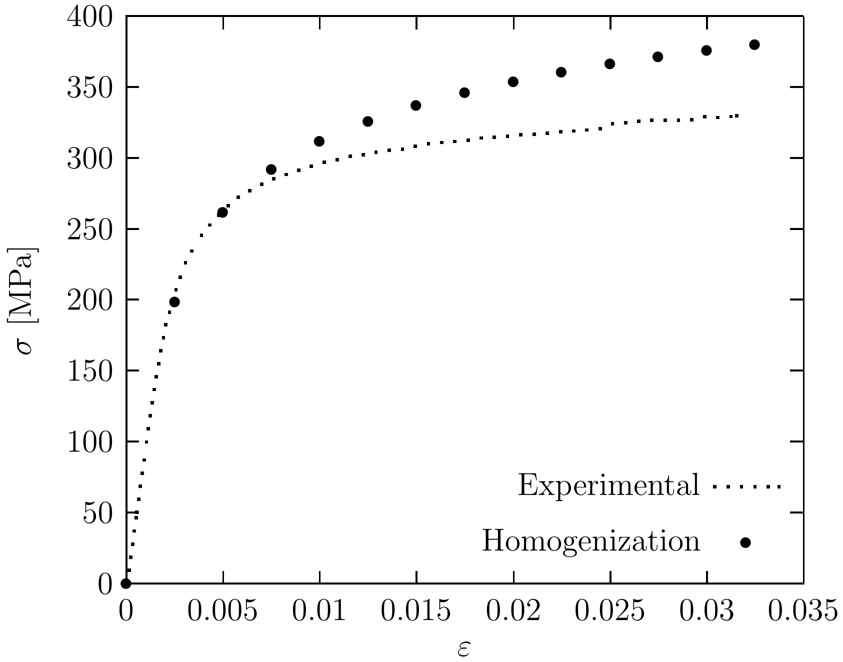

Figure 4.14: Comparison between experimental data and homogenization results for Incusil™ABA®-9 vol.% SiC.

For a least squares fit, the parameters are determined as the minimizer $\tilde{\boldsymbol{x}}$ of the sum of the square residuals

$$F(\boldsymbol{x}) = \frac{1}{2}\sum_{i=1}^{m}(f_i(\boldsymbol{x}))^2 = \frac{1}{2}\left\|\boldsymbol{f}(\boldsymbol{x})\right\|^2 = \frac{1}{2}\boldsymbol{f}(\boldsymbol{x})^T\boldsymbol{f}(\boldsymbol{x}) \tag{4.2}$$

Thus the identification problem becomes the problem of the minimization of the objective function F with respect to the unknown parameters $\boldsymbol{x}$.

The objective function is assumed to be smooth enough for the following Taylor expansion be valid

$$F(\boldsymbol{x}+\boldsymbol{h}) = F(\boldsymbol{x}) + \boldsymbol{h}^T\boldsymbol{F}'(\boldsymbol{x}) + \frac{1}{2}\boldsymbol{h}^T\boldsymbol{H}\boldsymbol{h} + O(\|\boldsymbol{h}\|^3) \tag{4.3}$$

where $\boldsymbol{F}'(\boldsymbol{x})$ is the gradient

$$\boldsymbol{F}'(\boldsymbol{x}) = \begin{pmatrix} \frac{\partial F}{\partial x_1}(\boldsymbol{x}) \\ \vdots \\ \frac{\partial F}{\partial x_n}(\boldsymbol{x}) \end{pmatrix} \tag{4.4}$$

and $\boldsymbol{H}$ is the Hessian matrix

$$\boldsymbol{H} = \boldsymbol{F}''(\boldsymbol{x}) = \left[\frac{\partial^2 F}{\partial x_i \partial x_j}(\boldsymbol{x})\right] \tag{4.5}$$

If $\tilde{\boldsymbol{x}}$ is a local minimizer it is a stationary point and the Hessian matrix is positive definite

$$\boldsymbol{F}'(\boldsymbol{x}) = 0 \tag{4.6}$$

$$\boldsymbol{h}^T \boldsymbol{H} \boldsymbol{h} > \delta \left\| \boldsymbol{h} \right\|^2 \tag{4.7}$$

where δ is some positive constant. From equations (4.6) and (4.7) it is evident that in order to find $\tilde{\boldsymbol{x}}$ it is necessary to calculate the derivatives of F. Provided that $\boldsymbol{f}$ has continuous second partial derivatives, it is possible to write its Taylor series

$$\boldsymbol{f}(\boldsymbol{x}+\boldsymbol{h}) = \boldsymbol{f}(\boldsymbol{x}) + \boldsymbol{J}_f(\boldsymbol{x})\boldsymbol{h} + O(\left\|\boldsymbol{h}\right\|^2) \tag{4.8}$$

where $\boldsymbol{J}$ is the Jacobian matrix containing the first partial derivatives of the function components

$$(\boldsymbol{J}_f(\boldsymbol{x}))_{ij} = \frac{\partial f_i}{\partial x_j}(\boldsymbol{x}) \tag{4.9}$$

From (4.2) it follows that

$$\frac{\partial F}{\partial x_j} = \sum_{i=1}^{m} f_i(\boldsymbol{x}) \frac{\partial f_i}{\partial x_j}(\boldsymbol{x}) \tag{4.10}$$

thus the gradient (4.6) of F is

$$\boldsymbol{F}'(\boldsymbol{x}) = \boldsymbol{J}_f(\boldsymbol{x})^T \boldsymbol{f}(\boldsymbol{x}) \tag{4.11}$$

From (4.10) it can be seen that the (j,k) element of the Hessian matrix is

$$\frac{\partial^2 F}{\partial x_j \partial x_k} = \sum_{i=1}^{m} \left(\frac{\partial f_i}{\partial x_j}(\boldsymbol{x}) \frac{\partial f_i}{\partial x_k}(\boldsymbol{x}) + f_i(\boldsymbol{x}) \frac{\partial^2 f_i}{\partial x_j \partial x_k}(\boldsymbol{x}) \right) \tag{4.12}$$

showing that

$$\boldsymbol{F}''(\boldsymbol{x}) = \boldsymbol{J}_f(\boldsymbol{x})^T \boldsymbol{J}_f(\boldsymbol{x}) + \sum_{i=1}^{m} f_i(\boldsymbol{x}) f_i''(\boldsymbol{x}) \tag{4.13}$$

In identification approaches, the optimization algorithm plays an essential role since the convergence rate of the identification process and the resulting residual errors depend directly on the effectiveness of the optimization step. In order to ensure the reliability of the identification method, the developments have been based on the well known MATLAB® optimization toolbox. There are several algorithms for solving non-linear least squares problems [79], each of them having of course specific advantages and limits. The present identification problem required robustness, accuracy and fast convergence. Thus the Levenberg-Marquardt algorithm [79, 81] was chosen.

If (4.6) is imposed for the linear approximation (4.8) of the components of $\boldsymbol{f}$, the following equation for determining the step in the descent direction $\boldsymbol{h}$ is obtained:

$$\boldsymbol{J}_f(\boldsymbol{x})^T \boldsymbol{J}_f(\boldsymbol{x}) \boldsymbol{h} = -\boldsymbol{J}_f(\boldsymbol{x})^T \boldsymbol{f}(\boldsymbol{x}) \tag{4.14}$$

This way of calculating the descent direction is that of Gauss-Newton method. This approach has very good performance if $\boldsymbol{x}$ is near the local minimizer but far from it the Hessian matrix $\boldsymbol{J}(\boldsymbol{x})^T\boldsymbol{J}(\boldsymbol{x})$ may not be positive definite thus the calculated direction might even be not descent (for further details refer to [79]). To overcome this problem, in Levenberg-Marqardt algorithm a damping parameter $\mu > 0$ is introduced into the stationarity condition (4.14) which becomes

$$(\boldsymbol{J}_f(\boldsymbol{x})^T\boldsymbol{J}_f(\boldsymbol{x}) + \mu\boldsymbol{I})\boldsymbol{h} = -\boldsymbol{J}_f(\boldsymbol{x})^T\boldsymbol{f}(\boldsymbol{x}) \tag{4.15}$$

The damping parameter has three main effects:

1. it ensures that $\boldsymbol{h}$ is a descent direction;
2. for large values of μ a short step in the steepest descent direction is obtained $\boldsymbol{h} = -\boldsymbol{F}'/\mu$
3. small values of μ lead to almost a Gauss-Newton step, which has good performance in the final stages of the identification when $\boldsymbol{x}$ is close to $\tilde{\boldsymbol{x}}$

The performance of the algorithm depends then on the way μ evolves during the iterations. In the MATLAB® optimization toolbox, μ is a function of a variable α, which is a metric of the non-linearity of $F(\boldsymbol{x})$ and is estimated by searching for a minimum $\boldsymbol{x}^\alpha$ of a cubic interpolation $F_C(\boldsymbol{x})$ of the error function (based on the values obtained in the current iteration $F(\boldsymbol{x}^i)$ and in the previous one $F(\boldsymbol{x}^{i-1})$). The effectiveness of the linear interpolation compared to the cubic one tells then whether μ has to be increased or not (the implemented identification algorithm is reported in Table 4.2).

At the end of the process it is possible to have an a posteriori estimate of how the incertitude of the experimental results affects that of the identified parameters $\boldsymbol{x}^{id}$ by including the experimental scatter Δy_i in (4.1):

$$f_i + \Delta f_i = y_i + \Delta y_i - M(\boldsymbol{x}, u_i) \tag{4.16}$$

at the end of the identification process the residuals are negligible and (4.16) becomes

$$\Delta\boldsymbol{f} \approx \Delta\boldsymbol{y} \tag{4.17}$$

by introducing (4.16) into (4.8) the overdetermined system of equations

$$\Delta\boldsymbol{f} = \boldsymbol{J}_f(\boldsymbol{x}^{id})\Delta\boldsymbol{x}^{id} \tag{4.18}$$

is obtained, where $\Delta\boldsymbol{x}^{id}$ is the variation of the constitutive parameters and can be computed by solving (4.18) in the sense of least squares.

Definition of an initial parameter vector $\boldsymbol{x}^0$.
Iterative procedure repeated for a maximum number of iterations if the required convergence is not achieved:

1. calculation of the error vector $\boldsymbol{f}(\boldsymbol{x}^i)$ and of its derivatives $\boldsymbol{J}_f(\boldsymbol{x}^i)$
2. evaluation of the damping parameter μ for the current iteration:
    (a) linear extrapolation of the error function $F_L(\boldsymbol{x}^i + \boldsymbol{h}^i)$
    (b) cubic interpolation of the error function $F_C(\boldsymbol{x})$ from the values of $F(\boldsymbol{x}^{i-1})$ and $F(\boldsymbol{x}^i)$ and search for the minimum $\boldsymbol{x}^\alpha$ leading to $F_C(\boldsymbol{x}^\alpha)$ and to α
    (c) calculation of μ_i:
        i. if $F_L(\boldsymbol{x}^i + \boldsymbol{h}^i) < F_C(\boldsymbol{x}^\alpha)$ then $\mu_i = \frac{\mu_{i-1}}{1+\alpha}$
        ii. if $F_L(\boldsymbol{x}^i + \boldsymbol{h}^i) > F_C(\boldsymbol{x}^\alpha)$ then $\mu_i = \mu_{i-1} + \frac{\boldsymbol{f}_C(\boldsymbol{x}^\alpha) - \boldsymbol{f}(\boldsymbol{x}^i + \boldsymbol{h}^i)}{\alpha}$
3. evaluation of the descent direction $\boldsymbol{h}^i$ by solving $(\boldsymbol{J}_f(\boldsymbol{x}^i)^T \boldsymbol{J}_f(\boldsymbol{x}^i) + \mu^i \boldsymbol{I})\boldsymbol{h}^i = -\boldsymbol{J}_f(\boldsymbol{x}^i)^T \boldsymbol{F}(\boldsymbol{x}^i)$
4. assessment along the descent direction $\boldsymbol{h}^i$ of β which minimizes $\boldsymbol{f}(\boldsymbol{x}^i + \beta \boldsymbol{h}^i)$ by means of a line search procedure
5. update of the vector parameter $\boldsymbol{x}^{i+1} = \boldsymbol{x}^i + \beta \boldsymbol{h}^i$

Table 4.2: The implemented identification algorithm.

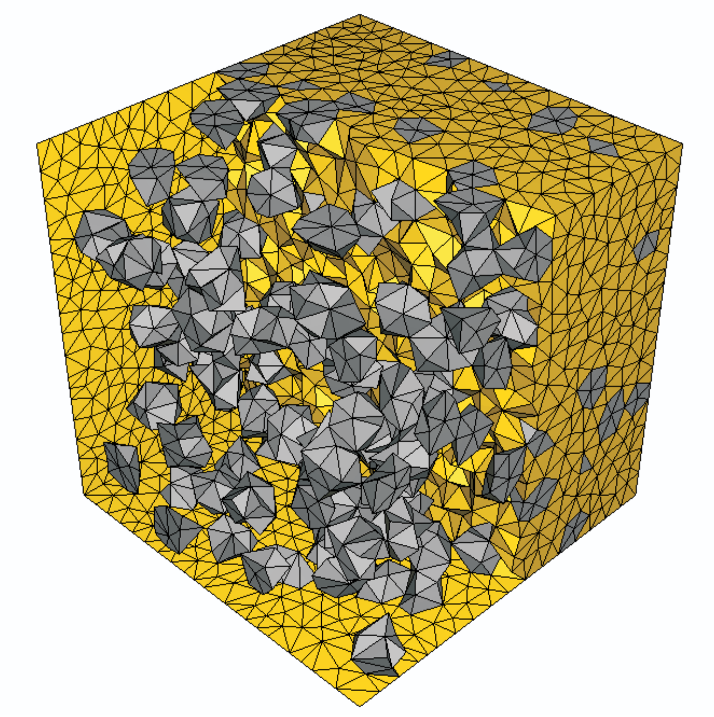

Figure 4.15: Model for the inverse homogenization of Incusil™ABA®-9 vol.% SiC.

4.3.2 Application to the Composite Filler

The homogenization model presented in Chapter 3 was combined with the previously described identification procedure and applied to assess the uniaxial tensile stress-strain curve of the matrix metal in the composite filler.

Since the maximum measured strain was about 0.03 (for the composite with 9 vol.% SiC) unit cells with size $\xi \approx 11$ (3.8) were chosen. Note that this choice for the value of ξ is conservative: as shown in Chapter 3 such a value corresponds to the estimated RVE size, for a maximum applied strain of 0.03, of a composite with similar mechanical properties of the constituents but 25 vol.% of reinforcement.

The homogenization models consisted of unit cells with an edge length of 400 µm, containing 126, 254 and 381 particles, respectively. The particle average volume was $4.49 \cdot 10^5$ µm^3 with $3.3 \cdot 10^4$ µm^3 standard deviation, corresponding to an average equivalent diameter of 44 ± 1 µm (which is the characteristic particle size of the mesh 325 SiC actually used). The models for the three compositions are reported in Figures 4.15, 4.16 and 4.17. The particles were assigned a linear elastic behaviour, with a Young's modulus of 415 GPa and a Poisson's ratio of 0.16 [82], while the matrix was assumed to be elastoplastic and to

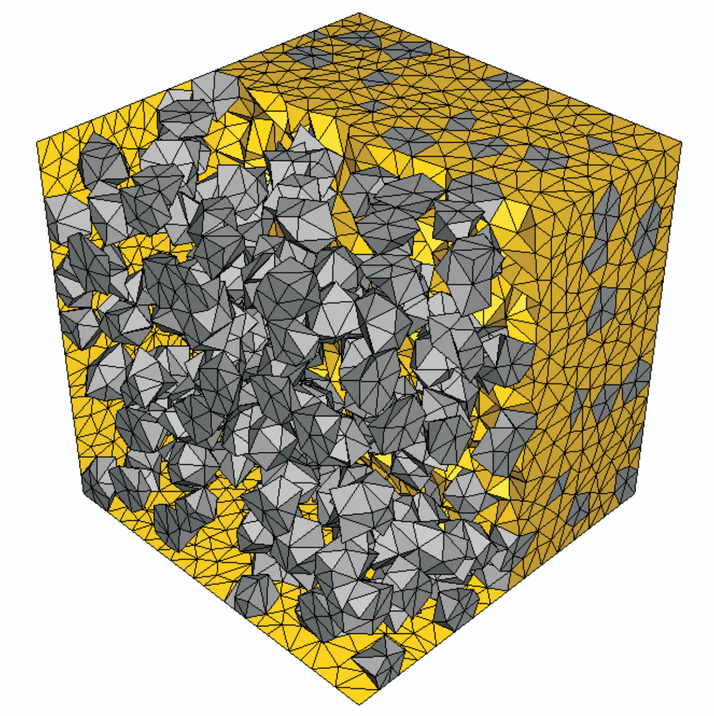

Figure 4.16: Model for the inverse homogenization of Incusil™ABA®-18 vol.% SiC.

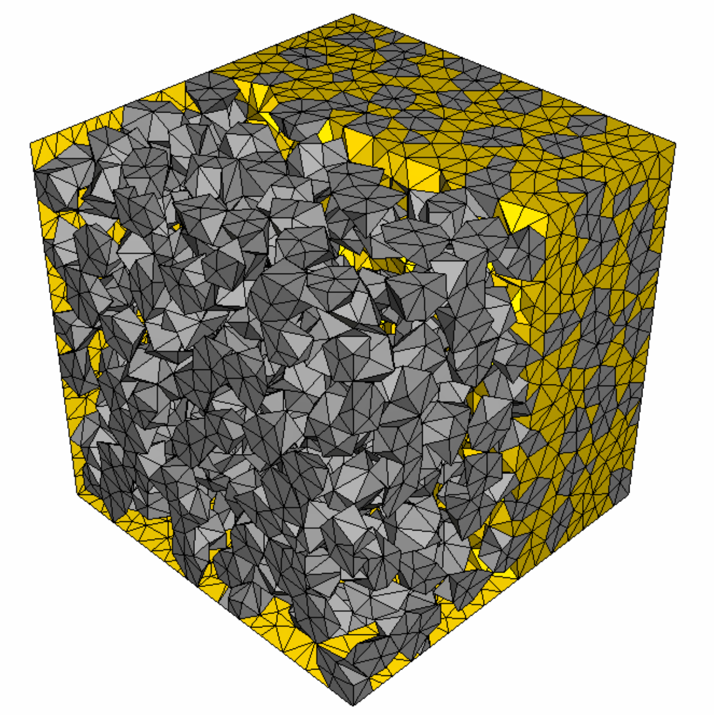

Figure 4.17: Model for the inverse homogenization of Incusil™ABA®-27 vol.% SiC.

E^0 [MPa]	σ_y^0 [MPa]	σ_∞^0 [MPa]	B^0	K^0 [MPa]
88832	120	150	500	900

Table 4.3: Initial values for the constitutive parameters of the matrix alloy.

follow the von Mises yield criterion (3.13) with Voce's [114] isotropic hardening law

$$\sigma = \sigma_y + \sigma_\infty(1 - e^{-B\varepsilon^p}) + K\varepsilon^p \tag{4.19}$$

where ε^p is the equivalent plastic strain and σ_y the yield stress, while σ_∞, B and K are the parameters which govern the exponential and the linear part of the strain hardening. The four constants in (4.19) and Young's modulus are the unknowns of the identification procedure (for Poisson's ratio the value 0.3 was assumed) and govern the response of the homogenization model which is actually the fitting model. To avoid conditioning problems, the values of the parameters in the vector $\boldsymbol{x}$ were normalized by their initial values:

$$\boldsymbol{x} = \begin{pmatrix} \frac{E}{E^0} \\ \frac{\sigma_y}{\sigma_y^0} \\ \frac{\sigma_\infty}{\sigma_\infty^0} \\ \log_{B^0} B \\ \frac{K}{K^0} \end{pmatrix} \tag{4.20}$$

The initial values of the parameters are summarized in Table 4.3 (E^0 was determined as the ratio $\bar{\sigma}/\varepsilon$ for $\varepsilon = 0.001$ obtained from the tensile test of Incusil™ABA®, Figure 4.3). Simulations were carried out under mixed static-kinematic boundary conditions (3.25). In this case displacements were not directly imposed at the nodes on the tensile faces but rather at virtual nodes rigidly linked to these faces by means of kinematic couplings [1]. Thus, to have the homogenized mechanical behaviour, it was not necessary to compute the average stress over the RVE but only the reactions at the virtual nodes, that being a major advantage in terms of computing time and implementation complexity. The residuals (4.1) were computed as the difference between the model response in terms of displacement and reaction in the tensile direction at one of the virtual nodes and the average experimental data. Each algorithm iteration i consisted of eight to ten finite element simulations: one to evaluate $F(\boldsymbol{x}^i)$, five for $\boldsymbol{J}_f(\boldsymbol{x}^i)$, two to four to find a suitable value of β. The algorithm was allowed to perform five iterations for each of the three composites. In the case of Incusil™ABA®-9 vol.% SiC four instead of five parameters were identified as Incusil™ABA®-9 vol.% SiC Young's Modulus was imposed to be constant since during a first identification attempt it was found out that the algorithm tended to identify an unrealistically high value (around 200 GPa). The evolutions of the identified parameters (this time normalized by the final value) and of the error are reported in Figures 4.18 to

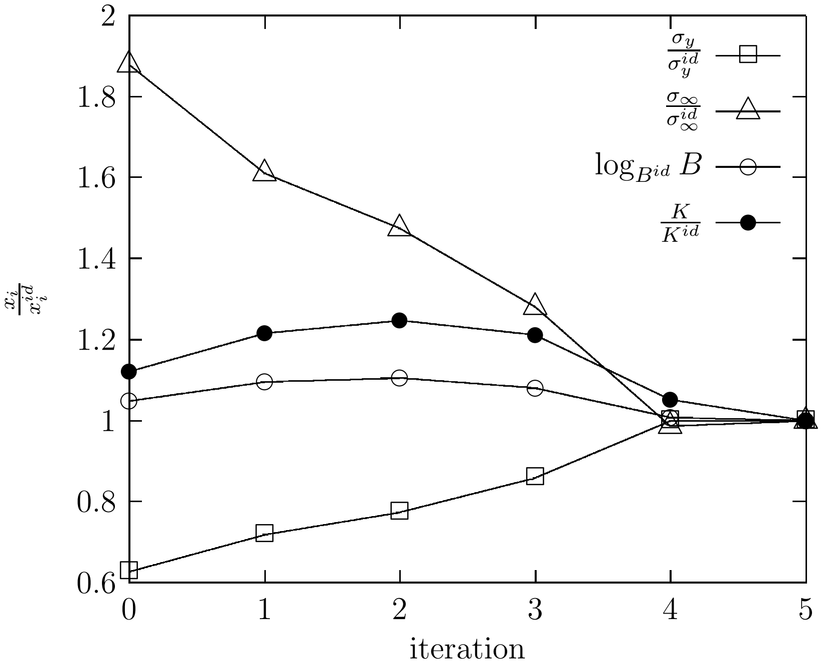

Figure 4.18: Evolution of the values of the constitutive parameters of Incusil™ABA®-9 vol.% SiC during the identification procedure.

4.21. By comparing the convergence of the different parameters in the three models it can be observed that imposing a constant Young's modulus (as in the case of Incusil™ABA®-9 vol.% SiC) has a detrimental effect on the convergence rate of the other constitutive parameters especially the yield stress; this is due to the fact that the yield stress remains the only free parameter which controls the onset of plasticity. Nevertheless the results of identification are satisfactory. The diagram of the evolution of the error function during the identification process confirms that the chosen algorithm is robust: even when the initial value of the error function is large (as it is for both Incusil™ABA®-18 vol.% SiC and Incusil™ABA®-27 vol.% SiC) the algorithm converges. In all the three identifications the final value of the error function is below 0.01: 0.007, 0.002 and 0.003 for the composites with with 9, 18, 27 vol.% SiC, respectively. The worse performance of the algorithm in the case of Incusil™ABA®-9 vol.% SiC can be explained by the fact that the algorithm was not allowed to identify the linear behaviour of the matrix material since Young's modulus had been assigned a constant value.

The identified uniaxial stress-strain curves of the matrix materials in the composites (figure 4.22) are significantly different from that of Incusil™ABA®: as expected their behaviour becomes non linear at lower stress levels; moreover they present a lower hardening, which decreases as the SiC content in the composite increases. This trend suggests that the "consumption" of titanium leads to softer alloys. However, a deep understanding of

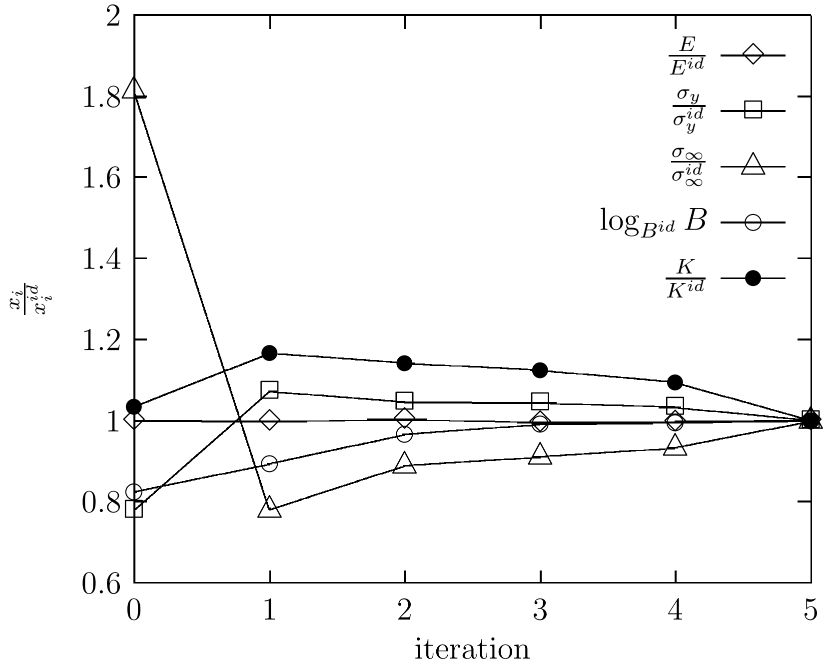

Figure 4.19: Evolution of the values of the constitutive parameters of Incusil™ABA®-18 vol.% SiC during the identification procedure.

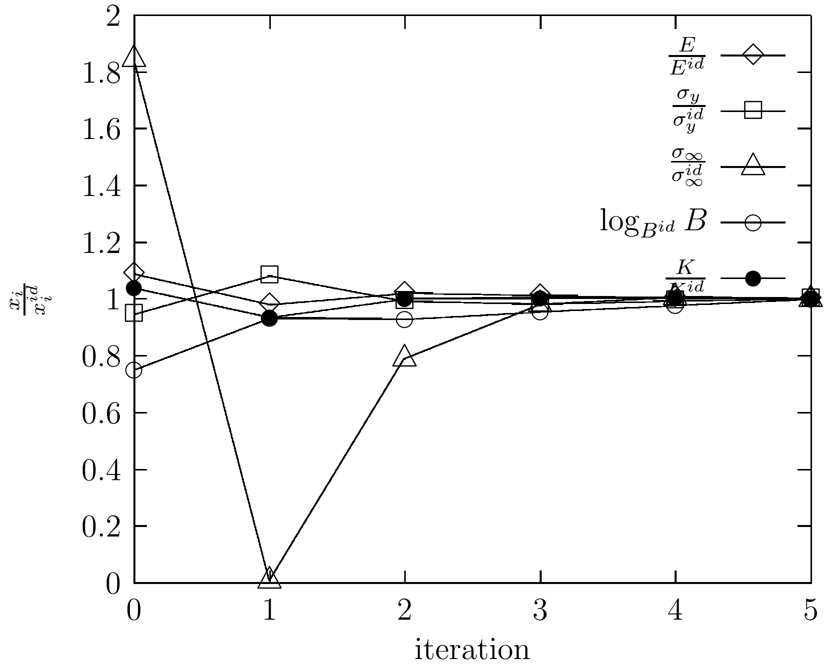

Figure 4.20: Evolution of the values of the constitutive parameters of Incusil™ABA®-27 vol.% SiC during the identification procedure.

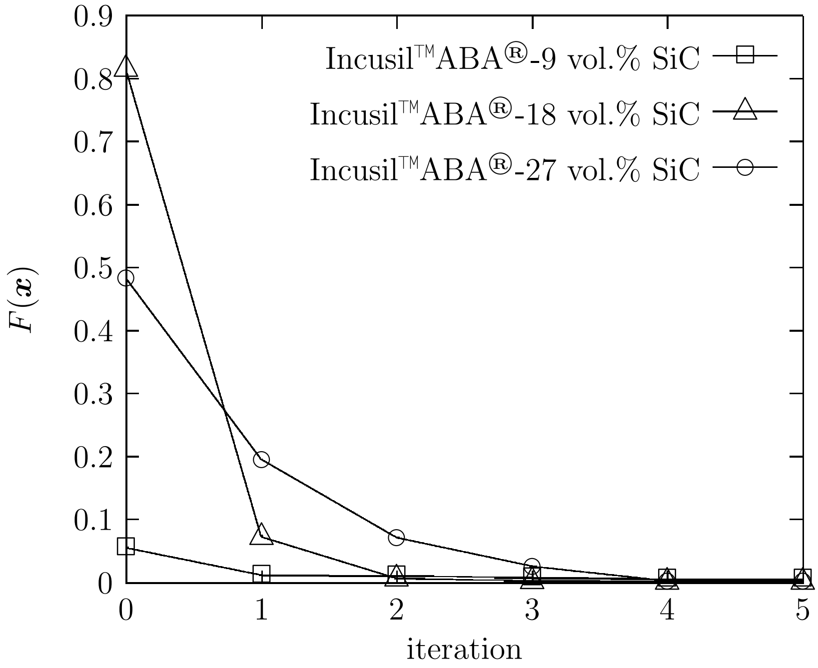

Figure 4.21: Evolution of the objective function during the identification procedure.

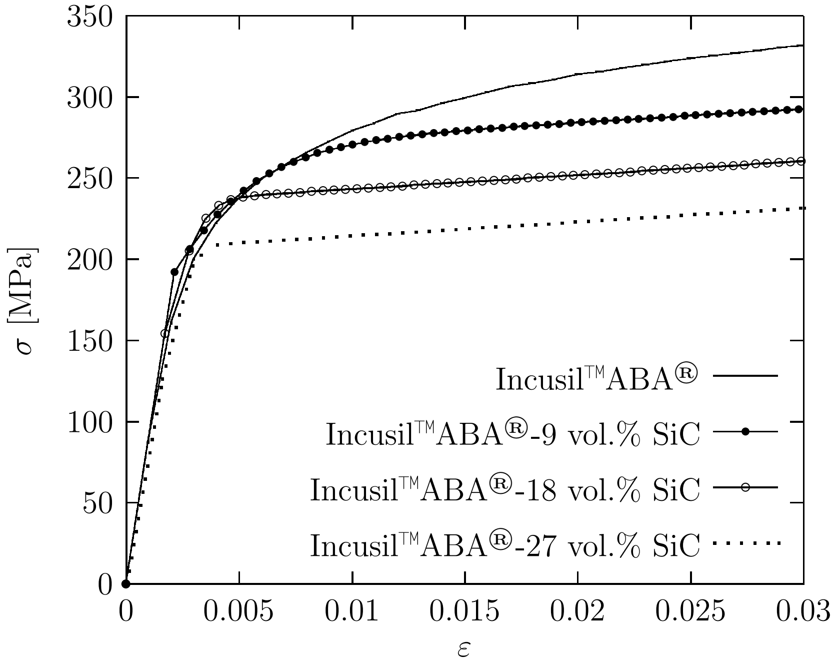

Figure 4.22: Comparison between the stress-strain curve of Incusil™ABA®and those of the matrix alloys in the composites.

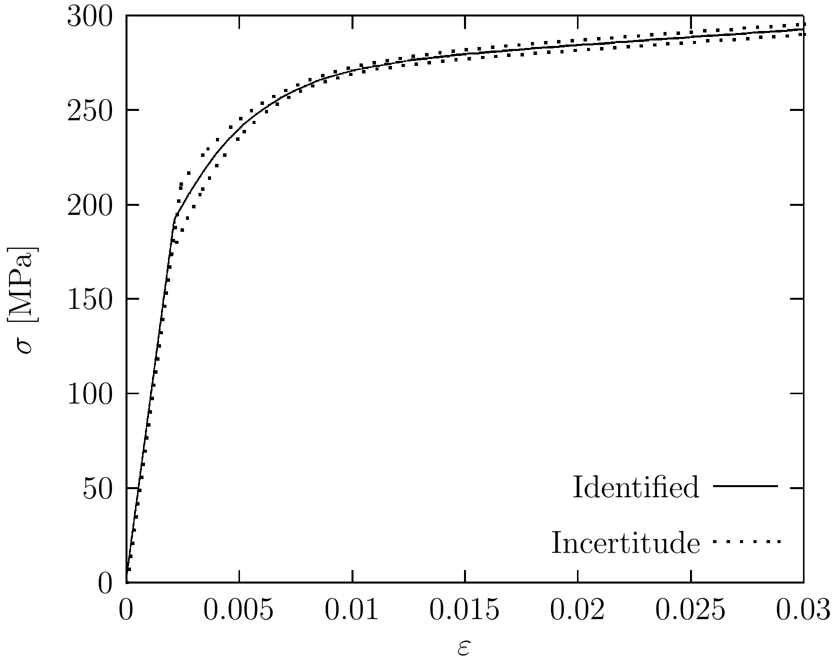

Figure 4.23: Identified stress-strain curve of the matrix alloy of Incusil™ABA®-9 vol.% SiC.

this effect (e.g. whether it is due to the presence of the Cu_4Ti and Cu_2InTi phases or to the small amount of titanium dissolved in the other phases or to other mechanisms) exceeds the purposes of this work. The present findings suggest that there be room for optimization of the titanium content of Incusil™ABA® not only with respect to the wetting behaviour but also to the mechanical properties which eventually do influence the residual stresses in brazed joints.

The results of the a posteriori evaluation of the uncertainty of the identified mechanical behaviours are reported in Figures 4.23, 4.24 and 4.25. The standard deviation $\hat{\sigma}(\varepsilon)$ of the stress-strain curves was introduced in (4.16) as Δy_i , the experimental scatter, and the variations of the identified constitutive parameters were calculated by means of (4.18).

The experimental scatter has almost no influence on the identified stress-strain curve for Incusil™ABA®-9 vol.% SiC, which proves the robustness of the adopted approach. In the case of the other two composites, Incusil™ABA®-18 vol.% SiC and Incusil™ABA®-27 vol.% SiC, the uncertainty increases in the linear part of the hardening (especially for Incusil™ABA®-27 vol.% SiC). This is due to the fact that the measured ultimate strain (about 0.0045 for Incusil™ABA®-27 vol.% SiC) was sufficiently large to have a reliable identification of the first part of the plastic region of the curve, thus of four parameters out of five (E, σ_y, σ_∞ and B), but not of the slope K of the linear contribution to the hardening.

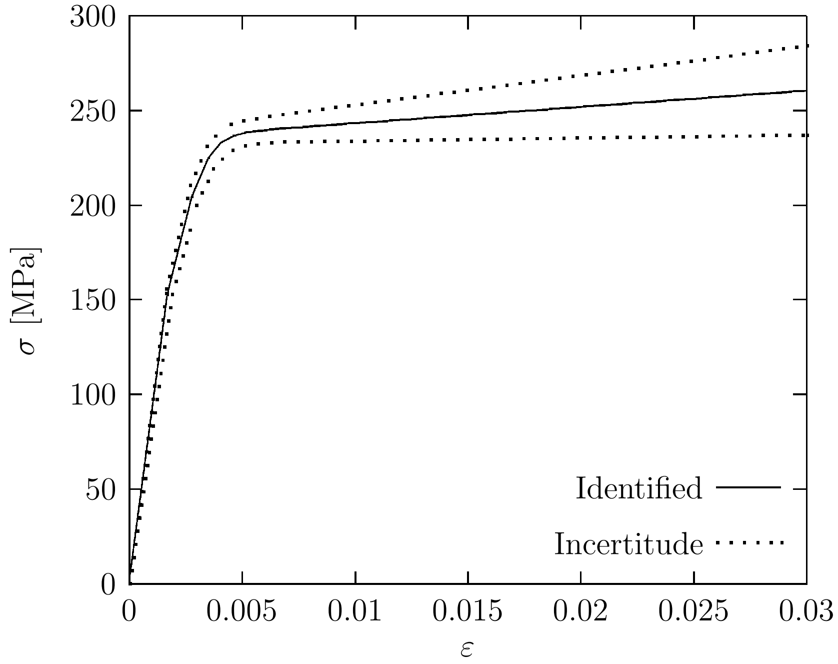

Figure 4.24: Identified stress-strain curve of the matrix alloy of Incusil™ABA®-18 vol.% SiC.

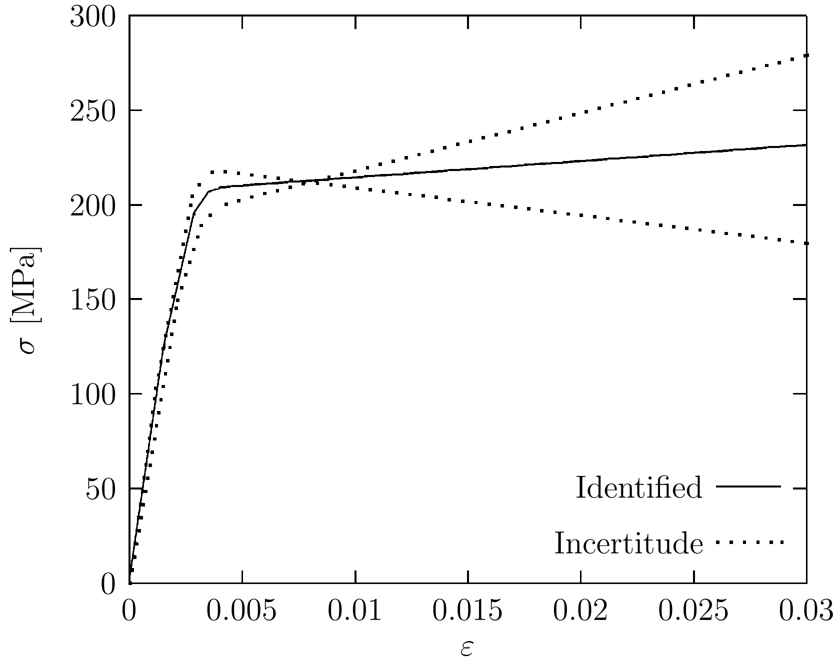

Figure 4.25: Identified stress-strain curve of the matrix alloy of Incusil™ABA®-27 vol.% SiC.

4.4 Temperature Dependent Mechanical Properties of the Composite Filler

The brazing process takes place at about 750 ℃ (section 2.4). Therefore to simulate the cooling of the joints it is necessary to evaluate how the mechanical properties of the brazing fillers vary in this temperature range. While the properties of SiC are almost constant [82] those of Incusil™ABA® and of the alloys in the composite drastically change with temperature. In particular a large decrease in the yield stress and in the ultimate stress is expected between 300 ℃ and 400 ℃ [70, 71]. During the present project the experimental work was limited to room temperature because extending the experimental characterization of the materials to a wider range of temperatures would have been too demanding both in terms of time and of production costs since a large amount of specimens should be produced. Thus an alternative approach for the assessment of temperature dependent properties is proposed. Since no temperature dependent data are reported in the literature for Incusil™ABA®, its uniaxial behaviour and those in the composite were assumed to have an analogous dependence on temperature to that of CusilABA® ($Cu_{63}Ag_{35.25}Ti_{1.75}$), an active brazing alloy whose mechanical behaviour has been the subject of thorough studies at Sandia National Laboratories in recent years [83, 84]. The obtained temperature dependent mechanical properties of the alloys and those of SiC were introduced into the homogenization model to eventually obtain the temperature dependent elastic and plastic properties of the composite fillers.

4.4.1 Temperature Dependent Mechanical Properties of the Filler Alloys

In the cited works the mechanical behaviour of CusilABA® has been experimentally assessed in a wide range of temperatures, from room temperature up to 748 ℃ (the results are summarized in Table 4.4). Since the two alloys have different solidus temperatures $\mathrm{T}_{\mathrm{S}}^{\mathrm{C}}$ and $\mathrm{T}_{\mathrm{S}}^{\mathrm{I}}$ (815 ℃ and 605 ℃ for CusilABA® and Incusil™ABA®, respectively), in order to assign to the Young's modulus and the yield stress of Incusil™ABA® and of the matrix alloys in the composites the same evolution of those of CusilABA®, the temperature range of interest was normalised by the solidus temperatures $\mathrm{T}_{\mathrm{S}}^{\mathrm{C}}$ and the two properties by their values at room temperature $\mathrm{T}_{\mathrm{RT}}^{\mathrm{C}}$ (the diagrams of $\frac{\mathrm{E}^{\mathrm{C}}}{\mathrm{E}_{\mathrm{RT}}^{\mathrm{C}}}\left(\frac{\mathrm{T}^{\mathrm{C}}}{\mathrm{T}_{\mathrm{RT}}^{\mathrm{C}}}\right)$ and $\frac{\sigma_y^{\mathrm{C}}}{\sigma_{y\mathrm{RT}}^{\mathrm{C}}}\left(\frac{\mathrm{T}^{\mathrm{C}}}{\mathrm{T}_{\mathrm{RT}}^{\mathrm{C}}}\right)$ are reported in Figure 4.26). This way it was possible to compute for each CusilABA® data point $(\mathrm{E}_i^{\mathrm{C}}, \mathrm{T}_i^{\mathrm{C}})$ or $(\sigma_{yi}^{\mathrm{C}}, \mathrm{T}_i^{\mathrm{C}})$ the corresponding Incusil™ABA® (or matrix alloy) data point

T[°C]	E[MPa]	σ_y[MPa]
20	93600	330
250	83900	290
350	81000	250
450	77800	200
550	73500	75
650	67400	22.8
748	59100	10

Table 4.4: Temperature dependent mechanical properties of CusilABA®.

T[°C]	E[MPa]	ν	CTE[°C^{-1}]
16	88832	0.3	$1.82 \cdot 10^{-5}$
194	79626		
271	76874		
349	73837		
427	69756		
504	63967		
580	56089		

Table 4.5: Temperature dependent mechanical properties of Incusil™ABA®.

$(\mathrm{E}_i^{\mathrm{I}}, \mathrm{T}_i^{\mathrm{I}})$ or $(\sigma_{yi}^{\mathrm{I}}, \mathrm{T}_i^{\mathrm{I}})$ by means of the following

$$\mathrm{T}^{\mathrm{I}} = \mathrm{T}^{\mathrm{C}} \frac{\mathrm{T}_{\mathrm{S}}^{\mathrm{I}}}{\mathrm{T}_{\mathrm{S}}^{\mathrm{C}}} \tag{4.21}$$

$$\mathrm{E}^{\mathrm{I}}(\mathrm{T}^{\mathrm{I}}) = \mathrm{E}^{\mathrm{I}}(\mathrm{T}_{\mathrm{RT}}^{\mathrm{I}}) \frac{\mathrm{E}^{\mathrm{C}}(\mathrm{T}^{\mathrm{C}})}{\mathrm{E}^{\mathrm{C}}(\mathrm{T}_{\mathrm{RT}}^{\mathrm{C}})} \tag{4.22}$$

$$\sigma_y^{\mathrm{I}}(\mathrm{T}^{\mathrm{I}}) = \sigma_y^{\mathrm{I}}(\mathrm{T}_{\mathrm{RT}}^{\mathrm{I}}) \frac{\sigma_y^{\mathrm{C}}(\mathrm{T}^{\mathrm{C}})}{\sigma_y^{\mathrm{C}}(\mathrm{T}_{\mathrm{RT}}^{\mathrm{C}})} \tag{4.23}$$

The results obtained for the Young's moduli and for the yield stresses of the three matrix alloys are summarized in Table 4.6. To obtain the full stress-strain curves, equation (4.23) was applied to the whole plastic region (the results are reported in Figures 4.27 to 4.30). As expected there is a big drop in the material flow stress between 300 °C and 400 °C and at temperatures above 580 °C the material ultimate strengths are less than 10 MPa.

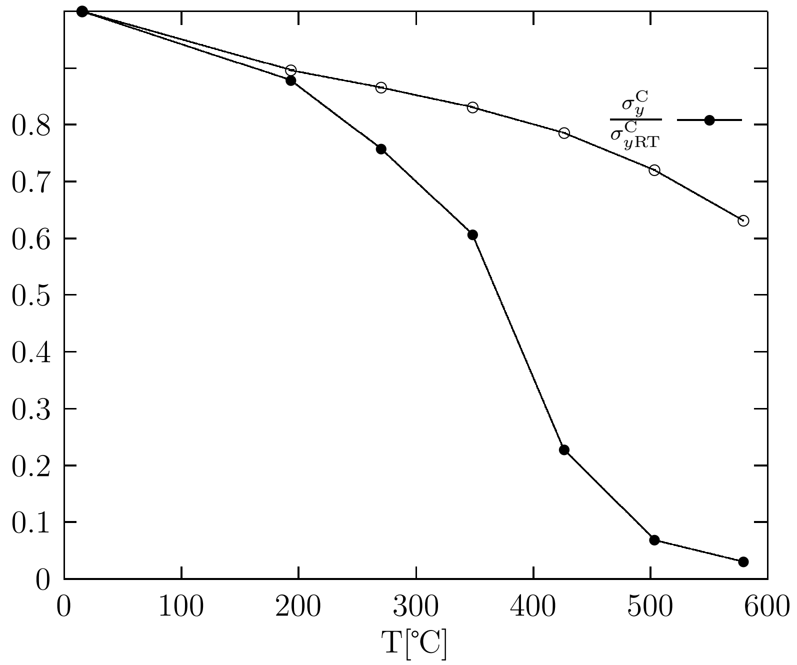

Figure 4.26: Evolution of Young's modulus and of the yield stress as a function of temperature.

	Incusil™ABA® 9 vol.% SiC matrix alloy		Incusil™ABA® 18 vol.% SiC matrix alloy		Incusil™ABA® 27 vol.% SiC matrix alloy	
T [°C]	E[MPa]	σ_y[MPa]	E[MPa]	σ_y[MPa]	E[MPa]	σ_y[MPa]
16	88832	192	88947	154	81539	126
194	79626	169	79729	136	73089	111
271	76874	145	76973	117	70563	96
349	73837	116	73932	93	67775	77
427	69756	44	69846	35	64029	29
504	63967	13	64049	11	58715	9
580	56089	6	56162	5	51484	4

Table 4.6: Temperature dependent mechanical properties of the matrix alloys in the composite fillers.

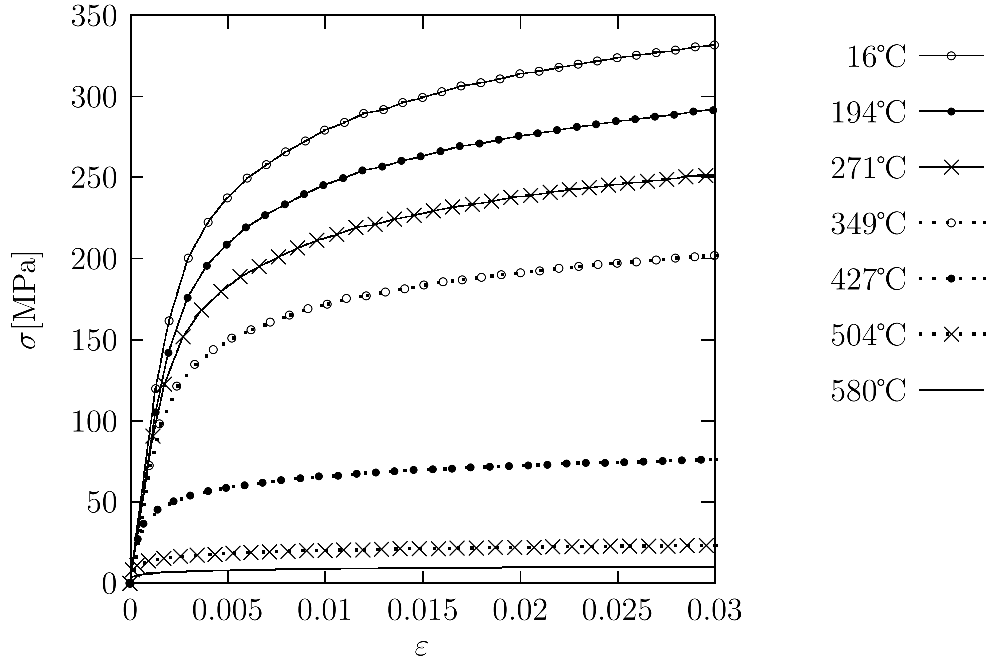

Figure 4.27: Temperature dependent stress-strain curves of Incusil™ABA®.

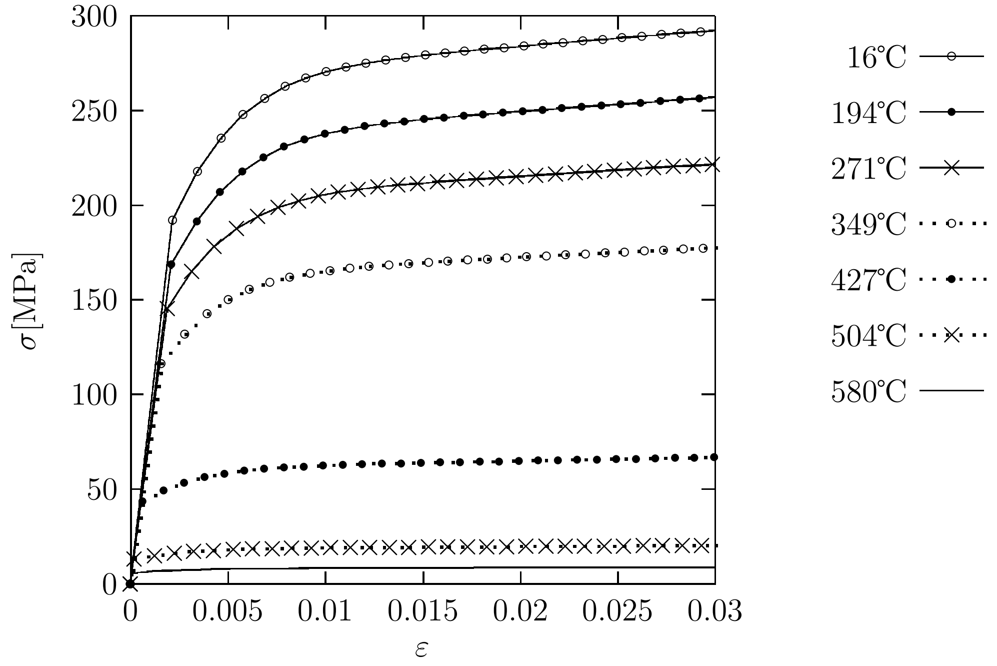

Figure 4.28: Temperature dependent stress-strain curves of the matrix alloy in the composite Incusil™ABA®-9 vol.% SiC.

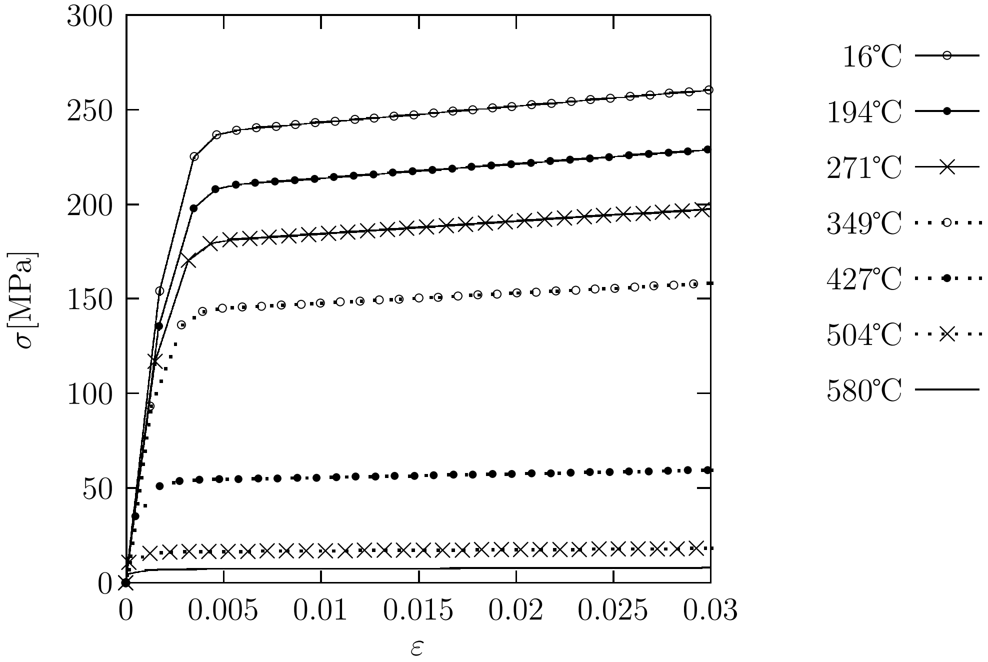

Figure 4.29: Temperature dependent stress-strain curves of the matrix alloy in the composite Incusil™ABA®-18 vol.% SiC.

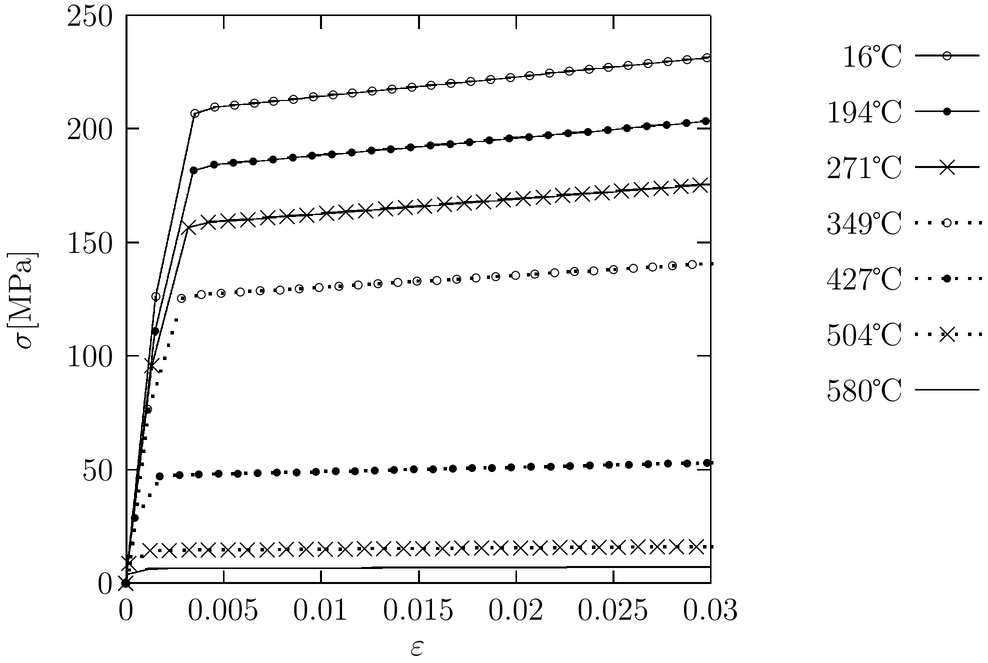

Figure 4.30: Temperature dependent stress-strain curves of the matrix alloy in the composite Incusil™ABA®-27 vol.% SiC.

4.4.2 Homogenization of the Composite Properties at Different Temperatures

After having assessed the properties of the matrix metals all over the temperature range of interest, it was possible to apply the model presented in Chapter 3 to carry out the homogenization of the mechanical behaviour of the composites, that is to say the elastic properties, the coefficient of thermal expansion and the uniaxial stress-strain curves.

Homogenization was carried out for the seven temperature values at which the properties of the matrix alloys had been assessed previously: 16 ℃, 194 ℃, 271 ℃, 349 ℃, 427 ℃, 504 ℃ and 580 ℃. Despite the availability of the experimental data presented in 4.1, homogenization of the stress-strain curves was performed also at room temperature (16 ℃) in order to obtain a smooth interpolation of the curves.

Simulations were carried out under mixed static-kinematic boundary conditions (3.25) up to the experimentally obtained nominal average uniaxial strain, that is to say 0.03, 0.01 and 0.045 for Incusil™ABA®-9 vol.% SiC, Incusil™ABA®-18 vol.% SiC and Incusil™ABA®-27 vol.% SiC, respectively. Since the contrast between the properties of the matrix materials and those of the particles is more pronounced at higher temperatures, the adopted unit cell size was larger ($\xi \approx 14$) than that considered for the inverse homogenization procedure ($\xi \approx 11$). The three unit cells had 247, 476 and 796 particles, for the composites with 9 vol.% SiC, 18 vol.% SiC and 27 vol.% SiC, respectively. As in the case of the inverse homogenization, the compatibilty of the particle size with that of the mesh 325 SiC powder used in the experiments was verified (the three models are displayed in Figures 4.31, 4.32 and 4.33).

The temperature dependent properties previously obtained were assigned to the matrix materials. Their Poisson's coefficients and CTEs were assumed to have the same values of those of Incusil™ABA®, that is to say 0.3 and $1.82 \cdot 10^{-5}$ ℃$^{-1}$ (declared by the producer) and to remain constant over the considered temperature range. The SiC particles were assigned temperature dependent elastic properties and a constant CTE, according to the data reported in [82] and summarized in Table 4.7.

Three simulations were carried out for each composite at each temperature: one for the elastic properties another for the CTE and a third one to assess the elastoplastic stress-strain curve. The calculation of the homogenized properties was carried out according to the framework presented in Chapter 3: the full stiffness matrix and the coefficients of thermal expansion were computed and the obtained composite behaviour proved to be isotropic. The results of the homogenization procedure of the elastic properties and of the coefficient of thermal expansion are reported in Tables 4.8 and 4.9, while the stress-strain curves of three composites at the different considered temperatures are displayed in Figures 4.34, 4.35 and 4.36.

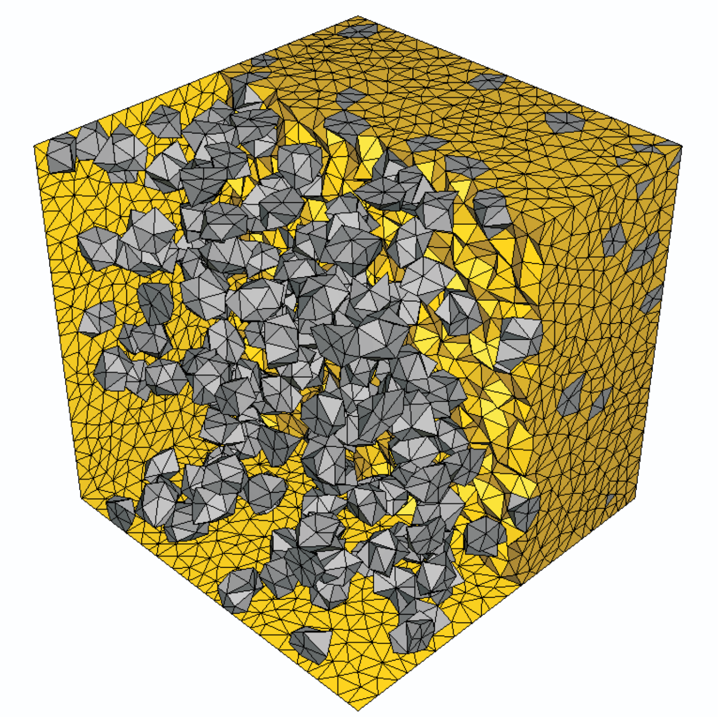

Figure 4.31: Model for the homogenization of Incusil™ABA®-9 vol.% SiC.

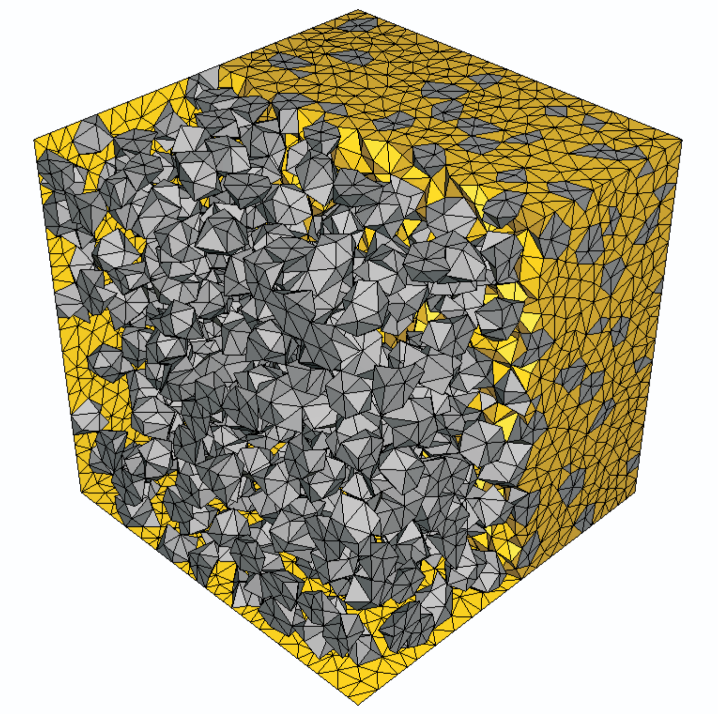

Figure 4.32: Model for the homogenization of Incusil™ABA®-18 vol.% SiC.

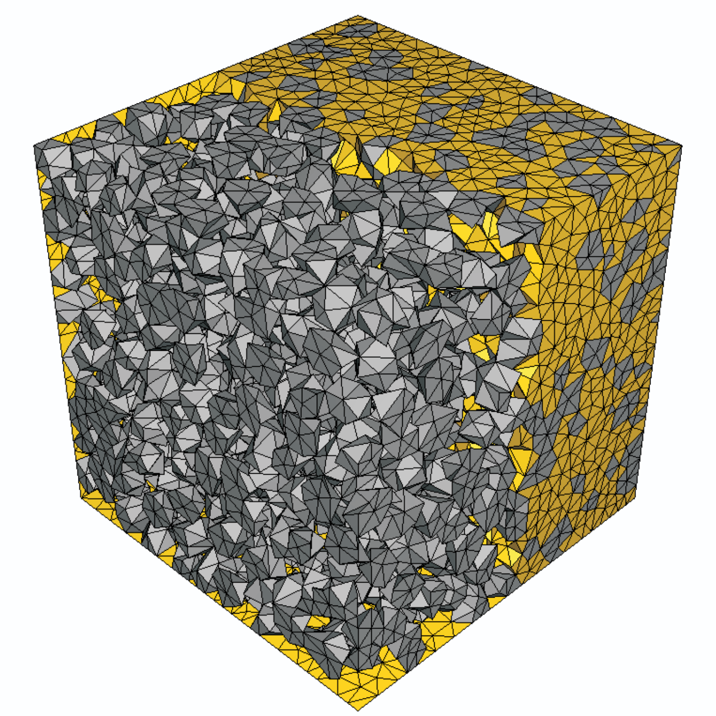

Figure 4.33: Model for the homogenization of Incusil™ABA®-27 vol.% SiC.

T[°C]	E[GPa]	ν	CTE[°C^{-1}]
16	415	0.160	$4.4 \cdot 10^{-6}$
194	411	0.160	
271	409	0.159	
349	407	0.159	
427	406	0.159	
504	404	0.159	
580	402	0.159	

Table 4.7: Temperature dependent mechanical properties of SiC particles.

	Incusil™ABA® 9 vol.% SiC		Incusil™ABA® 18 vol.% SiC		Incusil™ABA® 27 vol.% SiC	
T[°C]	E[MPa]	ν	E[MPa]	ν	E[MPa]	ν
16	101690	0.2887	116985	0.2765	126694	0.2626
194	91795	0.2885	103374	0.2760	116403	0.2618
271	88794	0.2885	106561	0.2759	113285	0.2615
349	85501	0.2884	99795	0.2758	109767	0.2612
427	81121	0.2883	95126	0.2754	105198	0.2606
504	74843	0.2881	88306	0.2751	98423	0.2599
580	64231	0.2877	78938	0.2743	89130	0.2585

Table 4.8: Temperature dependent elastic properties of the composite fillers.

	Incusil™ABA® 9 vol.% SiC	Incusil™ABA® 18 vol.% SiC	Incusil™ABA® 27 vol.% SiC
T[°C]	CTE[°C^{-1}]	CTE[°C^{-1}]	CTE[°C^{-1}]
16	$1.646 \cdot 10^{-5}$	$1.472 \cdot 10^{-5}$	$1.306 \cdot 10^{-5}$
194	$1.651 \cdot 10^{-5}$	$1.480 \cdot 10^{-5}$	$1.317 \cdot 10^{-5}$
271	$1.653 \cdot 10^{-5}$	$1.486 \cdot 10^{-5}$	$1.324 \cdot 10^{-5}$
349	$1.655 \cdot 10^{-5}$	$1.489 \cdot 10^{-5}$	$1.329 \cdot 10^{-5}$
427	$1.656 \cdot 10^{-5}$	$1.491 \cdot 10^{-5}$	$1.332 \cdot 10^{-5}$
504	$1.657 \cdot 10^{-5}$	$1.493 \cdot 10^{-5}$	$1.335 \cdot 10^{-5}$
580	$1.660 \cdot 10^{-5}$	$1.500 \cdot 10^{-5}$	$1.344 \cdot 10^{-5}$

Table 4.9: Temperature dependent CTEs of the composite fillers.

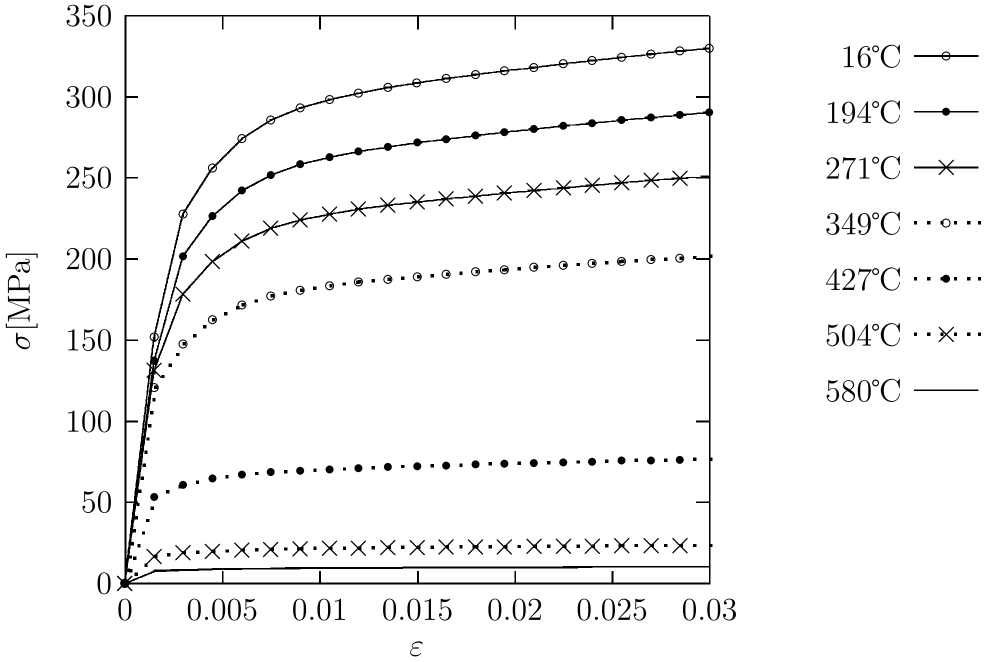

Figure 4.34: Temperature dependent stress-strain curves of Incusil™ABA®-9 vol.% SiC.

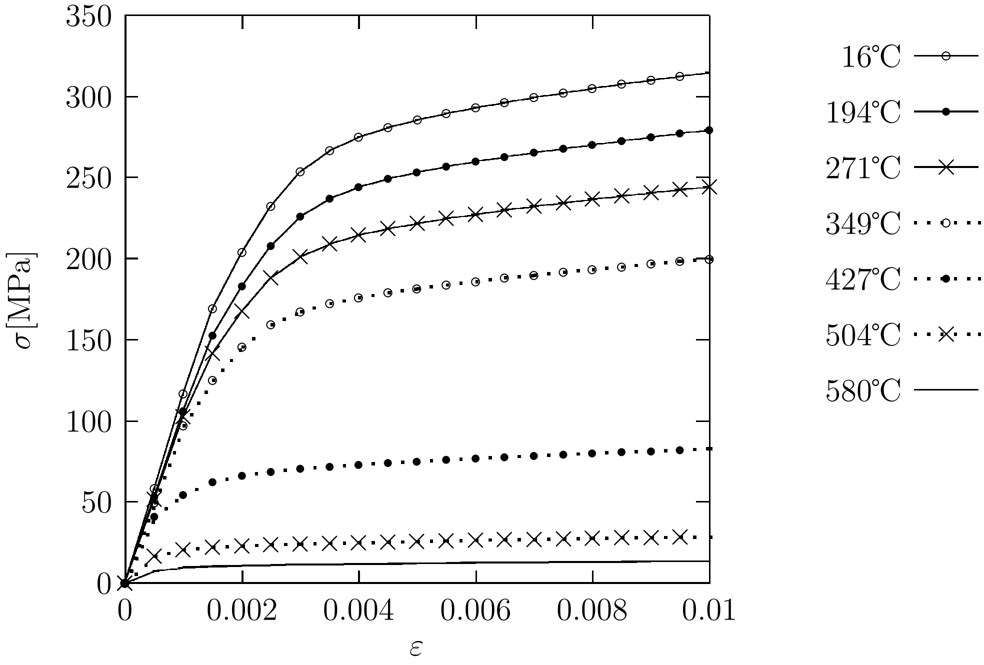

Figure 4.35: Temperature dependent stress-strain curves of Incusil™ABA®-18 vol.% SiC.

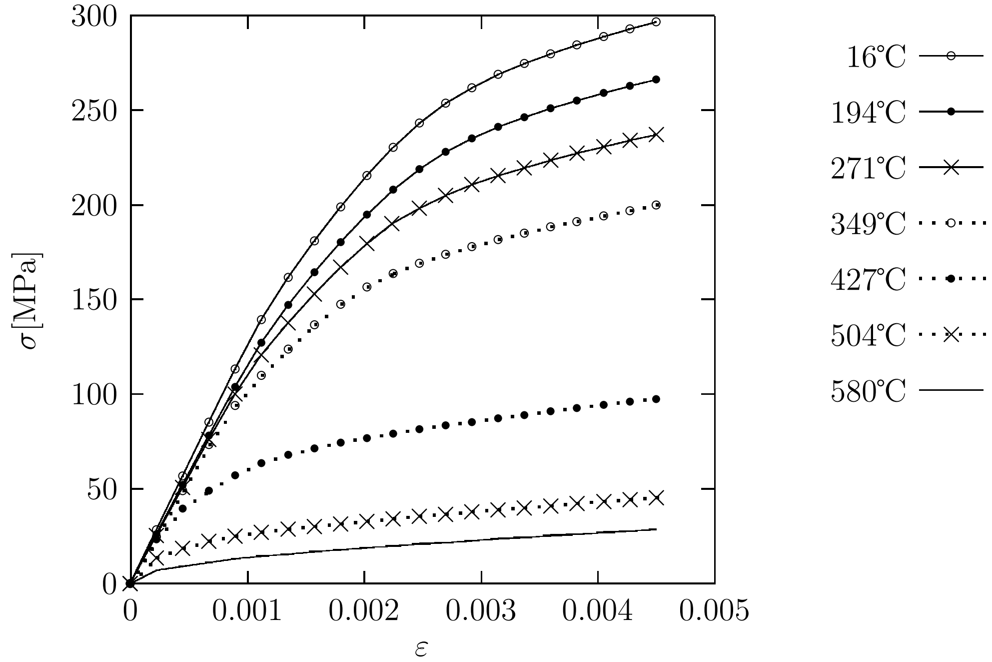

Figure 4.36: Temperature dependent stress-strain curves of Incusil™ABA®-27 vol.% SiC.

Chapter 5

Characterization of Ceramic-Metal Joints

Once the mechanical properties of particle reinforced brazing fillers had been assessed it was possible to study how they influence the characteristics of ceramic-metal joints. The experimental investigation on the joints followed two main directions: on one hand the residual strains were measured by X-ray diffraction while on the other hand the joint performance was evaluated by 4-point bend tests. Moreover, optical microscopy and SEM/EDX investigations were carried out with the aim of comparing the composite filler microstructures in the joints and in the tensile specimens. In parallel, finite element models were developed both for the prediction of residual stresses and for the evaluation of the evolution of the stress state in the joints during the bend tests. Finally a parametric finite element model was implemented to study different material assemblies and brazing gaps. The combination of the results of the experiments and of the simulations gives an insight on the understanding of how the different mechanical and geometrical parameters influence the residual stress state and suggests some of the guidelines to follow when designing a ceramic-metal joint.

5.1 Residual stress evaluation by X-ray diffraction

As already mentioned in section 1.2.2, among a number of methods available for experimental residual stress analysis, X-ray diffraction methods, employing the characteristic radiation emitted from a X-ray tube or medium-energy synchrotron radiation, are very suitable for investigating the residual stresses both on the surface layers of bulk materials and in thin films and allow the determination of the whole stress tensors of all crystalline phases (a review of the subject can be found in [75]).

5.1.1 Fundamental concepts in diffraction stress analysis

When a polycrystalline material is subjected to stress, the lattice spacing d of the lattice planes varies as a function of the load and of the orientation of the lattice planes with respect to the loading direction. By XRD it is possible to measure direction-dependent lattice spacings, which depend on the wavelength λ and on the diffraction angle 2θ according to Bragg's law:

$$\lambda = 2d^{hkl} sin\theta^{hkl} \tag{5.1}$$

where hkl are Laue's indices. Note that the lattice spacing is measured in the direction of the diffraction vector. Usually the diffraction angle is obtained from the position of the maximum or of the centroid of the hkl diffraction line. Then it is possible to calculate the elastic strain of the hkl planes:

$$\varepsilon^{hkl} = \frac{\left(d^{hkl} - d_0^{hkl}\right)}{d_0^{hkl}} \tag{5.2}$$

where d_0^{hkl} is the strain-free or reference lattice spacing of the hkl lattice planes.

The direction of the strain measurement (the direction of the diffraction vector) is usually identified by the angles φ and ψ, where ψ is the angle of inclination of the specimen surface normal with respect to the diffraction vector and φ denotes the rotation of the specimen around the specimen surface normal. A diffraction line contains information on the elastic strain of crystallites only for such crystallites that have their hkl planes oriented perpendicular to the diffraction vector, so only the elastic strain of a subgroup of crystallites composing a polycrystalline specimen is analysed in a lattice-strain measurement. In general, the strain measured by XRD is not equal to the mechanical strain in the same direction, characterized by (ψ, φ), as the mechanical strain is an average over all crystallites in the sample, while the diffraction strain represents only a subgroup. Thus, it is of fundamental importance in diffraction stress analysis to distinguish diffraction averages from the average components of mechanical strain. For diffraction stress analyses three reference frames are usually adopted (Figure 5.1):

1. The crystal reference frame $\left(x_1^C, x_2^C, x_3^C\right)$: In general, a convention for the definition of an orthonormal crystal system has to be adopted [36, 87, 88]. In the case of cubic crystal symmetry, the axes are chosen to coincide with the axes of the crystal lattice.

2. The specimen reference frame $\left(x_1^S, x_2^S, x_3^S\right)$: The x_3^S axis is oriented perpendicular to the specimen surface and the x_1^S and x_2^S axes lie in the surface plane. If a preferred direction within the plane of the surface exists, e.g. in the present case the direction parallel to the joint interface, the x_1^S direction is usually oriented along this preferred direction.

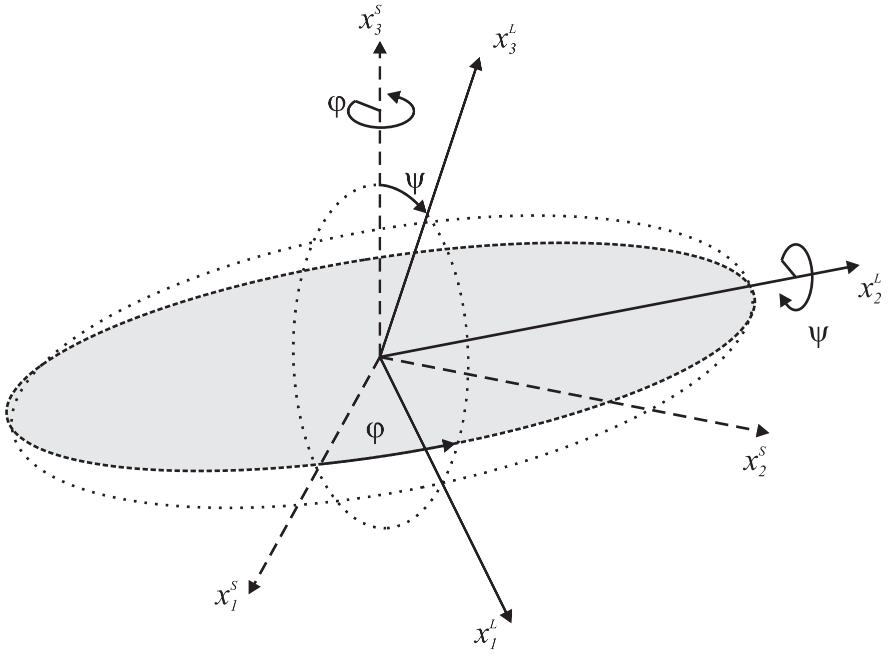

Figure 5.1: Schematic of the specimen and laboratory reference frames.

3. The laboratory reference frame $\left(x_1^L, x_2^L, x_3^L\right)$: This frame is chosen in such a way that the x_3^L axis coincides with the diffraction vector. For $\varphi = \psi = 0$, the laboratory frame of reference coincides with the specimen frame of reference.

The simplest specimen for diffraction stress analysis is a polycrystal composed of elastically isotropic crystallites. The basic principle of the method will be discussed for such a specimen first, then the effects of single crystal elastic anisotropy will be introduced.

For a polycrystal composed of elastically isotropic crystallites, Hooke's law holds for both the macroscopic body and for every crystallite in the aggregate and thus also for the strain probed by X-ray diffraction:

$$\left\langle \varepsilon_{ij}^S \right\rangle = D_{ijkl}^S \left\langle \sigma_{kl}^S \right\rangle = C_{ijkl}^D \left\langle \sigma_{ij}^C \right\rangle = \left(D_1 \delta_{ij} \delta_{kl} + \frac{1}{2} D_2 \frac{1}{2} \left(\delta_{ik} \delta_{jl} + \delta_{il} \delta_{jk} \right) \right) \left\langle \sigma_{kl}^S \right\rangle \tag{5.3}$$

where angular brackets indicate averages for all the crystallites and D_1 and $\frac{1}{2}D_2$ are

$$D_1 = -\frac{\nu}{E} \tag{5.4}$$

and

$$\frac{1}{2} D_2 = \frac{1+\nu}{E} \tag{5.5}$$

respectively. Moreover, D^S_{ijkl}, the compliance tensor of the body referred to the specimen reference frame can be set equal to D^C_{ijkl}, as the individual crystallites are elastically isotropic. The strain tensor is identical for all the crystallites, therefore

$$\varepsilon^{hkl}_{\varphi\psi} = \left\{\varepsilon^L_{33}\right\}^{hkl}_{\varphi\psi} = \varepsilon^L_{33} = \left\langle\varepsilon^L_{33}\right\rangle \tag{5.6}$$

where braces indicate averages for the diffracting crystallites only. The average strain $\left\langle\varepsilon^L_{33}\right\rangle$ can be calculated from the strain tensor ε^S_{ij} in the frame of reference of the specimen:

$$\varepsilon^{hkl}_{\varphi\psi} = \left\langle\varepsilon^L_{33}\right\rangle = m^S_i \left\langle\varepsilon^S_{ij}\right\rangle m^S_j \tag{5.7}$$

where $\boldsymbol{m}^S$ is defined as

$$\boldsymbol{m}^S = \begin{pmatrix} sin\psi cos\varphi \\ sin\psi sin\varphi \\ cos\psi \end{pmatrix} \tag{5.8}$$

By substitution of $\left\langle\varepsilon^S_{ij}\right\rangle$ in (5.3), the so-called $sin^2\psi$ law, relating the diffraction strain to the components of the mechanical stress tensor expressed in the specimen frame of reference, is obtained:

$$\begin{aligned}\varepsilon^{hkl}_{\varphi\psi} = {} & \frac{1}{2}D_2 sin^2\psi \left(\left\langle\sigma^S_{11}\right\rangle cos^2\varphi + \left\langle\sigma^S_{12}\right\rangle sin(2\varphi) + \left\langle\sigma^S_{22}\right\rangle sin^2\varphi\right) + \\ & + \frac{1}{2}D_2 \left(\left\langle\sigma^S_{13}\right\rangle cos\varphi sin(2\psi) + \left\langle\sigma^S_{23}\right\rangle sin\varphi sin(2\psi) + \left\langle\sigma^S_{33}\right\rangle cos^2\psi\right) + \\ & + D_1 \left(\left\langle\sigma^S_{11}\right\rangle + \left\langle\sigma^S_{22}\right\rangle + \left\langle\sigma^S_{33}\right\rangle\right)\end{aligned} \tag{5.9}$$

Note that, for a polycrystalline aggregate subjected to a homogeneous stress field and consisting of elastically isotropic crystallites, equation (5.9) holds also in the presence of crystallographic texture and direction-dependent grain interaction. The name of the equation stems from the proportionality of the measured strain to $sin^2\psi$ if the principal stress frame of reference is adopted for the specimen frame of reference: in this case, a plot of the measured strain versus $sin^2\psi$ yields a straight line (for constant φ) and the components of the stress tensor can be extracted from the slopes of the straight lines plotted for various values of ψ.

In practice, polycrystals composed of elastically isotropic crystallites are seldom met. In a polycrystal composed of elastically anisotropic crystallites, stresses and strains vary over the differently oriented crystallites in the specimen, in contrast with a polycrystal composed of elastically isotropic crystallites, where stresses and strains are equal for all differently oriented crystallites. In the presence of this intrinsic elastic anisotropy, the distribution of stresses and strains that occurs is the result of the elastic grain interaction. Although the individual crystallites are anisotropic, the whole body can exhibit a macroscopic isotropic elastic behaviour and this is the case of the so-called quasi-isotropic materials. It can be shown, by exploiting the symmetries of the elastic properties of subgroups of grains as selected by a diffraction experiment, that the concept of diffraction elastic constants can be extended to this set of materials. In this case a similar $sin^2\psi$ law is obtained, in which the elastic constants D_1 and $\frac{1}{2}D_2$ are replaced by elastic constants which depend on the crystallographic orientation hkl:

$$\begin{aligned}
\varepsilon_{\varphi\psi}^{hkl} &= \left\{\varepsilon_{33}^{L}\right\}_{\varphi\psi}^{hkl} = \\
&\frac{1}{2}D_2^{hkl} sin^2\psi \left(\left\langle\sigma_{11}^S\right\rangle cos^2\varphi + \left\langle\sigma_{12}^S\right\rangle sin(2\varphi) + \left\langle\sigma_{22}^S\right\rangle sin^2\varphi\right) + \\
&+ \frac{1}{2}D_2^{hkl} \left(\left\langle\sigma_{13}^S\right\rangle cos\varphi sin(2\psi) + \left\langle\sigma_{23}^S\right\rangle sin\varphi sin(2\psi) + \left\langle\sigma_{33}^S\right\rangle cos^2\psi\right) + \\
&+ D_1^{hkl} \left(\left\langle\sigma_{11}^S\right\rangle + \left\langle\sigma_{22}^S\right\rangle + \left\langle\sigma_{33}^S\right\rangle\right)
\end{aligned} \tag{5.10}$$

Note that according to the right-hand side of equation (5.10), in contrast with equation (5.9), the diffraction strain depends on the reflection hkl. Stresses and strains of individual crystallites are not equal to the corresponding mechanical averages. Thus averaging brackets and averaging braces have to be used.

The ceramic composite used in this project is microscopically isotropic [13]. Therefore strain and stresses were computed according to (5.10). XRD techniques can be applied to macroscopically anisotropic materials as well. However, since the subject is not closely related to the present work, it is not presented (refer to the specific literature, e.g. [75]).

5.1.2 The testing facility

In general, microstructures are inhomogeneous and/or anisotropic thus, as stated in section 5.1.1, diffraction analyses require the variation of the orientation of the diffraction vector with respect to the specimen reference system. Parallel-beam diffractometers are particularly suitable for this purpose since they provide an instrumental diffraction line broadening which is independent of the orientation of the diffraction vector. This feature is made possible by the parallel-beam geometry which involves less instrumental aberrations than conventional focusing geometries.

All the measurements were carried out at Max Planck Institute for Metals Research in Stuttgart by means of a novel generation instrument consisting of a Bruker AXS D8 Discover X-ray diffractometer equipped with an Eulerian cradle (four-circle goniometer). Cu-Kα radiation emerging from the focus (0.1×1 mm^2) of a rotating anode source (Bruker AXS Turbo X-ray source), operating at 50 kV and 20 mA, is converted into a quasi parallel beam by a single reflection X-ray mirror (FOX2D, XENOCS). As the mirror is mounted under a takeoff angle of 6° the focus size seen by the optic is 0.1×0.1 mm^2. The size of the beam at the mirror exit is 1×1 mm^2, and is then reduced by means of a circular collimator. The diffracted beam passes through a parallel plate collimator with an acceptance angle of

0.23° before being detected by a scintillation counter (for further details refer to [120]). An overall view of the instrument and images of the main components are reported in Figures 5.2 and 5.3.

Figure 5.2: Overall view of the XRD facility.

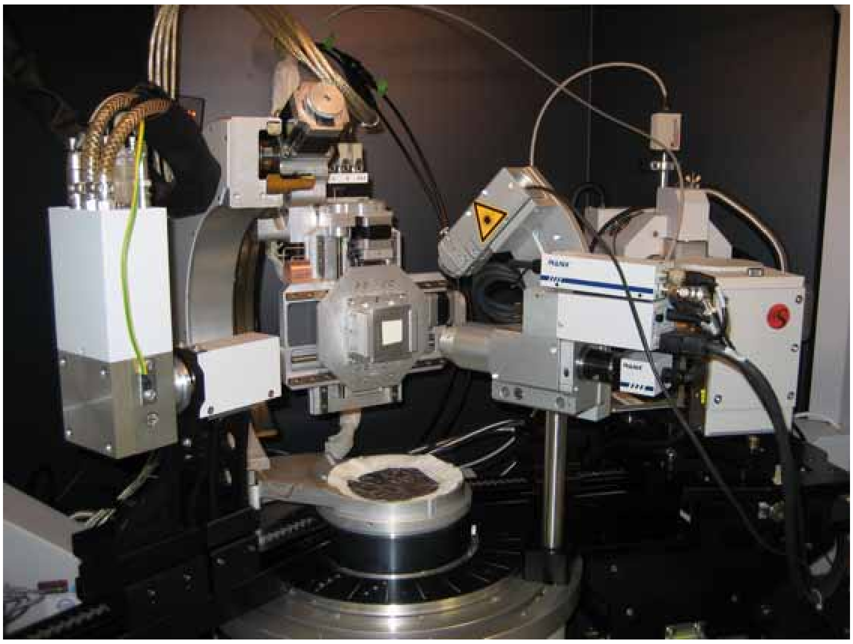

(a)

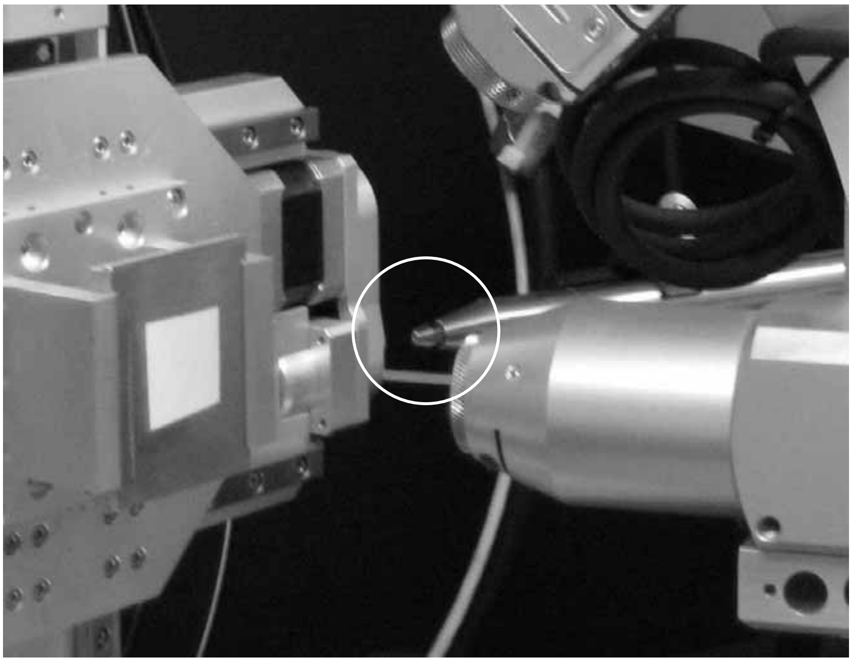

(b)

Figure 5.3: The main components of of the XRD facility: a) from left to right: the scintillation counter, the goniometer (in this case, a fluorescent sample is mounted for instrument calibration), the position detector (consisting of a laser source and a CCD camera), the X-ray lens (partially hidden); b) the X-ray circular collimator.

5.1.3 Results and Discussion

Four specimens were investigated by XRD: two joints brazed by pure Incusil™ABA® and two joints brazed by Incusil™ABA®-27 vol.% SiC. Measurements were carried out on the ceramic joining partner on the 4 mm wide face and a 200 µm diameter circular beam was used. The specimens were mounted on the goniometer via a supporting plate (Figure 5.4), then by using the facility position detector the system was aligned to have for each specimen the x_2^S axis parallel to the ceramic 25 mm long edge (a different position setting was recorded for each specimen). Since the specimens had not been polished to avoid inducing modifications of the surface stress state, the actual position of the ceramic-braze interface was detected both visually (as previously reported, the system is equipped with a CCD camera) and by means of a XRD linescan in x_2^S direction.

Measurements were taken on a grid of six positions on each specimen, according to the schematic reported in Figure 5.5. In the choice of the measurement locations, a fundamental aspect, which was considered, is the change of the shape and size of the irradiated area [59]. If a cylindrical beam is used (and this was the case), the intersection with the surface is an ellipse, which becomes increasingly elongated with increasing sample tilt ψ. Moreover the intersection becomes more elliptical at small 2θ angles and measurements should not be taken at $2\theta < 20°$.

After a preliminary study by finite element simulations, it was checked that for the chosen diffraction peaks, the irradiated area does not intersect the ceramic region close to the interface, in which both the experimental and the model results are affected by stress concentrations. Furthermore, finite element simulations show that in the region where the measurements were taken the ceramic stress state is an almost uniaxial compression, $\langle \sigma_{11}^S \rangle$. Therefore the general stress-strain equation (5.10) reduces to:

$$\varepsilon_{\varphi\psi}^{hkl} = D_1^{hkl} \langle \sigma_{11}^S \rangle + \frac{1}{2} D_2^{hkl} \langle \sigma_{11}^S \rangle \, sin^2\psi cos^2\varphi \tag{5.11}$$

In this case to assess the stress value it is sufficient to measure $\varepsilon_{\varphi\psi}^{hkl}$ at several ψ angles at $\varphi = 0$: when $\varepsilon_{\varphi\psi}^{hkl}$ is plotted as a function of $sin^2\psi$ a straight line is obtained and $\langle \sigma_{11}^S \rangle$ can be deduced from its slope. Equation (5.11) can be applied only if d_0^{hkl} is known. When this is not the case, as for the present measurements, it is possible to obtain d^{hkl} as a function of $sin^2\psi$ by introducing (5.2) into (5.11):

$$d^{hkl} = d_0^{hkl} + D_1^{hkl} \langle \sigma_{11}^S \rangle d_0^{hkl} + \frac{1}{2} D_2^{hkl} \langle \sigma_{11}^S \rangle \, sin^2\psi cos^2\varphi d_0^{hkl} \tag{5.12}$$

If d^{hkl} is plotted against $sin^2\psi$ and the slope m and the intercept b, the following system of two equations and two unknowns, d_0^{hkl} and $\langle \sigma_{11}^S \rangle$, is obtained:

$$m = \frac{1}{2} D_2^{hkl} \langle \sigma_{11}^S \rangle \, cos^2\varphi d_0^{hkl} \tag{5.13}$$

$$b = d_0^{hkl} + D_1^{hkl} \left\langle \sigma_{11}^S \right\rangle d_0^{hkl} \tag{5.14}$$

Thus it is still sufficient to carry out measurements at several ψ angles at $\varphi = 0$ to obtain the value of $\left\langle \sigma_{11}^S \right\rangle$. After a preliminary study it was chosen to measure the shift for the diffraction peak 210 for Si_3N_4, $2\theta \approx 35.91°$, and 111 for TiN, $2\theta \approx 36.41°$. Note that both choices satisfy the condition $2\theta > 20°$. The peaks were fitted by a linear combination of a Gaussian and a Cauchy-Lorentz distribution. At each sampling point, seven measurements were taken, with ψ varying from 0° to 60° with a step of 10°, for a measurement duration of 10 hours for each location (which corresponds to 2.5 days per specimen).

A linear fit of the data was performed to assess the values of m and b, which were then introduced into (5.13) and (5.14) to obtain $\left\langle \sigma_{11}^S \right\rangle$ in each phase. The assumed values of the crystal elastic constants D_1^{hkl} and $1/2D_2^{hkl}$ were those reported in the database at Max Planck Institut: -1130 MPa^{-1} and 7990 MPa^{-1} for Si_3N_4 and -490 MPa^{-1} and 2890 MPa^{-1} for TiN. The average stress in the composite was computed by weighting the stress on the two phases by their volume fractions which are 0.798 for Si_3N_4 and 0.202 for TiN, obtained by assuming densities of 3.19 g/cm^3 and 5.4 g/cm^3, respectively [44]. The precision of the measurements depends on three main aspects:

- uncertainties related to the ceramic material: the values of the elastic constants were not directly measured but extracted from a database as well as the densities; moreover the presence of an intergranular glassy phase [13] was neglected;
- uncertainties related to the quality of the joints: the joints chosen for the measurements could only be visually inspected before the measurements; therefore possible sources of perturbation of the strain field such as slight misalignments or defects in the interface could not be excluded a priori;
- uncertainties related to the instrument itself: typically the counting-statistical error of each measured peak position is about 0.006° and directly influences the uncertainty of the linear regression.

To quantify how the data scatter in the $\sin^2 \psi$ plots affects the values of the residual stresses, a study of error propagation was carried out and the standard errors on the coefficients m and b were calculated as well as their impact on the stress values: while the standard error on b is negligible, the average standard error on m is about 25% for Si_3N_4 and 50% for TiN. To take into account the other factors an additional 10% uncertainty was added to that calculated via error propagation. The obtained total uncertainty is compatible with analogous results reported in literature [66, 85]. An example of a linear fit is reported in Figure 5.6, while the results of all the measurements are summarized in Table 5.1.

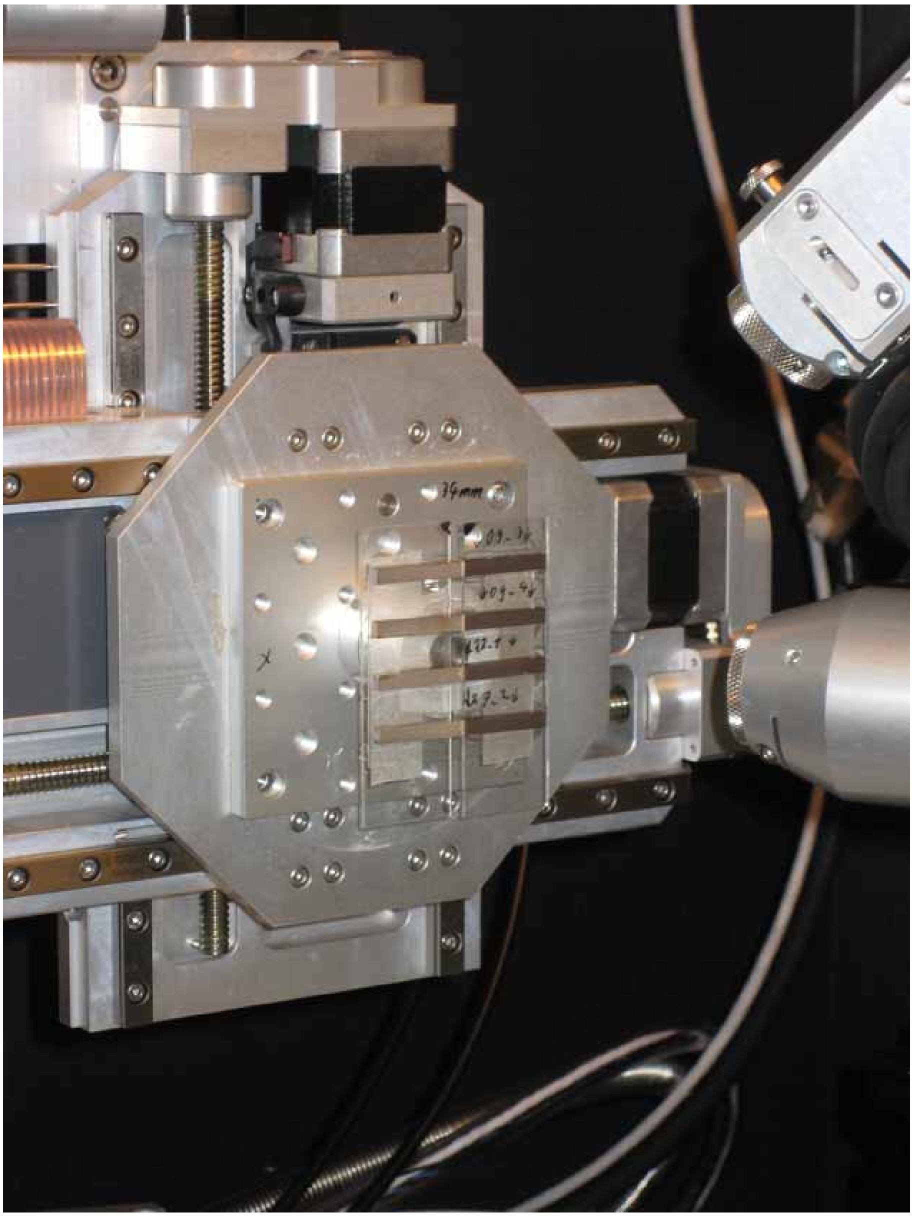

Figure 5.4: The ceramic-metal joints mounted on the XRD facility.

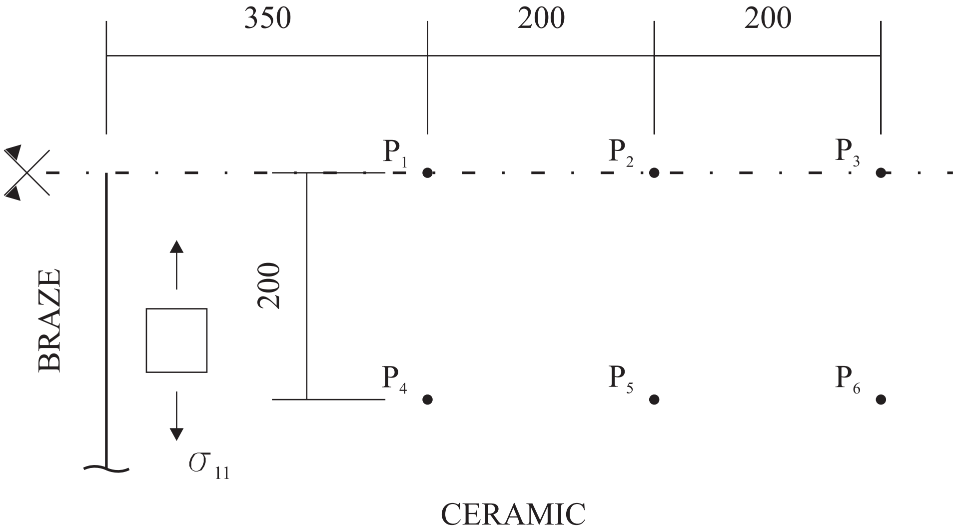

Figure 5.5: Schematic of the positions chosen for XRD measurements (units: µm).

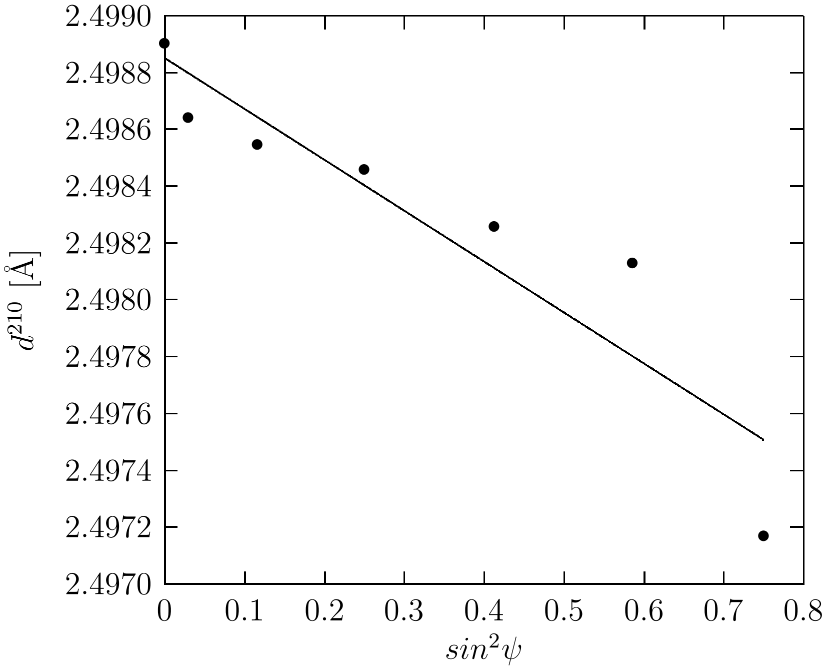

Figure 5.6: Example of a linear fit to $\left\langle \sigma_{11}^{S} \right\rangle$: the data points refer to Si_3N_4 and the measurements were taken at point 4 on specimen LC060903_3 (Incusil™ABA®-27 vol.% SiC). The linear fit parameters are $m = -1.7922 \cdot 10^{-3}$ and $b = 2.4988$ Å.

P	Phase	Incusil™ABA®		Incusil™ABA®-27 vol.% SiC	
		LC060627_1	LC060627_2	LC060903_3	LC060903_4
1	Si_3N_4	-81±12	-75±7	-67±24	-42±10
	TiN	-353±114	-79±127	-341±61	-170±111
	average	-136±33	-76±31	-122±31	-68±31
2	Si_3N_4	-56±15	-66±13	-36±23	-42±19
	TiN	-307±76	-111±104	-365±79	-264±108
	average	-107±27	-76±31	-102±34	-87±37
3	Si_3N_4	-60±7	-43±8	-63±21	-81±23
	TiN	-350±48	-84±105	-214±111	-355±68
	average	-119±15	-51±27	-93±39	-137±32
4	Si_3N_4	-73±11	-95±18	-90±17	-87±18
	TiN	-426±25	-316±67	-146±125	-340±63
	average	-144±14	-140±28	-101±39	-138±27
5	Si_3N_4	-50±9	-74±27	-40±12	-83±9
	TiN	-297±70	-242±29	-185±121	458±72
	average	-100±21	-108±27	-69±34	-158±22
6	Si_3N_4	-52±17	-65±13	-47±13	-96±19
	TiN	-365±85	-161±95	-93±165	455±88
	average	-115±30	-84±30	-56±44	-168±33

Table 5.1: Results of XRD measurements (units: MPa).

5.2 4-Point Bend Tests

The mechanical strength of the joints was characterized by 4-point bend tests with an upper load span l_2 of 20 mm and a lower load span l_1 of 40 mm and a cross-head velocity of 0.015 mm/s. This test setup was derived from test standard EN 843-1 [3] and, as reported in Chapter 1, similar configurations are reported in literature. The tests were carried out on an Instron 5848 Microtester equipped with a ±2 kN load cell (Figure 5.7 shows a specimen during testing). The applied moment and the maximum nominal applied stress were calculated according to beam theory:

$$M = \frac{P}{4}(l_1 - l_2) \tag{5.15}$$

$$\sigma_{max} = \frac{6M}{bh^2} \tag{5.16}$$

where P is the total applied load (measured by the load cell) while b and h are the section width and height, 4 mm and 3 mm, respectively). It is important to highlight that σ_{max}

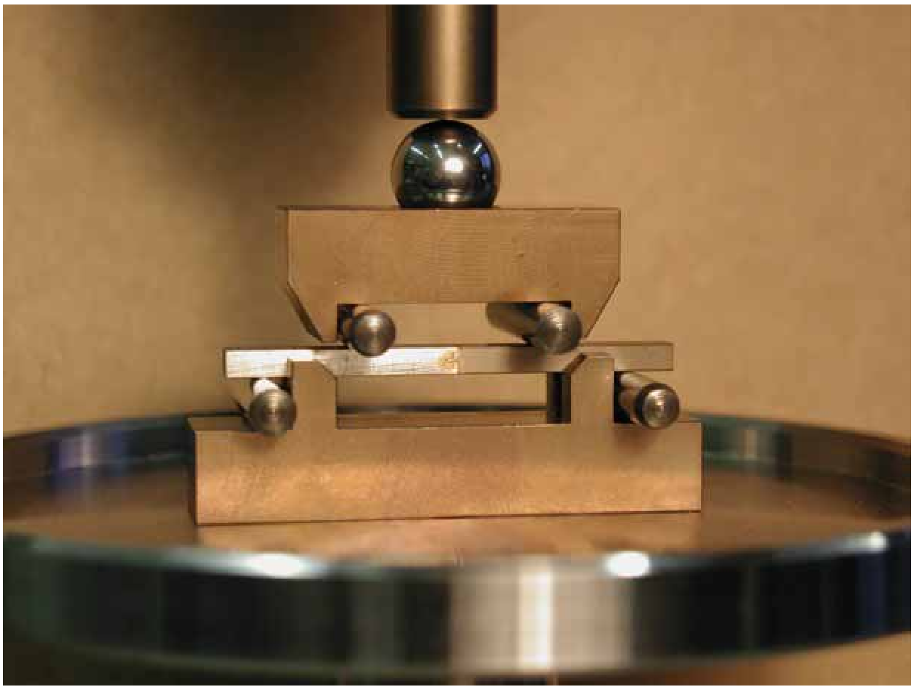

Figure 5.7: A specimen during a 4-point bend test.

is a nominal stress, calculated as if the specimen were a homogeneous beam, and not the maximum principal stress in the material.

For each braze layout at least six specimens were tested. The nominal bend strengths were calculated from the rupture load according to (5.16). After bend tests it was also possible to measure the actual joint thickness: the filler in excess was ground away and the broken sample polished, then the thickness was measured by optical microscopy. The results are summarized in Table 5.2. Joints with Incusil™ABA® and Incusil™ABA®-18 vol.% SiC showed the highest average strengths (354 MPa and 341 MPa, respectively) while lower results were obtained for Incusil™ABA®-9 vol.% SiC and Incusil™ABA®-27 vol.% SiC (272 MPa and 247 MPa, respectively). The typical standard deviation was about 60 MPa, which is compatible with that of the bend strength of the ceramic (785±51 MPa, [13]).

5.3 Microstructural Analysis

Specimens for optical and electron microscopy analyses of the braze were extracted from the ceramic-metal joints after 4-point bend tests and hot mounted in a conductive phenolic resin (Struers PolyFast). Grinding and polishing were carried out by following the same procedure adopted for the specimens obtained from those for tensile tests, which is

Braze layout	Number of specimens	Ave. thickness [µm]	Ave. strength [MPa]	St. Dev. [MPa]
Incusil™ABA®	10	35	354	62
Incusil™ABA®-9 vol.% SiC	6	317	272	68
Incusil™ABA®-18 vol.% SiC	7	316	341	28
Incusil™ABA®-27 vol.% SiC	6	399	247	72

Table 5.2: Results of the 4-point bend tests.

described in section 4.2.

The microstructures of Incusil™ABA® and of the composite fillers in the joints were investigated by EDX technique with the objective of comparing the phase compositions with those of the tensile specimens. The micrographs were taken by using the BSE signal and the phase weight compositions were assessed by EDX point measurement (three measurements were taken for each phase). One specimen for each Incusil™ABA®-SiC composite was analysed and the results of EDX point measurements are summarized in Table 5.3 and the corresponding BSE images in Figure 5.8.

In Incusil™ABA® and in the composite matrix materials the same four main phases were identified. In the following they will be referred to with the same names indicated named in Chapter 4: AgIn, Cu, Cu_4Ti and Cu_2InTi. The experimental data summarized in Table 5.3 highlight that the phase compositions of the filler metals in the joints are very similar to those in the tensile specimens (Table 4.1).

However, while the compositions of the single phases are similar, even without carrying out stereological analyses it could be observed that the volume fractions of Cu_4Ti and Cu_2InTi phases were lower than in the corresponding tensile specimens (with the same amount of reinforcement), to the point that in some Incusil™ABA®-27 vol.% SiC joints, these phases were absent (as a consequence the composition of these two phases for the Incusil™ABA®-27 vol.% SiC joints is not indicated in Table 5.3). This can be explained by the fact that in the case of the joints the filler alloy wets not only the particle surface but also those of the joining partners, thus more titanium participates to interface reactions. Due to this further decrease of Cu_4Ti and Cu_2InTi phases, the Incusil™ABA® and the composite matrix alloys probably have a slightly different mechanical behaviour from that identified by tensile tests and inverse homogenization. Nevertheless the incertitude on the filler mechanical behaviour related to this phenomenon is negligible if compared to those depending on other aspects, such as the assumptions on the influence of temperature on the mechanical properties or on the isotropic hardening of the composite.

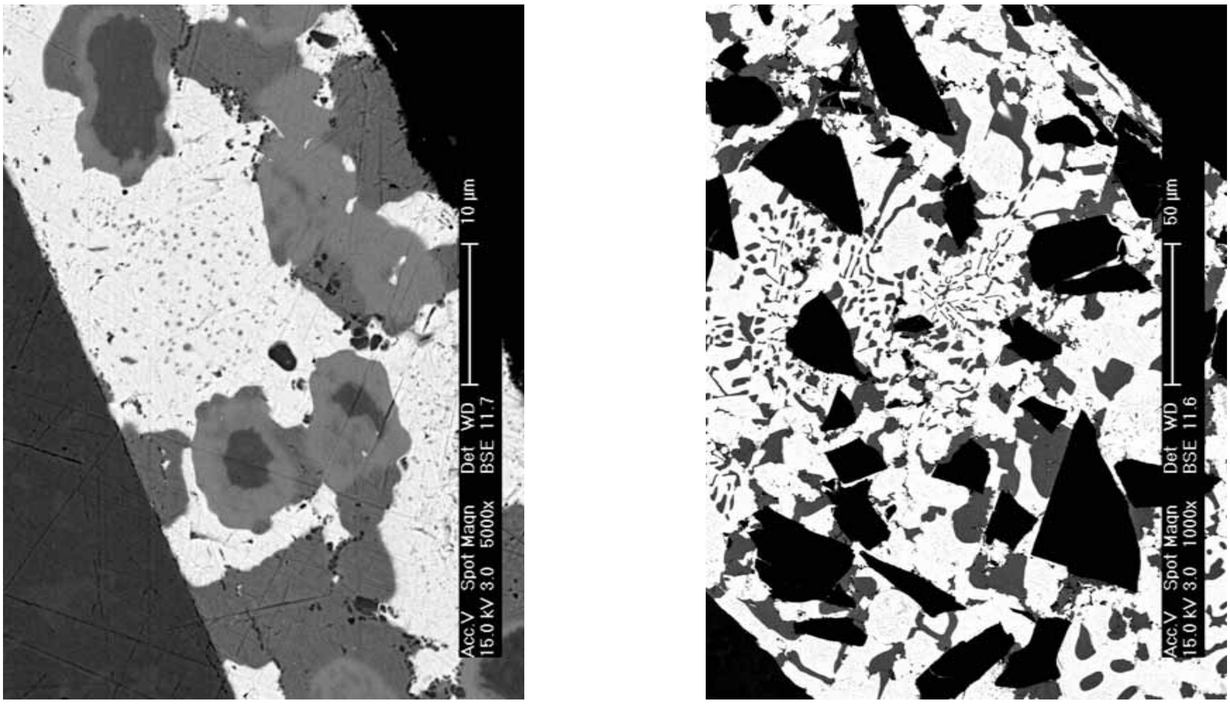

(a) Incusil™ABA®

(b) Incusil™ABA®-9 vol.% SiC

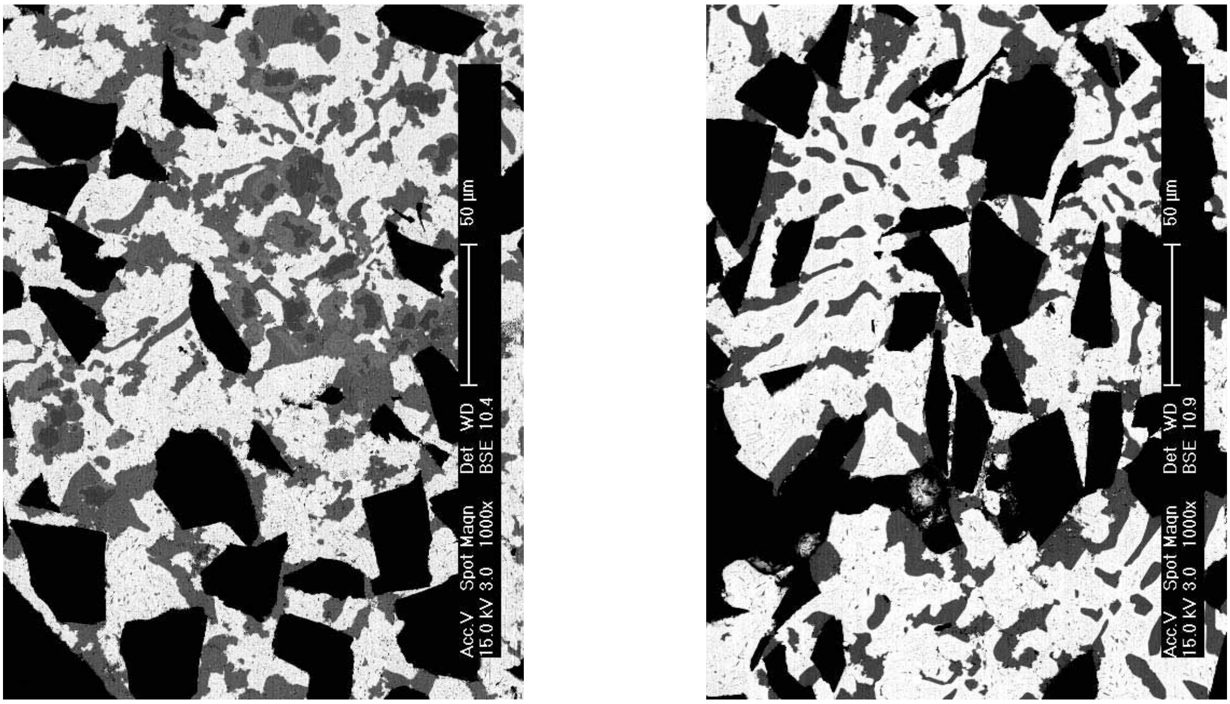

(c) Incusil™ABA®-18 vol.% SiC

(d) Incusil™ABA®-27 vol.% SiC

Figure 5.8: BSE images of the four Incusil™ABA®-SiC composites in the joints.

Material	Phase	Ag[wt.%]	In[wt. %]	Ti[wt.%]	Cu[wt.%]
Incusil™ABA®	AgIn	80.9	13.8	0.1	5.2
	Cu	4.3	2.6	1.1	92.0
	Cu_4Ti	2.5	1.2	15.0	81.2
	Cu_2InTi	4.5	26.6	16.0	52.9
Incusil™ABA®-9 vol.% SiC	Ag,In	79.2	15.0	0.2	5.6
	Cu	3.3	2.8	1.0	92.9
	Cu_4Ti	2.1	1.0	4.8	82.1
	Cu_2InTi	2.1	29.0	15.6	53.3
Incusil™ABA®-18 vol.% SiC	AgIn	78.6	15.6	0.2	5.6
	Cu	5.2	3.1	1.9	89.8
	Cu_4Ti	2.1	1.0	14.8	82.1
	Cu_2InTi	2.3	24.0	13.9	59.8
Incusil™ABA®-27 vol.% SiC	AgIn	76.3	17.4	0.2	6.1
	Cu	3.5	5.1	0.7	90.7
	Cu_4Ti	-	-	-	-
	Cu_2InTi	-	-	-	-

Table 5.3: Weight compositions of the phases of the four Incusil™ABA®-SiC composites in the joints.

5.4 Heat Transfer Problem

Residual stresses develop in ceramic-metal joints during the cooling from brazing (750 ℃) to room temperature. In the simulation of this process, the first investigated aspect was the possible coupling between the thermomechanical and the heat transfer problems, that is to say the influence of the temperature distribution on the strain and stress fields.

The specimens are quite small (3x4x50 mm^3); moreover, the cooling process takes place in the vacuum furnace in high vacuum conditions such that temperature decreases slowly (its evolution with time is reported in Figure 2.2) with a cooling rate always lower than 10 ℃/min. These two facts suggest that there should be no significant temperature gradients in the joints, which was confirmed by means of a preliminary heat transfer simulation.

A two dimensional finite element model of a joint with a 50 µm interlayer of Incusil™ABA® was considered (4-node linear elements were used). The materials were assigned the thermal properties reported in Table 5.4. Given the purpose of the simulation, to be on the safe side, a much faster cooling process was modelled: the specimen surface was imposed to reach room temperature from 800 ℃ in one minute and it was observed that the temperature in the specimen is almost uniform throughout the whole cooling process (the maximum temperature difference between the core and the surface of the ceramic joining partner is less than 4 ℃. In addition, note that the choice of a two dimensional model is conservative, since a three dimensional model would lead to a lower temperature difference (a much larger surface would participate to the heat exchange).

Following these results it was concluded that the cooling process could be studied as a thermo-mechanical problem in which the temperature varies uniformly all over the specimen.

5.5 Thermomechanical Problem

After having tackled the heat transfer aspects it was possible to develop finite element models for the comparison with experimental results. Thus simulations of the cooling process for the prediction of residual stresses and simulations of 4-point bend test were carried out. In the following section the main features adopted in the finite element models will be described, then the obtained results will be compared with the corresponding experimental data.

5.5.1 The Finite Element Model

A three-dimensional finite element model of the ceramic-metal joint specimen was developed by using ABAQUS®. The model features are described following the same order in which they are generated in the software.

Geometry and Mesh

The first step in developing a finite element model is usually the generation of the object geometry. In the case of the ceramic-metal joints studied in this thesis, this step was straightforward and the model geometry was drawn directly by using the tools included in ABAQUS® with no need to use any additional CAD software, as it is often the case when analysing systems with more complex geometries.

From a preliminary study it was assessed that residual stresses develop only in a close region around the braze, as it can also be concluded by considering the two joining partners as beam-like structures to which Saint-Venant's principle applies; furthermore, the results of 4-point bend tests show that the joints always break in the ceramic material close to the interface with the braze. These considerations showed that it was not necessary to model the whole joint but only the central region, thus it was possible to significantly reduce the model size and only the central 10 mm of the specimen were considered. Moreover, the model could be further simplified by exploiting the two symmetries. However, to simulate

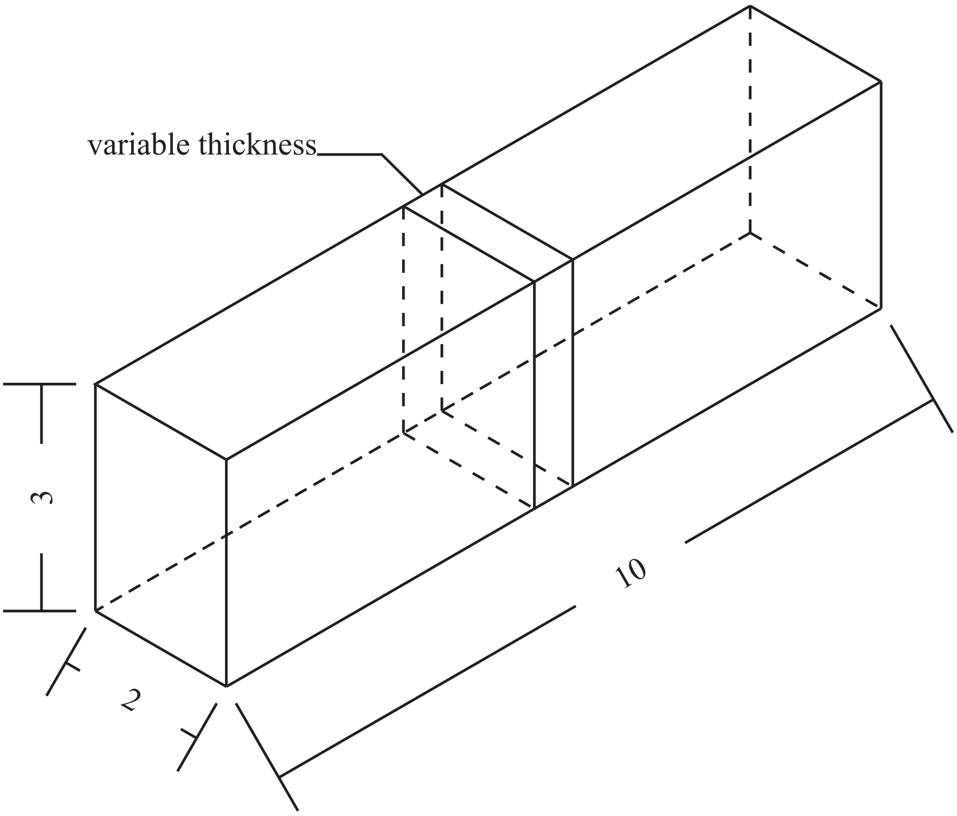

Figure 5.9: Geometry of the finite element model (units: mm).

bending as a second loading step after cooling on the same models, only one symmetry plane was considered. Material properties were assigned by partitioning the model volume into three regions. The joint thickness was varied by editing the partition sketch (a schematic of the model geometry is depicted in Figure 5.9). While the advantages of such a simple specimen geometry are evident, especially for the experimental activity, this choice leads also to some complexity in the modelling and interpretation of the experimental and numerical results. As already stated in section 1.2.2, in the case of joints between two flat surfaces the stress field exhibits singularities at the free edges and even when plasticity is considered, as it is the case in the present work, these stress concentrations affect the response of the model in the nearby region (the effect of stress singularities in joints have been the subject of specific studies reported in literature [5, 62]). In the present work, in order to limit as much as possible the region of the model influenced by the high stress gradients, fine meshes were used in the braze region, of course with a consequent increase in computing time. The adopted mesh is depicted in Figure 5.10: far from the braze region larger elements are used (the typical element is 115 × 115 × 250 μm^3) while in the central part the mesh is refined in the direction normal to the braze layer, with an element thickness of 12.5 µm. 20-node quadratic brick elements with reduced integration were used.

Material Properties

The steel and the ceramic were assumed to remain in the elastic range throughout both the processing and the mechanical testing and were assigned the temperature dependent mechanical properties which are summarized in Tables 5.5 and 5.6. Those of the steel were obtained from the producer data sheet, while those of the ceramics from literature [13]. The braze fillers were assigned the properties obtained according to the procedure described in Chapter 4 and summarized in Tables 4.5, 4.8 and 4.9 and Figures 4.27 to 4.30.

Boundary Conditions and Loads

The simulations consisted of two stages: a first cooling step, during which the specimen reaches room temperature and a second loading step, during which the specimen undergoes a 4-point bend test.

One first important issue to deal with was constituted by the modelling of the influence of the cooling ratio on stress relaxation: as described in section 2.4 the brazing of ceramic-metal joints was carried out at 750 ℃ and during the following slow cooling the creep of the filler could play an important role. Since time-dependence could not be implemented because of the lack of experimental data (as valid calculations would require constitutive laws for the filler which accurately predict the strain rate over a wide range of temperatures), it was assumed that the arising residual stresses were completely relieved when cooling from processing temperature down to 580 ℃. Below this temperature, residual stresses developed depending only on the elastoplastic behaviour of the brazing alloy. Thus in the cooling simulation the specimen temperature varied from 580 ℃, the reference stress-free state, to 20 ℃, temperature at which the four point bend test was modelled. These assumptions were also supported by the findings of the already cited study on Cusil®ABA [83, 84].

As previously stated, only the central part of the specimen is modelled while the regions of the joining partners which are not modelled can be assimilated to beams, in other words the end sections keep planar during deformation. This feature was included in the model by imposing kinematic couplings [1] at the end faces: the longitudinal (in the specimen length direction) displacements of the nodes of each end face were rigidly constrained to the six degrees of freedom of a virtual node on the symmetry plane at a distance of 1 mm from the face (Figure 5.11). During the cooling the specimens lay on the brazing jig, which substantially lets the specimen free to shrink. Thus in the simulation isostatic

Material	Density [kg/m^3]	Thermal Conductivity [W/(m·K)]	Specific Heat [J/(kg·K)]
Si_3N_4/TiN	3200	25	1000
steel	7850	34	500
Incusil™ABA®	9700	70	300

Table 5.4: Thermal properties assigned to the materials in the heat transfer simulation.

T[℃]	E[GPa]	ν	CTE[℃$^{-1}$]
20	330	0.3	-
100			$2.80 \cdot 10^{-6}$
200			$3.08 \cdot 10^{-6}$
300			$4.40 \cdot 10^{-6}$
400			$3.50 \cdot 10^{-6}$
500			$3.66 \cdot 10^{-6}$
600			$3.79 \cdot 10^{-6}$

Table 5.5: Temperature dependent mechanical properties of Si_3N_4/TiN (the CTE at 20 ℃ is not indicated since this is the reference temperature).

T[℃]	E[GPa]	ν	CTE[℃$^{-1}$]
20	210	0.3	-
100	205		$1.11 \cdot 10^{-5}$
200	195		$1.21 \cdot 10^{-5}$
300	185		$1.29 \cdot 10^{-5}$
400	175		$1.35 \cdot 10^{-5}$
500	165		$1.39 \cdot 10^{-5}$
600	155		$1.41 \cdot 10^{-5}$

Table 5.6: Temperature dependent mechanical properties of Böhler E200 steel (the CTE at 20 ℃ is not indicated since this is the reference temperature).

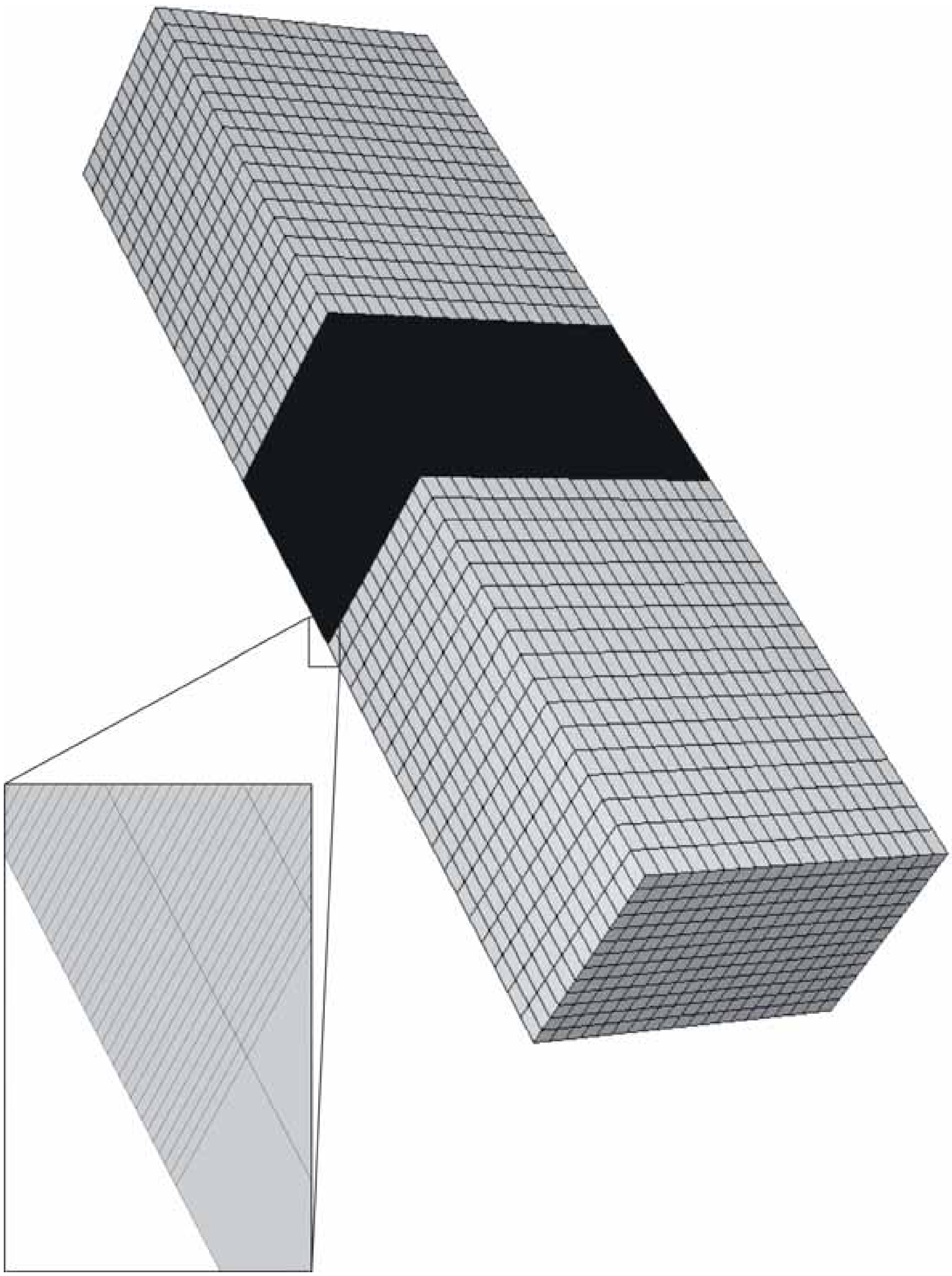

Figure 5.10: The mesh of finite element of the joint.

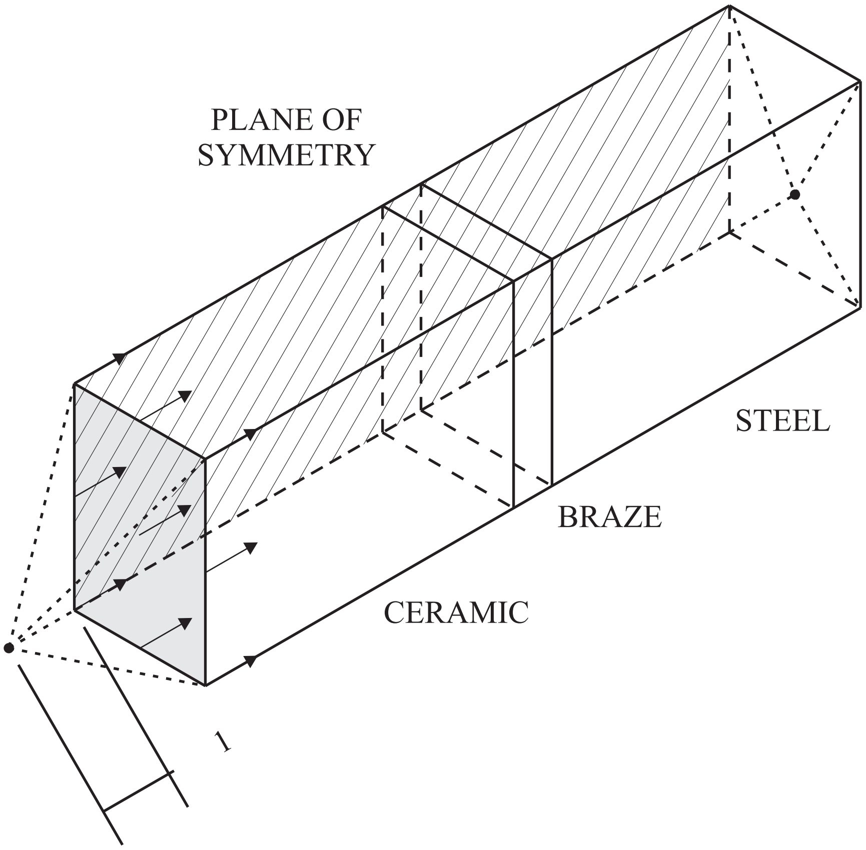

Figure 5.11: The kinematic couplings (dimensions are in millimeters).

boundary conditions were imposed at the virtual nodes while symmetry conditions were applied on the nodes lying on the symmetry plane. To simulate bending opposite rotations were applied at the virtual nodes and the bending moment was measured as the reaction moment at a virtual node.

5.5.2 Metric of Failure

The bend test results show that the joints always break in the ceramic joining partner at a small distance from the interface. Therefore, to compare the different joint layouts and to check the agreement between experimental and numerical results, a metric of failure for the ceramic material is required. Ceramics are brittle materials and the composite Si_3N_4/TiN is no exception. Thus in the present work three different metrics of brittle failure were applied to the results of the finite element modelling: maximum tensile stress, elastic strain energy and failure probability.

Maximum tensile stress

The simplest fracture criterion for brittle materials, associated to the names of Galileo, Rankine and Navier [27] assumes that a material breaks in tension or compression when the maximum or minimum principal stress reaches a critical value, with the limit in tension much lower in absolute value than that in compression. The main advantage of this criterion derives from its simplicity; moreover, principal stresses are one of the default outputs in every finite element commercial code.

Elastic strain energy

The maximum tensile residual stress has frequently been used as strength metric. However, this criterion has some severe limitations both from the theoretical point of view (e.g. the maximum value of a certain component of residual stresses alone cannot explain fracture) and in numerical applications since the presence of the high stress gradients can affect the results of FE calculations. These problems were addressed first in [12] and then in [91] by using the total strain energy in the ceramic as a metric for failure. According to the authors the advantages of this approach are a lower dependency on the mesh formulation and rapid convergence of strain energy. The strain energy in the ceramic was calculated by multiplying the strain energy density magnitude at each Gauss point g by the associated volume V_g:

$$U = \sum_g \frac{1}{2}\sigma_{ij}\varepsilon_{ij}V_g \tag{5.17}$$

Failure probability

The most commonly used approach for the treatment of the statistics of brittle failure is Weibull's, which is based on two main assumptions (for an extended description of the application of Weibull's theory to ceramics refer to [115]):

1. a weakest link argument: the material is homogeneous in the sense of the distribution of flaws throughout the volume and failure at any flaw leads to total failure;
2. a distribution function: it characterizes the stress dependence of the cumulative failure probability per unit volume at the limit of an infinitesimal volume.

These assumptions lead to the following expression for the survival probability:

$$P_s = e^{-\int_V \left(\frac{\sigma-\sigma_u}{\sigma_0}\right)^m dV} \tag{5.18}$$

Note that V must be nondimensional so it should be expressed as V/V_0 where V_0 is some chosen unit volume. The three constants m, σ_u and σ_0 are generally treated as empirical parameters and determined experimentally. The parameter σ_u is the stress level below which there is zero probability of failure. For ceramics the remote possibility exists of having a very large flaw in a specimen so that the safest assumption is to take $\sigma_u = 0$ as it is usually done. Weibull's approach allows the treatment to be extended to situations where stress varies with position in the specimen such as four point bend tests at quarter points; in this case the failure probability assumes the form:

$$P_f = 1 - e^{-\left(\frac{\sigma_{4b}}{\sigma_0}\right)^m \frac{V(m+2)}{4(m+1)^2}} \tag{5.19}$$

where σ_{4b} has the following expression:

$$\sigma_{4b} = \frac{\sigma_0}{V^{\frac{1}{m}}} \left(\frac{4\,(m+1)^2}{m+2}\right)^{\frac{1}{m}} \Gamma\left(1+\frac{1}{m}\right) \tag{5.20}$$

where $\Gamma\,(x)$ is the Gamma function.

Weibull parameters for the composite Si_3N_4/TiN, used in the present work were determined in 4-point bending (with the same setup used for the joints) during the already cited precedent project at EMPA, but the results were not included in the relative publication [13]. The obtained values for m and σ_0 are 14.8 and 810.8 MPa, respectively (for a chosen unit volume V_0 of 1 mm^3).

In [31] Weibull's approach is generalized to multiaxial stress states and the failure probability depends on the values of the three principal stresses:

$$P_f = 1 - e^{-\int_V \left(\left(\frac{\sigma_I}{\sigma_0}\right)^m + \left(\frac{\sigma_{II}}{\sigma_0}\right)^m + \left(\frac{\sigma_{III}}{\sigma_0}\right)^m\right) dV} \tag{5.21}$$

where σ_I, σ_{II} and σ_{III} are the positive principal stresses or are assigned the zero value in case the principal stresses are compressive.

Since in the case of the joints it is not possible to determine an analytical expression for the stress state it is not possible to assess the specific values of Weibull parameters, thus the values obtained from bend tests on the bulk ceramic material were adopted. As a consequence P_f calculated according to (5.21) loses its meaning of absolute probability of failure. Nevertheless it can be interpreted as a relative indicator of the stress state and can be used to compare different braze configurations. The value of P_f of the whole ceramic joining partner was calculated by extracting the values of the principal stresses and of the associated volume at each Gauss point:

$$P_f = 1 - e^{-\sum_g \left(\left(\frac{\sigma_I}{\sigma_0}\right)^m + \left(\frac{\sigma_{II}}{\sigma_0}\right)^m + \left(\frac{\sigma_{III}}{\sigma_0}\right)^m\right) V_g} \tag{5.22}$$

5.5.3 Residual Stress Predictions

This section focuses on the results of the first step of the simulations, the cooling, and especially on the two assemblies on which XRD measurements were carried out: a joint brazed with Incusil™ABA® and another with Incusil™ABA®-27 vol.% SiC. Models were developed for all the joints which were tested in 4-point bending:

- 35 µm thick Incusil™ABA® braze;
- 320 µm thick Incusil™ABA®-9 vol.% SiC braze;
- 320 µm thick Incusil™ABA®-18 vol.% SiC braze;
- 400 µm thick Incusil™ABA®-27 vol.% SiC braze.

In all the cases the residual stresses after cooling are higher in the corner regions of the ceramic at a small distance (about 100 µm) from the interface and not at the interface itself (Figure 5.12). This effect is due to the specimen geometry (the edge is responsible for this concentration effect) and is beneficial from the point of view of the interpretation of the simulation results since maximum stresses are recorded in elements which are sufficiently far from the interface (according to [117] the results obtained within the two elements closest to the singularity are not valid and in the present case the maximum is found at six elements from the interface). These considerations led to the conclusion that for the present geometry the influence of the stress concentration at the interface on the failure metrics based on single stress values is negligible.

Figures 5.13, 5.14 and 5.15 show the plots of the three chosen failure metrics against temperature during cooling for the four considered joints. These diagrams lead to some remarks on the differences between the joint assemblies and on the significance of the failure metrics:

- the values of all the failure metrics exhibit a significant increase between 450 ℃ and 300 ℃, as expected, since in this range of temperature there is the largest increase in the flow stresses of the filler metals.
- The plots of the maximum principal stress and of the failure probability for the joint with Incusil™ABA®-18 vol.% SiC and Incusil™ABA®-27 vol.% SiC highlight that these two systems exhibit a decrease in the peak values of residual stresses during the last stage of the cooling process. This is due to the redistribution of stress which derives from the development of plastic strain also in the core the braze. Such an effect has to be evaluated carefully since it directly depends on the filler metal properties: Incusil™ABA®-18 vol.% SiC and especially Incusil™ABA®-27 vol.% SiC were assumed to have a limited ultimate strain (as stated in section 4.4.2, homogenization was carried out up to the maximum strain obtained in the tensile tests) while in the case of the joint they could have a larger one.

- The joint with Incusil™ABA® exhibits the lowest residual maximum principal stress after cooling, about 438 MPa, and the joint with Incusil™ABA®-9 vol.% SiC the highest, 474 MPa.

- The results obtained with the failure metric based on the maximum principal stress and on the failure probability are equivalent with the latter being a sort of amplification of the former; this derives from the fact that in the region where residual stresses are higher the stress state is almost uniaxial. Thus the mid and the minimum principal stress have almost no influence on the result of (5.21).

- The results provided by the strain energy failure metric are not in agreement with those obtained with the other approaches: Figure 5.15 shows that in the case of the joint with Incusil™ABA® the amount of elastic strain energy stored in the ceramic after cooling is much larger than for the other joints. This is confirmed by the contour plots of the strain energy density for the Incusil™ABA® and Incusil™ABA®-27 vol.% SiC joints (Figures 5.16 and 5.17), which show that in the first specimen the strain energy in the core region is higher than in the second. However, this difference in the strain energy is mainly due to the higher compressive stresses in the region for Incusil™ABA® (the contour plots of the minimum principal stress in the two cases are reported Figures 5.18 and 5.19). This remark leads to conclude that the failure criterion based on strain energy can be misleading since it assumes that compressive and tensile stress states have the same influence on the failure of the ceramic material.

The data by XRD were not compared directly with finite element results for the corresponding locations but rather with the average stress component which was computed by accounting for the average illuminated area, which varies as a function of the tilt angle (as described in section 5.1.3). Figures 5.20 to 5.23 summarize the results. As already stated in section 5.1.3 the experimental uncertainty is compatible with analogous results reported in literature [66, 85]. It can be seen that there is a good agreement between experimental data and numerical estimations for both Incusil™ABA® joints (Figures 5.20 and 5.21) and for one Incusil™ABA®-27 vol.% SiC specimen, LC060609_3, while for the other, LC060609_4, numerical and experimental results are quite far, with the latter exhibiting an increase of stresses far from the interface, a trend which is opposite to the expected one. This anomaly suggests the presence of a defect, possibly a not perfect interface between ceramic and braze which could have caused some stress relief at the local level.

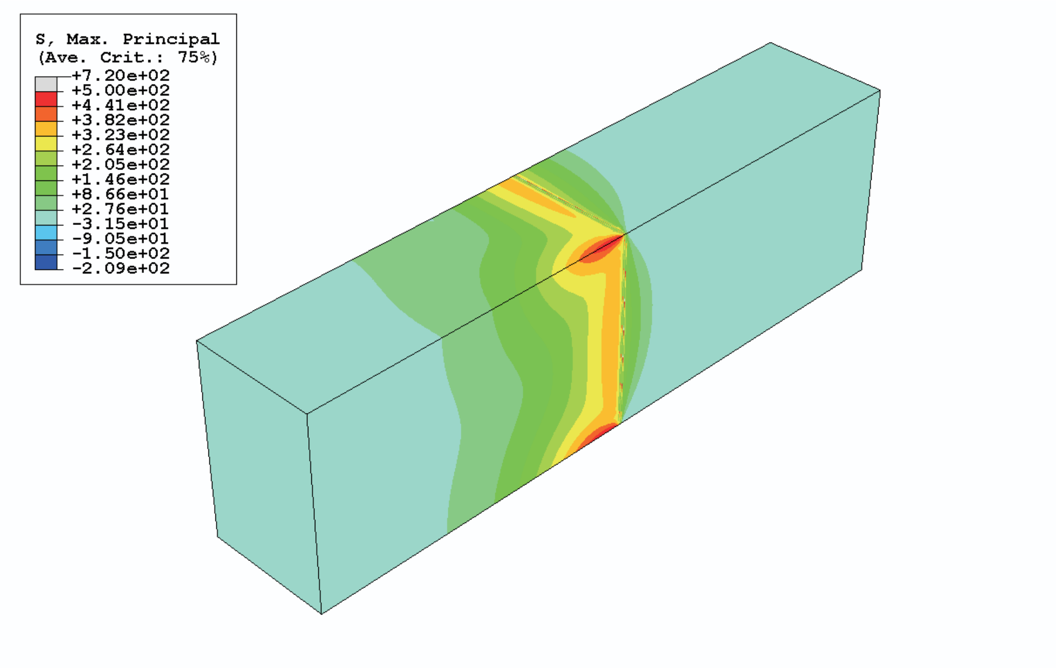

Figure 5.12: Maximum principal stress distribution after cooling: stresses are higher along the ceramic edges at a small distance from the interface with the braze (units: MPa).

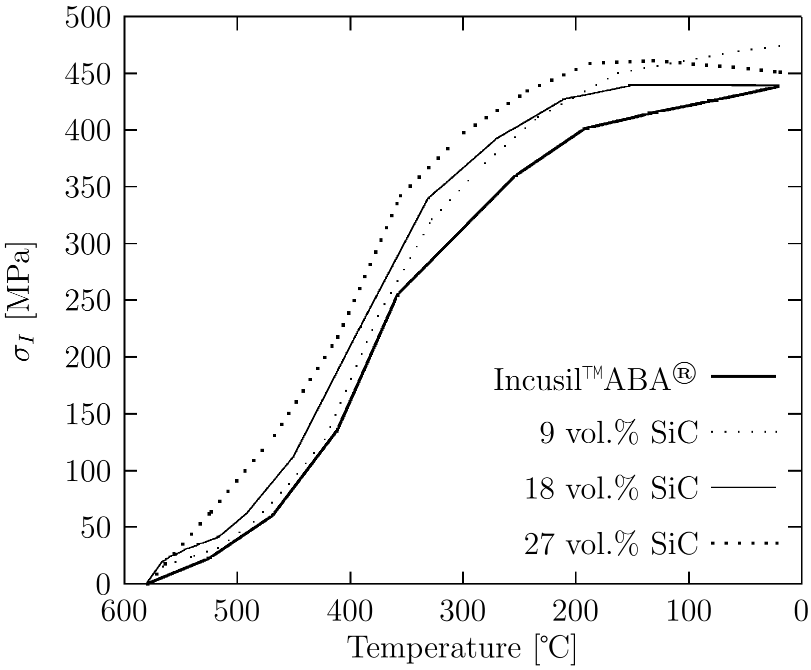

Figure 5.13: Evolution of the volume maximum principal stress in the ceramic during cooling.

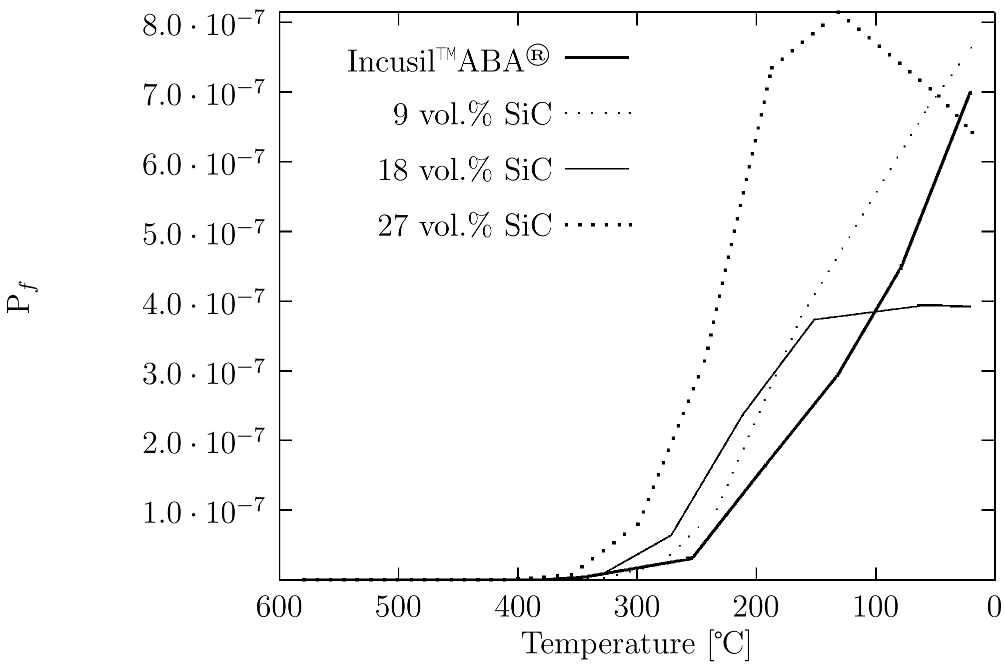

Figure 5.14: Evolution of the failure probability (5.21) of the ceramic joining partner during cooling.

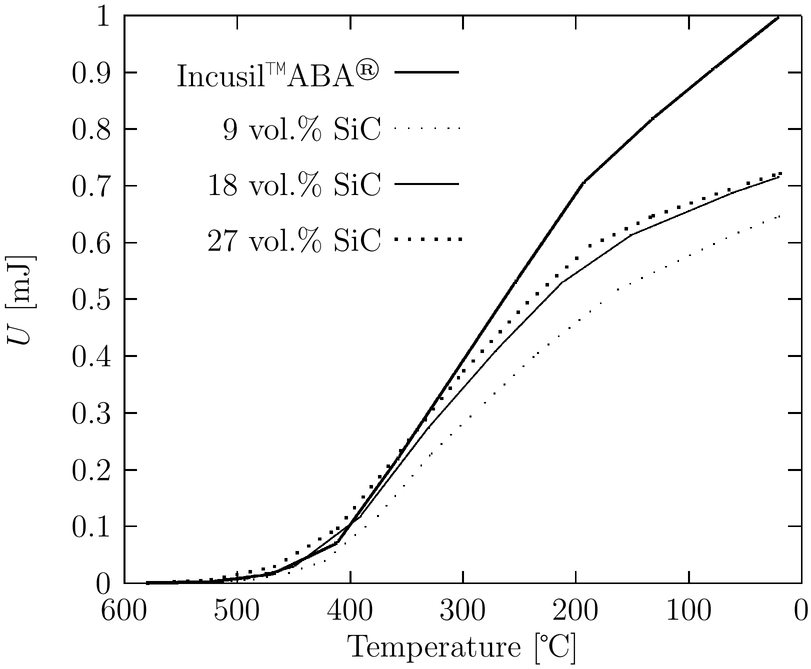

Figure 5.15: Evolution of the strain energy in the ceramic during cooling.

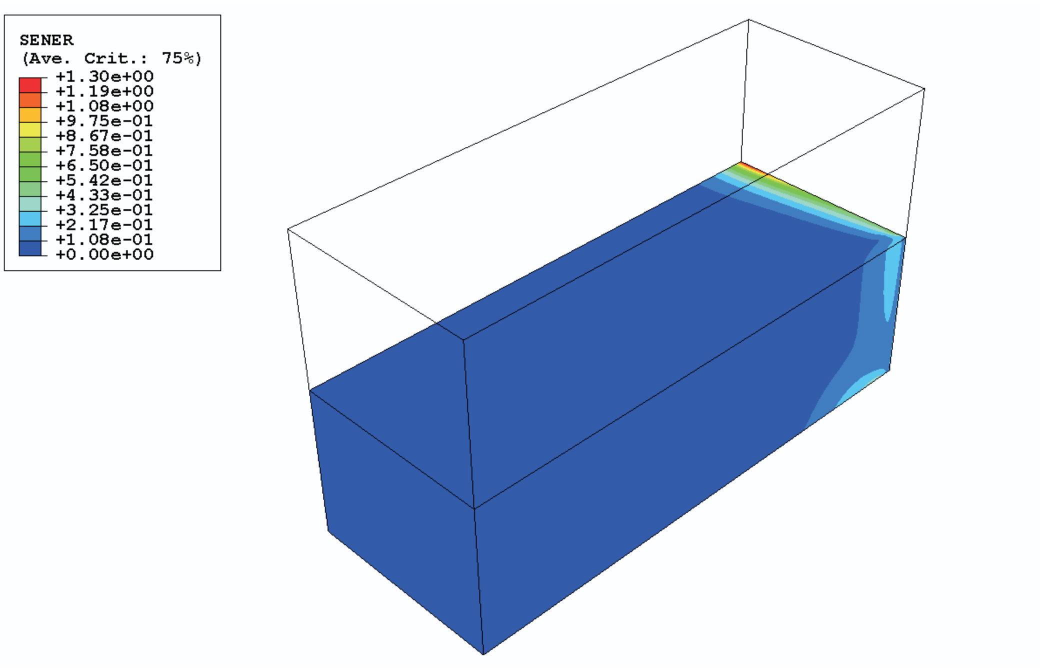

Figure 5.16: Strain energy density distribution after cooling inside the ceramic joining partner in the Incusil™ABA® specimen (units: mJ).

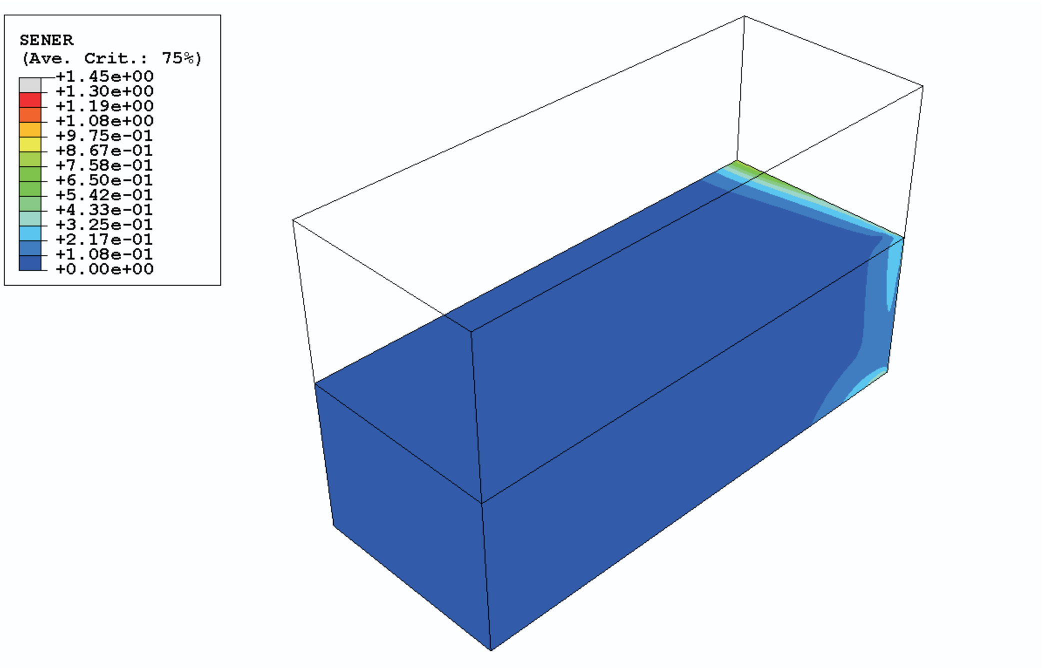

Figure 5.17: Strain energy density distribution after cooling inside the ceramic joining partner in the Incusil™ABA®-27 vol.% SiC specimen (units: mJ).

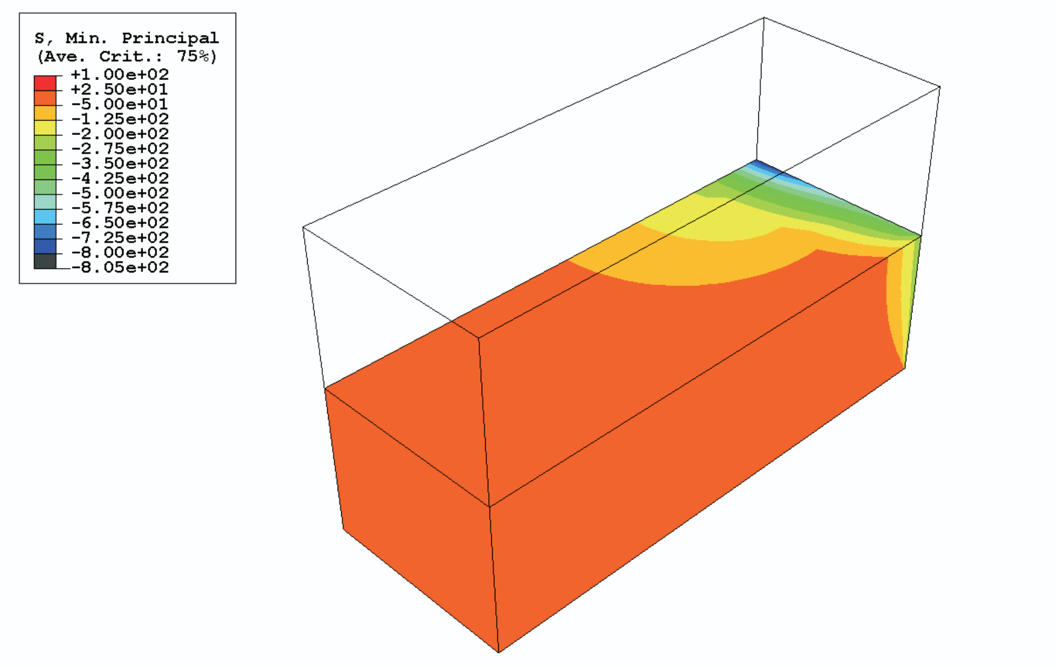

Figure 5.18: Minimum principal stress distribution after cooling inside the ceramic joining partner in the Incusil™ABA® specimen (units: MPa).

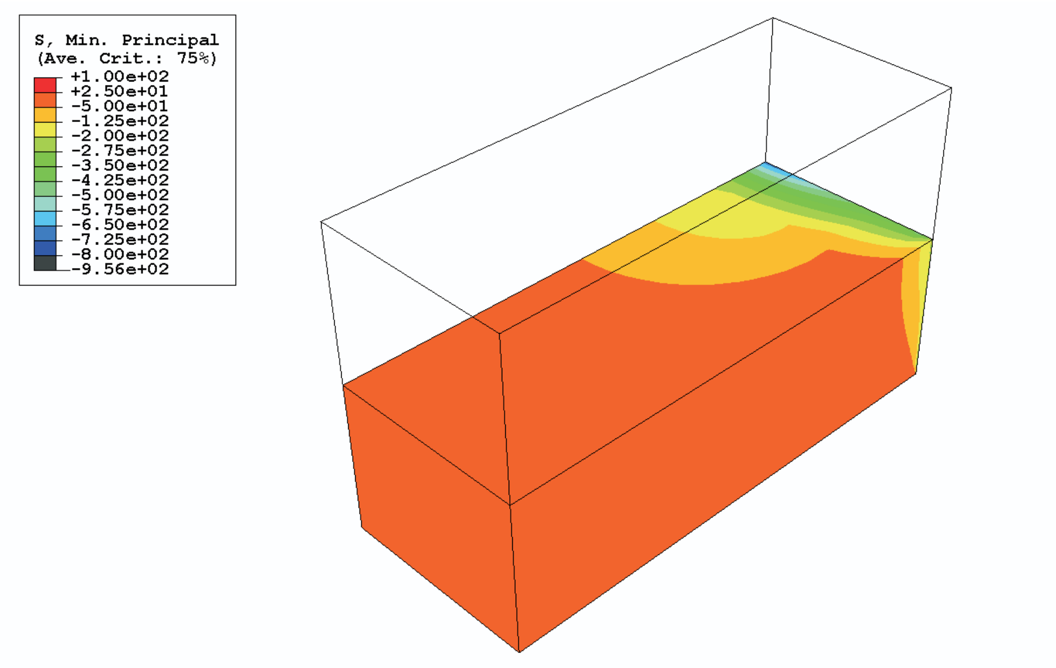

Figure 5.19: Minimum principal stress distribution after cooling inside the ceramic joining partner in the Incusil™ABA®-27 vol.% SiC specimen (units: MPa).

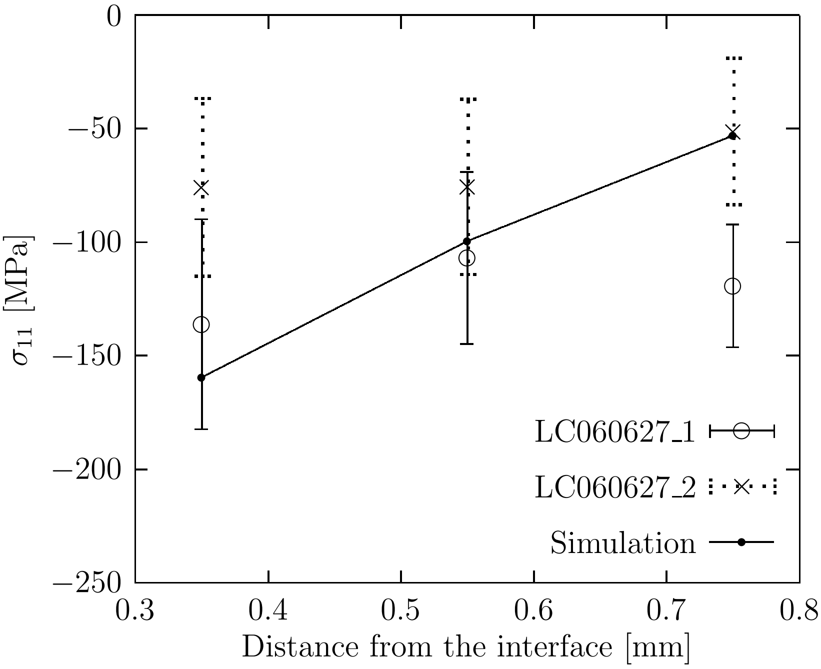

Figure 5.20: Comparison between XRD measurements at points 1 to 3 (along the specimen axis) and numerical results for the two joints brazed with Incusil™ABA®.

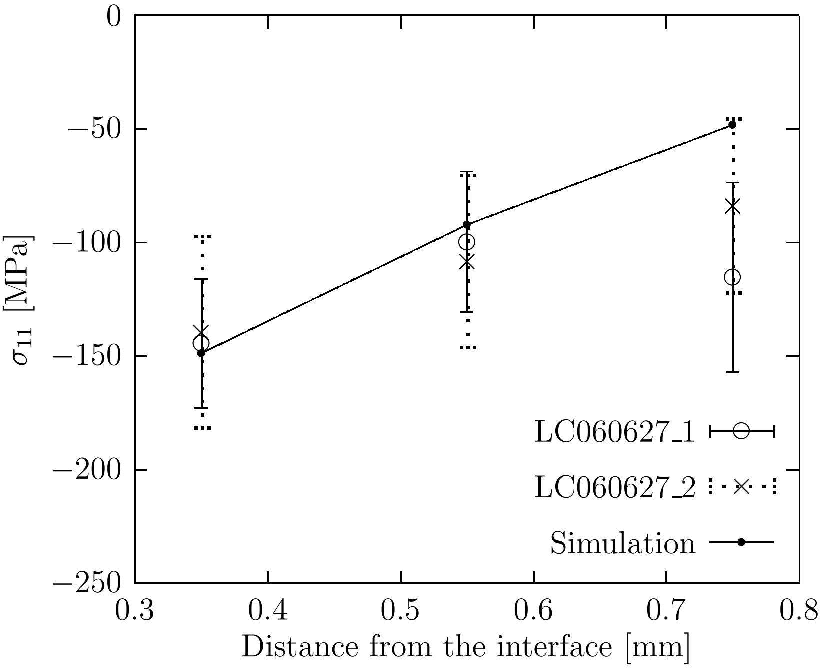

Figure 5.21: Comparison between XRD measurements at points 4 to 6 (200 µm from the specimen axis) and numerical results for the two joints brazed with Incusil™ABA®.

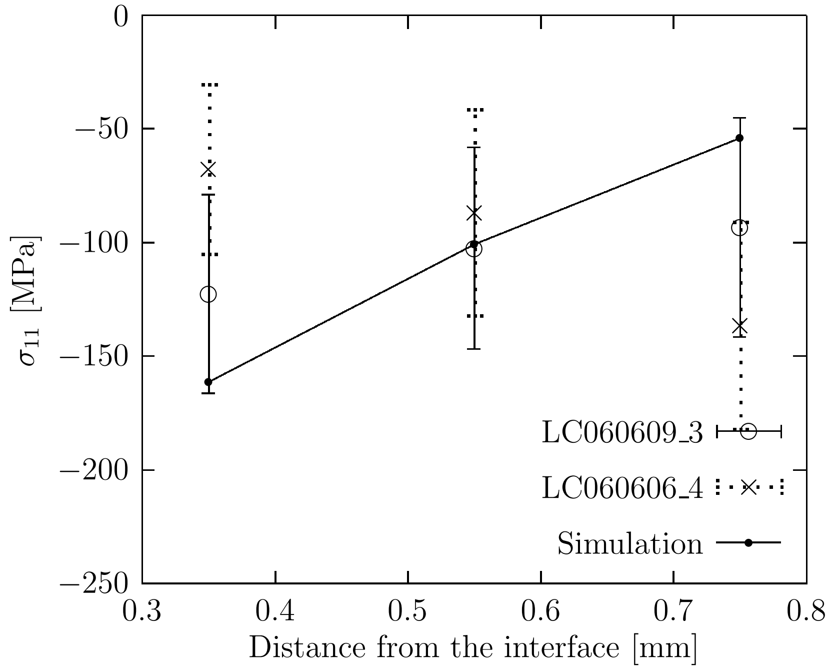

Figure 5.22: Comparison between XRD measurements at points 1 to 3 (along the specimen axis) and numerical results for the two joints brazed with Incusil™ABA®-27 vol.% SiC.

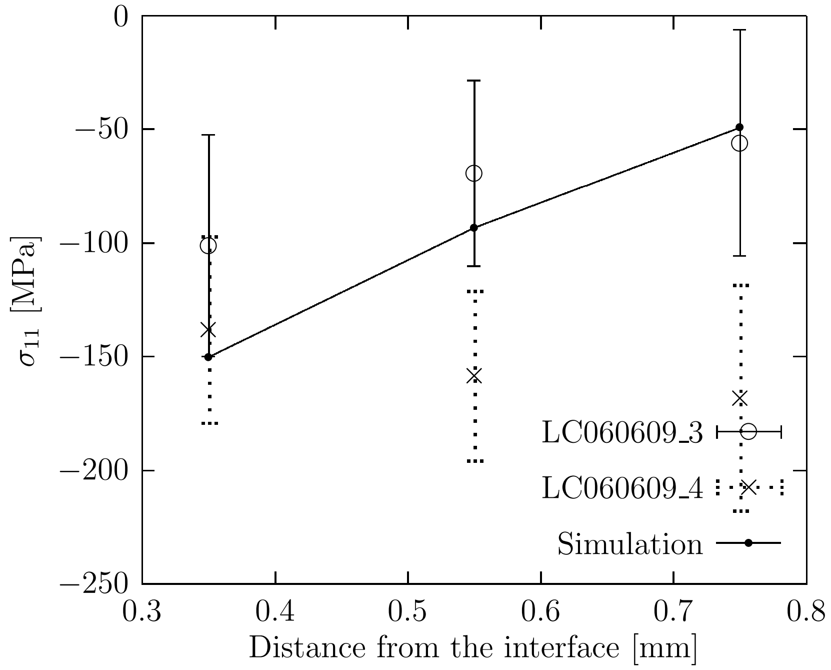

Figure 5.23: Comparison between XRD measurements at points 4 to 6 (200 µm from the specimen axis) and numerical results for the two joints brazed with Incusil™ABA®-27 vol.% SiC.

5.5.4 Simulation of 4-Point Bend Tests

The simulation of the 4-point bend test followed that of the cooling, as described in section 5.5.1. Figure 5.24 shows the distribution of the maximum principal stress in the ceramic during bending: it can be observed that the region where stresses are higher is again around the edge at a short distance from the interface (of course on the tensile side), which is in agreement with fracture observations (section 5.2). Furthermore, far from the braze the stress distribution is linear along the thickness of the specimen, as predicted by beam theory, with the maximum principal stress coinciding with the stress component normal to the joining partner section (this is confirmed by the contour plot of the longitudinal stress 5.25).

In Figures 5.26 to 5.29 the results of the simulations are reported along with those of the mechanical tests for each of the considered systems: for each simulation the maximum principal stress in the ceramic is plotted against the nominal applied stress and compared with an experimental point having as abscissa the nominal bend strength (with the relative standard deviation) and as ordinate the bend strength of the composite Si_3N_4/TiN (with the standard deviation, as well). It can be observed that in the case of Incusil™ABA® experiments and simulations are in good agreement while for the other joint layouts the simulations tend to underestimate the stress level. Provided that the assumption of a maximum principal stress failure criterion is acceptable, this discrepancy might be due to an underestimation of the composite fillers hardening (as already mentioned in section 5.5.3): during bending additional plastic strain is developed in the braze region and larger areas reach the equivalent plastic strain value beyond which the stress-strain curve flattens. The difference in the structural behaviour between the joint with Incusil™ABA® and those with the composite fillers is confirmed by Figure 5.30 where the plots of the maximum principal stress in the ceramic against the nominal applied stress are compared for the four joints: the behaviour of the joint with Incusil™ABA® is linear while the others exhibit a decreasing stiffness as the applied load increases.

The other two failure metrics were assessed for the bending simulations as well: the failure probability criterion proved to be also in this case an amplification of that based on the maximum principal stress (as shown in Figure 5.31) while Figure 5.32 shows that the criterion based on the strain energy does not yield significant results in describing the joints in bending: since the total strain energy is considered, the responses of the different joints tend to be similar (furthermore note that only the strain energy of the modelled portion of ceramic joining partner was considered).

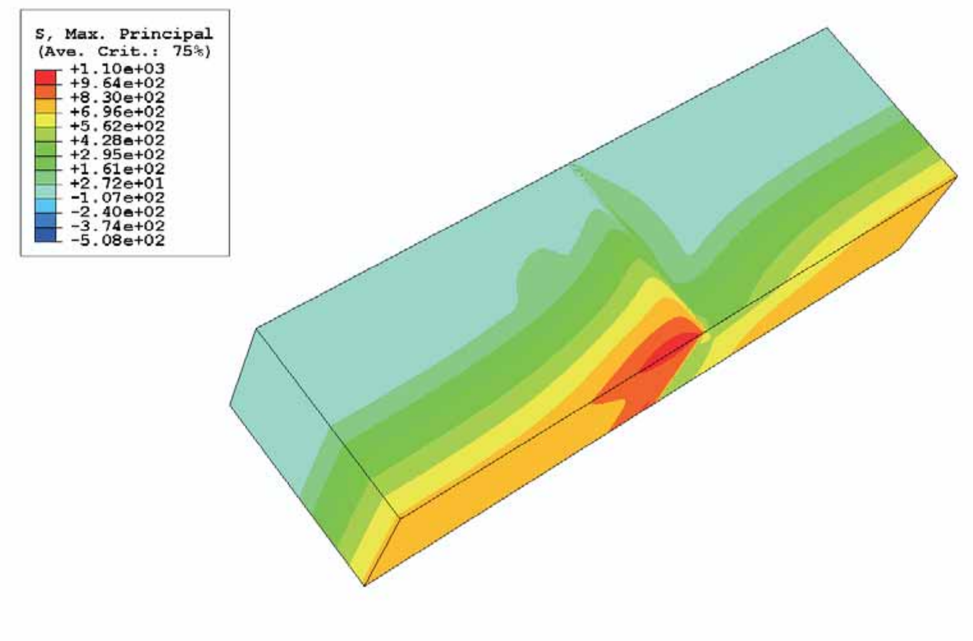

Figure 5.24: Maximum principal stress distribution in the Incusil™ABA® joint under an applied moment of about 2 Nm: stresses are higher along the ceramic edges at a small distance from the interface with the braze (units: MPa).

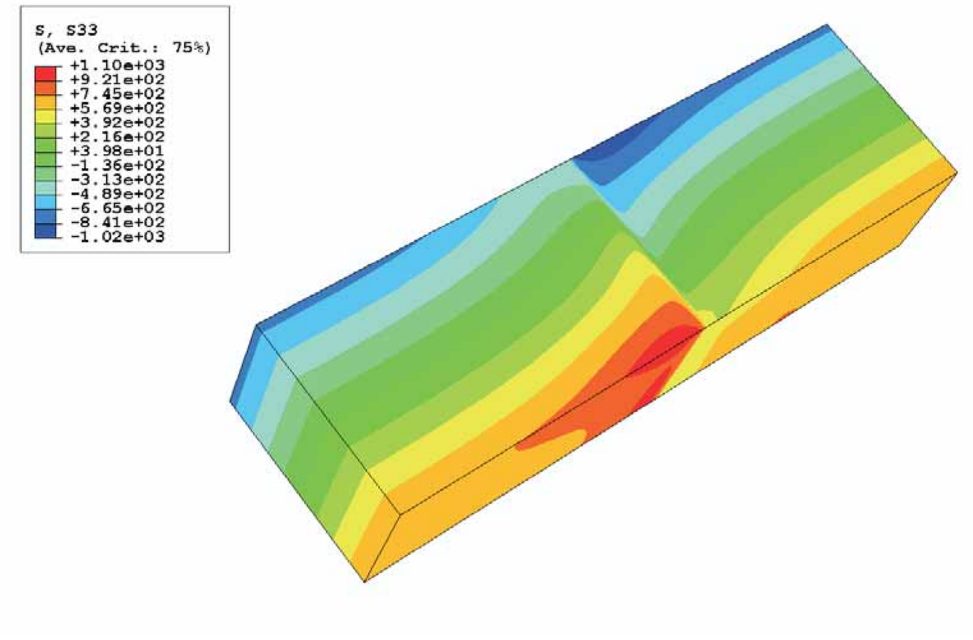

Figure 5.25: Longitudinal stress distribution in the Incusil™ABA® joint under an applied moment of about 2 Nm: far from the interface stresses evolve linearly along the joint thickness as predicted by beam theory (units: MPa).

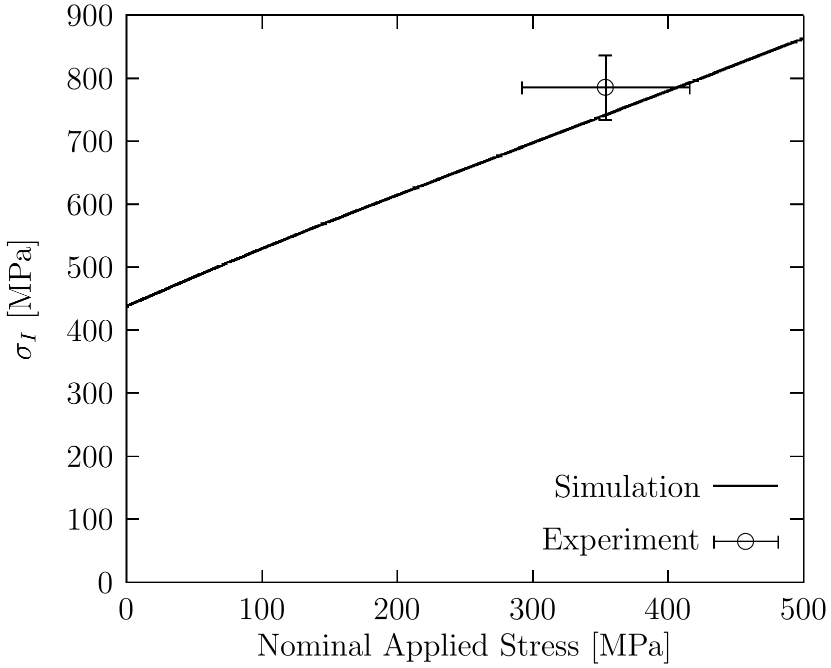

Figure 5.26: Four point bend test: comparison between simulations and experiments for joints with Incusil™ABA®.

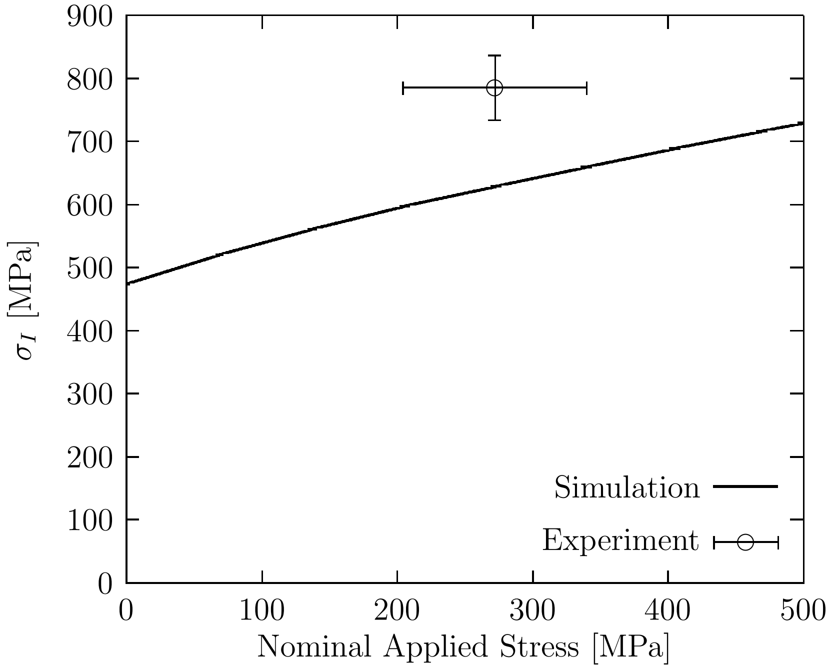

Figure 5.27: Four point bend test: comparison between simulations and experiments for joints with Incusil™ABA®-9 vol.% SiC.

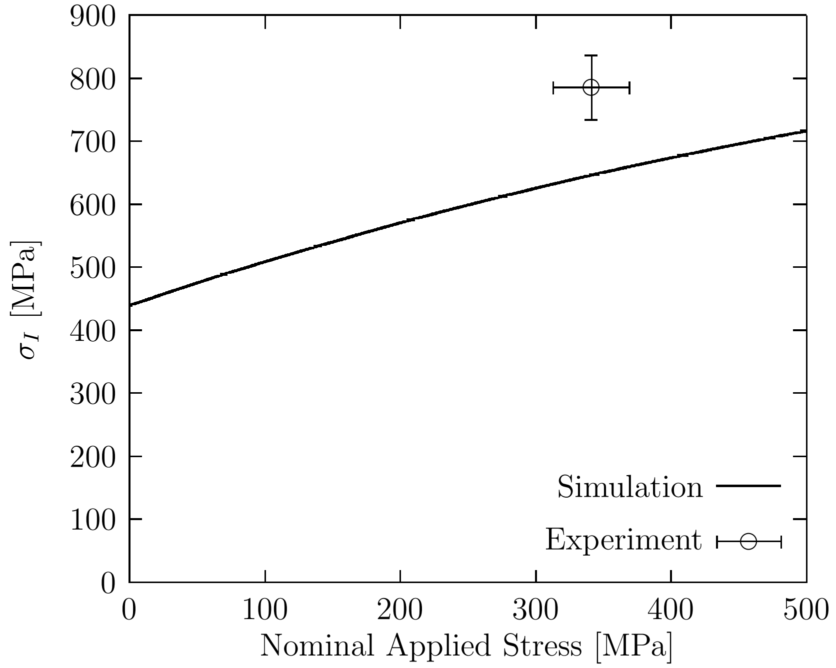

Figure 5.28: Four point bend test: comparison between simulations and experiments for joints with Incusil™ABA®-18 vol.% SiC.

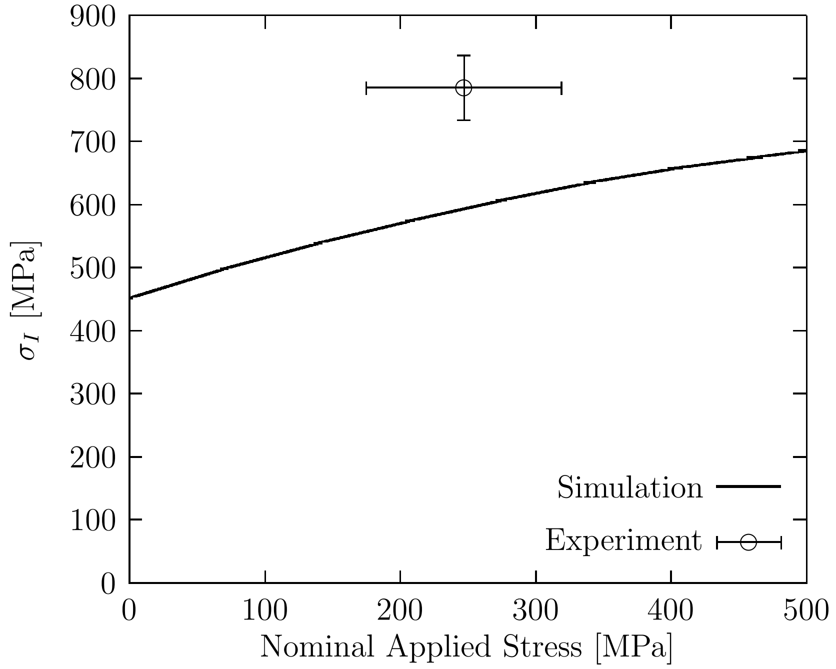

Figure 5.29: Four point bend test: comparison between simulations and experiments for joints with Incusil™ABA®-27 vol.% SiC.

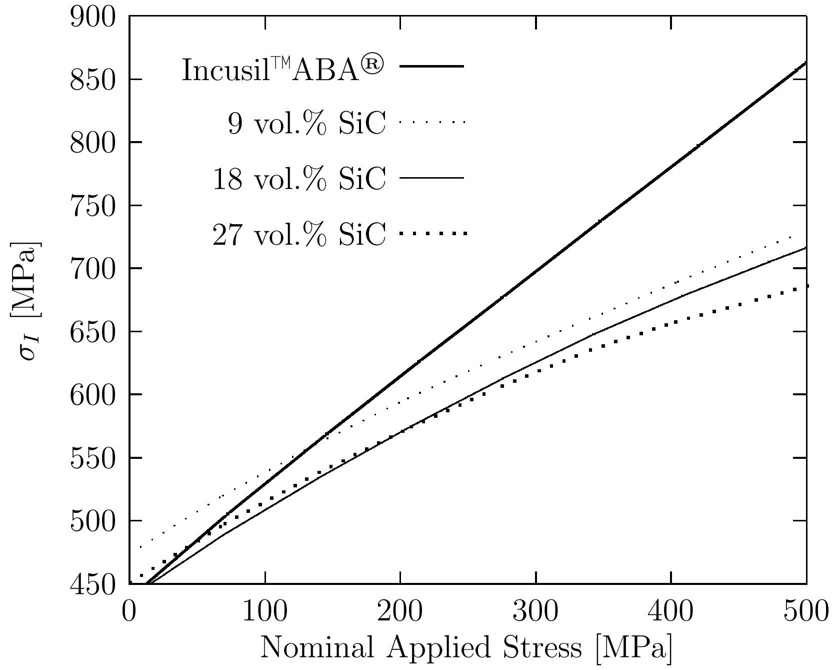

Figure 5.30: Evolution of the volume maximum principal stress in the ceramic during the bend test.

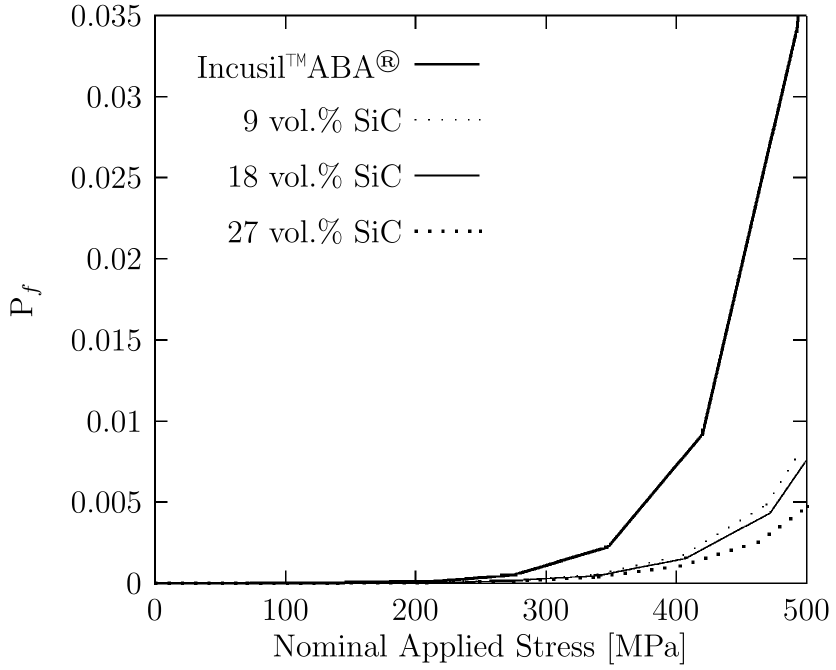

Figure 5.31: Evolution of the failure probability (5.21) of the ceramic joining partner during the bend test.

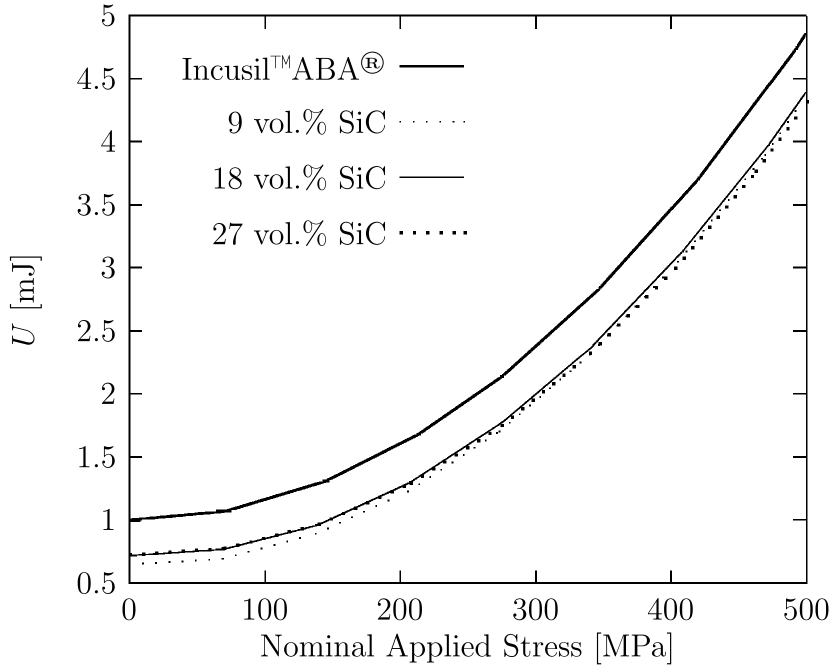

Figure 5.32: Evolution of the strain energy in the ceramic during the bend test.

5.6 Parametric Study

The experiments and the simulations show that the development of plastic strain in the braze is a determinant factor in the development of residual stresses. However, in the choice of the brazing alloy for a ceramic metal assembly, the importance of the plastic properties of the filler alloy has traditionally been put in second order, in favour of other parameters such as the brazing temperature, the brazing gap or the coefficient of thermal expansion. To study the role and the weight of each of these parameters, a parametric finite element model for the prediction for residual stresses was developed.

5.6.1 Parametric Model

In this section the finite element model will be described by following the same order adopted for the bend specimen model. The model was implemented in ABAQUS® by means of a Python script.

Geometry and Mesh

Given the large number of simulations involved in a parametric study, a three dimensional model would be too demanding in terms of computation time. Therefore an axisymmetric

material	E[GPa]	ν	CTE[℃$^{-1}$]
Al_2O_3	150	0.22	$8.2 \cdot 10^{-6}$
WC	627	0.2	$5.1 \cdot 10^{-6}$
Si_3N_4/TiN	330	0.26	$3.79 \cdot 10^{-6}$
Steel	210	0.3	$1.41 \cdot 10^{-5}$
Kovar®	138	0.317	$6.15 \cdot 10^{-6}$

Table 5.7: Thermomechanical properties of the joining partners considered in the parametric model.

model was implemented: the total length of the joint was imposed to be 50 mm and the radius 2.5 mm (a solid visualization of the specimen is shown in Figure 5.33).

The central part of the joint (2.5 mm), including the braze, was meshed finely with 0.0125 mm thick elements, while in the rest of the model the mesh was coarser, with 0.25 mm thick elements. The element size in the radial direction was imposed to be constant, 0.125 mm, corresponding to twenty elements along the radius (Figure 5.34 shows a detail of the mesh). 8-node biquadratic elements with reduced integration were used.

Six different values of the joint thickness were considered: 0.025 mm, 0.05 mm, 0.1 mm, 0.25 mm, 0.5 mm and 1 mm.

Material properties

Five different joining partners were considered: three ceramic materials (alumina, which has a relatively high CTE, tungsten carbide, which has a very high Young's modulus, and the composite Si_3N_4/TiN) and two metal alloys (Kovar®, which has a low CTE, and the same steel considered in the rest of the work). The thermomechanical properties of these materials are summarized in Table 5.7.

The braze filler was assumed to be elastic perfectly plastic: Young's modulus and Poisson's coefficient were assigned the values of 75 GPa and 0.3, constant with temperature, while the yield stress was assumed to decrease linearly with temperature and to reach a minimum value of 10 MPa at 0.75 T_B, where T_B is the brazing temperature.

Three different values for each parameter were considered: 50 MPa, 150 MPa and 250 MPa for the yield stress at room temperature and 700 ℃, 850 ℃ and 1000 ℃ for the brazing temperature. The CTE was assigned four values: $5.0 \cdot 10^{-6}$ ℃$^{-1}$, $1.0 \cdot 10^{-5}$ ℃$^{-1}$, $1.5 \cdot 10^{-5}$ ℃$^{-1}$ and $2.0 \cdot 10^{-5}$ ℃$^{-1}$.

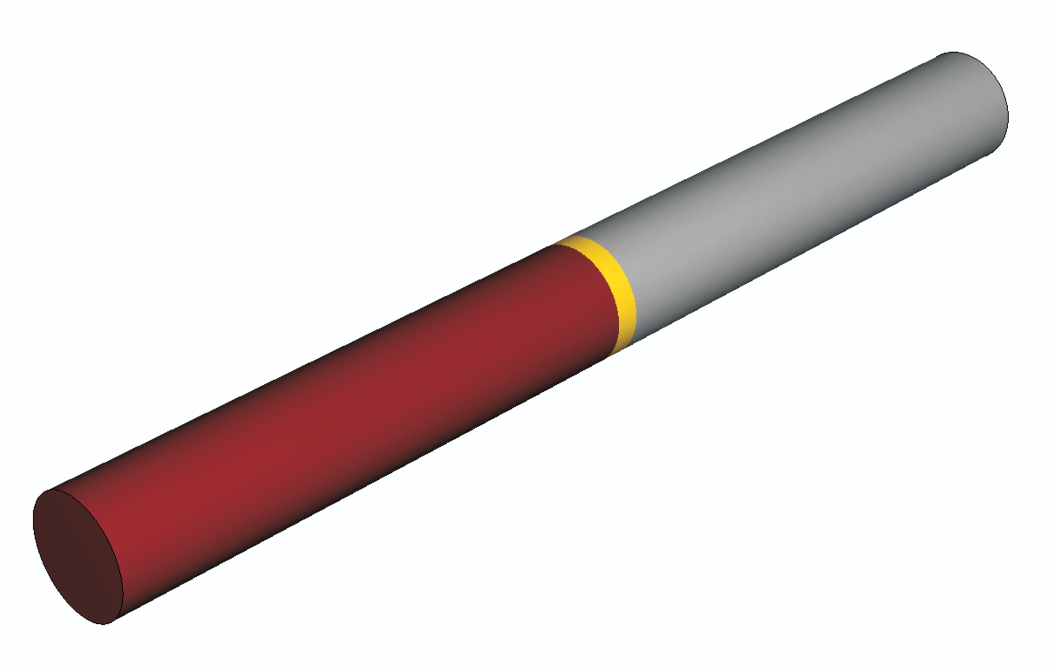

Figure 5.33: Three dimensional visualization of the axisymmetric model used for the parametric study.

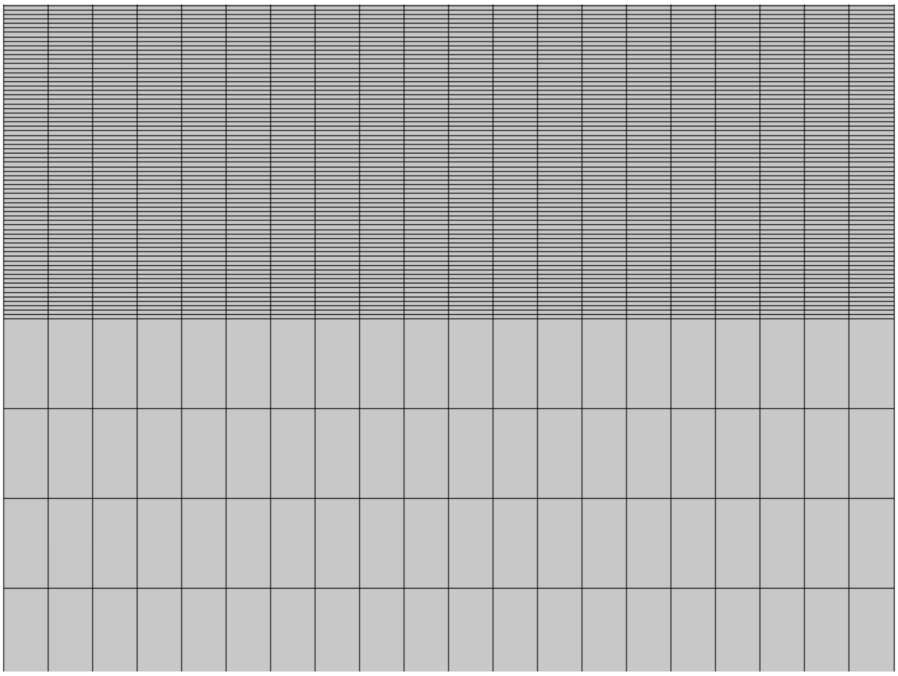

Figure 5.34: Transition between coarse and fine mesh in the axisymmetric model used for the parametric study.

Boundary conditions and loads

Since in the parametric model only the cooling step was considered, isostatic boundary conditions were applied. The specimen was imposed to uniformly cool down to 20 ℃ from 0.75 T_B.

Metric of failure

The study on the beam specimen showed that, among the examined failure metrics, the maximum principal stress is the most appropriate to make comparisons between different braze layouts. Therefore it was chosen for this a parametric study, too. While in the beam specimen the maximum principal stress in the ceramic occurred at a certain distance from the interface (thanks to the edge effect), in the cylindrical joint the highest stress concentration is located at the singular point. To overcome this problem it was chosen to exclude from the region of interest the 300 µm of ceramic closer to the interface with the braze.

5.6.2 Results and discussion

For each of the considered joints 216 simulations were carried out. In the following the results will be presented by considering the influence of each parameter separately and some of the results of the simulations will be reported (for the full set of results refer to appendix A).

Influence of the brazing temperature

In all the considered assemblies it was observed that the brazing temperature had nearly no influence on the residual stresses, as it can be seen in Figure 5.35 for the joint WC-steel: given the yield stress and the CTE of the filler metal, the plots of the maximum principal residual stress against the braze temperature are almost flat. This result is quite important since in the traditional approach a preference is given to alloys with lower brazing temperatures. This approach derives from the fact that residual stresses were estimated by means of simple models based on elasticity, thus they roughly depended on the mismatch between the CTEs of the two joining partners multiplied by the brazing temperature. If plasticity is introduced it can be observed that the difference in the brazing temperature does not lead to higher residual stresses but results in a larger amount of plastic strain in the braze. This can be developed provided the filler metal is sufficiently ductile, as it is always the case for commonly used braze alloys, which often exhibit ultimate strains larger than 0.2.

Influence of filler metal plastic properties

The development of plastic strain in the braze is the mechanism which influences more significantly residual stresses. As a consequence the yield stress of the filler metal is a fundamental parameter. The results of the simulations show that braze fillers with lower yield stresses lead to lower residual stresses both for joints in which the mismatch between the CTEs of the two joining partners is large (as the Si_3N_4/TiN-steel system) and for joints in which the CTEs are similar (as in the case of WC and Kovar®). The results for these two joints are reported in Figure 5.36. In both cases a brazing gap of 0.1 mm and a brazing temperature of 700 ℃ are considered, while the braze filler has a CTE of $2 \cdot 10^{-5}$ ℃$^{-1}$.

Influence of the CTE of the filler metal

As stated previously all the factors which can improve the development of plastic strain in the braze metal will have a positive effect on residual stress relief and this is the case of the CTE, too. Simulations show that in general it is better that the filler metal has a CTE higher than those of the base metals (as it is often the case with conventional filler alloys) while the worst effects are obtained when the CTE has an intermediate value. This result is explained by the fact that the development of plastic strain is proportional to the CTE mismatch not only between the ceramic and the metal but also between the filler alloy and each of the joining partners. Figure 5.37 shows the results for the two joints Si_3N_4/TiN-steel and Al_2O_3-steel. The brazing gap is 0.1 mm, the brazing temperature 700 ℃ and the yield stress of the braze material 150 MPa: in all cases the lowest residual stresses are obtained with the highest CTE for the filler. These results are remarkable since they confirm that reducing the CTE of the braze metal does not lead in general to an increase of the joint performance. As stated in Chapter 1 some successful attempts in this direction are present in literature (e.g. in [128, 129] it is reported that when the braze metal in an Al_2O_3-steel is reinforced with carbon fibers a higher joint strength is obtained). In all these cases the improvement in the joint performance is not to be attributed to the CTE reduction but to some other effect.

Influence of the brazing gap

The brazing gap is the only geometrical parameter which was considered in this study. By changing its value it is possible to influence the structural behaviour of the braze layer which can vary from that of an interlayer to that of a three dimensional body. Simulations show that small brazing gaps (typically less than 100 µm) in most cases lead to lower residual stress: the braze filler is subject to a larger shear deformation which leads to large plastic strains. As a consequence small brazing gaps are recommendable in most cases. However, when the difference between the CTEs of the two joining partners is less

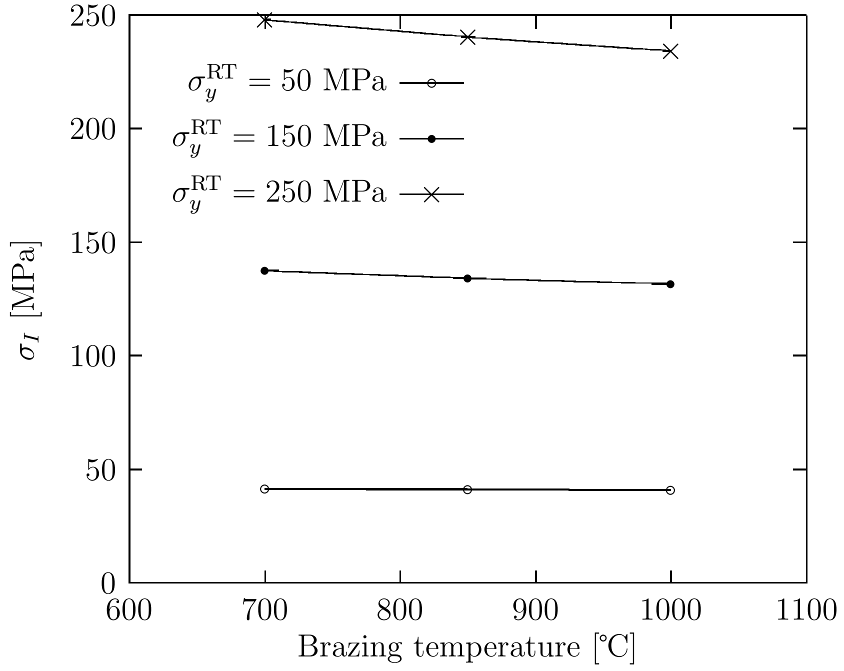

Figure 5.35: Evolution of the maximum principal stress in the ceramic as a function of the brazing temperature for the joint WC-steel (the CTE of the filler metal is $2 \cdot 10^{-5}$ ℃$^{-1}$).

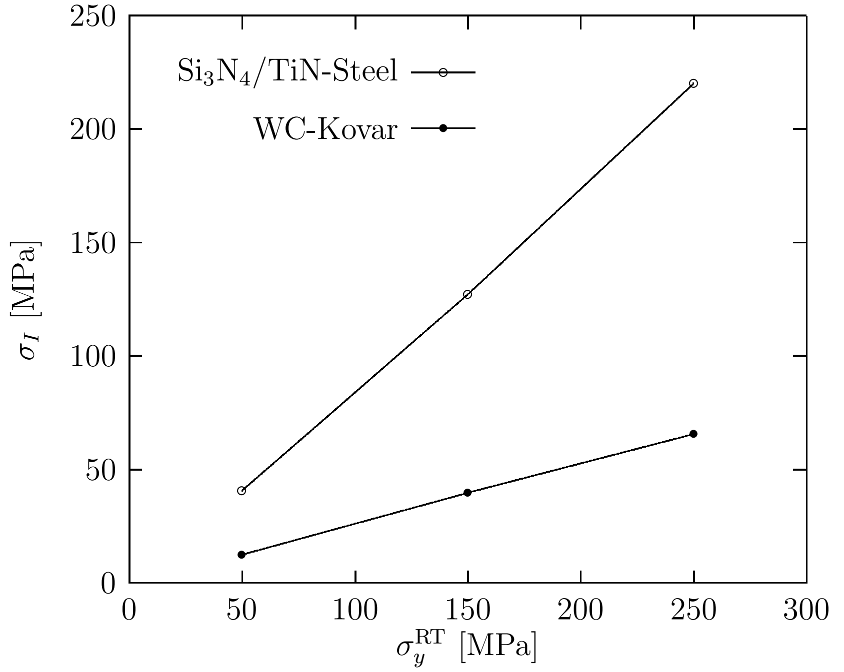

Figure 5.36: Evolution of the maximum principal stress in the ceramic as a function of the filler metal yield stress (the CTE of the filler metal is $2 \cdot 10^{-5}$ ℃$^{-1}$).

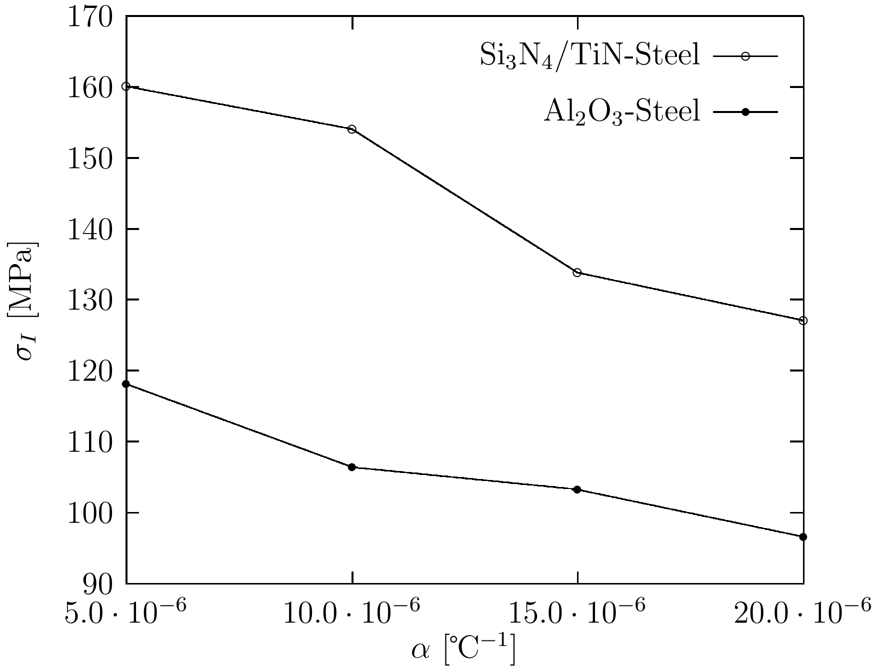

Figure 5.37: Evolution of the maximum principal stress in the ceramic as a function of the filler metal CTE.

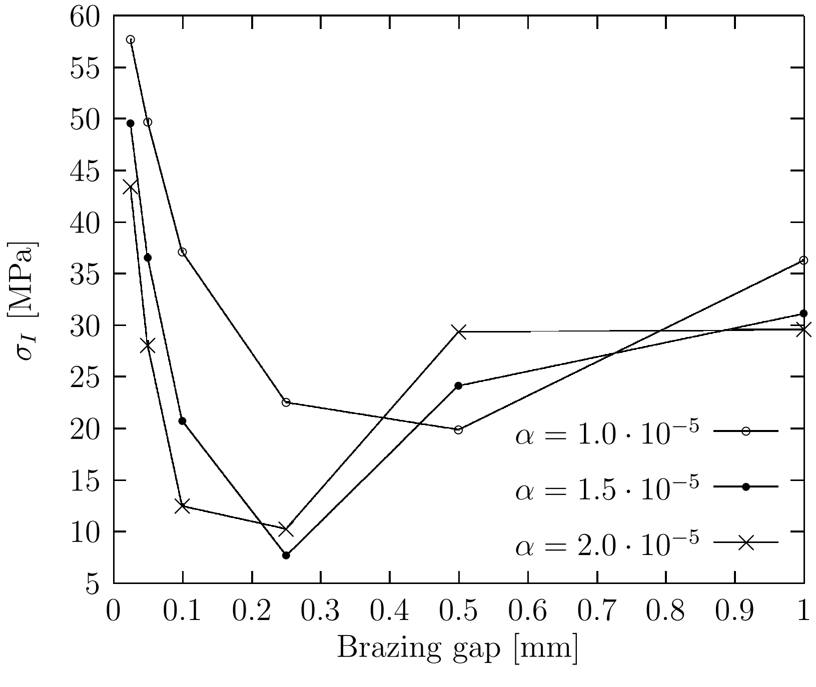

Figure 5.38: Evolution of the maximum principal stress in the ceramic as a function of the brazing gap (the brazing temperature is 700 °C and the yield stress of the filler metal 50 MPa).

important (Si_3N_4/TiN-Kovar®, WC-Kovar® and Al_2O_3-steel) larger brazing gaps can be beneficial, probably because in these cases the thermal stresses related to the elastic strain of the braze filler play a non negligible role. Therefore having a larger amount of a material with a lower Young's modulus in the joint can improve residual stress relief. The case of the WC-Kovar® joint is reported in Figure 5.38.

Chapter 6

Summary, Conclusions and Perspectives

Residual stresses play a major role in determining the strength of ceramic-metal joints, thus predicting and controlling them is of vital importance. The most important factor affecting the residual stress state is represented by the thermomechanical properties of the filler. To study how variations of the properties of the braze alloy influence residual stresses, an active brazing filler metal, Incusil™ABA®, was modified by adding SiC particles and was used to join a ceramic composite, Si_3N_4/TiN, to steel. By reinforcing the filler, interlayers with tailored thicknesses can be formed thus it is possible to study the role of the brazing gap, too.

One first result which was achieved during this work is the development of procedures for the production and testing of both joints and bulk active filler specimens. Then the bulk specimens were tested in tension while the joints in bending. The residual strain in the ceramic was measured by XRD.

At the same time much effort was produced on the modelling side: a homogenization model was developed for the characterization of the composite fillers while pertinent finite element models accompanied and guided the experiments on the joints.

The composite Incusil™ABA®-SiC can be considered a metal matrix composite reinforced with randomly arranged particles. There is a vast amount of literature which deals with the characterization of the mechanical behaviour of MMCs: many models were developed which consider different geometries and constitutive laws of the reinforcement (fibres, whiskers or particles, rigid, elastic or elastoplastic). In this work a novel technique to generate three dimensional microstructural models for the homogenization of the mechanical properties of particle reinforced composites was developed. Particles were created in an already existent tetrahedral mesh, obtained by means of the CDT. Thus models for materials with different compositions can be developed from the same mesh without the need to draw and mesh the model geometry for each of the considered reinforcement volume fractions. Moreover a polyhedral reinforcement morphology is obtained, with particles resembling those of the ceramic powders often used as reinforcement. As validation, the model was applied for the homogenization of the elastoplastic behaviour of a PRMMC whose properties are reported in literature. The effective stress-strain curve obtained by homogenization fitted very well the experimental data, proving the consistency of the proposed approach.

Since the microstructural analyses showed that the matrix materials in the composite fillers are quite different from Incusil™ABA® an inverse homogenization procedure was developed. The homogenization model was integrated in an identification loop based on the Levenberg-Marquardt algorithm to assess the mechanical properties of the matrix alloys in the composites. The output of the identification was used to carry out a classical homogenization. The obtained temperature dependent mechanical properties of the composite fillers were used as input data for the simulation of the behaviour of the joints.

The modelling of the joint lead to tackle the problem of identifying a suitable failure criterion for the ceramic material. Three criteria proposed in literature, maximum principal stress, elastic strain energy and failure probability, were adopted and the comparison of the respective results lead to conclude that the maximum principal stress, despite its simplicity, is the most reliable indicator. The finite element predictions of the residual stress field in the joints resulted compatible the the XRD measurements. The modelling of the four point bend tests was also compared with experimental results and showed a good agreement, especially for the joints brazed with Incusil™ABA®.

The present project has been carried out with a combined experimental and modelling approach and some possible further developments in both domains are identifiable:

- Experimental characterization of the filler metal mechanical properties: the reinforced fillers showed a limited ductility in the tensile tests while in the joints large plastic strains develop. To validate and extend the obtained results two main experiments can be envisioned: tensile specimens with the same composition of the matrix metal could be produced and tested with the aim of checking the results of the inverse homogenization, while to validate those of the straightforward homogenization the behaviour of the composite fillers in the joints could be identified from tests on the joints themselves (an analogous procedure has been successfully applied to identify the properties of solder alloys in copper joints [29, 30]). Due to the brittleness of ceramics this procedure however would not be directly applicable to the ceramic-metal joints. Therefore other base metals should be chosen (one candidate could be Inconel®718, since it exhibits a high yield stress, about 1200 MPa, even after undergoing the brazing cycle). Moreover, to improve the accuracy of the simulation of the cooling process after brazing, tests at high temperature should be carried out and creep could be characterized too.

- Residual strain measurements: to improve the accuracy of XRD measurements the joint geometry could be optimized with the objective of having large ceramic surface regions with an almost constant stress distribution (e.g. lap joints). In this case larger X-ray beams could be used and strain could be measured at several points, thus improving the quality of the measurements.

- Homogenization model: the algorithm to generate particles can be improved to meet wider requirements in terms of reinforcement volume fraction and of particle size distribution. To generate particles having aspect ratios larger than one, sets of two or more vertices, instead of single vertices, could be chosen as nucleation sites while larger particles could be generated by assigning the inclusion material not only to the elements which share the nucleation point, or points, but also to the surrounding layers of tetrahedra. Both solutions could then be extended to study materials in which particles are not randomly oriented. Moreover other material constitutive behaviours could be taken into account (e.g. elastoplasticity of the particles or viscoplasticity of the matrix) along with the effect of the residual stresses deriving from the fabrication process.

- Inverse homogenization model: the approach could be applied for the identification of the properties of the metal matrix in PRMMC, in which size effects are expected (e.g. the increase of hardening due to particle size and interparticle distance [61, 76]). Furthermore with the broadening of the capabilities of the homogenization model the inverse homogenization could be performed for material properties other than elastoplasticity.

Appendix A

Parametric Model

In this appendix the output of the parametric finite element model of the cooling process is summarized. The results are grouped according to the joining partners. For each assembly twelve diagrams are provided, in which σ_I in the ceramic is plotted against the brazing gap at constant α and σ_y^{RT}.

A.1 Si_3N_4/TiN-steel

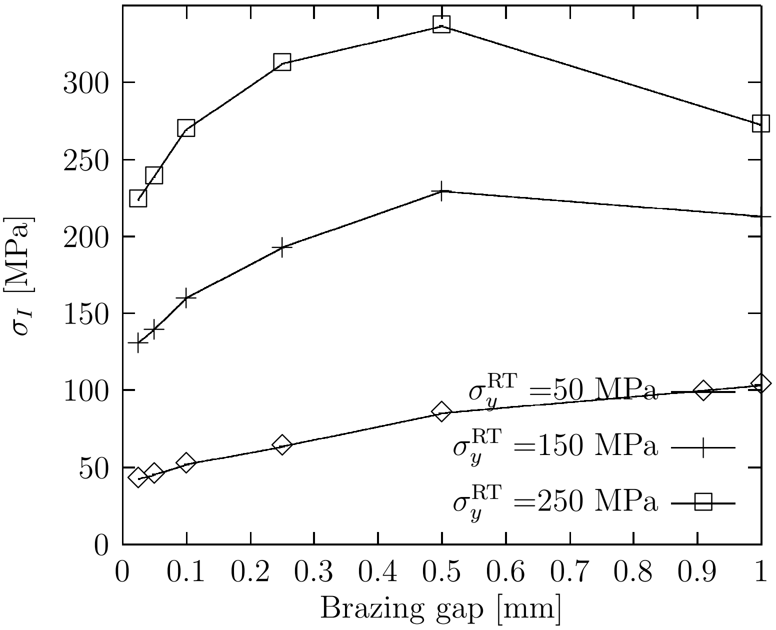

Figure A.1: Si_3N_4/TiN-steel: $\alpha = 5.0 \cdot 10^{-6}$ °C^{-1}, brazing temperature 700°C.

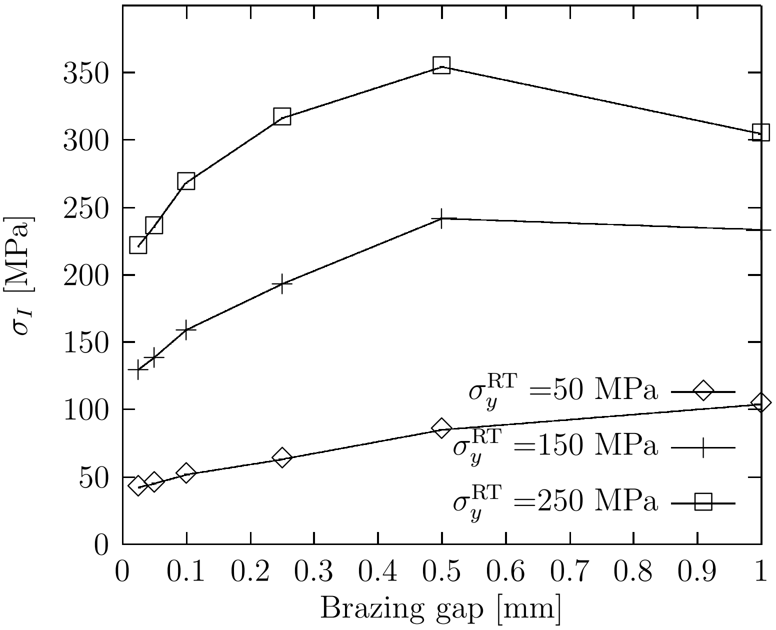

Figure A.2: Si_3N_4/TiN-steel: $\alpha = 5.0 \cdot 10^{-6}$ ℃$^{-1}$, brazing temperature 850℃.

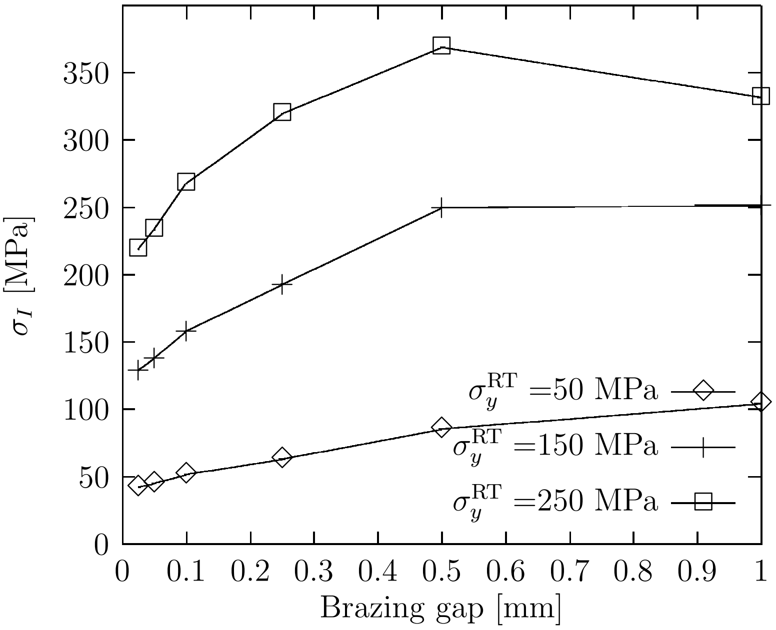

Figure A.3: Si_3N_4/TiN-steel: $\alpha = 5.0 \cdot 10^{-6}$ ℃$^{-1}$, brazing temperature 1000℃.

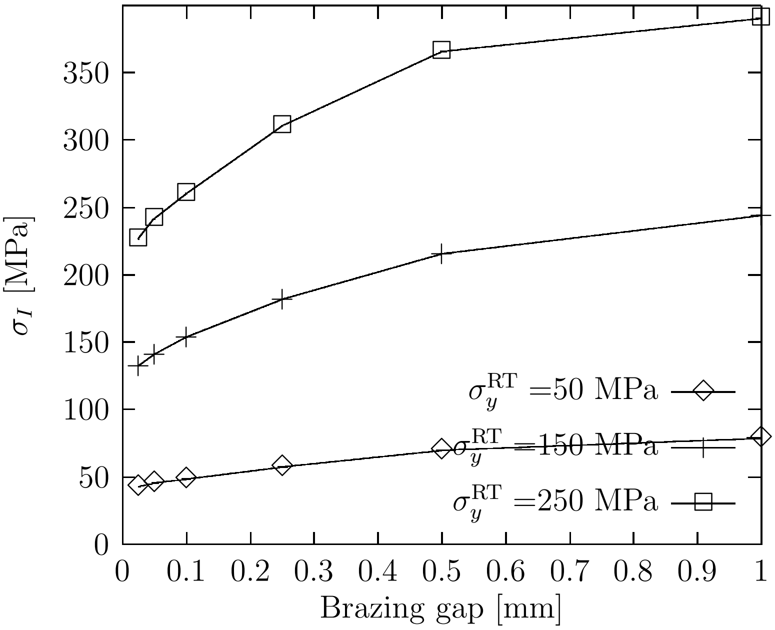

Figure A.4: Si$_3$N$_4$/TiN-steel: $\alpha = 1.0 \cdot 10^{-5}$ ℃$^{-1}$, brazing temperature 700℃.

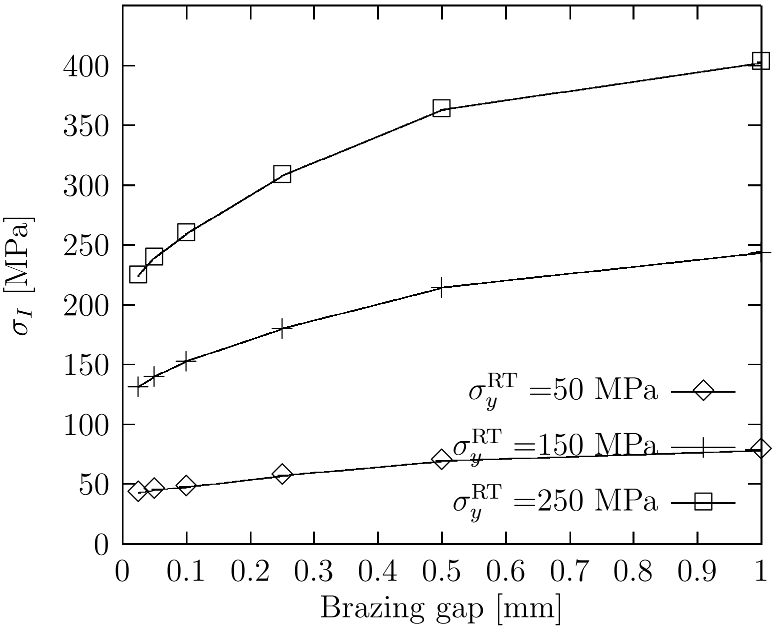

Figure A.5: Si$_3$N$_4$/TiN-steel: $\alpha = 1.0 \cdot 10^{-5}$ ℃$^{-1}$, brazing temperature 850℃.

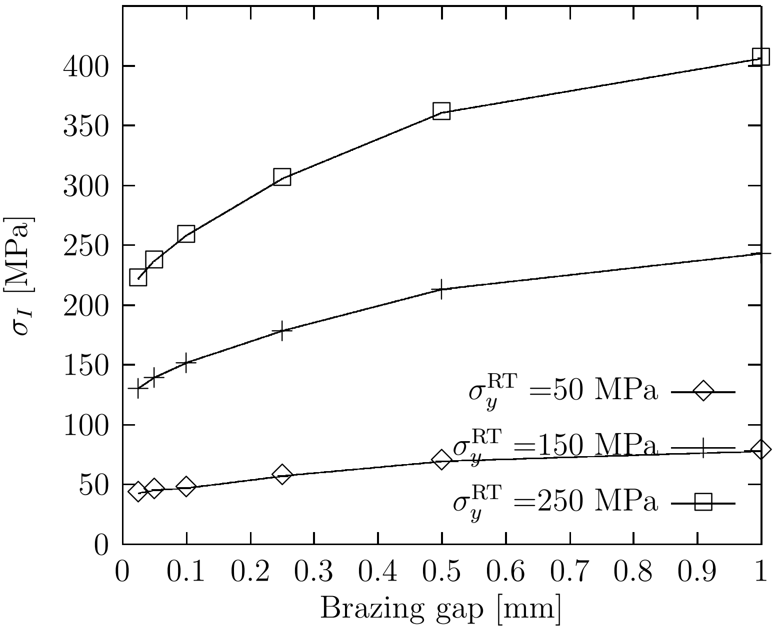

Figure A.6: Si_3N_4/TiN-steel: $\alpha = 1.0 \cdot 10^{-5}$ ℃$^{-1}$, brazing temperature 1000℃.

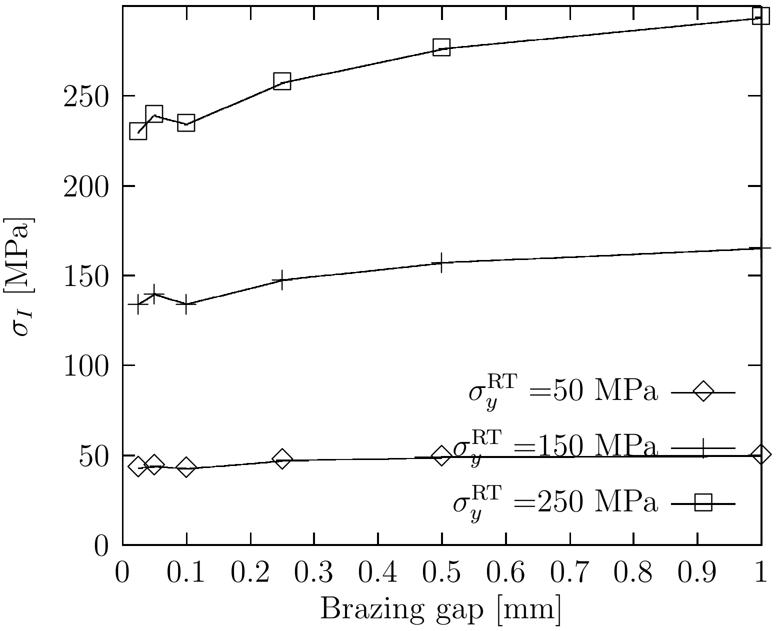

Figure A.7: Si_3N_4/TiN-steel: $\alpha = 1.5 \cdot 10^{-5}$ ℃$^{-1}$, brazing temperature 700℃.

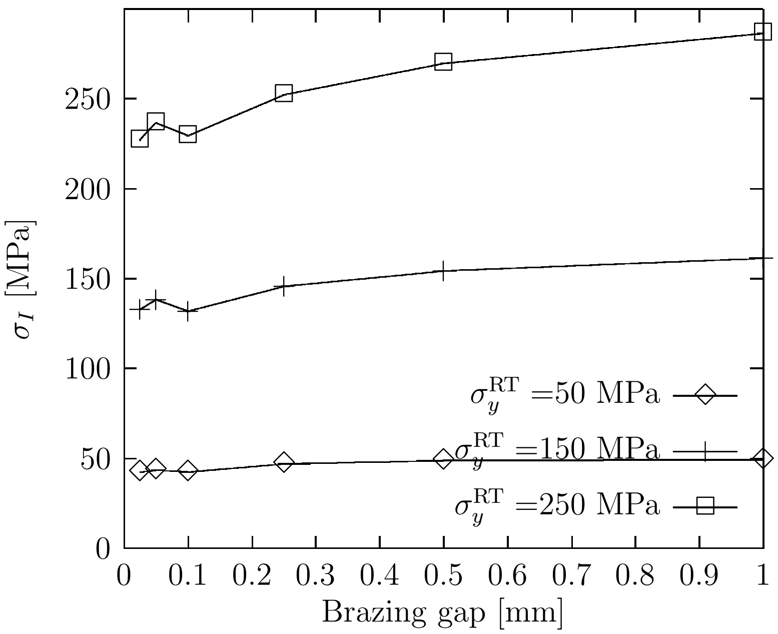

Figure A.8: Si$_3$N$_4$/TiN-steel: $\alpha = 1.5 \cdot 10^{-5}$ ℃$^{-1}$, brazing temperature 850℃.

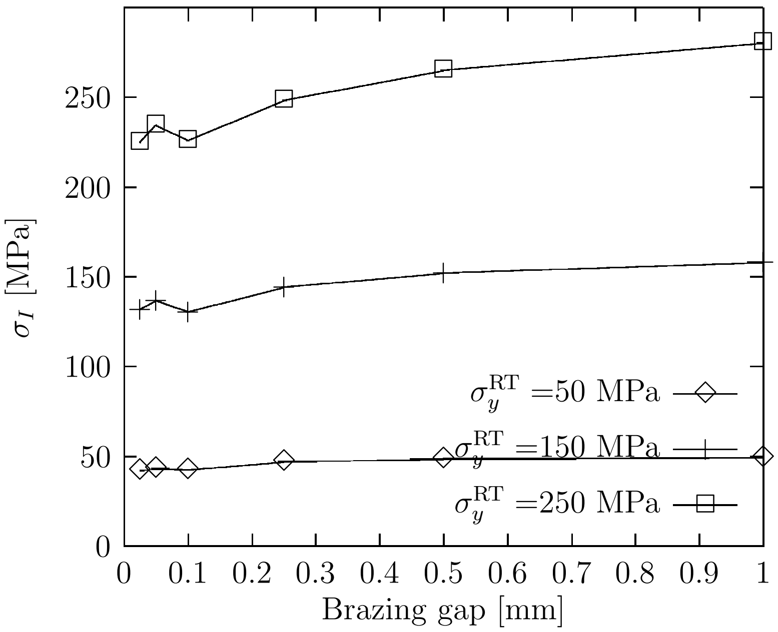

Figure A.9: Si$_3$N$_4$/TiN-steel: $\alpha = 1.5 \cdot 10^{-5}$ ℃$^{-1}$, brazing temperature 1000℃.

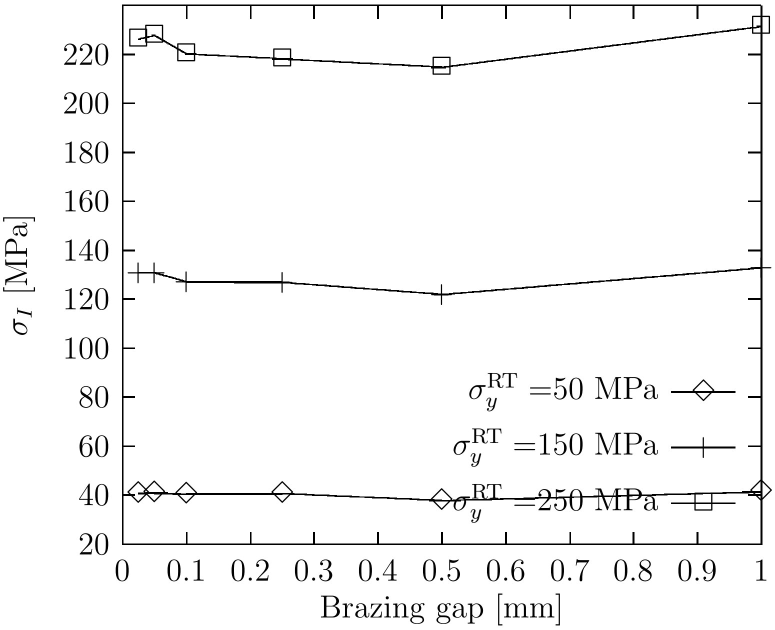

Figure A.10: Si_3N_4/TiN-steel: $\alpha = 2.0 \cdot 10^{-5}$ ℃$^{-1}$, brazing temperature 700℃.

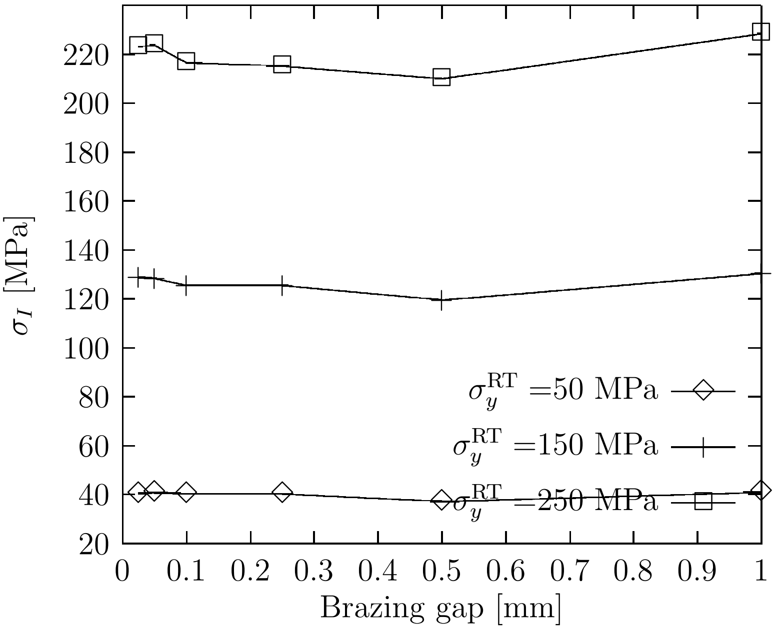

Figure A.11: Si_3N_4/TiN-steel: $\alpha = 2.0 \cdot 10^{-5}$ ℃$^{-1}$, brazing temperature 850℃.

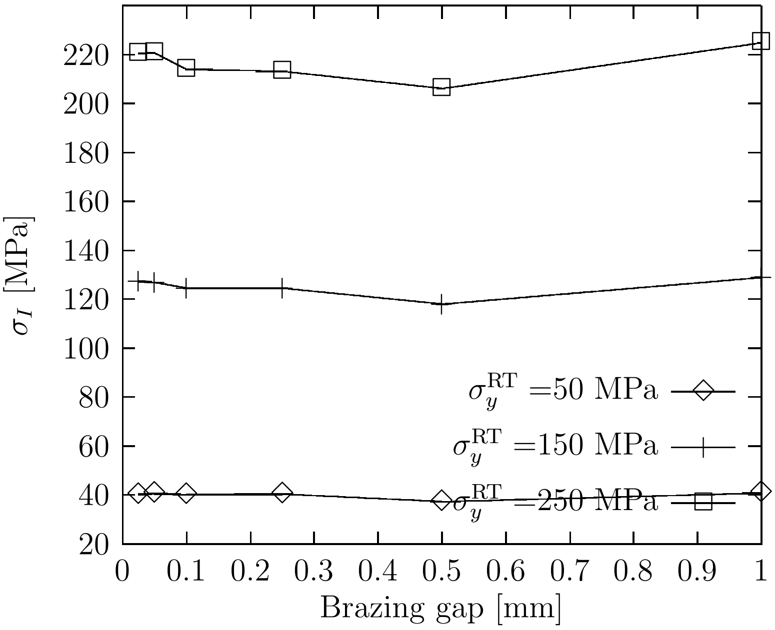

Figure A.12: Si$_3$N$_4$/TiN-steel: $\alpha = 2.0 \cdot 10^{-5}$ ℃$^{-1}$, brazing temperature 1000℃.

A.2 Si$_3$N$_4$/TiN-Kovar®

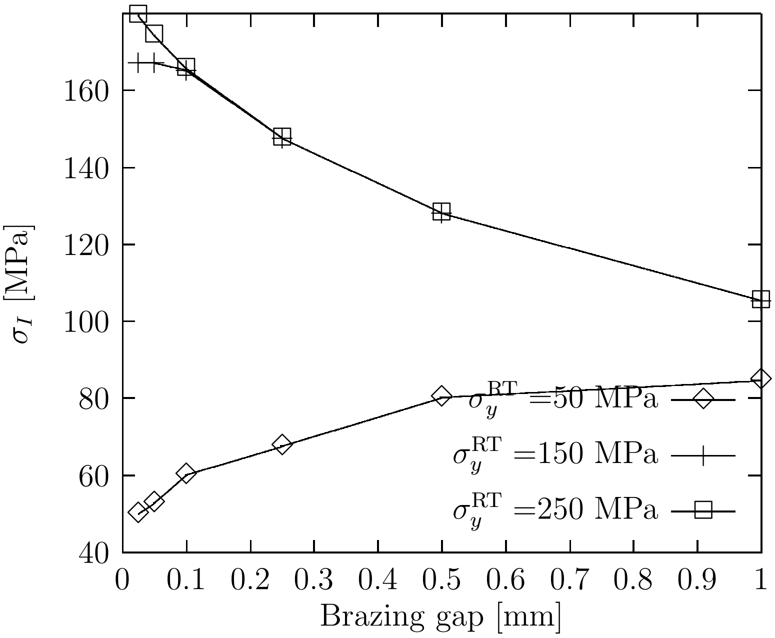

Figure A.13: Si$_3$N$_4$/TiN-Kovar®: $\alpha = 5.0 \cdot 10^{-6}$ ℃$^{-1}$, brazing temperature 700℃.

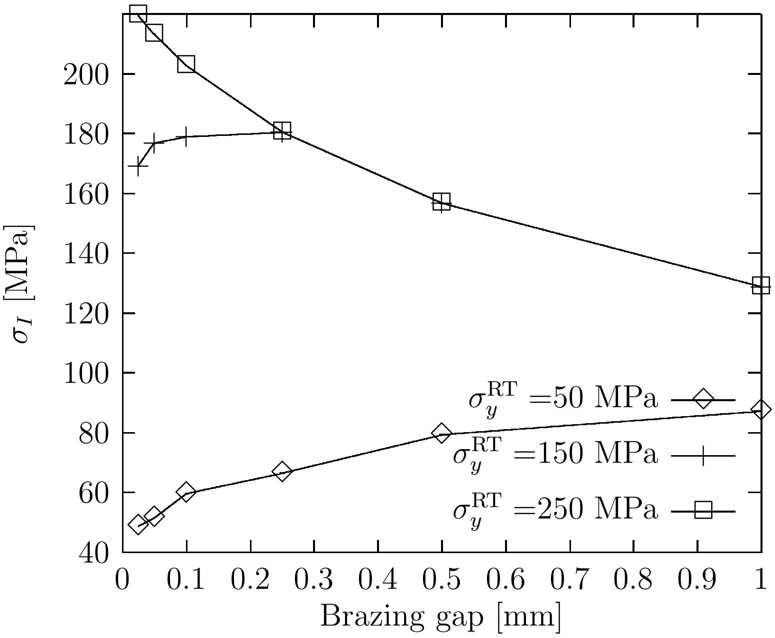

Figure A.14: Si_3N_4/TiN-Kovar®: $\alpha = 5.0 \cdot 10^{-6}$ ℃$^{-1}$, brazing temperature 850℃.

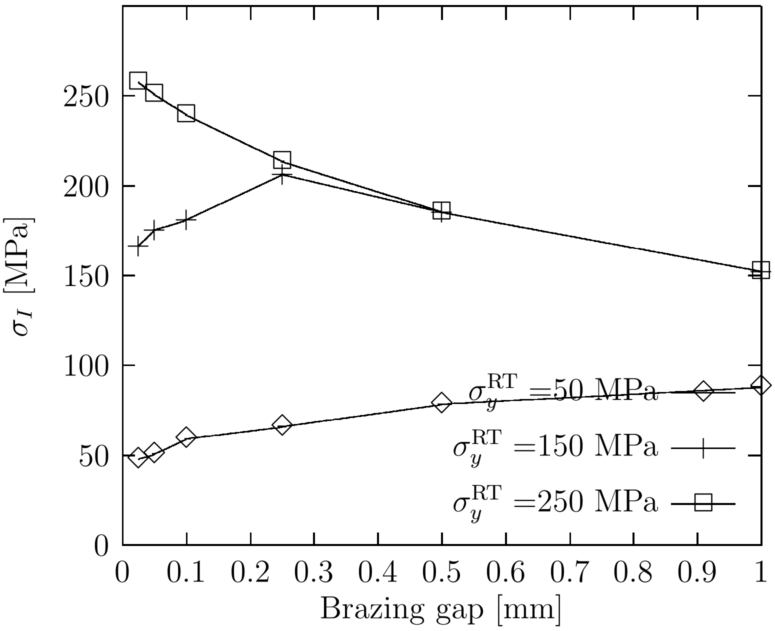

Figure A.15: Si_3N_4/TiN-Kovar®: $\alpha = 5.0 \cdot 10^{-6}$ ℃$^{-1}$, brazing temperature 1000℃.

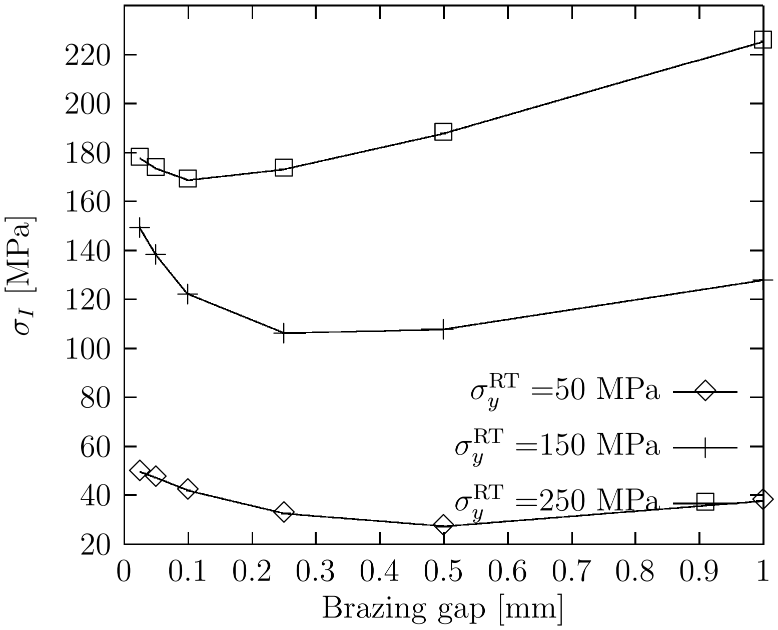

Figure A.16: Si_3N_4/TiN-Kovar®: $\alpha = 1.0 \cdot 10^{-5}$ ℃$^{-1}$, brazing temperature 700℃.

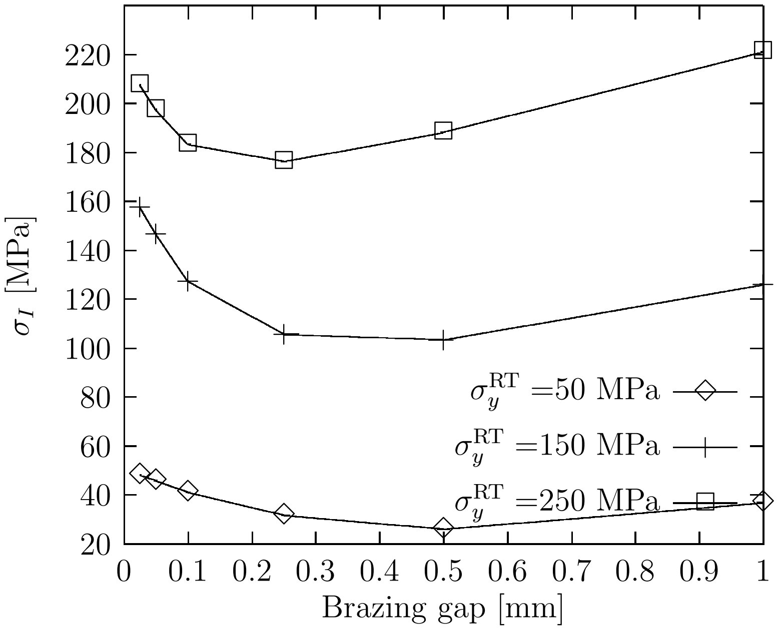

Figure A.17: Si_3N_4/TiN-Kovar®: $\alpha = 1.0 \cdot 10^{-5}$ ℃$^{-1}$, brazing temperature 850℃.

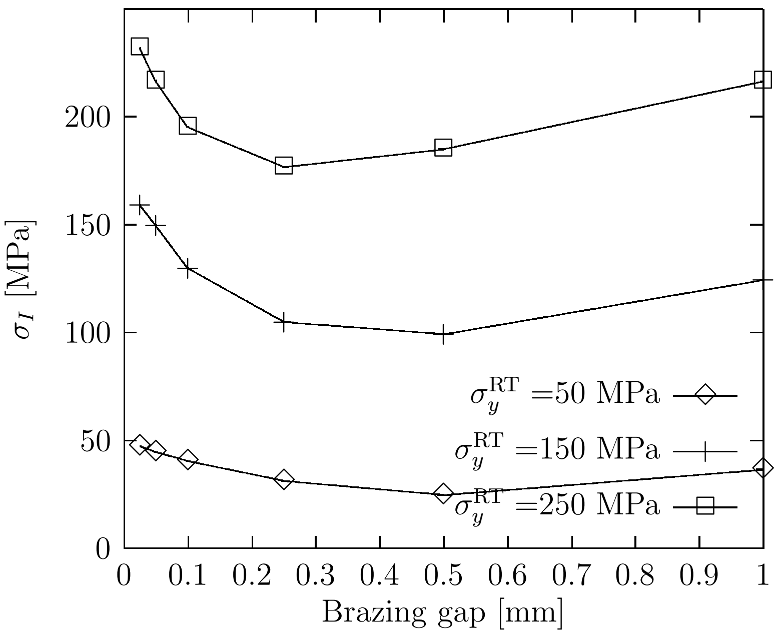

Figure A.18: Si_3N_4/TiN-Kovar®: $\alpha = 1.0 \cdot 10^{-5}$ ℃$^{-1}$, brazing temperature 1000℃.

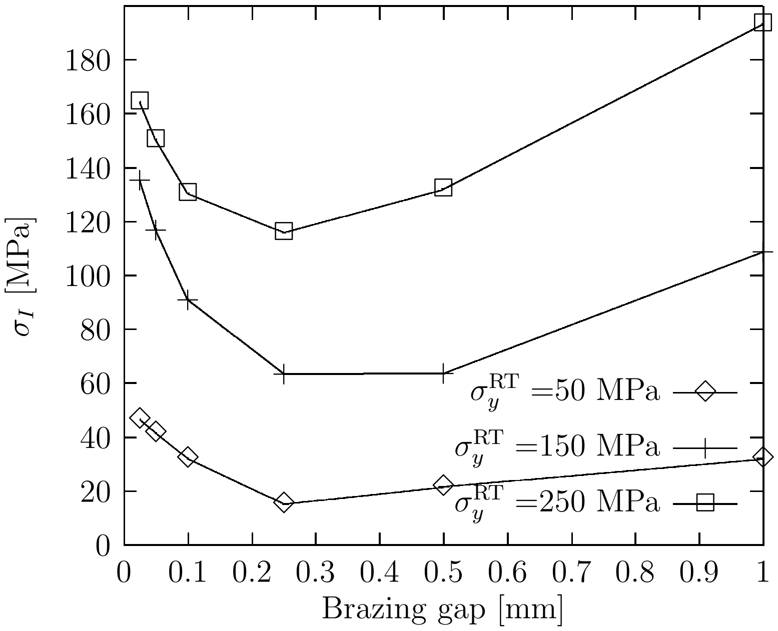

Figure A.19: Si_3N_4/TiN-Kovar®: $\alpha = 1.5 \cdot 10^{-5}$ ℃$^{-1}$, brazing temperature 700℃.

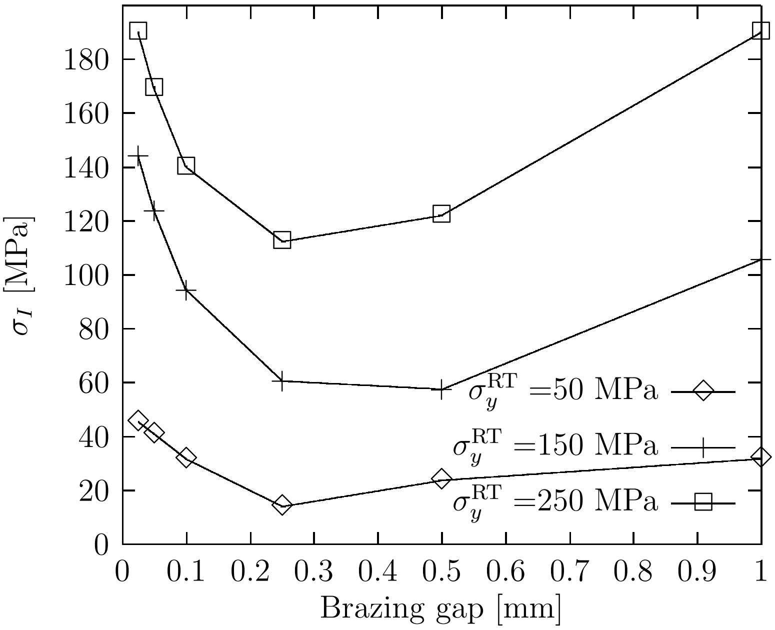

Figure A.20: $\mathrm{Si_3N_4}$/TiN-Kovar®: $\alpha = 1.5 \cdot 10^{-5}$ ℃$^{-1}$, brazing temperature 850℃.

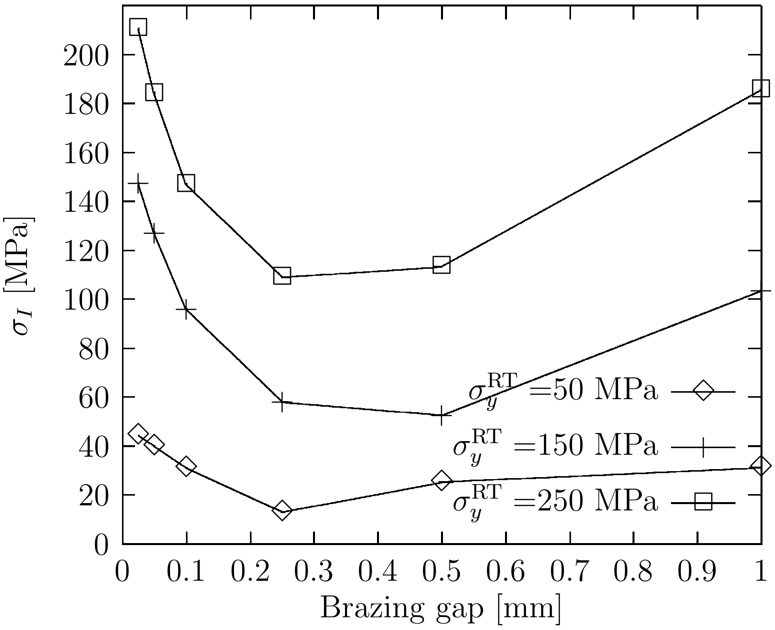

Figure A.21: $\mathrm{Si_3N_4}$/TiN-Kovar®: $\alpha = 1.5 \cdot 10^{-5}$ ℃$^{-1}$, brazing temperature 1000℃.

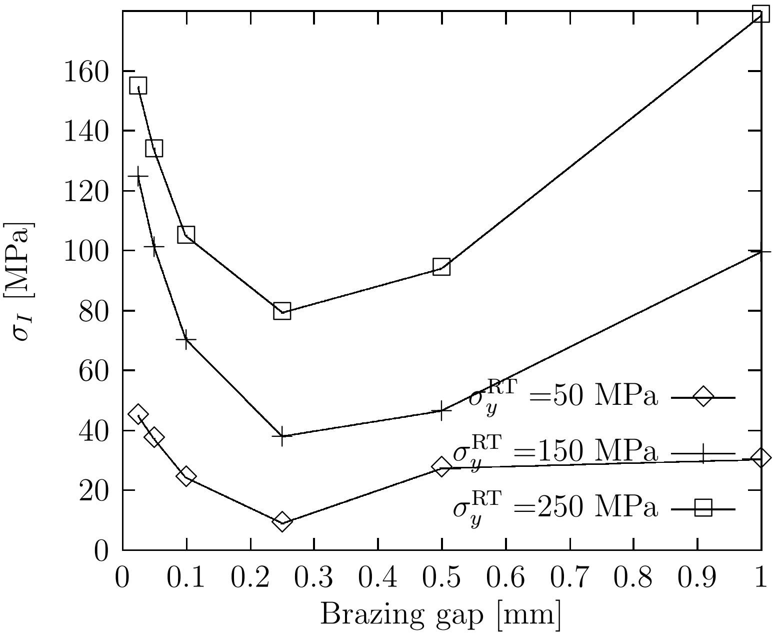

Figure A.22: Si_3N_4/TiN-Kovar®: $\alpha = 2.0 \cdot 10^{-5}$ ℃$^{-1}$, brazing temperature 700℃.

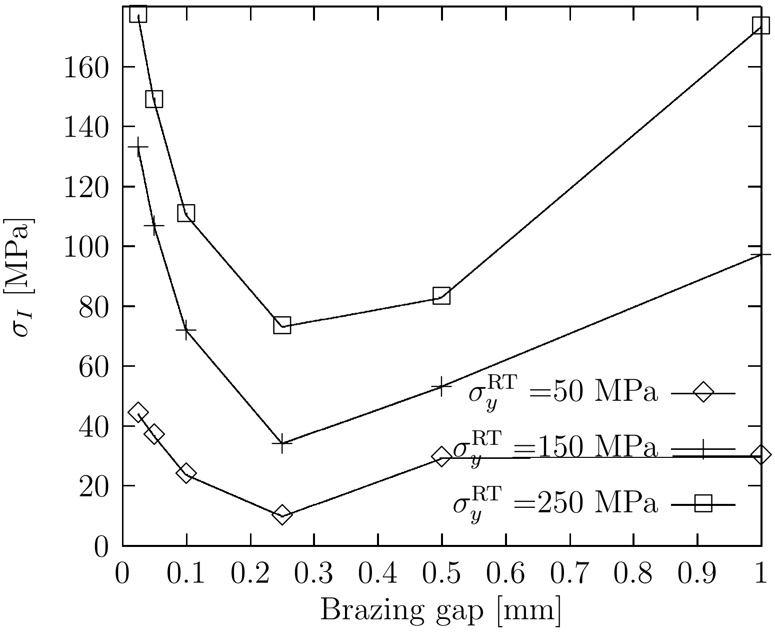

Figure A.23: Si_3N_4/TiN-Kovar®: $\alpha = 2.0 \cdot 10^{-5}$ ℃$^{-1}$, brazing temperature 850℃.

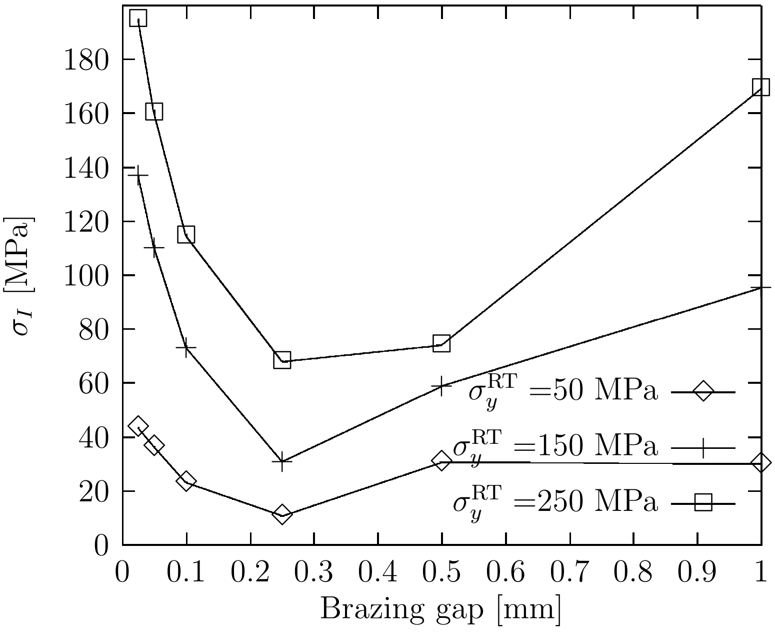

Figure A.24: Si_3N_4/TiN-Kovar®: $\alpha = 2.0 \cdot 10^{-5}$ ℃$^{-1}$, brazing temperature 1000℃.

A.3 WC-steel

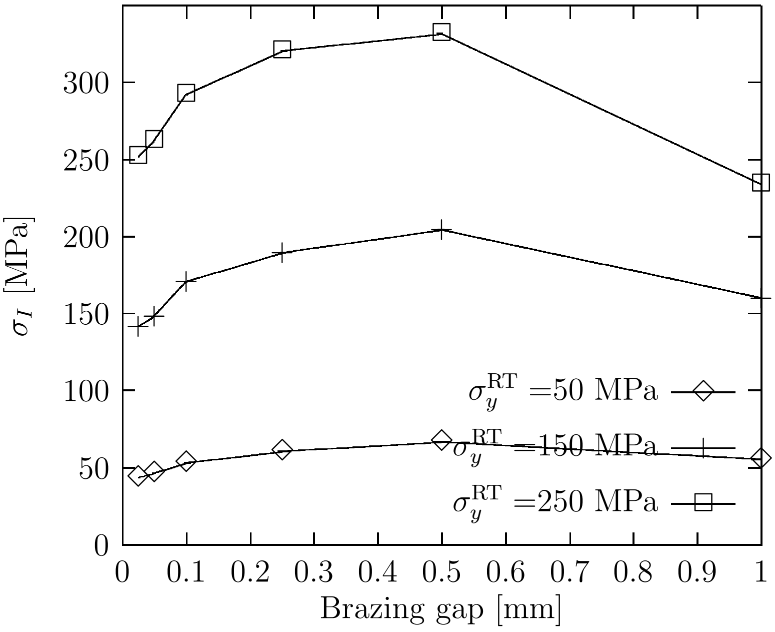

Figure A.25: WC-steel: $\alpha = 5.0 \cdot 10^{-6}$ ℃$^{-1}$, brazing temperature 700℃.

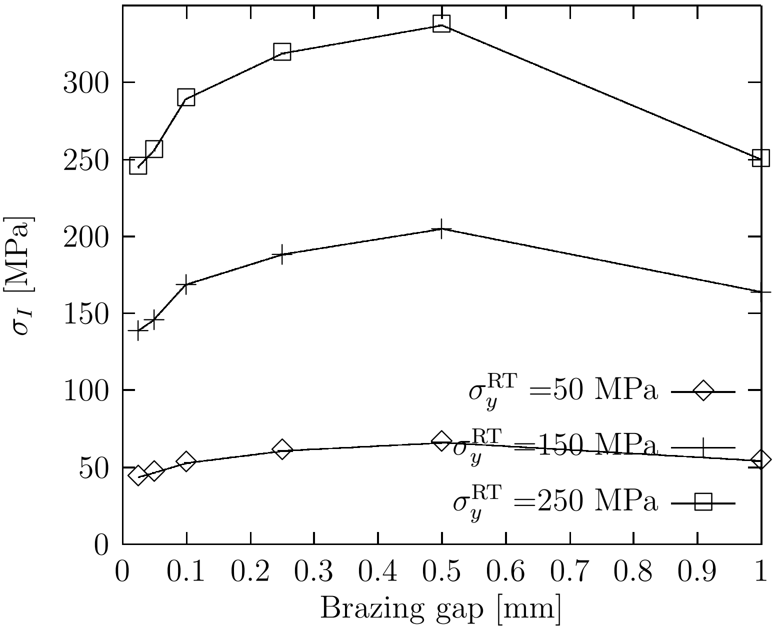

Figure A.26: WC-steel: $\alpha = 5.0 \cdot 10^{-6}$ °C^{-1}, brazing temperature 850°C.

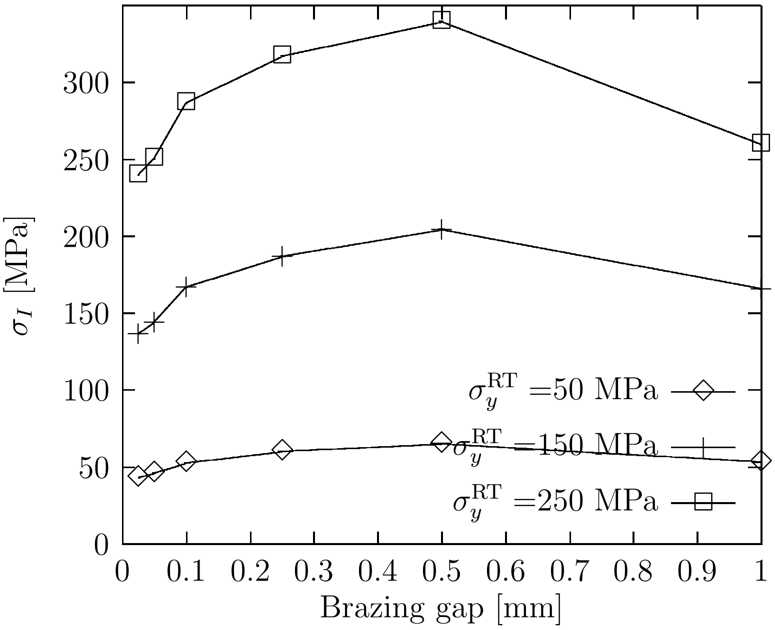

Figure A.27: WC-steel: $\alpha = 5.0 \cdot 10^{-6}$ °C^{-1}, brazing temperature 1000°C.

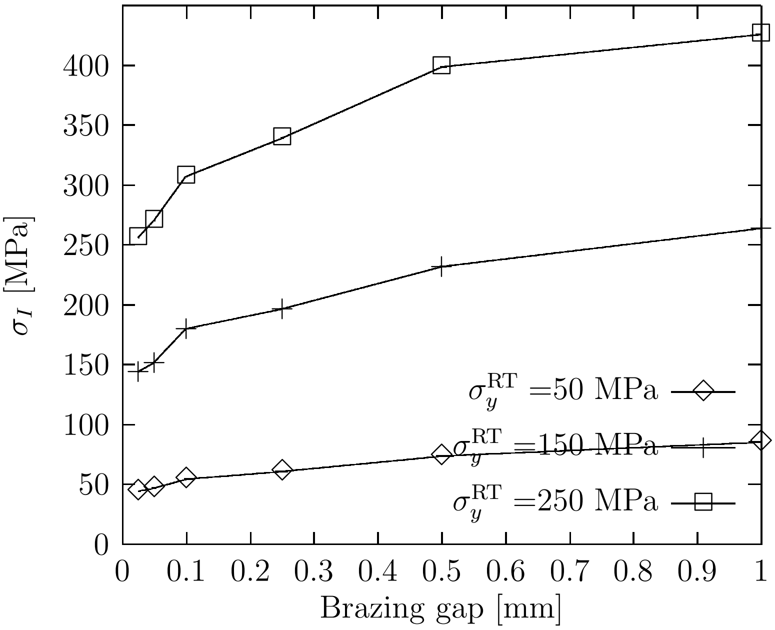

Figure A.28: WC-steel: $\alpha = 1.0 \cdot 10^{-5}$ °C^{-1}, brazing temperature 700°C.

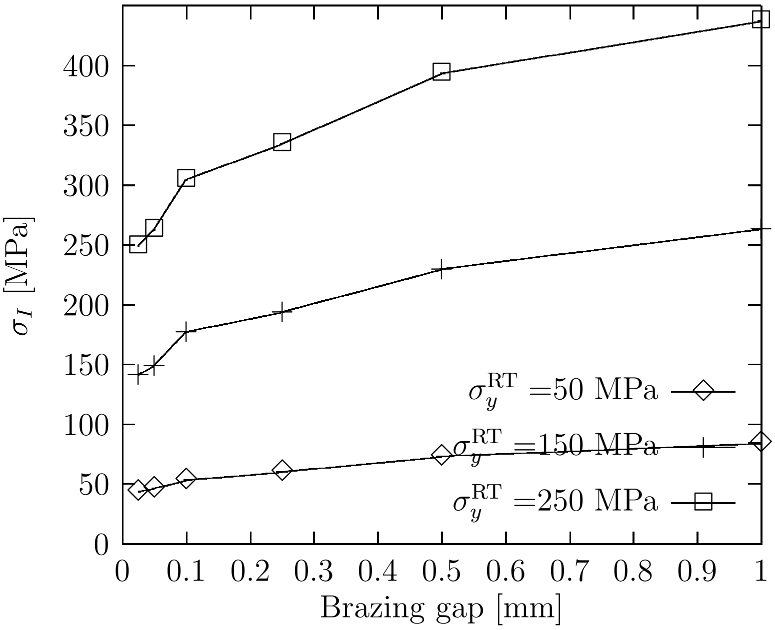

Figure A.29: WC-steel: $\alpha = 1.0 \cdot 10^{-5}$ °C^{-1}, brazing temperature 850°C.

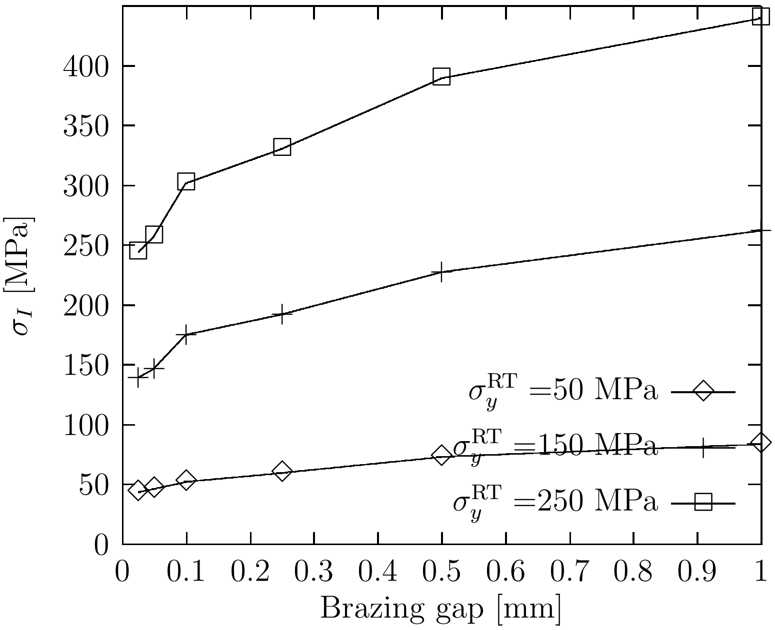

Figure A.30: WC-steel: $\alpha = 1.0 \cdot 10^{-5}$ °C^{-1}, brazing temperature 1000°C.

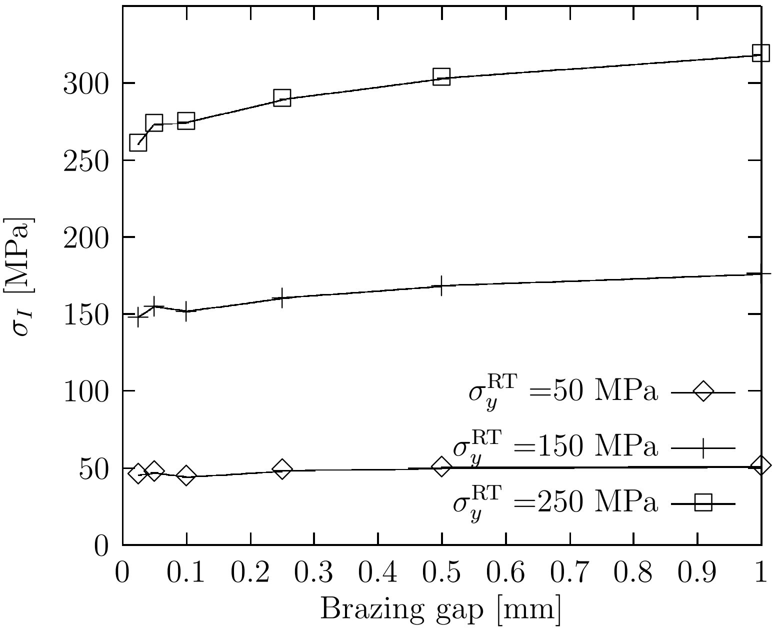

Figure A.31: WC-steel: $\alpha = 1.5 \cdot 10^{-5}$ °C^{-1}, brazing temperature 700°C.

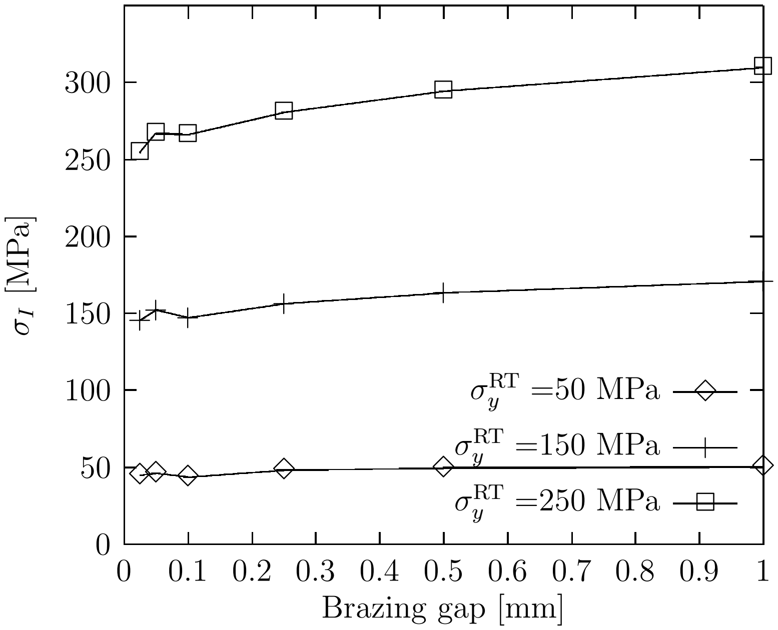

Figure A.32: WC-steel: $\alpha = 1.5 \cdot 10^{-5}$ °C^{-1}, brazing temperature 850°C.

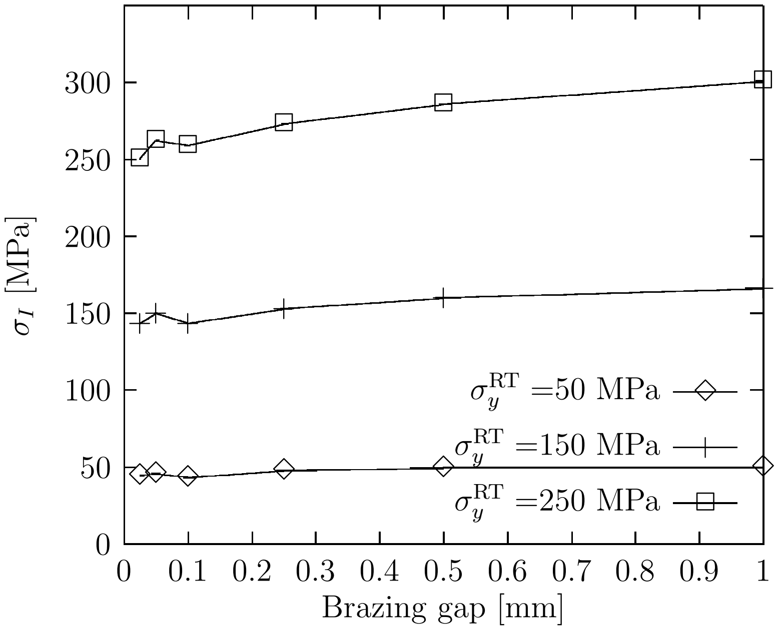

Figure A.33: WC-steel: $\alpha = 1.5 \cdot 10^{-5}$ °C^{-1}, brazing temperature 1000°C.

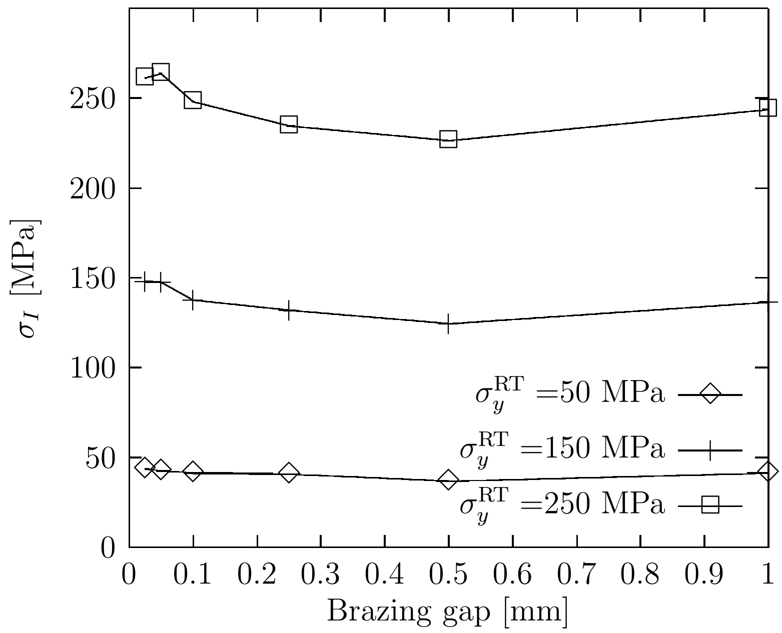

Figure A.34: WC-steel: $\alpha = 2.0 \cdot 10^{-5}$ ℃$^{-1}$, brazing temperature 700℃.

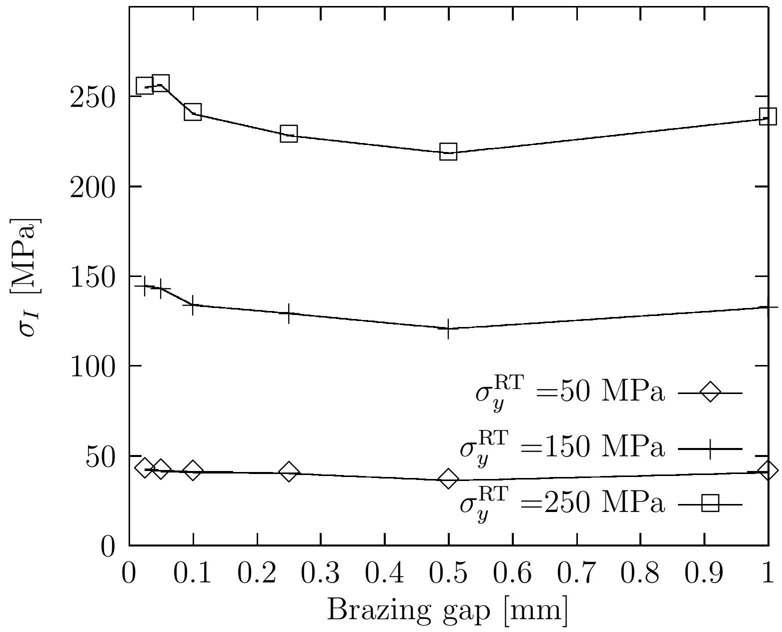

Figure A.35: WC-steel: $\alpha = 2.0 \cdot 10^{-5}$ ℃$^{-1}$, brazing temperature 850℃.

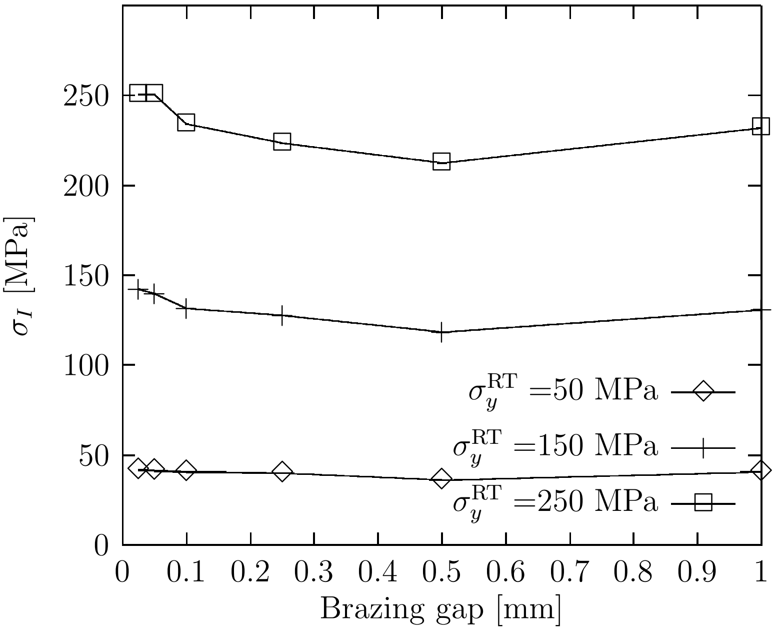

Figure A.36: WC-steel: $\alpha = 2.0 \cdot 10^{-5}$ °C^{-1}, brazing temperature 1000°C.

A.4 WC-Kovar®

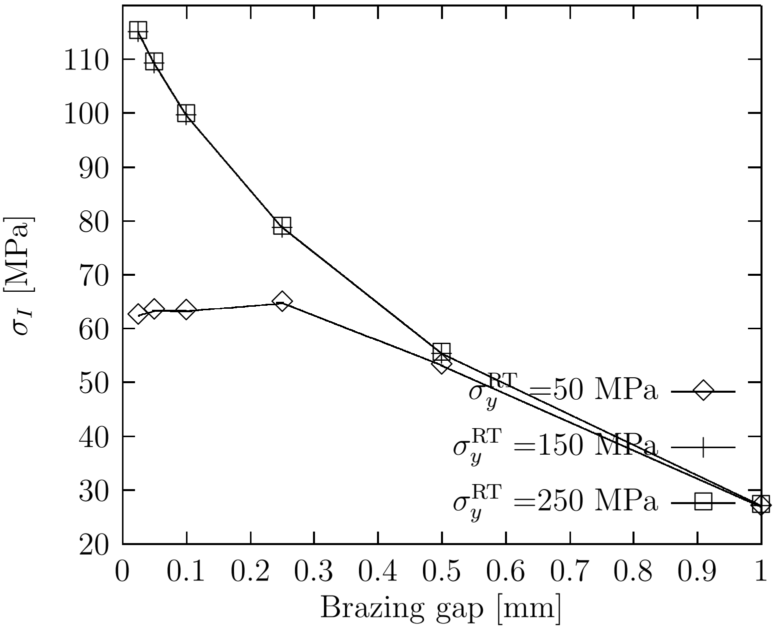

Figure A.37: WC-Kovar®: $\alpha = 5.0 \cdot 10^{-6}$ °C^{-1}, brazing temperature 700°C.

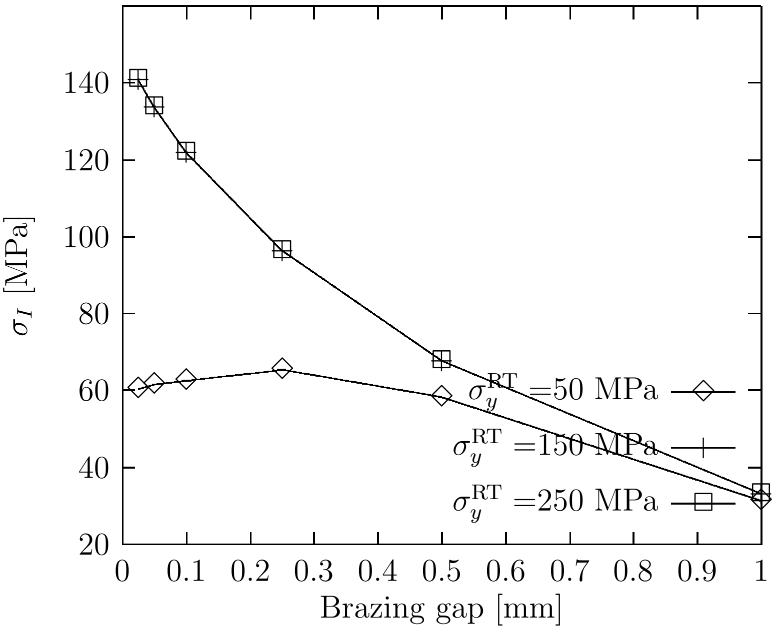

Figure A.38: WC-Kovar®: $\alpha = 5.0 \cdot 10^{-6}$ ℃$^{-1}$, brazing temperature 850℃.

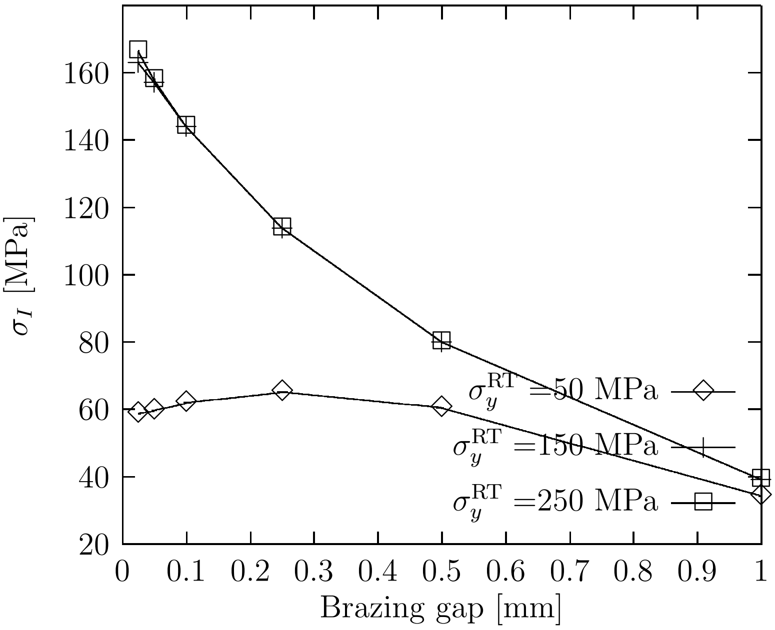

Figure A.39: WC-Kovar®: $\alpha = 5.0 \cdot 10^{-6}$ ℃$^{-1}$, brazing temperature 1000℃.

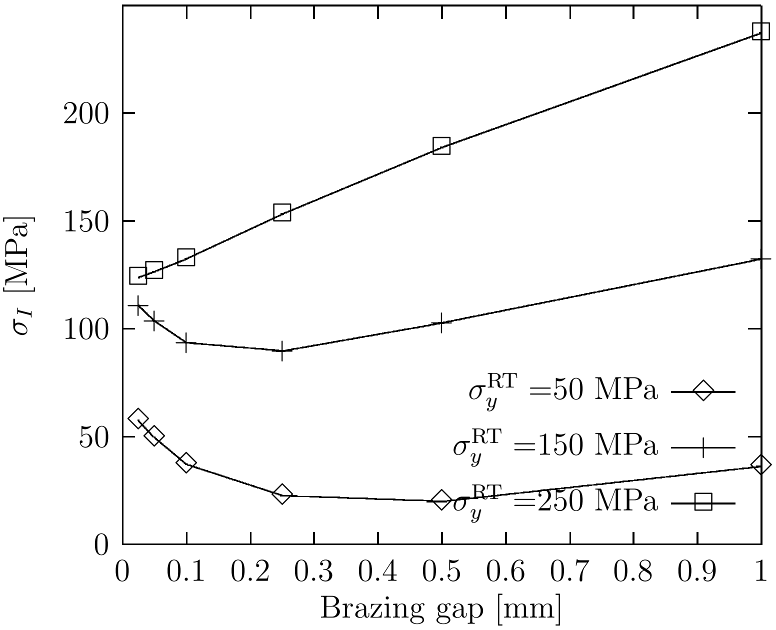

Figure A.40: WC-Kovar®: $\alpha = 1.0 \cdot 10^{-5}$ °C^{-1}, brazing temperature 700°C.

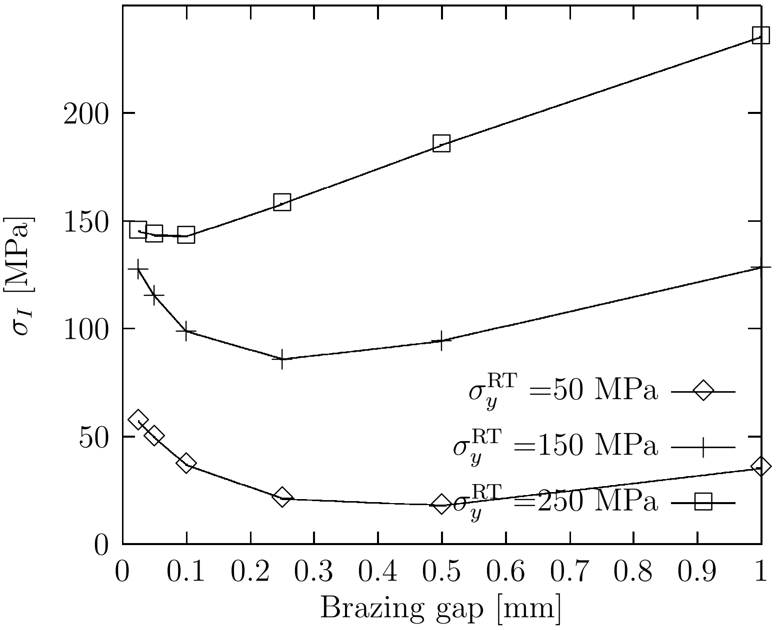

Figure A.41: WC-Kovar®: $\alpha = 1.0 \cdot 10^{-5}$ °C^{-1}, brazing temperature 850°C.

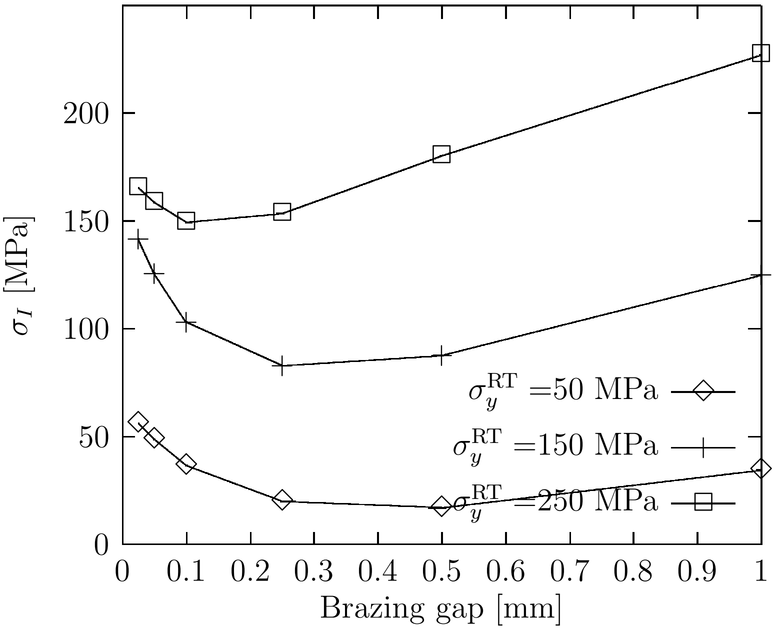

Figure A.42: WC-Kovar®: $\alpha = 1.0 \cdot 10^{-5}$ ℃$^{-1}$, brazing temperature 1000℃.

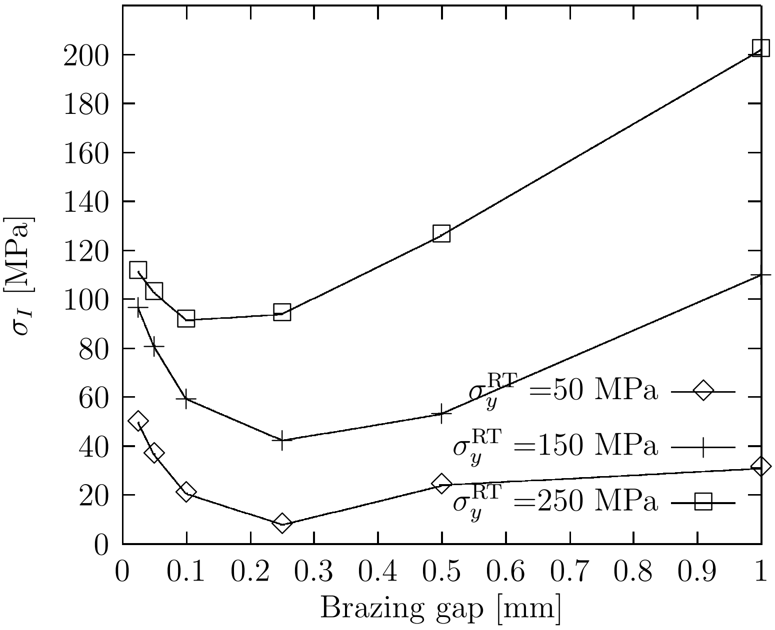

Figure A.43: WC-Kovar®: $\alpha = 1.5 \cdot 10^{-5}$ ℃$^{-1}$, brazing temperature 700℃.

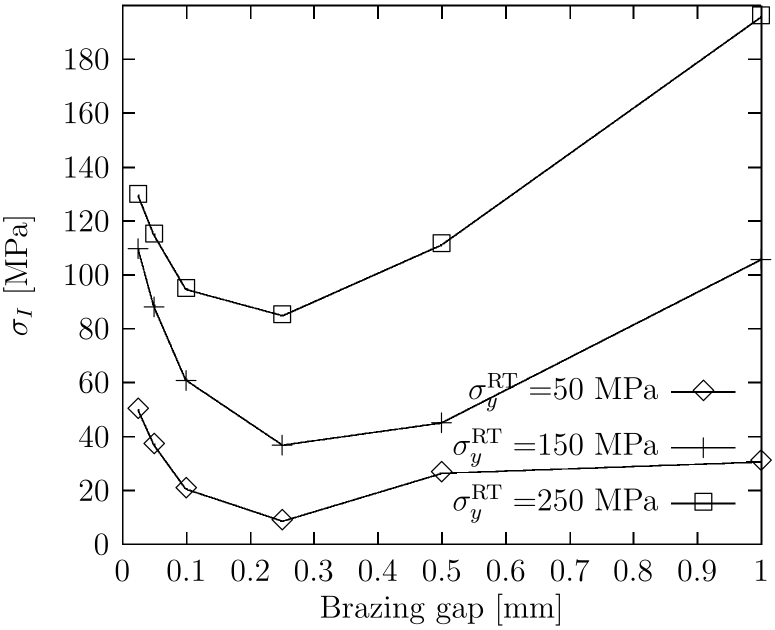

Figure A.44: WC-Kovar®: $\alpha = 1.5 \cdot 10^{-5}$ ℃$^{-1}$, brazing temperature 850℃.

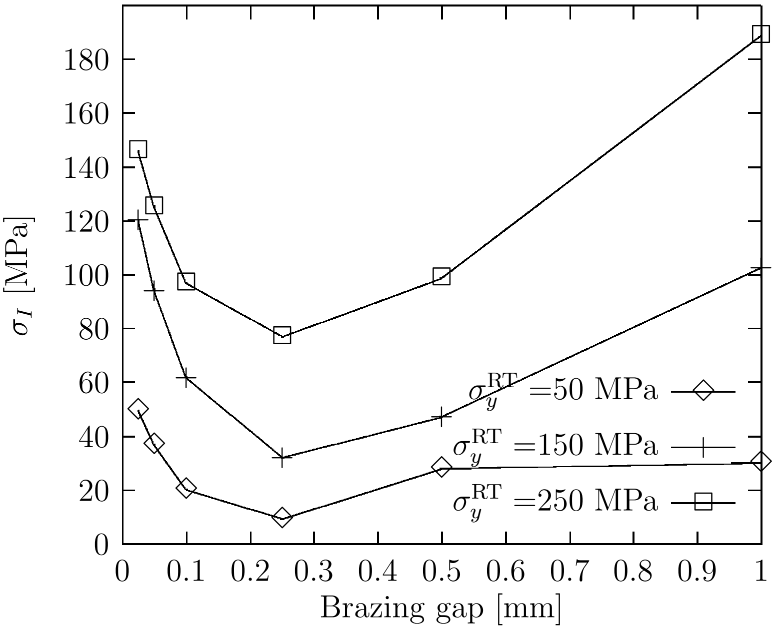

Figure A.45: WC-Kovar®: $\alpha = 1.5 \cdot 10^{-5}$ ℃$^{-1}$, brazing temperature 1000℃.

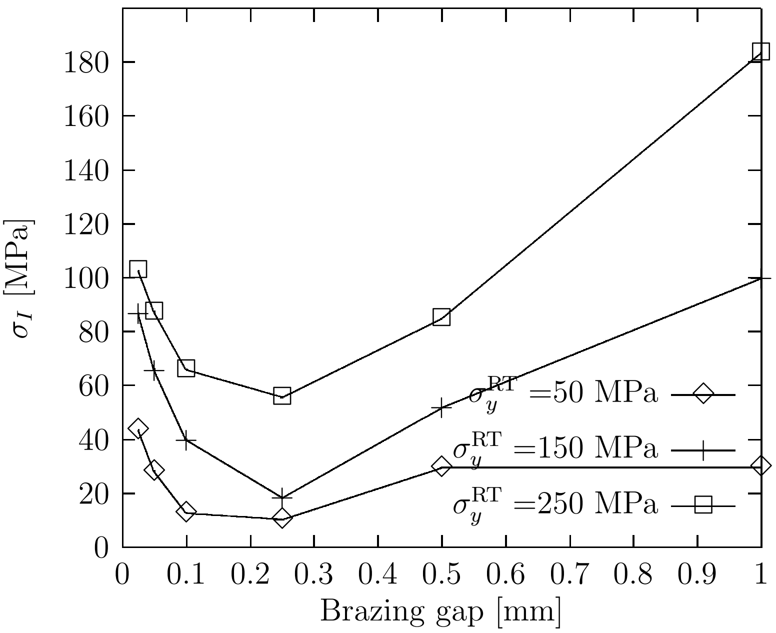

Figure A.46: WC-Kovar®: $\alpha = 2.0 \cdot 10^{-5}$ °C^{-1}, brazing temperature 700°C.

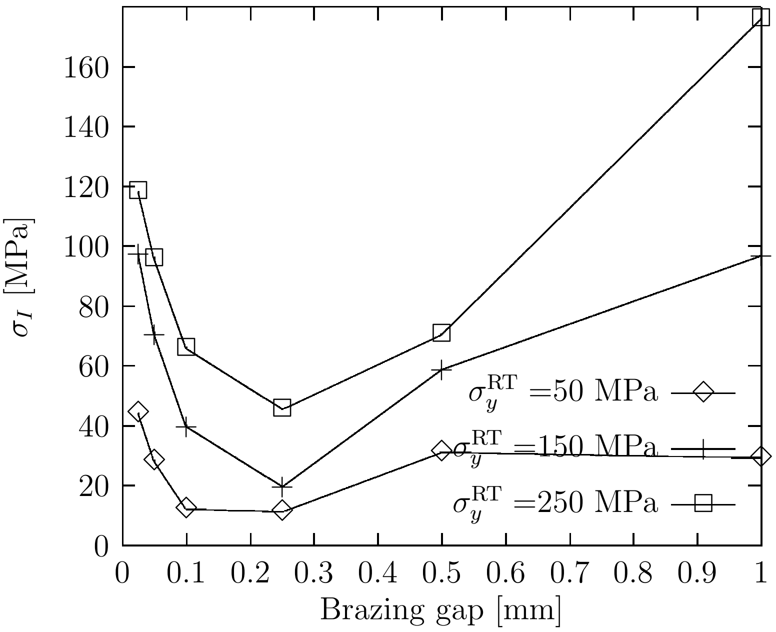

Figure A.47: WC-Kovar®: $\alpha = 2.0 \cdot 10^{-5}$ °C^{-1}, brazing temperature 850°C.

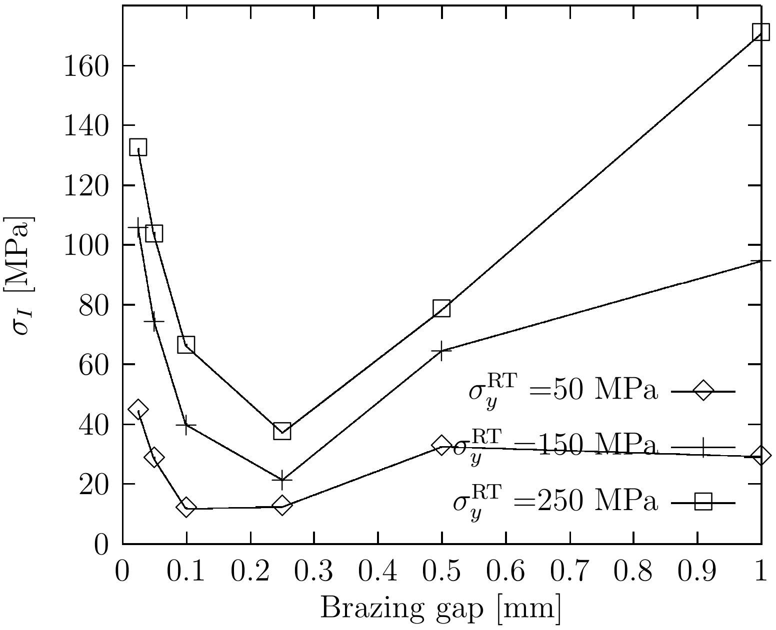

Figure A.48: WC-Kovar®: $\alpha = 2.0 \cdot 10^{-5}$ °C^{-1}, brazing temperature 1000°C.

A.5 Al_2O_3-steel

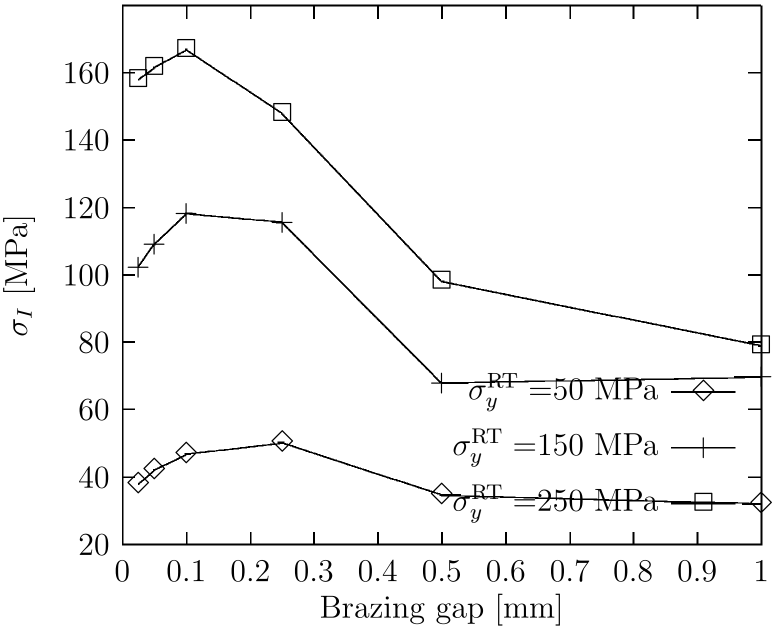

Figure A.49: Al_2O_3-steel: $\alpha = 5.0 \cdot 10^{-6}$ °C^{-1}, brazing temperature 700°C.

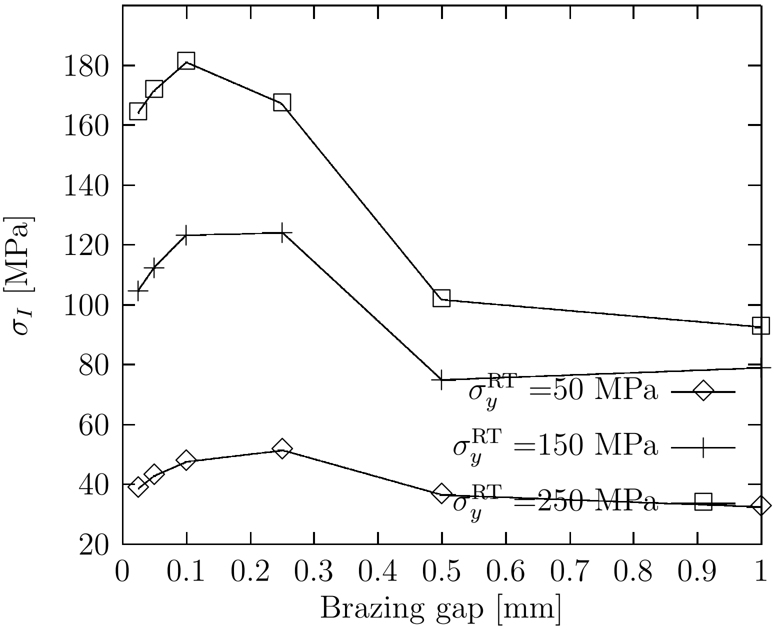

Figure A.50: Al_2O_3-steel: $\alpha = 5.0 \cdot 10^{-6}$ °C^{-1}, brazing temperature 850°C.

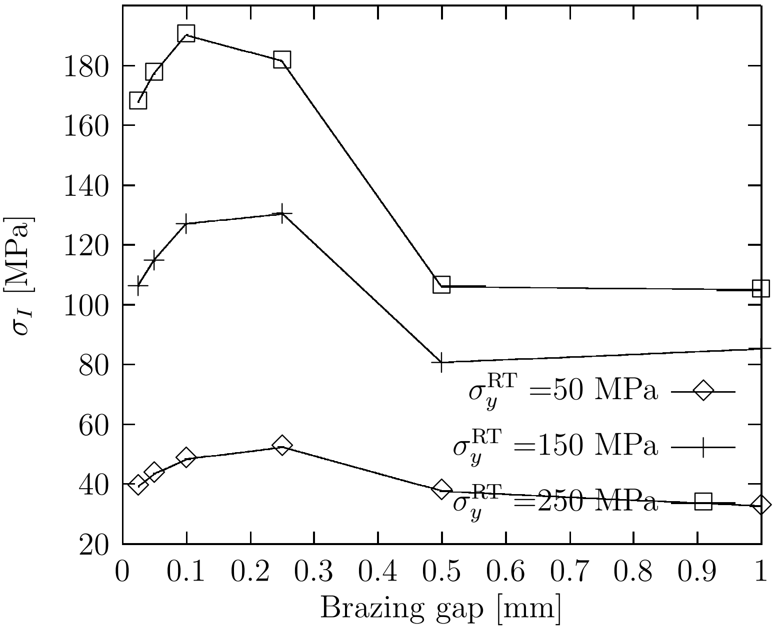

Figure A.51: Al_2O_3-steel: $\alpha = 5.0 \cdot 10^{-6}$ °C^{-1}, brazing temperature 1000°C.

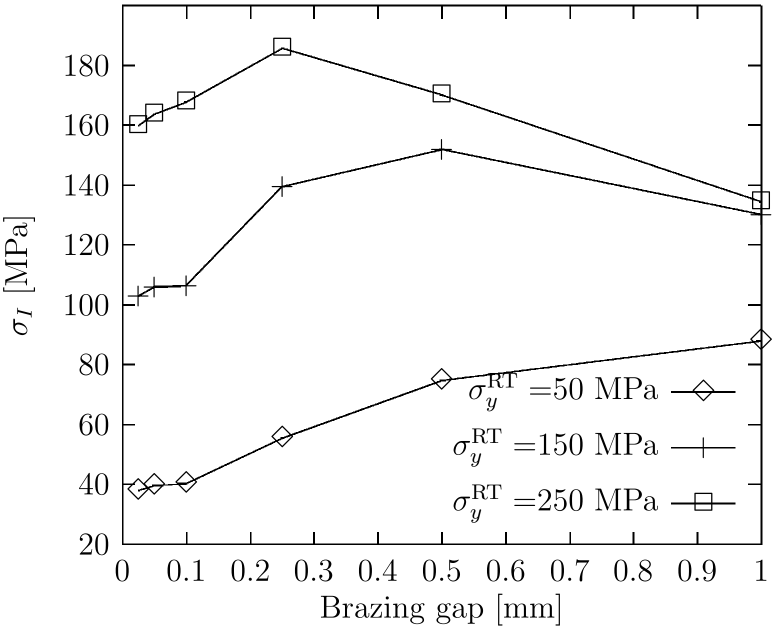

Figure A.52: Al$_2$O$_3$-steel: $\alpha = 1.0 \cdot 10^{-5}$ ℃$^{-1}$, brazing temperature 700℃.

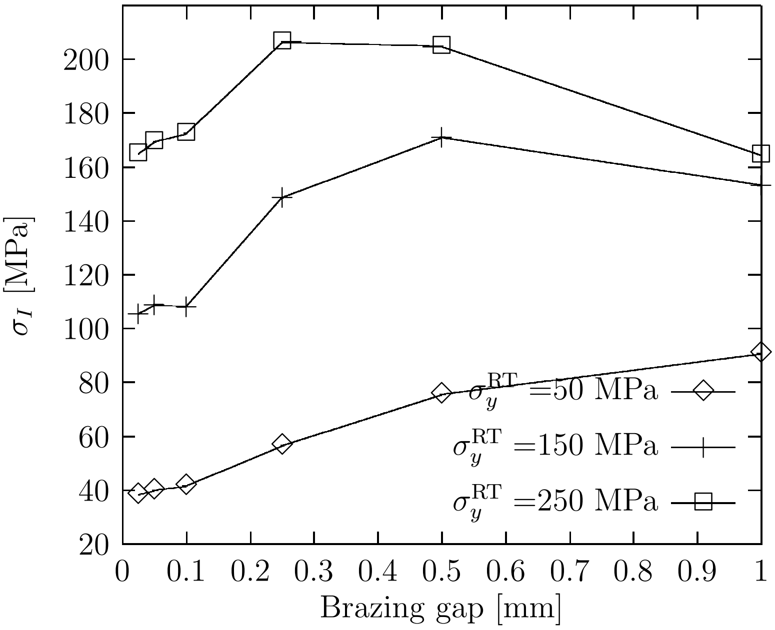

Figure A.53: Al$_2$O$_3$-steel: $\alpha = 1.0 \cdot 10^{-5}$ ℃$^{-1}$, brazing temperature 850℃.

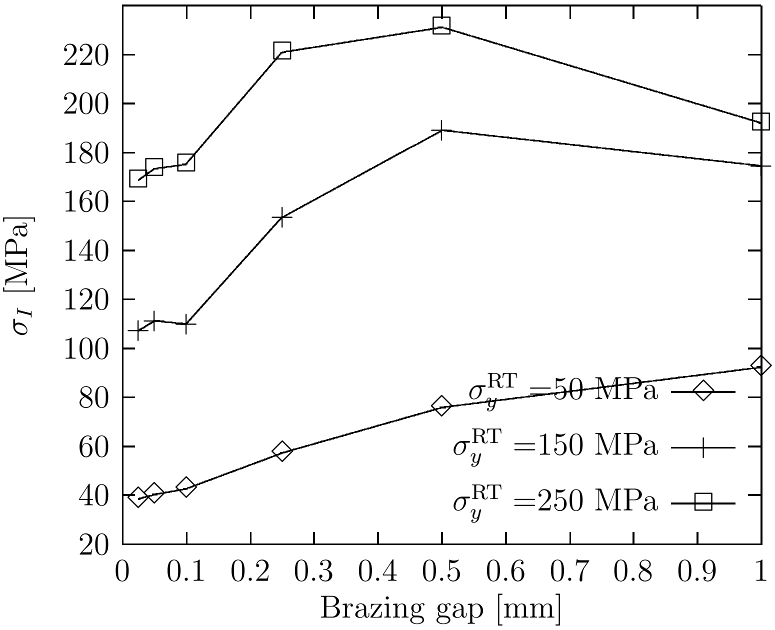

Figure A.54: Al_2O_3-steel: $\alpha = 1.0 \cdot 10^{-5}$ ℃$^{-1}$, brazing temperature 1000℃.

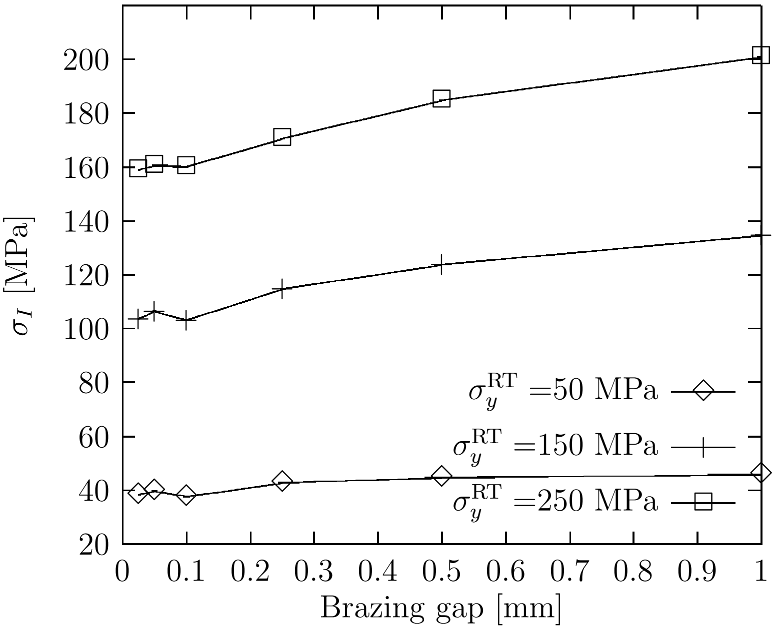

Figure A.55: Al_2O_3-steel: $\alpha = 1.5 \cdot 10^{-5}$ ℃$^{-1}$, brazing temperature 700℃.

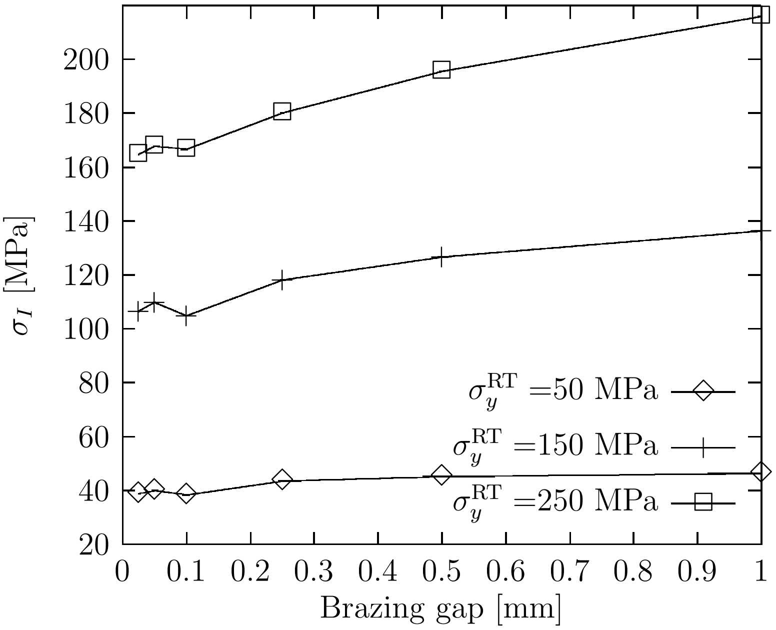

Figure A.56: Al_2O_3-steel: $\alpha = 1.5 \cdot 10^{-5}$ ℃$^{-1}$, brazing temperature 850℃.

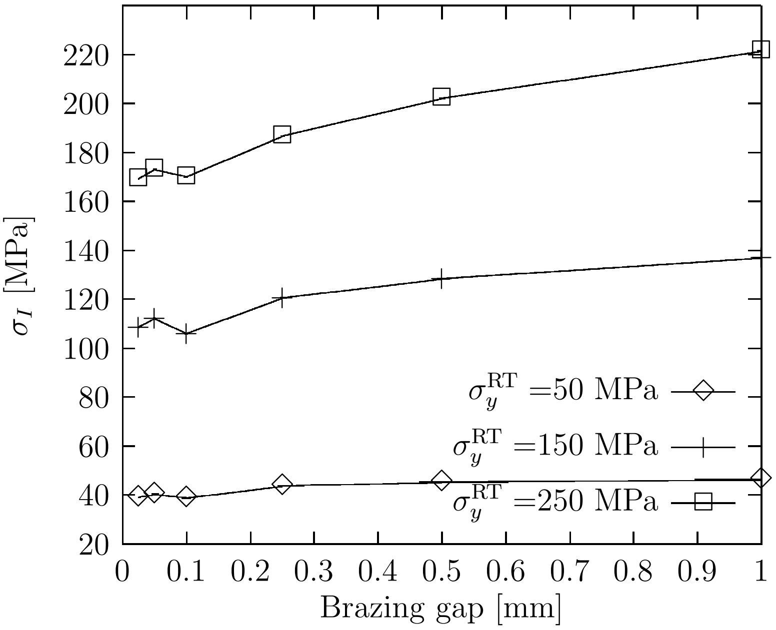

Figure A.57: Al_2O_3-steel: $\alpha = 1.5 \cdot 10^{-5}$ ℃$^{-1}$, brazing temperature 1000℃.

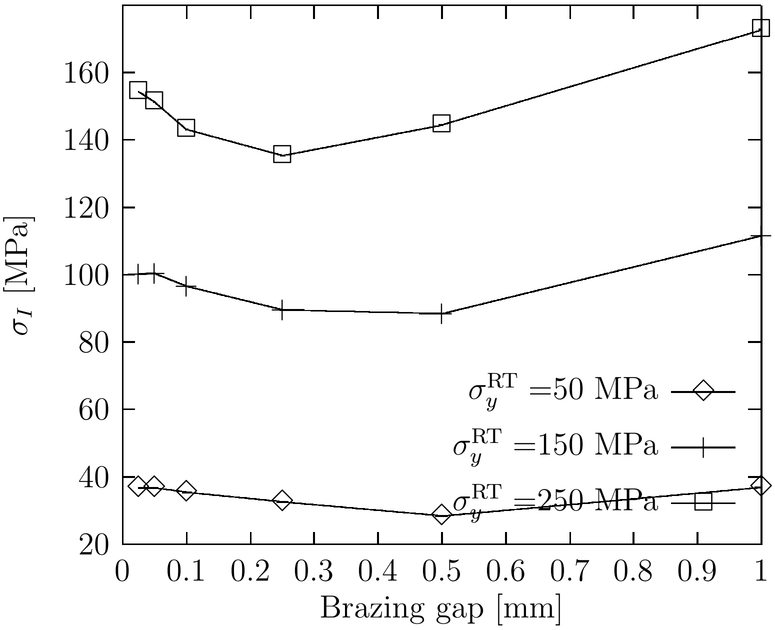

Figure A.58: Al_2O_3-steel: $\alpha = 2.0 \cdot 10^{-5}$ ℃$^{-1}$, brazing temperature 700℃.

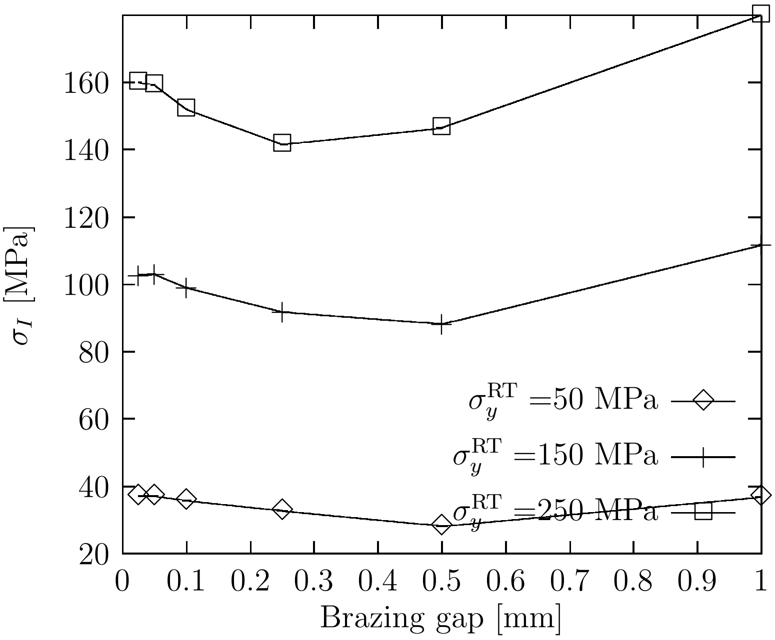

Figure A.59: Al_2O_3-steel: $\alpha = 2.0 \cdot 10^{-5}$ ℃$^{-1}$, brazing temperature 850℃.

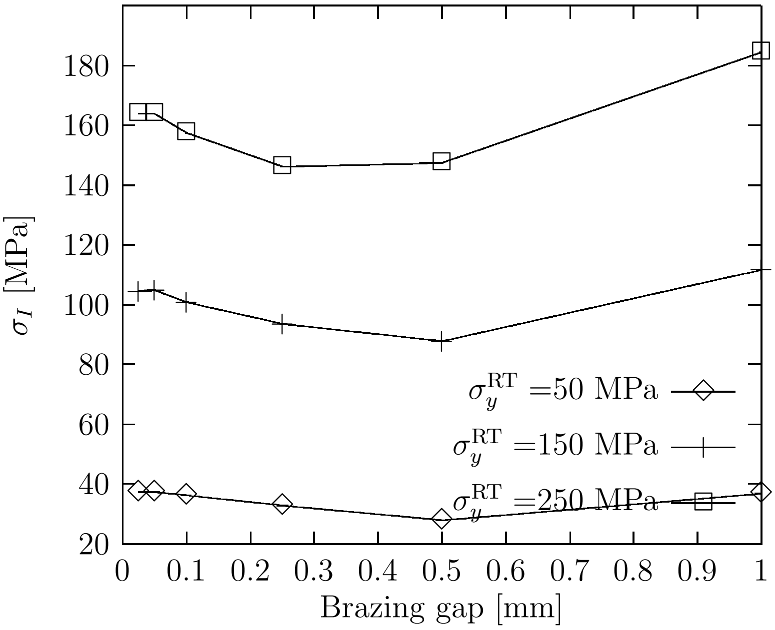

Figure A.60: Al_2O_3-steel: $\alpha = 2.0 \cdot 10^{-5}$ ℃$^{-1}$, brazing temperature 1000℃.

A.6 Al_2O_3-Kovar®

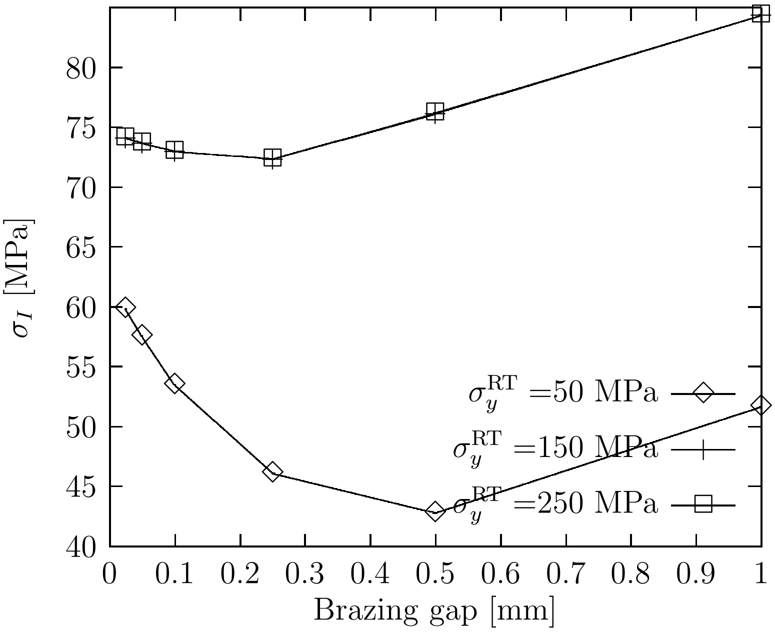

Figure A.61: Al_2O_3-Kovar®: $\alpha = 5.0 \cdot 10^{-6}$ ℃$^{-1}$, brazing temperature 700℃.

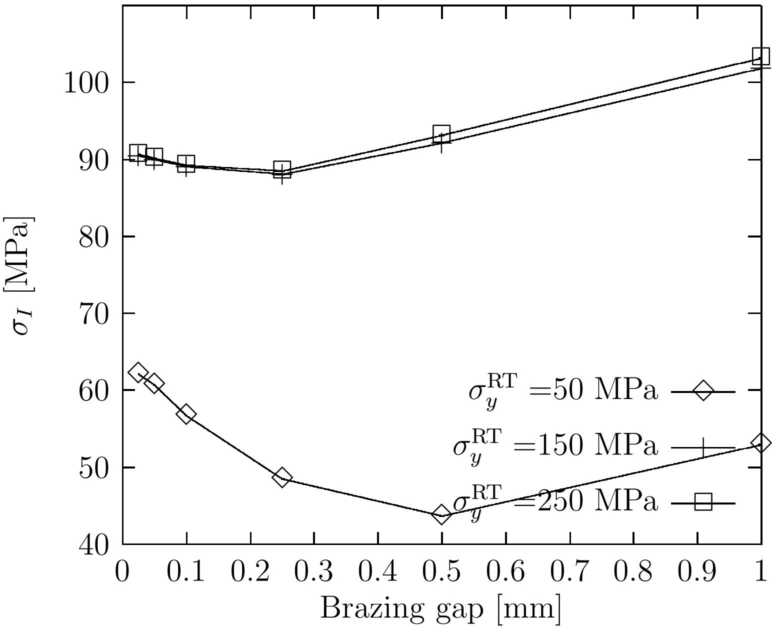

Figure A.62: Al_2O_3-Kovar®: $\alpha = 5.0 \cdot 10^{-6}$ ℃$^{-1}$, brazing temperature 850℃.

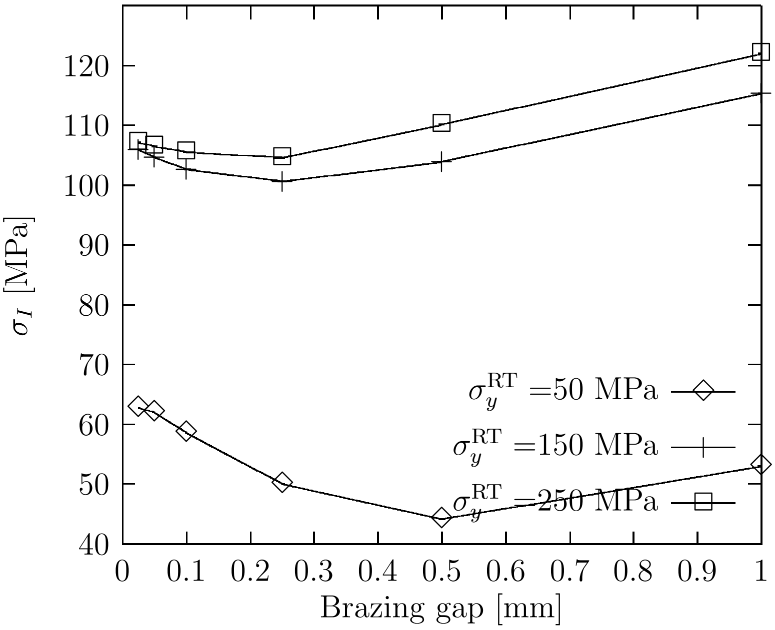

Figure A.63: Al_2O_3-Kovar®: $\alpha = 5.0 \cdot 10^{-6}$ ℃$^{-1}$, brazing temperature 1000℃.

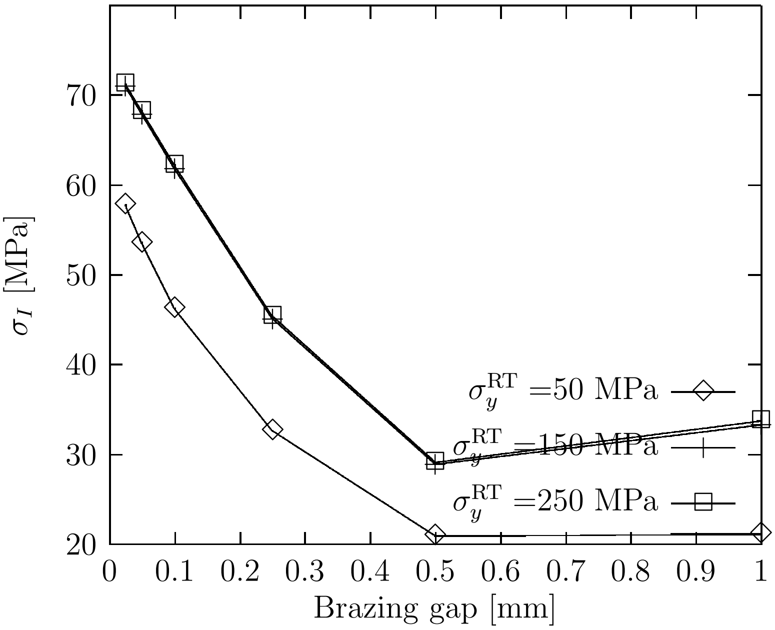

Figure A.64: Al$_2$O$_3$-Kovar®: $\alpha = 1.0 \cdot 10^{-5}$ ℃$^{-1}$, brazing temperature 700℃.

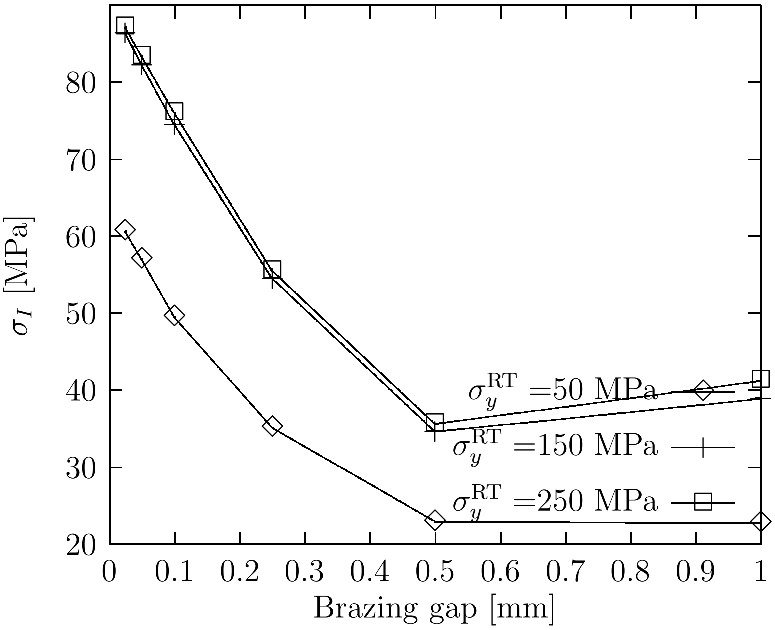

Figure A.65: Al$_2$O$_3$-Kovar®: $\alpha = 1.0 \cdot 10^{-5}$ ℃$^{-1}$, brazing temperature 850℃.

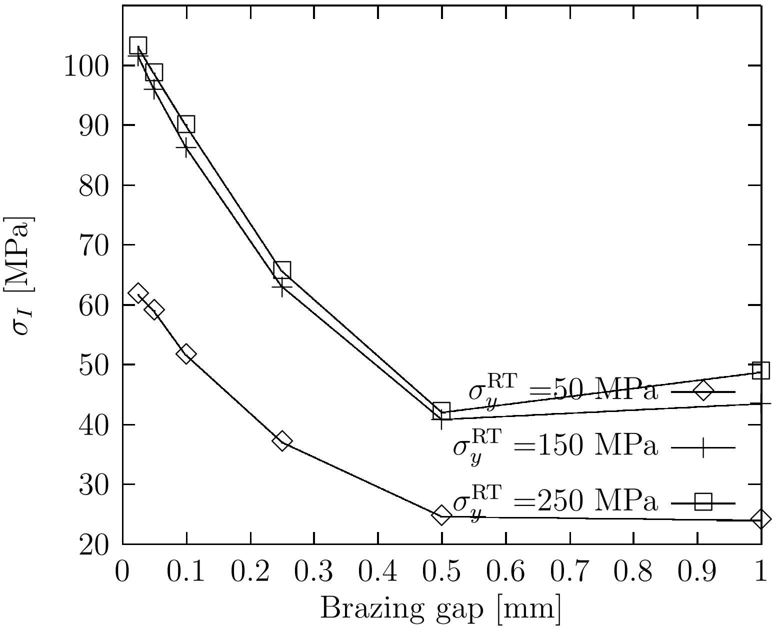

Figure A.66: Al_2O_3-Kovar®: $\alpha = 1.0 \cdot 10^{-5}$ ℃$^{-1}$, brazing temperature 1000℃.

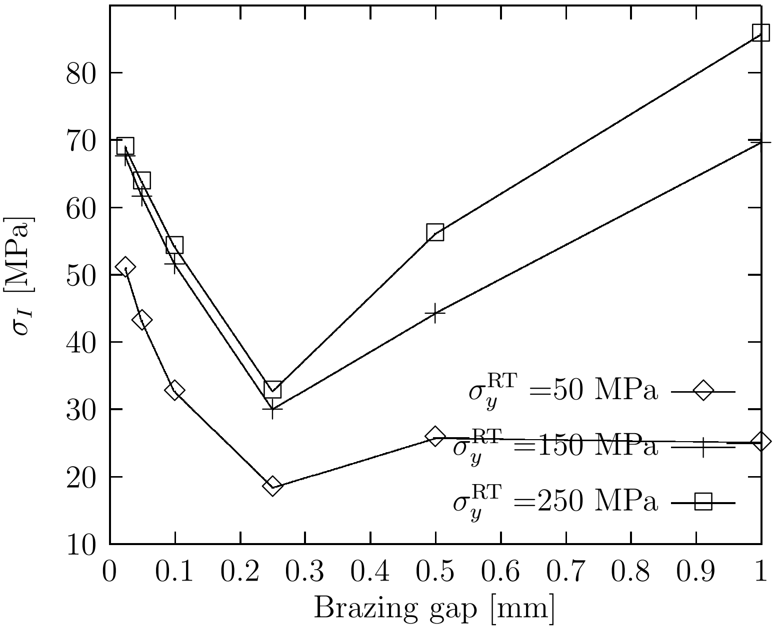

Figure A.67: Al_2O_3-Kovar®: $\alpha = 1.5 \cdot 10^{-5}$ ℃$^{-1}$, brazing temperature 700℃.

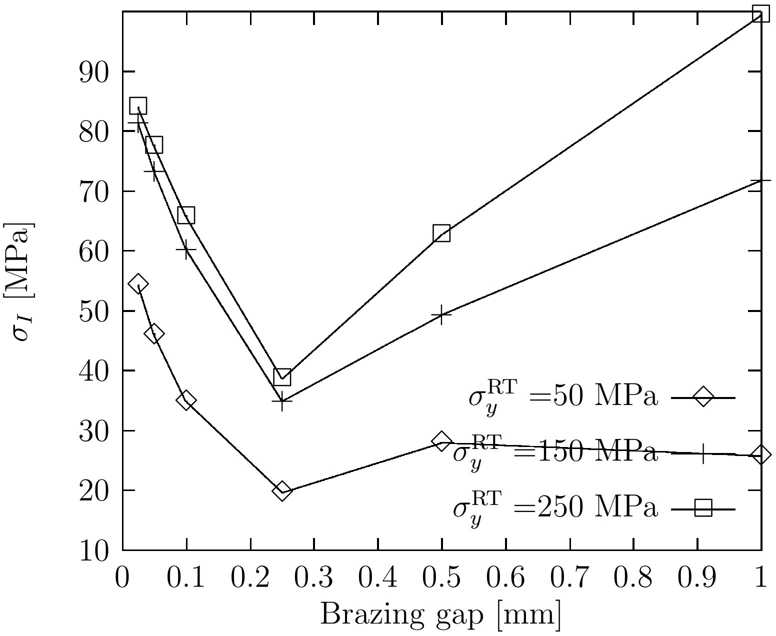

Figure A.68: Al$_2$O$_3$-Kovar®: $\alpha = 1.5 \cdot 10^{-5}$ °C^{-1}, brazing temperature 850°C.

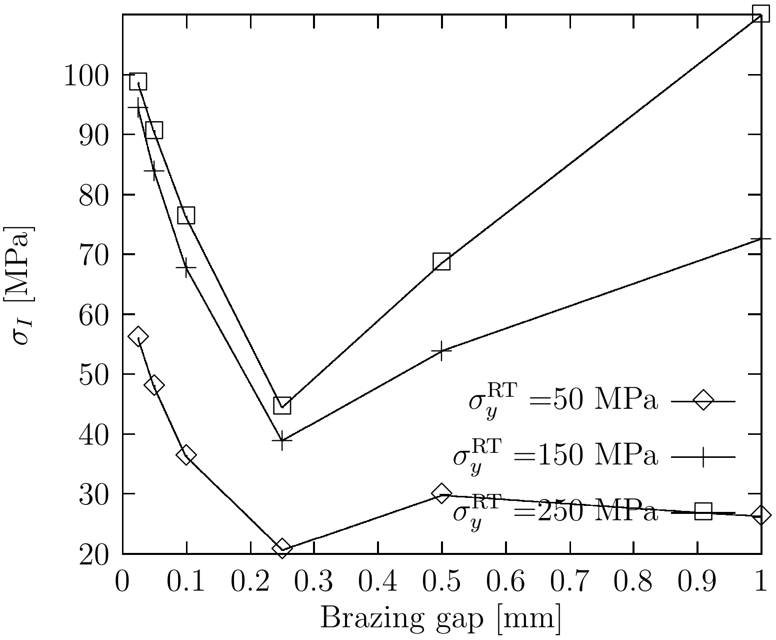

Figure A.69: Al$_2$O$_3$-Kovar®: $\alpha = 1.5 \cdot 10^{-5}$ °C^{-1}, brazing temperature 1000°C.

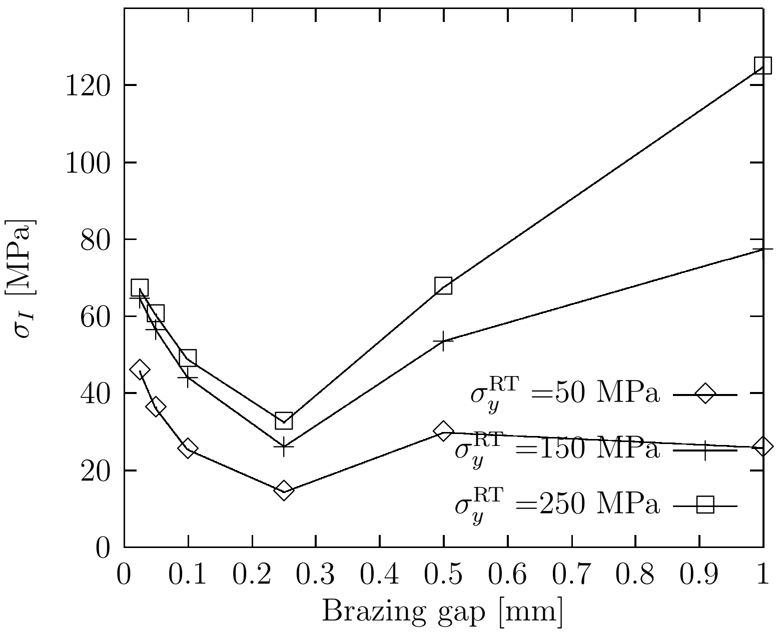

Figure A.70: Al_2O_3-Kovar®: $\alpha = 2.0 \cdot 10^{-5}$ ℃$^{-1}$, brazing temperature 700℃.

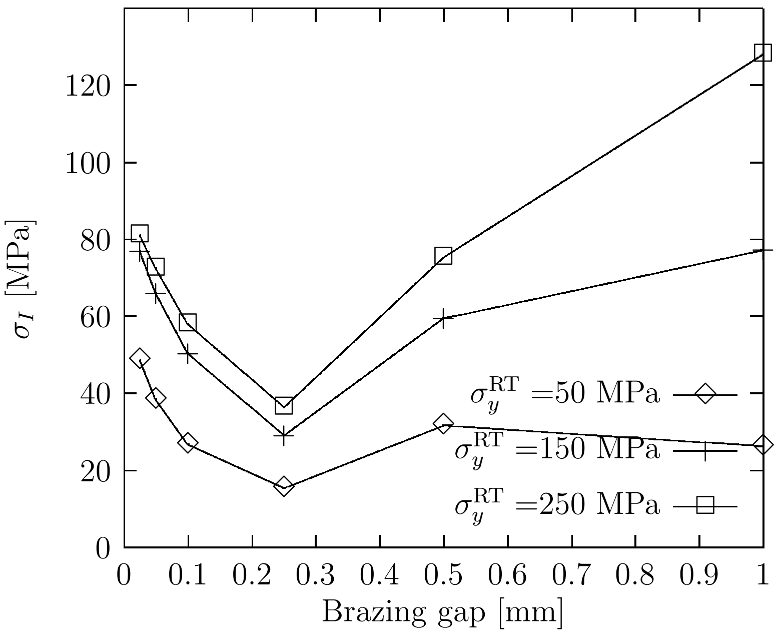

Figure A.71: Al_2O_3-Kovar®: $\alpha = 2.0 \cdot 10^{-5}$ ℃$^{-1}$, brazing temperature 850℃.

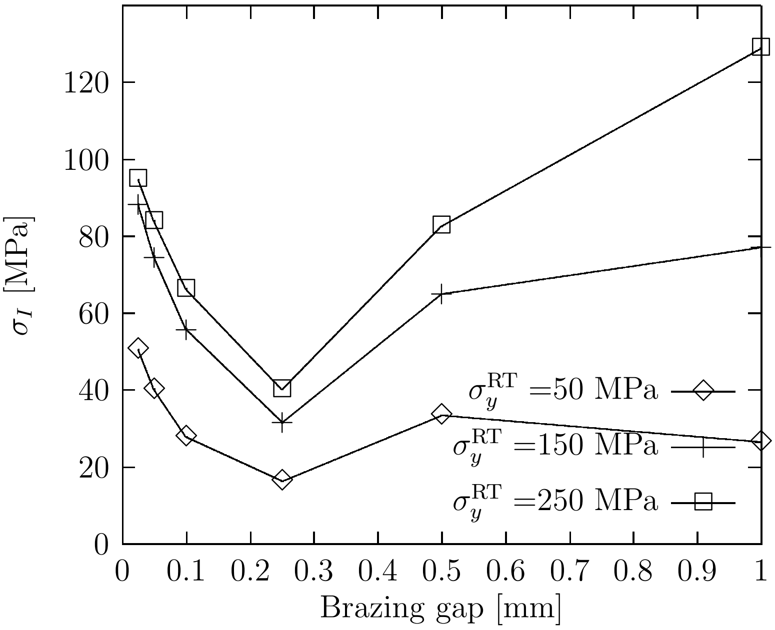

Figure A.72: Al_2O_3-Kovar®: $\alpha = 2.0 \cdot 10^{-5}$ ℃$^{-1}$, brazing temperature 1000℃.

Bibliography

[1] *ABAQUS 6.5 Analysis User's Manual.*

[2] ASTM E 8M - 94a Standard Test Methods for Tension Testing of Metallic Materials [Metric], 1995.

[3] EN843-1 Advanced technical ceramics - Monolithic ceramics - Mechanical properties at room temperature - Part 1: Determination of flexural strength, 1995.

[4] A. Abed, P. bin Hussain, I.S. Jalham, and A. Hendry. Joining of sialon ceramics by a stainless steel interlayer. *Journal of the European Ceramic Society*, 21(16):2803–2809, 2001.

[5] A. R. Akisanya. On the singular stress field near the edge of bonded joints. *Journal of Strain Analysis*, 32(4):301–311, 1997.

[6] O.M. Akselsen. Review: Advances in brazing of ceramics. *Journal of Materials Science*, 27:1989–2000, 1992.

[7] R. Arroyave and T.W. Eagar. Metal substrate effects on the thermochemistry of active brazing interfaces. *Acta Materialia*, 51(16):4871–4880, 2003.

[8] C. Badini, G. M. La Vecchia, P. Fino, and T. Valente. Forging of 2124/SiCp composite: preliminary studies of the effects on microstructure and strength. *Journal of Materials Processing Technology*, 116(2-3):289–297, 2001.

[9] A. Bartlett, A.D. Evans, and M. Rühle. Residual Stress Cracking of Metal/Ceramic Bonds. *Acta metall. mater.*, 39(7):1579–1585, 1991.

[10] V. Bhosle, E. G. Baburaj, M. Miranova, and K. Salama. Dehydrogenation of TiH2. *Materials Science and Engineering A*, 356(1-2):190–199, 2003.

[11] V. Bissig, M. Galli, and J. Janczak-Rusch. Comparison of Three Different Active Filler Metals Used for Brazing Ceramic-to-Ceramic and Ceramic-to-Metal. *Advanced Engineering Materials*, 8(3):191–196, 2006.

[12] B. E. Blackwell. *A framework for determining the mechanical properties of dissimilar material joints.* PhD thesis, Massachusetts Institute of Technology, 1996.

[13] G. Blugan, M. Hadad, J. Janczak-Rusch, J. Kuebler, and T. Graule. Fractography, Mechanical Properties, and Microstructure of Commercial Silicon Nitride-Titanium Nitride Composites. *Journal of the American Ceramic Society*, 88(4):926–933, 2005.

[14] G. Blugan, J. Janczak-Rusch, and J. Kuebler. Properties and fractography of Si3N4/TiN ceramic joined to steel with active single layer and double layer braze filler alloys. *Acta Materialia*, 52(15):4579–4588, 2004.

[15] H. J. Böhm. A Short Introduction to Basic Aspects of Continuum Mechanics. Technical report, Institute of Lightweight Structures and Aerospace Engineering, Vienna University of Technology, Austria, 1998.

[16] H. J. Böhm and W. Han. Comparisons between three-dimensional and two-dimensional multi-particle unit cell models for particle reinforced metal matrix composites. *Modelling and Simulation in Materials Science and Engineering*, 9:47–65, 2001.

[17] A. Borbely, H. Biermann, and O. Hartmann. FE investigation of the effect of particle distribution on the uniaxial stress-strain behaviour of particulate reinforced metal-matrix composites. *Materials Science and Engineering A*, 313(1-2):34–45, 2001.

[18] A. Borbely, F. F. Csikor, S. Zabler, P. Cloetens, and H. Biermann. Three-dimensional characterization of the microstructure of a metal-matrix composite by holotomography. *Materials Science and Engineering A*, 367(1-2):40–50, 2004.

[19] M. Bornert, T. Bretheau, and P. Gilormini. *Homogenization in Mechanics of Materials.* ISTE Publishing Company, 2007.

[20] J. L. Bucaille, A. Rossoll, B. Moser, S. Stauss, and J. Michler. Determination of the matrix in situ flow stress of a continuous fibre reinforced metal matrix composite using instrumented indentation. *Materials Science and Engineering A*, 369(1-2):82–92, 2004.

[21] M. Buchmann, R. Gadow, and J. Tabellion. Experimental and numerical residual stress analysis of layer coated composites. *Materials Science and Engineering A*, 288(2):154–159, 2000.

[22] H.C. Cao, M.D. Thouless, and A.D. Evans. Residual Stresses and Cracking in Brittle Solids Bonded with a Thin Ductile Layer. *Acta Metall.*, 36(8):2037–2046, 1988.

[23] Yan Ping Cao and Jian Lu. A new method to extract the plastic properties of metal materials from an instrumented spherical indentation loading curve. *Acta Materialia*, 52(13):4023–4032, 2004.

[24] N. Chawla, X. Deng, and D.R.M. Schnell. Thermal expansion anisotropy in extruded SiC particle reinforced 2080 aluminum alloy matrix composites. *Materials Science and Engineering: A*, 426(1-2):314–322, 2006.

[25] N. Chawla, R.S. Sidhu, and V.V. Ganesh. Three-dimensional visualization and microstructure-based modeling of deformation in particle-reinforced composites. *Acta Materialia*, 54(6):1541–1548, 2006.

[26] C.-C. Chiu. Determination of the Elastic Modulus and Residual Stresses in Ceramic Coatings Using a Strain Gage. *J. Am. Ceram. Soc.*, 73(7):1999–2005, 1990.

[27] L. Corradi Dell'Acqua. *Meccanica delle Strutture, 1, Il Comportamento dei Mezzi Continui*. McGraw-Hill, 1992.

[28] J. Cugnoni. *Identification par recalage modal et fréquentiel des propriétés constitutives de coques en matériaux composites*. PhD thesis, EPFL, 2004.

[29] J. Cugnoni, J. Botsis, and J. Janczak-Rusch. Size and Constraining Effects in Lead-Free Solder Joints. *Advanced Engineering Materials*, 8(3):184–191, 2006.

[30] J. Cugnoni, J. Botsis, V. Sivasubramanian, and J. Janczak-Rusch. Experimental and numerical studies on size and constraining effects in lead-free solder joints doi:10.1111/j.1460-2695.2006.01077.x. *Fatigue & Fracture of Engineering Materials and Structures*, 30(5):387–399, 2007.

[31] F. Deschaux-Beaume, F. Schmidt, N. Frety, T. Cutard, J. C. Boyer, and C. Levaillant. Numerical simulation of failure prediction for ceramic tools: comparison with forging test results. *Journal of Materials Processing Technology*, 92-93:502–507, 1999.

[32] W. J. Drugan and J. R. Willis. A micromechanics-based nonlocal constitutive equation and estimates of representative volume element size for elastic composites. *Journal of the Mechanics and Physics of Solids*, 44(4):497–524, 1996.

[33] H. D. Espinosa and P. D. Zavattieri. A grain level model for the study of failure initiation and evolution in polycrystalline brittle materials. Part I: Theory and numerical implementation. *Mechanics of Materials*, 35(3-6):333–364, 2003.

[34] J. Feder. Random sequential adsorption. *Journal of Theoretical Biology*, 87(2):237–254, 1980.

[35] Lian Gao, Jingguo Li, Takafumi Kusunose, and Koichi Niihara. Preparation and properties of TiN-Si3N4 composites. *Journal of the European Ceramic Society*, 24(2):381–386, 2004.

[36] C. Giacovazzo, H. L Monaco, D. Voterbo, F. Scordari, G. Gilli, G. Zanotti, and M. Catti. *Fundamentals of crystallography.* Oxford: Oxford University Press, 2005.

[37] C. Gonzalez, J. Segurado, and J. LLorca. Numerical simulation of elasto-plastic deformation of composites: evolution of stress microfields and implications for homogenization models. *Journal of the Mechanics and Physics of Solids*, 52(7):1573–1593, 2004.

[38] Z. Hashin and S. Shtrikman. A variational approach to the theory of the elastic behaviour of multiphase materials. *Journal of the Mechanics and Physics of Solids*, 11(2):127–140, 1963.

[39] S. Hazanov and C. Huet. Order relationships for boundary conditions effect in heterogeneous bodies smaller than the representative volume. *Journal of the Mechanics and Physics of Solids*, 42(12):1995–2011, 1994.

[40] M.Y. He and A.D. Evans. The Strength and Fracture of Metal/Ceramic Bonds. *Acta metall. mater.*, 39(7):1587–1593, 1991.

[41] M. R. Hill and W.-Y. Lin. Residual Stress Measurement in a Ceramic-Metallic Graded Material. *Journal of Engineering Materials and Technology*, 124(2):185–191, 2002.

[42] R. Hill. Elastic properties of reinforced solids: Some theoretical principles. *Journal of the Mechanics and Physics of Solids*, 11(5):357–372, 1963.

[43] E. L. Hinrichsen, J. Feder, and T. Jossang. Geometry of random sequential adsorption. *Journal of Statistical Physics*, 44(5 - 6):793–827, 1986.

[44] H. Holleck. Material Selection for Hard Coatings. *Journal of Vacuum Science and Technology A*, 4(6):2661–2669, 1986.

[45] C.-H. Hsueh. Some Considerations of Determination of Residual Stresses and Young's Moduli in Ceramic Coatings. *J. Am. Ceram. Soc.*, 74(7):1646–1649, 1991.

[46] J. L. Huang, M. T. Lee, H. H. Lu, and D. F. Lii. Microstructure, fracture behavior and mechanical properties of TiN/Si3N4 composites. *Materials Chemistry and Physics*, 45(3):203–209, 1996.

[47] P. Hussain and A. Isnin. Joining of austenitic stainless steel and ferritic stainless steel to sialon. *Journal of Materials Processing Technology*, 113(1-3):222–227, 2001.

[48] O.T. Iancu. *Berechnung von thermischen Eigenspannungsfeldern in Keramik/Metall-Verbunden.* PhD thesis, 1989.

[49] O.T. Iancu. Non-Singular Wedge Combinations of the Free Edge of a Brazed Ceramic-Metal Joint. *Computers and Structures*, 33(3):873–878, 1989.

[50] O.T. Iancu, D. Munz, B. Eigenmann, B. Scholtes, and E. Macherauch. Residual Stress State of Brazed Ceramic/Metal Compunds, Determined by Analytical Methods and X-ray Residual Stress Measurements. *J. Am. Ceram. Soc.*, 73(5):1144–1149, 1990.

[51] J. Intraner. Review of Some Processes for Ceramic-to-Metal Joining. *Materials and Manufacturing Processes*, 8(3):353–373, 1993.

[52] T. Iung and M. Grange. Mechanical behaviour of two-phase materials investigated by the finite element method: necessity of three-dimensional modeling. *Materials Science and Engineering A*, 201(1-2):L8–L11, 1995.

[53] D. Johnson-Walls, A.G. Evans, D.B. Marshall, and M.R. James. Residual Stresses in Machined Ceramic Surfaces. *J. Am. Ceram. Soc.*, 69(1):44–47, 1986.

[54] T. Kanit, S. Forest, I. Galliet, V. Mounoury, and D. Jeulin. Determination of the size of the representative volume element for random composites: statistical and numerical approach. *International Journal of Solids and Structures*, 40(13-14):3647–3679, 2003.

[55] P. Kenesei, A. Borbely, and H. Biermann. Microstructure based three-dimensional finite element modeling of particulate reinforced metal-matrix composites. *Materials Science and Engineering A*, 387-389:852–856, 2004.

[56] J. H. Kim and S. B. Lee. Stress intensity factors and crack initiation directions for ceramic/metal joint. *Theoretical and Applied Fracture Mechanics*, 30(1):27–38, 1998.

[57] T. W. Kim and S. W. Park. Effects of Interface and Residual Stress on Mechanical Properties of Ceramic/Metal System. *Key Engineering Materials*, 183-187:1279–1284, 2000.

[58] U.E. Klotz, F.A. Khalid, and H.-R. Elsener. Nanocrystalline phases and epitaxial interface reactions during brazing of diamond grits with silver based Incusil-ABA alloy. *Diamond and Related Materials*, 15(10):1520–1524, 2006.

[59] U. F. Kocks, H.-R. Wenk, and C. N. Tom. *Texture and Anisotropy: Preferred Orientations in Polycrystals and Their Effect on Materials Properties.* Cambridge University Press, 1998.

[60] C. Kohnle, O. Mintchev, and S. Schmauder. Elastic and plastic fracture energies of metal/ceramic joints. *Computational Materials Science*, 25(1-2):272–277, 2002.

[61] M. Kouzeli and A. Mortensen. Size dependent strengthening in particle reinforced aluminium. *Acta Materialia*, 50(1):39–51, 2002.

[62] S. P. Kovalev, P. Miranzo, and M. I. Osendi. Finite Element Simulation of Thermal Residual Stresses in Joining Ceramics with Thin Metal Interlayers. *Journal of the American Ceramic Society*, 81(9):2342–2348, 1998.

[63] S. Y. Kweon and S. K. Choi. Prediction of residual stress-induced cracking by finite element analysis. *Scripta Metallurgica et Materialia*, 32(3):359–364, 1995.

[64] H. Lan and T.A. Venkatesh. Determination of the elastic and plastic properties of materials through instrumented indentation with reduced sensitivity. *Acta Materialia*, 55(6):2025–2041, 2007.

[65] B.-T. Lee, Y.-J. Yoon, and K.-H. Lee. Microstructural characterization of electroconductive Si3N4-TiN composites. *Materials Letters*, 47(1-2):71–76, 2001.

[66] S.-B. Lee and J.-H. Kim. Finite-element analysis and X-ray measurement of the residual stresses of ceramic/metal joints. *Journal of Materials Processing Technology*, 67(1-3):167–172, 1997.

[67] S.-B. Lee, H. Kobayashi, and J. W. Huh. Fatigue strength and fracture mechanism of ceramic-metal joints under cyclic bending. *International Journal of Fatigue*, 17(6):427–435, 1995.

[68] W.-C. Lee. Strength of Si3N4/Ni-Cr-Fe alloy joints with test methods: shear, tension, three-point and four-point bending. *Journal of Materials Science*, 32:6657–6670, 1997.

[69] V.M. Levin. Thermal Expansion Coefficients of Heterogeneous Materials. *Mekhanika Tverdogo Tela*, 2:88–94, 1967.

[70] A. Levy. Thermal Residual Stresses in Ceramic-to-Metal Brazed Joints. *J. Am. Ceram. Soc.*, 74(9):2141–2147, 1991.

[71] A. Levy, A. Tobin, and G. Busch. Residual Stress Analysis and Microstrctural Observations of Ceraic-to-Metal Brazed Joints. *Metal-Ceramic Joining*, pages 133–151, 1990.

[72] J. Li and P. Xiao. Fabrication and characterisation of silicon carbide/superalloy interfaces. *Journal of the European Ceramic Society*, In Press, Corrected Proof.

[73] J.-G. Li. Wetting of Ceramic Materials by Liquid Silicon, Aluminium and Metallic Melts Containing Titanium and Other Reactive Elements. A Review. *Ceramics International*, 20:391–412, 1994.

[74] J. Q. Li, X. R. Zeng, J. N. Tang, and P. Xiao. Fabrication and thermal properties of a YSZ-NiCr joint with an interlayer of YSZ-NiCr functionally graded material. *Journal of the European Ceramic Society*, 23(11):1847–1853, 2003.

[75] J. Ligot, U. Welzel, P. Lamparter, A. C. Vermeulen, and E. J. Mittemeijer. Stress analysis of polycrystalline thin films and surface regions by X-ray diffraction doi:10.1107/S0021889804029516. *Journal of Applied Crystallography*, 38(1):1–29, 2005.

[76] Z. Ling, L. Luo, and B. Dodd. Experimental study on the formation of shear bands and effect of microstructure in Al-2124/SiCp composites under dynamic compression. *Journal de Physique IV*, C8:453–457, 1994.

[77] H. T. Liu and L. Z. Sun. Effects of thermal residual stresses on effective elastoplastic behavior of metal matrix composites. *International Journal of Solids and Structures*, 41(8):2189–2203, 2004.

[78] J. Mackerle. FEM and BEM analysis and modelling of residual stresses: A bibliography (1998-1999). *Finite Elements in Analysis and Design*, 37(3):253–262, 2001.

[79] K. Madsen, H. B. Nielsen, and O. Tingleff. Methods for Non-Linear Least Squares Problems, 1999.

[80] E. Martin, A. Forn, and R. Nogue. Strain hardening behaviour and temperature effect on Al-2124/SiCp. *Journal of Materials Processing Technology*, 143-144:1–4, 2003.

[81] J. J. Moré. The Levenberg-Marquardt algorithm: implementation and theory. In G. A. Watson, editor, *Lecture notes in mathematics. Numerical analysis*, volume 630, pages 105–116. Springer Verlag, Berlin, 1977.

[82] R. G. Munro. Material Properties of a Sintered alpha-SiC. *Journal of Physical and Chemical Reference Data*, 26:1195–1203, 1997.

[83] M. K. Neilsen, S. N. Burchett, C. M. Stone, and J. J. Stephens. A Viscoplastic Theory for Braze Alloys. Technical Report SAND96-0984, SANDIA, 1996.

[84] M. K. Neilsen, J. J. Stephens, and J. H. Gieske. A viscoplastic model for the eutectic silver-copper braze alloy. In F. M. Hosking, editor, *IBSC 2003*, page 9.5, San Diego, CA, 2003. AWS-ASM.

[85] Y. Nemoto, K. Ueda, M. Satou, A. Hasegawa, and K. Abe. Analysis and measurement of residual stress distribution of vanadium/ceramics joints for fusion reactor applications. *Journal of Nuclear Materials*, 258-263(2):1517–1522, 1998.

[86] M.G. Nicholas. *Joining Processes: Introduction to brazing and diffusion bonding.* Kluwer Academic Publishers, 1998.

[87] I. C. Noyan and J. B. Cohen. *Residual Stress Measurement by Diffraction and Interpretation.* Springer-Verlag, 1987.

[88] J. F. Nye. Physical properties of crystals: their representation by tensors and matrices. Oxford: Clarendon Press, 2004, 2004.

[89] C. Ohms, A. G. Youtsos, A. Bontenbal, and F. M. Mulder. Neutron diffraction facilities at the high flux reactor, Petten. *Physica B: Condensed Matter*, 276-278:160–161, 2000.

[90] T. Okamoto. Interfacial Structure of Metal-Ceramic Joints. *ISIJ International*, 30(12):1033–1040, 1990.

[91] J. W. Park, P. F. Mendez, and T. W. Eagar. Strain energy distribution in ceramic-to-metal joints. *Acta Materialia*, 50(5):883–899, 2002.

[92] Jin-Woo Park and Thomas W. Eagar. Strain energy release in ceramic-to-metal joints with patterned interlayers. *Scripta Materialia*, 50(4):555–559, 2004.

[93] M. K. Park and S. Bank. A Computational Investigation on Metal/Ceramic Joints under Thermal Cyclic Loadings. *Key Engineering Materials*, 183-187:529–534, 2000.

[94] A. Passerone and M. L. Muolo. Joining Technology in Metal-Ceramic Systems. *Materials and Manufacturing Processes*, 15(5):631–648, 2000.

[95] S.D. Peteves and M.G. Nicholas. Materials Factors Affecting Joining of Silicon Nitride Ceramics. *Metal-Ceramic Joining*, pages 43–65, 1990.

[96] G. J. Qiao, C. G. Zhang, and Z. H. Jin. Thermal cyclic test of alumina/kovar joint brazed by Ni-Ti active filler. *Ceramics International*, 29(1):7–11, 2003.

[97] M. D. Rintoul and S. Torquato. Reconstruction of the Structure of Dispersions. *Journal of Colloid and Interface Science*, 186(2):467–476, 1997.

[98] R.A. Schapery. Thermal Expansion Coefficients of Composite Materials Based on Energy Principles. *Journal of Composite Materials*, 2:380–404, 1968.

[99] V. M. Sglavo, M. Bonafini, and A. Prezzi. Procedure for residual stress profile determination by curvature measurements. *Mechanics of Materials*, 37(8):887–898, 2005.

[100] J. D. Sherwood. Packing of spheroids in three-dimensional space by random sequential addition. *Journal of Physics A: Mathematical and General*, 30(24):L839–L843, 1997.

[101] H. Si. TetGen A Quality Tetrahedral Mesh Generator and Three-Dimensional Dalaunay Triangulator, Version 1.3, User's Manual, 2005.

[102] R.S. Sidhu and N. Chawla. Three-dimensional (3D) visualization and microstructure-based modeling of deformation in a Sn-rich solder. *Scripta Materialia*, 54(9):1627–1631, 2006.

[103] V. Stamos, V. Kostopulos, and S.D. Peteves. Fracture Toughness Calibration of the Si3N4/Fe Joint System: a Parametric Study. *Fatigue and Fracture of Engineering Materials and Structures*, 19(4):441–450, 1996.

[104] J. J. Stephens. Elevated temperature creep properties for selected active metal braze alloys. In *Creep and Fracture of Engineering Materials and Structures*, pages 555–565. The Minerals, Metals and Materials Society, 1997.

[105] J. J. Stephens, S. N. Burchett, and F. M. Hosking. Residual Stresses in Metal/Ceramic Brazes: Effect of Creep on Finite Element Analysis Results. *Metal-Ceramic Joining*, pages 23–41, 1990.

[106] P. M. Suquet. Elements of Homogenization for Inelastic Solid Mechanics. *Lecture Notes in Physics*, 272:194–278, 1985.

[107] Colby C. Swan. Techniques for stress- and strain-controlled homogenization of inelastic periodic composites. *Computer Methods in Applied Mechanics and Engineering*, 117(3-4):249–267, 1994.

[108] M. Takahashi, N. Okabe, X. Zhu, and K. Kagawa. Strength estimation of ceramic-metal joints with various interlayer thickness. *Fatigue and Fracture of Engineering Materials and Structures*, 26(5):391–398, 2003.

[109] N. D. Tinsley, J. Huddleston, and M. R. Lacey. The Reduction of Residual Stress Generated in Metal-Ceramic Joining. *Materials and Manufacturing Processes*, 13(4):491–504, 1998.

[110] D. Travessa, M. Ferrante, and G. den Ouden. Diffusion bonding of aluminium oxide to stainless steel using stress relief interlayers. *Materials Science and Engineering A*, 337(1-2):287–296, 2002.

[111] P. T. Vianco, F. M. Hosking, J. J. Stephens, C. A. Walker, M. K Neilsen, S. J. Glass, and S.L. Monroe. Aging of Brazed Joints - Interface Reactions in Base Metal/Filler Metal Couples - Part I: Low-Temperature Ag-Cu-Ti Filler Metal. *Welding Research Supplement to Welding Journal*, (October):201s–210s, 2002.

[112] P. T. Vianco, F. M. Hosking, J. J. Stephens, C. A. Walker, M. K Neilsen, S. J. Glass, and S.L. Monroe. Aging of Brazed Joints - Interface Reactions in Base Metal/Filler Metal Couples - Part II: High-Temperature Au-Ni-Ti Braze Alloy. *Welding Research Supplement to Welding Journal*, (November):256s–264s, 2002.

[113] A.V. Virkar and J.F. Jue. Measurement of Residual Stresses in Oxide ZrO2 Three-Layer Composites. *J. Am. Ceram. Soc.*, 71(3):C–148–C–151, 1988.

[114] E. Voce. The relationship between stress and strain for homogeneous deformation. *Journal Institute of Metals*, 74:537–562, 1948.

[115] J. B. Wachtman. *Mechanical Properties of Ceramics*. Wiley-Interscience, 1996.

[116] X. L. Wang, B. H. Rabin, R. L. Williamson, S. A. David, C. R. Hubbard, and S. Spooner. Mapping of the residual stress distribution in a brazed zirconia-iron joint. *Materials Science and Engineering A*, 211(1-2):45–53, 1996.

[117] J. D. Whitcomb, I. S. Raju, and J. G. Goree. Reliability of the finite element method for calculating free edge stresses in composite laminates. *Computers & Structures*, 15(1):23–37, 1982.

[118] R.L. Williamson, B.H. Rabin, and J.T. Drake. Finite element analysis of thermal residual stresses at graded ceramic-metal interfaces. Part I. Model description and geometrical effects. *Journal of Applied Physics*, 74(2):1310–1320, 1993.

[119] R.L. Williamson, B.H. Rabin, and J.T. Drake. Finite element analysis of thermal residual stresses at graded ceramic-metal interfaces. Part II. Interface optimization for residual stress reduction. *Journal of Applied Physics*, 74(2):1321–1326, 1993.

[120] M. Wohlschlögel, T. U. Schülli, G. Maier, U. Welzel, and E. J. Mittemeijer. Characterization of a high performance laboratory parellel-beam diffractometer - bridging the gap to the synchrotron. In *Proceedings of the 10th European Powder Diffraction Conference (EPDIC) - Accepted for publication*, 2006.

[121] T. Yada and H. Koguchi. Reliability Evaluation of Joints of Ceramics and Metal (Consideration of Thermoelastic-Plastic Stress around the Interface of Jointed Dissimilar Materials). *JSME International Journal*, 34(2):163–170, 1991.

[122] M. Yang and K.-S. Kim. Interface fracture analysis of joints with a ductile interlayer. *International Journal of Fracture*, 64:201–210, 1993.

[123] J. H. You and G. Breitbach. Deformation of ductile braze layer in a joint element under cyclic thermal loads. *Fusion Engineering and Design*, 38(3):307–317, 1998.

[124] H.-Y. Yu, S. C. Sanday, and B. B. Rath. Residual Stresses in Ceramic-Interlayer-Metal Joints. *J. Am. Ceram. Soc.*, 76(7):1661–1664, 1993.

[125] C. Zhang, G. Qiao, and Z. Jin. Active brazing of pure alumina to Kovar alloy based on the partial transient liquid phase (PTLP) technique with Ni-Ti interlayer. *Journal of the European Ceramic Society*, 22(13):2181–2186, 2002.

[126] J. X. Zhang, R. S. Chandel, Y. Z. Chen, and H. P. Seow. Effect of residual stress on the strength of an alumina-steel joint by partial transient liquid phase (PTLP) brazing. *Journal of Materials Processing Technology*, 122(2-3):220–225, 2002.

[127] J. X. Zhang, R. S. Chandel, and H. P. Seow. Effects of chromium on the interface and bond strength of metal-ceramic joints. *Materials Chemistry and Physics*, 75(1-3):256–259, 2002.

[128] M. Zhu and D.D.L. Chung. Carbon Fiber Silver-Copper Laminate as a Composite Brazing Material for Metal-Ceramic Joining. *5th International SAMPE Electronics Conference*, pages 395–400, 1991.

[129] M. Zhu and D.D.L. Chung. Improving the strength of brazed joints to alumina by adding carbon fibres. *Journal of Materials Science*, 32:5321–5333, 1997.

[130] S. Zhu and W. Wlosinski. Joining of AlN ceramic to metals using sputtered Al or Ti film. *Journal of Materials Processing Technology*, 109(3):277–282, 2001.

Curriculum Vitæ

Matteo Galli

Personal Information:
Date of birth: 2nd May 1978.
Place of birth: Roma, Italy.

Education:
2003-2007: PhD student at LMAF (Laboratoire de mécanique appliquée et d'analyse de fiabilité) at EPFL.
2003: MS in civil engineering with a specialization in structures.
1997-2003: Student in civil engineering at Politecnico di Milano.

Teaching Experience:
2003-2007: Assistant for the course "Mechanics of Structures", Prof. I. Botsis, LMAF, EPFL.
2003, 2007: Assistant for the course "Continuum Mechanics", Prof. I. Botsis, LMAF, EPFL.

Publications:
Relief of the Residual Stresses in Ceramic-Metal Joints by a Layered Braze Structure, M.Galli, J.Botsis, and J.Janczak-Rusch, Advanced Engineering Materials 2006, 8(3), 197-201.
Comparison of Three Different Active Filler Metals Used for Brazing Ceramic-to-Ceramic and Ceramic-to-Metal, V.Bissig, M.Galli, and J.Janczak-Rusch, Advanced Engineering Materials 2006, 8(3), 191-196.
Selection and Design of Brazing Fillers for Metal-Ceramic Joints, V.Bissig, J.Janczak-Rusch, and M.Galli, Materials Science Forum 2007, 539-543, 4408-4012.
Experimental Assessment and Modeling of the Mechanical Behaviour of Particle Reinforced Active Braze Filler Metals, M.Galli, J.Botsis, and J.Janczak-Rusch, Proceedings of the 6th European Solid Mechanics Conference, ESMC 2006, 28 August 1 September, 2006 Budapest, Hungary.
An Elastoplastic Three Dimensional Homogenization Model for Particle Reinforced Composites, M.Galli, J.Botsis, and J.Janczak-Rusch, Computational Materials Science 2007, Accepted.